



Politecnico
di Torino

ScuDo
Scuola di Dottorato - Doctoral School
WHAT YOU ARE, TAKES YOU FAR



UNIVERSITÀ
DEGLI STUDI
DI TORINO

Doctoral Dissertation
Doctoral Program in Bioengineering and
medical and surgical sciences (34th Cycle)

Translating Computational Cardiology to Clinics: Improving Coronary Artery Disease Understanding, Prediction and Treatment via Computational Models

Maurizio Lodi Rizzini

* * * * *

Supervisor(s):

Prof. U. Morbiducci, Supervisor
Prof. D. Gallo, Co-Supervisor

Doctoral Examination Committee:

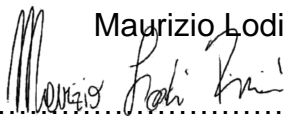
Prof. Sónia I. S. Pinto, Referee, University of Porto
Prof. Michele Conti, Referee, University of Pavia

Politecnico di Torino
2022

Declaration

This thesis is licensed under a Creative Commons License, Attribution - Noncommercial - NoDerivative Works 4.0 International: see www.creativecommons.org. The text may be reproduced for non-commercial purposes, provided that credit is given to the original author.

I hereby declare that the contents and organization of this dissertation constitute my own original work and does not compromise in any way the rights of third parties, including those relating to the security of personal data.


..... Maurizio Lodi Rizzini

2022

Abstract

Despite the dramatic advancement in medical care along the last two decades, coronary artery disease (CAD), consisting in the narrowing of coronary artery due to the formation of atherosclerotic plaques, is still the leading cause of death in western world. In the clinical framework, CAD severity may be assessed from an anatomical point of view relying on medical imaging and from a functional point of view, evaluating the flow impairment caused by the stenosis. These two not mutually exclusive but complementary approaches support the interventional cardiologist making decision on which lesions need to undergo percutaneous coronary intervention (PCI) and how to treat them. Parallel to the advancement in medical care, in the last decades computational methods have made strides and now candidate as promising tools to improve cardiovascular precision medicine and clinical decision medicine, with their capability of characterizing vessel-specific coronary hemodynamics with a spatial and temporal resolution unreachable with standard clinical measurements. Moving within this scenario this thesis work aims to test the potential and applicability of personalized computational fluid dynamics (CFD) simulations and automatic signal processing analysis to improve CAD diagnosis, understanding and treatment.

The first objective of this thesis was to explore the potential of wall shear stress (WSS), derived in a clinical framework with computational times compatible with the clinical practice, as a biomechanical marker for myocardial infarction (MI) prediction in mildly diseased coronary arteries. The analysis, focused on different aspects of WSS profiles, highlighted that the WSS profiles simulated within the clinical framework was adequately robust to discriminate lesions culprit for future MI, and that the variability of WSS expansion/contraction action exerted on the endothelium along the

cardiac cycle was a predictor stronger than the WSS magnitude and clinical currently adopted anatomical and functional quantities.

The second objective was to improve the understanding of the existing relationship between plaque phenotype, WSS patterns, and cellular response. This analysis, coupling intravascular imaging (optical coherence tomography, OCT), CFD simulations, and cellular gene expression, provided a clearer picture of the interplay between morphology, biomechanical stimuli, and *in vivo* cellular inflammatory pathways.

The clinical application of CFD-derived quantities is still hampered by the unavoidable assumptions made in the modelling of coronary hemodynamics. One of the major sources of uncertainty is due to inflow boundary conditions (BCs). The third objective of this thesis work was to quantify the budget of uncertainty related to velocity profile shape and flow rate values. These analyses indicated that three-dimensional velocity profile features affect CFD results only in the very proximal segment of coronary arteries.

Finally, the last objective of this thesis work was to improve CAD treatment through the analysis of the *in vivo* measured hemodynamic measure, the hyperemic pressure pullback signal. This analysis allowed to redefine the concept of disease length from a functional point view, overcoming the concept of anatomical defined disease length. Moreover, the mismatch between functional and anatomical disease length resulted a strong predictor of poor PCI outcome, giving insights for the improvement of CAD treatment.

In this era of great technological development, computational cardiology is becoming ready to be translated into clinical practice, presenting the potential to radically change patients' care, reducing cost and time for diagnosis and treatment. This thesis work wishes to contribute to the translation of *in silico* methods to interventional cardiology.

Contents

| | |
|--|----|
| 1. Introduction | 1 |
| 1.1 Coronary artery anatomy and physiology | 1 |
| 1.2 Coronary artery diseases | 3 |
| 1.2.1 Atherosclerosis plaque development | 3 |
| 1.2.2 The role of hemodynamics..... | 5 |
| 1.3 Hemodynamics descriptors | 7 |
| 1.3.1 Wall shear stress-based descriptors..... | 7 |
| 1.3.2 Helicity-based descriptors..... | 11 |
| 1.4 Clinical diagnosis of coronary artery disease | 13 |
| 1.4.1 Anatomical assessment of CAD | 14 |
| 1.4.1 Functional assessment of CAD..... | 16 |
| 1.5 Thesis objectives and outline | 18 |
| 2. Risk of Myocardial Infarction based on Endothelial Shear Stress Analysis Using Coronary Angiography | 23 |
| 2.1 Introduction | 24 |
| 2.2 Methods | 25 |
| 2.2.1 Study design..... | 25 |
| 2.2.2 Study population..... | 25 |
| 2.2.3 Coronary angiography and blood flow simulations | 26 |
| 2.2.4 Wall shear stress descriptors..... | 29 |
| 2.2.5 Statistical analysis | 32 |
| 2.3 Results..... | 32 |
| 2.3.1 Patients selection..... | 32 |

| | | |
|-------|---|----|
| 2.3.2 | Anatomical and functional parameters and risk for MI | 34 |
| 2.3.3 | Wall shear stress descriptors and risk for MI | 36 |
| 2.3.4 | Multivariable predictive models for MI..... | 39 |
| 2.3.5 | Time-to-event analysis..... | 42 |
| 2.4 | Discussion..... | 43 |
| 2.4.1 | A multidimensional approach to plaque vulnerability | 43 |
| 2.4.2 | Applicability and reliability of CFD simulations based on conventional angiography..... | 44 |
| 2.4.3 | Computational hemodynamics for MI prediction..... | 45 |
| 2.4.4 | Emerging role of TSVI | 46 |
| 2.4.5 | Limitations..... | 48 |
| 2.5 | Conclusions | 49 |
| 3. | Coronary Artery Plaque Rupture and Erosion: Role of Wall Shear Stress Profiling and Biological Patterns in Acute Coronary Syndromes..... | 50 |
| 3.1 | Introduction..... | 51 |
| 3.2 | Methods..... | 53 |
| 3.2.1 | Study design and population..... | 53 |
| 3.2.2 | Optical coherence tomography | 55 |
| 3.2.3 | Biological Analysis | 55 |
| 3.2.4 | Wall shear stress profiling..... | 58 |
| 3.2.4 | Wall shear stress profiling..... | 60 |
| 3.3 | Results | 61 |
| 3.2.1 | Biological Analysis | 61 |
| 3.2.2 | Wall shear stress profiling..... | 64 |
| 3.2.3 | Link between biology and wall shear stress profiling | 67 |
| 3.4 | Discussion | 68 |
| 3.5 | Conclusions..... | 71 |

| | |
|---|-----|
| 4. Does the inflow velocity profile influence physiologically relevant flow patterns in computational hemodynamic models of left anterior descending coronary artery? | 72 |
| 4.1 Introduction | 73 |
| 4.2 Methods | 75 |
| 4.2.1 Image data collection and 3D vessel reconstruction | 75 |
| 4.2.2 Computational hemodynamics and boundary conditions | 76 |
| 4.2.3 3D velocity profiles generation: analytical formulation | 77 |
| 4.2.4 Hemodynamic descriptors | 80 |
| 4.3 Results | 81 |
| 4.3.1 Near-wall hemodynamics | 81 |
| 4.3.1 Intravascular hemodynamics | 87 |
| 4.4 Discussion..... | 94 |
| 4.5 Conclusions | 97 |
| 5. Modelling coronary flows: impact of differently measured inflow boundary conditions on vessel-specific computational hemodynamic profiles | 98 |
| 5.1 Introduction | 99 |
| 5.2 Methods | 100 |
| 5.2.1 Patients selection and 3D vessel reconstruction..... | 101 |
| 5.2.2 Coronary flow rate estimation procedures | 102 |
| 5.2.3 Steady-state CFD simulations | 104 |
| 5.2.4 Unsteady-state CFD simulations | 105 |
| 5.2.5 Steady-state WSS-based descriptors | 106 |
| 5.2.5 Unsteady-state WSS-based descriptors | 107 |
| 5.2.6 Intravascular flow | 109 |
| 5.2.7 Statistical analysis | 110 |

| | |
|---|-----|
| 5.3 Results | 110 |
| 5.3.1 Coronary blood flow rate estimates | 110 |
| 5.3.2 Impact of flow rate estimation on steady-state WSS..... | 113 |
| 5.3.3 Impact of flow rate estimation on unsteady-state WSS..... | 119 |
| 5.3.4 Impact of flow rate estimation on unsteady-state WSS..... | 123 |
| 5.4 Discussion..... | 129 |
| 5.5 Conclusions | 133 |
| 6. Mismatch between morphological and functional assessment of the length of coronary artery disease..... | 134 |
| 6.1 Introduction | 135 |
| 6.2 Methods | 136 |
| 6.2.1 Study design | 136 |
| 6.2.2 Coronary angiographic analysis..... | 136 |
| 6.2.3 Optical Coherence Tomography | 138 |
| 6.2.4 Intracoronary pressure measurement and FFR pullback curve analysis..... | 138 |
| 6.2.4 Functional-anatomical mismatch (FAM) | 143 |
| 6.2.5 Procedure guidance and results | 144 |
| 6.2.6 Statistical analysis | 145 |
| 6.3 Results | 145 |
| 6.3.1 FFR pullback curve automatic classifier | 146 |
| 6.3.2 Functional anatomical mismatch..... | 149 |
| 6.4 Discussion..... | 153 |
| 6.5 Conclusions | 157 |
| 7. Conclusions and future works..... | 158 |
| 7.1 Summary and main contributions..... | 159 |
| 7.2 Future works | 164 |

| | |
|-------------------------------|-----|
| 8. References | 165 |
| 9. List of publications | 191 |
| Journal publications | 191 |
| Submitted manuscripts | 192 |
| Conference proceedings | 192 |

List of Figures

- Figure 1.1 Coronary anatomy and physiology.
Figure 1.2 Coronary artery typical waveforms.
Figure 1.3. Life cycle of atherosclerotic plaque.
Figure 1.4. Wall shear stress axial and secondary components.
Figure 1.5. Evolution of CAD diagnosis techniques.
Figure 1.6. Techniques for invasive anatomical assessment of CAD.
- Figure 2.1. Workflow of the study.
Figure 2.2. Normalized flow rate waveforms.
Figure 2.3. Action of the WSS at the blood-endothelium interface.
Figure 2.4. Relative anatomical lesion subdivision.
Figure 2.5. Flowchart of the patients included in the study.
Figure 2.6. Box plots of WSS-based descriptors in FCL and NCL.
Figure 2.7. Heat maps for clinical vs. expert CFD simulations.
Figure 2.8. ROC curves of the adopted wall shear stress descriptors.
Figure 2.9. ROC curves of the multivariate models.
Figure 2.10 Percentage of event rate at 5 years.
Figure 2.11. Time-to-event curves
Figure 2.12 Explanatory case of flow patterns and TSVI.
- Figure 3.1 Study design.
Figure 3.2 Angiography-OCT fusion.
Figure 3.3. Gene expression: CCS vs. unstable plaques.
Figure 3.4. Gene expression: IFC vs. RFC.
Figure 3.5. Wall shear stress magnitude.
Figure 3.6 Wall shear stress luminal distribution.
Figure 3.7 Surface area exposed to low wall shear stress magnitude.
Figure 3.8. Surface area exposed to high wall shear stress magnitude.
Figure 3.9 Biomechanical and molecular patterns of atherosclerotic plaques.
- Figure 4.1. Three-dimensional vessel reconstruction.
Figure 4.2. Generated velocity profiles.

Figure 4.3 Surface averaged WSS magnitude percentage difference.
Figure 4.4 Distribution of $|WSS|$ and percentage difference at the luminal surface: explanatory cases.
Figure 4.5 Distribution of $|WSS|$ at the luminal surface.
Figure 4.6 Theoretical vs. real entrance length.
Figure 4.7 Helical flow descriptors
Figure 4.8. Helical flow descriptors: percentage differences.
Figure 4.9. LNH isosurfaces visualization: explanatory cases.
Figure 4.10. LNH isosurfaces visualization.

Figure 5.1. Workflow of the study.
Figure 5.2. 3D vessel reconstructions.
Figure 5.3. Flow rate waveforms.
Figure 5.4. Flow rate analysis
Figure 5.5. WSS magnitude luminal distribution.
Figure 5.6. WSS magnitude luminal distribution: explanatory cases.
Figure 5.7. WSS magnitude quantitative analysis.
Figure 5.8. Low WSS magnitude surface area analysis.
Figure 5.9. normWSS quantitative analysis.
Figure 5.10. WSS directionality analysis.
Figure 5.11. Surface averaged WSS-based descriptors.
Figure 5.12. WSS-based descriptors correlation analysis.
Figure 5.13. SA for all WSS-based descriptors.
Figure 5.14. Similarity index for all WSS-based descriptors.
Figure 5.15. Steady-state WSS magnitude vs. unsteady-state TAWSS.
Figure 5.16. LNH isosurfaces visualization.
Figure 5.17. Helicity-based descriptors.
Figure 5.18. Helicity-based descriptors correlations.
Figure 5.19. Steady-state and unsteady-state helicity-based descriptors correlation.

Figure 6.1. Workflow of the study.
Figure 6.2. FFR pullback curve.
Figure 6.3. linearized FFR pullback curve.
Figure 6.4. Angiography-derived vs. OCT-derived FAM.
Figure 6.5. Automatic classifier visual performances.

Figure 6.6. Automatic classifier performance analysis.

Figure 6.7. Functional-anatomical length correlations.

Figure 6.8. FAM three-dimensional visualization: explanatory cases.

Figure 6.9. FAM correlations.

Figure 6.10. FAM sensitivity to serial lesions.

List of Tables

Table 2.1 WSS-based hemodynamic descriptors

Table 2.2. Clinical characteristics

Table 2.3 Results of QCA and vFFR analysis

Table 2.4 Results of the univariate prediction models (C-stat) for QCA and vFFR analysis

Table 2.5 Results of the univariate prediction models (C-stat) for TAWSS and TSVI

Table 2.6 Comparison of the predictive models for MI

Table 3.1 Baseline characteristics of the study population

Table 3.2 Effect of WSS on selected genes

Table 3.3 Biological results for gene expression

Table 3.4 Optical coherence tomography analysis results

Table 4.1 Percentage difference values of AWSS

Table 4.2 Entrance length

Table 4.3 Percentage difference values of average helicity intensity

Table 4.4 Absolute difference values of counter-rotating structures balance

Table 5.1 Unsteady-state WSS-based descriptors

Table 5.2 Helicity-based descriptors

Table 5.3 Flow rate and Reynolds numbers

Table 5.4 WSS-based descriptors surface averaged values

Table 6.1 Baseline clinical characteristics of the study population

Table 6.2 Anatomical, functional, and procedural characteristics

Chapter 1

Introduction

1.1 Coronary artery anatomy and physiology

Inside the cardiovascular system, coronary arteries play a key role, supplying oxygenated blood flow to the heart muscle. The two main coronary arteries are the left main and the right coronary arteries, both arising from small openings in correspondence of sinus of Valsalva (SV) in the ascending aorta¹ (Figure 1.1A).

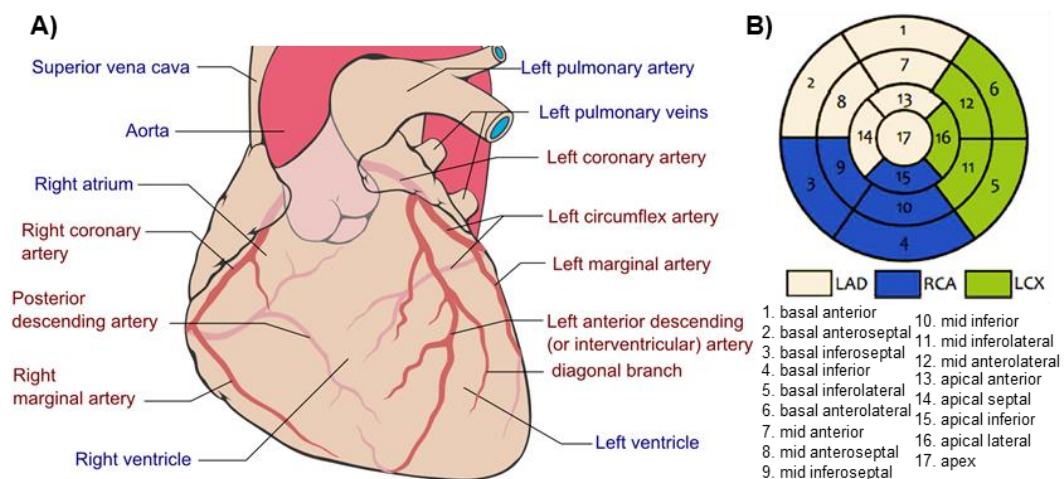


Figure 1.1 Coronary anatomy and physiology. A) Schematic coronary tree anatomy, coronary arteries are labeled in red text and other landmarks in blue text (https://www.wikiwand.com/en/Coronary_circulation). B) Circumferential plot of the myocardial segments with perfusion territories associated to each coronary artery branch: left anterior descending (LAD), left circumflex (LCX), and right coronary artery (RCA) (adapted from *Cerqueira et al.*²).

Left main coronary artery (LMCA) originates from the left SV and provide blood to the left part of the heart. After few centimeters from the ostium LMCA branches into left circumflex (LCX) and left anterior descending (LAD) coronary arteries. The LAD coronary artery follows the anterior intraventricular sulcus around the pulmonary trunk and provide blood flow to the front of the left side of the heart³ comprising basal anterior, basal anteroseptal, mid anterior, mid anteroseptal, apical anterior, apical septal segments, and the apex² (**Figure 1.1B**). The LCX coronary artery follows the coronary sulcus to the left encircling the heart muscle supplying blood to the outer side and back of the heart³, comprising basal inferolateral, basal anterolateral, mid inferolateral, mid anterolateral, and apical lateral segments² (**Figure 1.1B**).

Right coronary artery originates from the right SV and runs in the right portion of coronary sulcus delivering blood to the right atrium and to portions of both ventricles³ comprising basal inferoseptal, basal inferior, mid inferoseptal, mid inferior, and apical inferior segments² (**Figure 1.1B**) as well as to the electrical conduction system of the heart which regulates the heart rhythm.

Coronary blood flow is pulsatile and change during the cardiac cycle, exhibiting an opposite behavior with respect to the other systemic arteries. In detail the flow decreases during the systolic phase and present its maximum value during the diastole³. This is caused by the contraction of myocardial muscle which during systole compress the microvasculature within ventricular wall, increasing the hydraulic resistance and subsequently decreasing flow. When ventricles relax (diastolic phase) the compressive action stops and blood flow can increase reaching its peak before to fall with the decrease of aortic pressure. This behavior is more prominent in the left coronary artery (LCA) while RCA present a relative systolic dominance⁴⁻⁶ (**Figure 1.2**). This can be explained by the lower intraventricular pressure exerted on right with respect to the left ventricle causing a higher systolic pressure gradient in the RCA. Moreover, the myocardial microcirculatory resistance of right ventricular myocardium is significantly lower with respect to the left ventricle^{7,8}.

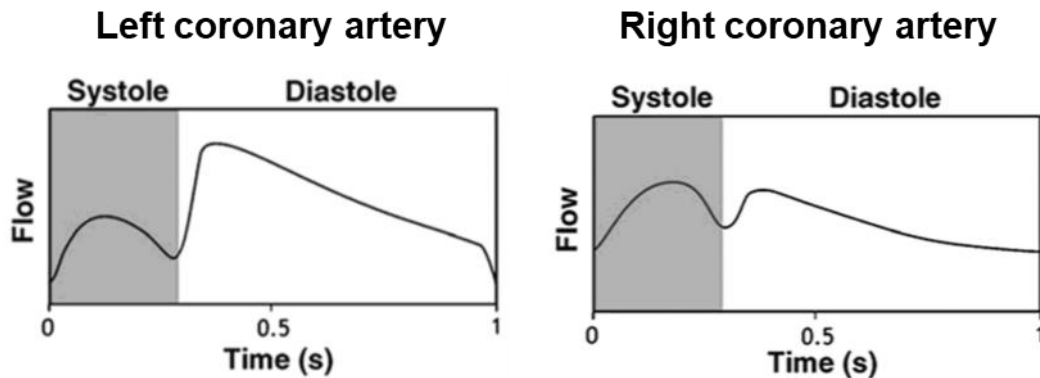


Figure 1.2 Coronary artery typical waveforms. Typical flow rate patterns at the left coronary artery (left) and the right coronary artery (right) over the cardiac cycle. Adapted from *Chatzizisis et al.*⁴.

1.2 Coronary artery diseases

Coronary artery disease (CAD) is the leading cause of death in western world resulting in about the 12% of death in the European Union in 2016⁹. CAD consists in the narrowing or the obstruction of epicardial coronary arteries with the subsequent deprivation of oxygenated flow to myocardium ultimately leading to the death of heart muscle causing the so-called myocardial infarction (MI). The main cause of CAD is the atherosclerosis, a complex and multifactorial pathological process which affect epicardial arteries causing the formation of a plaque composed of lipids and immune cells in the subendothelial space, called atheroma.

1.2.1 Atherosclerosis plaque development

In healthy arteries the endothelium, formed by a single layer of endothelial cells (EC), separates the arterial wall from the blood components of intravascular flow and produces vasoactive molecules, such as nitric oxide (NO) which as a vasodilator effect and endothelin (vasoconstrictor), preventing endothelial dysfunction¹⁰. An imbalance of these substances plays a key role in the initiation of atherosclerotic process. Although the underlying mechanisms of atherosclerosis are not fully elucidated there are two not mutually exclusive pathogenic hypothesis: the endothelial damage and the lipid hypothesis. Moreover, the most recent theories propose the inflammation as a key actor in each stage of atherosclerotic plaque development¹¹.

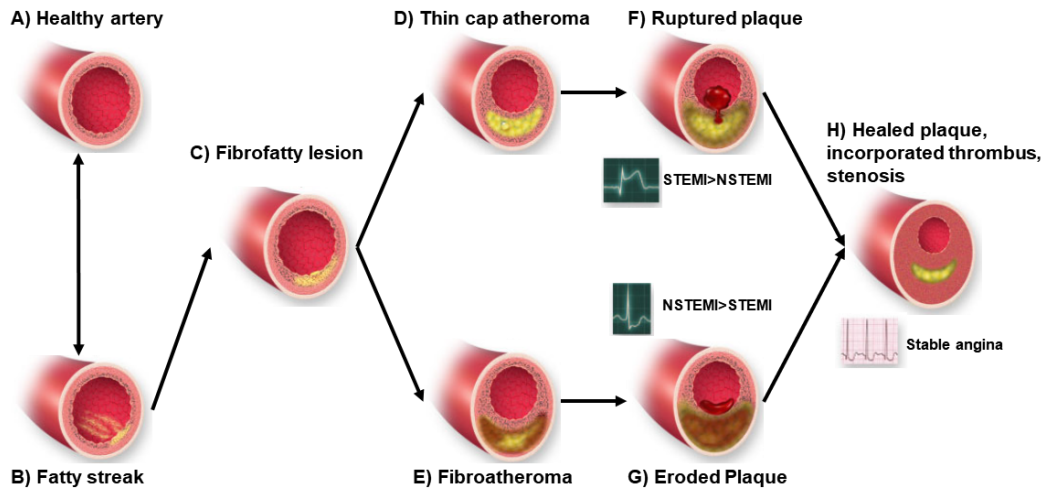


Figure 1.3. Life cycle of atherosclerotic plaque. A) a healthy artery. B) Initiation of fatty streak, at this stage the process may be reversible. C) fibrofatty lesion forms when smooth muscle cells (SMCs) migrate to the intima which covers the foam cells. In the evolution of the plaque foam cells and SMCs undergo death and extracellular lipid accumulates forming a lipid core covered by a fibrous cap. The fibrous cap could thin, due to the decreased synthesis and increased breakdown of extracellular matrix creating a thin cap atheroma (D). Another possible evolution involves an accumulation of more matrix than lipid resulting in a plaque with a thicker fibrous cap called fibroatheroma (E). Thin cap atheroma could rupture provoking thrombosis (F) with a prevalence of ST segment elevation myocardial infarction (STEMI) with respect to non-ST segment elevation myocardial infarction (NSTEMI). Fibroatheromas could more likely undergo to plaque erosion, complicated by the formation of a platelet-rich thrombus (white thrombus) and result in a prevalence of NSTEMI with respect to STEMI. Both ruptured and eroded plaques undergo to mechanisms typical of wound healing forming a healed plaque with a thicker fibrous cap less prone to rupture which could cause chronic stable angina (H). Adapted from *Libby*¹¹.

The first step is the development of a fatty streak at the arterial wall (**Figure 1.3B**). This may begin even in childhood and adolescence¹². It mainly depends on circulating risk factors, such as lipoproteins and systemic factors, like hypertension, smoking or obesity. Moreover, the focal nature of atherosclerosis, which develop at certain preferential sites, e.g., bifurcations or high curvature regions, introduce the disturbed flow as a factor in the development of atherosclerotic plaques, transducing the biomechanical signal into cellular pathways which may favor the lesion formation^{13,14}. In this first step the low-density lipoproteins (LDLs) accumulate inside the intima. Separated from the antioxidants circulating in the plasma LDL undergo to oxidation. Both experimental and human models show an accumulation of oxidized LDL in atherosclerotic plaques¹⁵. This accumulation leads to pro-atherogenic and pro-inflammatory processes

which activate smooth muscle cells (SMCs) attracting monocytes which transform in macrophage and take up lipids becoming foam cells.

The inflammation causes the production of extracellular proteoglycans, secreted by SMCs which augment the lipid-binding capacity. The accumulation of extracellular lipids provokes foam cells and SMCs death and triggering further inflammatory processes which play a key role in plaque progression. In this second study of evolution the plaque results in a fibrofatty lesion (**Figure 1.3C**) with a lipid-rich necrotic core covered by a fibrous cap just under the endothelium at the blood-wall interface.

The further evolution of plaque could lead to two different atherosclerotic plaques phenotypes: thin cap atheroma (**Figure 1.3D**) and fibroatheroma (**Figure 1.3E**). Thin-cap atheroma can rupture provoking the formation of a fibrin and red blood cells (RBCs) rich thrombus called red thrombus (**Figure 1.3F**) while fibroatheroma usually undergo to plaque erosion forming a platelet rich thrombus called white thrombus (**Figure 1.3G**). As a clinical manifestation plaque rupture is more prone to cause ST segment elevation myocardial infarction (STEMI), while plaque erosion more often gives rise to non-ST segment elevation myocardial infarction (NSTEMI)¹⁶.

Plaque rupture or erosion with subsequent thrombus formation could also be clinically silent and undergo to mechanisms typical of wound healing forming a healed plaque with a thicker fibrous cap (**Figure 1.3H**). This process may recur many times at a single site of arterial wall, resulting in multiple layers of healed tissue¹⁷ less prone to thrombus formation resulting in chronic angina.

1.2.2 The role of hemodynamics

As mentioned above, the focal nature and the location of atherosclerotic lesion in certain, geometrically predisposed areas, such as bifurcations, branching, or high curvature regions has introduced the hemodynamics as a triggering factor in the atherosclerosis initiation and development¹⁸. In particular wall shear stress (WSS) is a biomechanical cue sensed by multiple cell components and transduced to complex intra-cellular pathways which lead to the activation or deactivation of gene and protein expression.

Generally endothelial cells, exposed to unidirectional and high WSS align in the direction of flow assuming a quiescent state, for this region in healthy vessels and early atherosclerosis unidirectional WSS with magnitude values considered normal, in a range between 1 and 7 Pa, is considered atheroprotective¹⁹. On the contrary low and oscillating WSS is involved in endothelial cells activation leading to a pro-inflammatory state with the production of chemokines, cytokines, and adhesion molecules, leading to endothelial dysfunction²⁰.

In addition to WSS also intravascular flow features, such as helical flow patterns, observed in all human arteries was explained as a phenomenon which stabilize blood flow minimizing flow disturbances²¹ minimizing the area exposed to low and multidirectional WSS²². Moreover, very recently helical flow proved to be atheroprotective coronary arteries being associated with higher WSS regions²³ and a lower wall thickness change over time²⁴.

Hemodynamics in coronary arteries cannot be measured directly *in vivo* but need to be computed by solving the fluid motion equations: the Navier-Stokes equations. The most common adopted method to solve these equations is the computational fluid dynamics (CFD) which provide pressure and velocity fields, and subsequently WSS, at any point in space and time. Because of the complex four-dimensional nature of velocity and WSS vector fields in the last 40 years many descriptors were proposed to synthesize the information highlighting different characteristics. In the next paragraph the most used WSS- and velocity-based descriptors are presented.

1.3 Hemodynamics descriptors

Wall shear stress is a multifaceted parameter with a vectorial and four-dimensional nature. To synthesize the information many WSS-based descriptors were introduced during the last years accounting for WSS magnitude, pulsatility, multidirectionality, and topology.

1.3.1 Wall shear stress-based descriptors

Time averaged wall shear stress (TAWSS)

TAWSS is the simplest WSS-based descriptor, and it is calculated by integrating WSS-magnitude nodal values over the cardiac cycle:

$$\text{TAWSS}(\mathbf{x}) = \frac{1}{T} \int_0^T |\mathbf{WSS}(\mathbf{x}, t)| dt \quad (1.1)$$

Where T is the duration of cardiac cycle.

Oscillatory shear index (OSI)

OSI provide a numerical quantification of pulsatility of WSS vector field during the cardiac cycle. It quantifies the change of direction of WSS vector with respect to a predominant direction during the cardiac cycle and it is defined as²⁵:

$$\text{OSI}(\mathbf{x}) = 0.5 \left[1 - \frac{\left| \int_0^T \mathbf{WSS}(\mathbf{x}, t) dt \right|}{\int_0^T |\mathbf{WSS}(\mathbf{x}, t)| dt} \right] \quad (1.2)$$

OSI value ranges from zero when the instantaneous WSS vector does not change during the cardiac cycle to 0.5 when instantaneous WSS vector changes its direction in each time point of the cardiac cycle.

Relative residence time (RRT)

RRT is derived from the combination of TAWSS and OSI and it is defined as²⁶:

$$\text{RRT}(\mathbf{x}) = \frac{1}{(1-2\text{OSI}(\mathbf{x}))\text{TAWSS}(\mathbf{x})} \quad (1.3)$$

This index overcome the limitation of OSI which is not sensitive to WSS magnitude. In this way is possible to account for WSS magnitude and pulsatility.

Transverse wall shear stress (transWSS)

During the cardiac cycle WSS does not remain parallel to a single axis. The transWSS calculate the time-average over the cardiac cycle of WSS vector components orthogonal to the temporal mean WSS vector and it is defined as²⁷:

$$\text{transWSS}(\mathbf{x}) = \frac{1}{T} \int_0^T \left| \mathbf{WSS}(\mathbf{x}, t) \cdot \left(\mathbf{n} \times \frac{\int_0^T \mathbf{WSS}(\mathbf{x}, t) dt}{\left| \int_0^T \mathbf{WSS}(\mathbf{x}, t) dt \right|} \right) \right| dt \quad (1.4)$$

where \mathbf{n} is the normal to the vessel wall. The transWSS ranges between 0 and TAWSS value. Values near to 0 indicates that the flow remains approximatively parallel to a single axis during the cardiac cycle while high transWSS values indicates changes in flow direction during a large part of cardiac cycle or small changes in the direction of high-speed near-wall flow.

Cross flow index (CFI)

The instantaneous value of cross flow index CFI_i at the time point t_i can be defined as²⁸:

$$\text{CFI}_i(\mathbf{x}, t_i) = \frac{\mathbf{WSS}(\mathbf{x}, t_i)}{|\mathbf{WSS}(\mathbf{x}, t_i)|} \cdot \left(\mathbf{n} \times \frac{\int_0^T \mathbf{WSS}(\mathbf{x}, t) dt}{\left| \int_0^T \mathbf{WSS}(\mathbf{x}, t) dt \right|} \right) \quad (1.5)$$

Representing multidirectionality of WSS without consider its magnitude. It is the sine of the angle between the temporal mean of WSS vector and instantaneous WSS vector. The CFI results as the time average of these instantaneous components²⁸:

$$\text{CFI}(\mathbf{x}) = \frac{1}{T} \int_0^T \frac{\mathbf{WSS}(\mathbf{x}, t)}{|\mathbf{WSS}(\mathbf{x}, t)|} \cdot \left(\mathbf{n} \times \frac{\int_0^T \mathbf{WSS}(\mathbf{x}, t) dt}{\left| \int_0^T \mathbf{WSS}(\mathbf{x}, t) dt \right|} \right) dt \quad (1.6)$$

CFI ranges between 0 (no multidirectionality) and 1 (maximum multidirectionality).

Axial and secondary wall shear stress

WSS multidirectionality can be also described on the basis of vessel geometry, decomposing it in an axial direction (WSS_{ax}), defined by the tangent to the vessel centerline, correspondent to main flow direction, and secondary component (WSS_{sc}), orthogonal to the axial direction and related to secondary flows²⁹ (**Figure 1.4**).

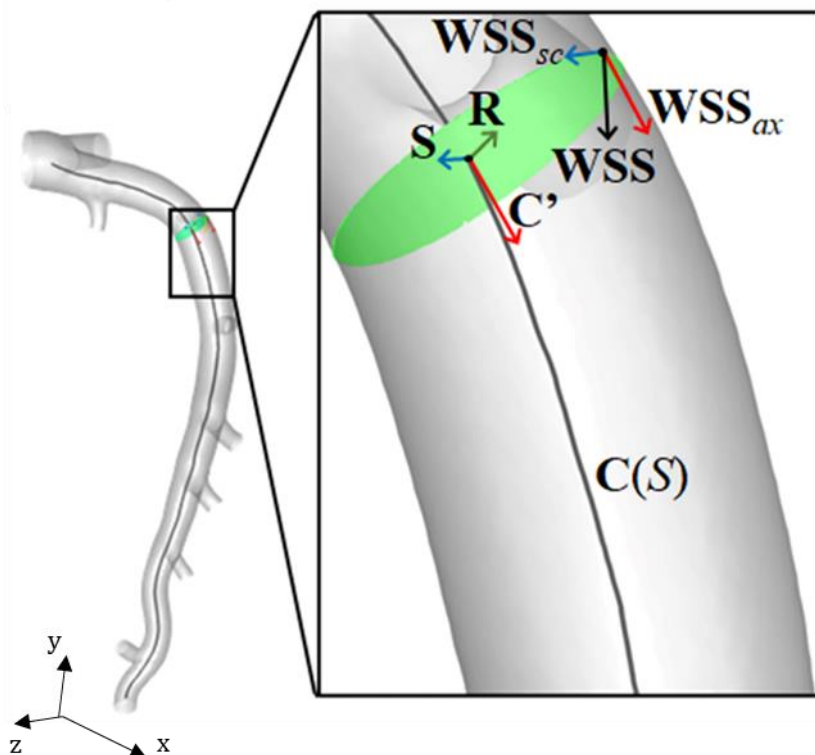


Figure 1.4. Wall shear stress axial and secondary components. Decomposition of wall shear stress (WSS) vector in its axial and secondary component. $\mathbf{C}(s)$ is the vessel centerline, \mathbf{C}' is the vector tangent to the centerline, \mathbf{R} is the vector orthogonal to \mathbf{C}' and normal to vessel surface, \mathbf{S} is the vector orthogonal to \mathbf{C}' and \mathbf{R} . Adapted from *De Nisco et al.*²⁴

WSS_{ax} is mathematically defined as²⁹:

$$WSS_{ax}(\mathbf{x}, t) = \frac{WSS(\mathbf{x}, t) \cdot \mathbf{C}'(\mathbf{x})}{|\mathbf{C}'(\mathbf{x})|} \frac{\mathbf{C}'(\mathbf{x})}{|\mathbf{C}'(\mathbf{x})|} \quad (1.7)$$

where \mathbf{C}' is the vector tangent to the vessel centerline \mathbf{C} .

WSS_{sc} can be obtained projecting the WSS vector along the direction of vector \mathbf{S} (**Figure 1.4**)²⁹:

$$\mathbf{WSS}_{sc}(\mathbf{x}, t) = \frac{\mathbf{WSS}(\mathbf{x}, t) \cdot \mathbf{S}(\mathbf{x})}{|\mathbf{S}(\mathbf{x})|} \frac{\mathbf{S}(\mathbf{x})}{|\mathbf{S}(\mathbf{x})|} \quad (1.8)$$

where \mathbf{S} is given by the external product of \mathbf{C}' and \mathbf{R} , the vector normal to vessel surface.

The information of axial and secondary component of WSS can be furtherly synthesized time averaging the two components:

$$TAWSS_{ax}(\mathbf{x}) = \frac{1}{T} \int_0^T |\mathbf{WSS}_{ax}(\mathbf{x}, t)| dt \quad (1.9)$$

$$TAWSS_{sc}(\mathbf{x}) = \frac{1}{T} \int_0^T |\mathbf{WSS}_{sc}(\mathbf{x}, t)| dt \quad (1.10)$$

And computing the ratio between the two components during the cardiac cycle:

$$WSS_{ratio}(\mathbf{x}) = \int_0^T \frac{|\mathbf{WSS}_{sc}(\mathbf{x}, t)|}{|\mathbf{WSS}_{ax}(\mathbf{x}, t)|} dt \quad (1.11)$$

When WSS_{ratio} is higher than 1 WSS_{sc} predominates during the cardiac cycle.

Wall shear stress topological skeleton

In the last years wall shear stress topological skeleton is obtaining a great interest, due to its ability to capture WSS features related to flow stagnation, separation and recirculation, as well as to blood-wall mass transfer³⁰⁻³⁴. Based on dynamical system theory the WSS vector field topological skeleton is composed by fixed points which are focal points where the WSS vanishes, and manifolds which are contraction or expansion regions which link fixed points.

The most widely adopted approach to identify WSS contraction and expansion region is the Lagrangian approach following the attracting or repelling behavior of the particles in the near-wall region. This approach demonstrated its potential in the analysis of WSS topological skeleton, but

it is extremely computational consuming, requiring the direct numerical integration to obtain the position of a great number of particles. Moreover, it requires a very refined spatial grid and very short time-steps to provide a reliable numerical integration. For these reasons very recently a Eulerian method able to identify WSS expansion and contraction regions was proposed³⁵.

Expansion and contraction regions are identified using the divergence of normalized WSS vector field³⁵:

$$\text{DIV}_{\text{WSS}}(\mathbf{x}, t) = \nabla \cdot \left(\frac{\mathbf{WSS}(\mathbf{x}, t)}{|\mathbf{WSS}(\mathbf{x}, t)|} \right) \quad (1.12)$$

Positive values of DIV_{WSS} identifies expansion regions, while negative values of DIV_{WSS} identifies contraction regions.

It is expected that WSS contraction and expansion action on EC is linked to vascular physiopathology. In particular, the high variability of WSS contraction and expansion during the cardiac cycle was recently linked to ascending aortic aneurysm wall degradation³⁶, long-term restenosis after carotid endarterectomy³⁷, and early-stage atherosclerosis in coronary arteries³⁸. The variation in WSS contraction/expansion action exerted on the endothelium of a vessel during the cardiac cycle is quantified using the WSS-based descriptor topological shear variation index (TSVI)³⁶:

$$\text{TSVI}(\mathbf{x}) = \left\{ \frac{1}{T} \int_0^T [\text{DIV}_{\text{WSS}}(\mathbf{x}, t) - \text{DIV}_{\text{WSS}}(\mathbf{x}, t)]^2 dt \right\}^{1/2} \quad (1.13)$$

1.3.2 Helicity-based descriptors

Local normalized helicity (LNH)

Helicity describes the local alignment between velocity (\mathbf{v}) and vorticity ($\boldsymbol{\omega}$) vectors. The kinetic helicity density H_k is defined as:

$$H_k(\mathbf{x}, t) = \mathbf{v}(\mathbf{x}, t) \cdot \boldsymbol{\omega}(\mathbf{x}, t) = \mathbf{v}(\mathbf{x}, t) \cdot \nabla \times \mathbf{v}(\mathbf{x}, t) \quad (1.14)$$

H_k is a pseudoscalar: its sign represents the right- or left-handed direction of helical blood flow patterns.

LNH was adopted to provide a qualitative picture of helical blood flow patterns inside blood vessels. Its Eulerian formulation is:

$$\text{LNH}(\mathbf{x}, t) = \frac{\mathbf{v}(\mathbf{x}, t) \cdot \boldsymbol{\omega}(\mathbf{x}, t)}{|\mathbf{v}(\mathbf{x}, t) \cdot \boldsymbol{\omega}(\mathbf{x}, t)|} \quad (1.15)$$

LNH is a normalized index and ranges between -1 and 1. Positive values of LNH are associated with the clockwise rotation (right-handed) of helical structures while negative values represent a counterclockwise rotation (left-handed).

Quantitative Eulerian helicity-based descriptors

LNH is a useful quantity for the visualization of helical flow structures in cardiovascular flows³⁹, but does not allow a quantitative analysis. Helical flow can be quantified using Lagrangian-based descriptors⁴⁰ or using more computationally convenient Eulerian descriptors defined as⁴¹:

$$h_1 = \frac{1}{T} \frac{1}{V} \int_0^T \int_V \mathbf{v}(\mathbf{x}, t) \cdot \boldsymbol{\omega}(\mathbf{x}, t) dV dt \quad (1.16)$$

$$h_2 = \frac{1}{T} \frac{1}{V} \int_0^T \int_V |\mathbf{v}(\mathbf{x}, t) \cdot \boldsymbol{\omega}(\mathbf{x}, t)| dV dt \quad (1.17)$$

$$h_3 = \frac{h_1}{h_2} \quad -1 \leq h_3 \leq 1 \quad (1.18)$$

$$h_4 = \frac{|h_1|}{h_2} \quad 0 \leq h_4 \leq 1 \quad (1.19)$$

where V is the integration volume.

The average helicity, h_1 , represents the average amount of helical flow during the cardiac cycle inside the integration volume; the helicity intensity, h_2 , quantifies the helicity intensity during the cardiac cycle inside the integration volume; the signed balance of helical flow structures, h_3 , measure the strength and prevalence (identified by the sign) of the relative rotations of helical flow structure; and the unsigned balance of helical flow structures, h_4 , measures only the strength of relative rotations of helical flow structures.

1.4 Clinical diagnosis of coronary artery disease

In its advanced state the atherosclerotic process in coronary arteries lead to the narrowing of arteries usually causing chest pain in the patients. Obviously, each atherosclerotic plaque is different, and interventional cardiologist have to decide when and how treat the disease.

The first method developed for the anatomical assessment of CAD was the invasive coronary angiography (ICA) which remain nowadays the gold standard. In the last decades (**Figure 1.5**) more sophisticated intravascular imaging techniques, i.e., optical coherence tomography (OCT), and intravascular ultrasound (IVUS) as well as non-invasive imaging techniques, i.e., coronary computed tomography angiography (CCTA) were introduced in clinical to further characterize the patients CAD to decide the most appropriate treatment⁴². Parallely to anatomical evaluation of CAD the functional assessment, i.e., pressure- and flow-based, such as fractional flow reserve (FFR), indices improved CAD diagnosis and treatment.

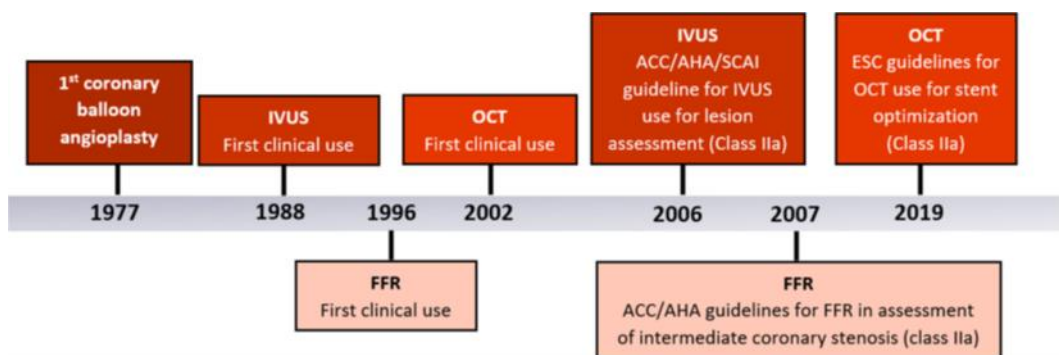


Figure 1.5. Evolution of CAD diagnosis techniques. After the first coronary angiography balloon angioplasty in 1977 several more advanced techniques were introduced to improve CAD diagnosis. In 1988 there was the first clinical use of IVUS, 8 years later, in 1996 FFR was introduced in clinical. OCT was then introduced in 2002. More recently the clinical use of these techniques was regulated, providing guidelines in 2006, 2007, and 2019 for IVUS, FFR, and OCT, respectively. Reprinted from *Steitieh et al.*⁴²

1.4.1 Anatomical assessment of CAD

The anatomical assessment of CAD is performed by means of medical imaging which can be invasive (i.e., ICA, IVUS, OCT) or non-invasive (i.e., CCTA).

Invasive coronary angiography

ICA (**Figure 1.6A**) is the most widely adopted anatomical-based diagnosis technique in interventional cardiology. The technique involves the insertion of a catheter in femoral or radial arteries to mini-invasively reach the coronary ostium using X-ray images as a guide. After the catheter is placed in the right position the contrast medium was injected to enhance the visibility of coronary arteries highlighting the local narrowing if present. The main advantage of this technique is the immediateness of information available to the interventional cardiologist. On the other hand, ICA present some limitations:

1. it is a two-dimensional imaging technique used to analyze the three-dimensional vascular structure. Many companies tried to overcome this limitation providing tools which allow the three-dimensional reconstruction starting from two angiographic projections. These algorithms, based on epipolar geometry, requires some assumptions, such as the elliptical shape of the vessel cross-section, without capturing the more complex blood vessel wall shape.
2. The inability to accurately assess the hemodynamic relevance of intermediate stenosis⁴³.

Intravascular ultrasound

IVUS (**Figure 1.6B**) is an invasive catheter-based imaging technique based on the reflection of sound waves and present a high penetration dept, allowing a detailed characterization of the atherosclerotic plaque, providing information about plaque size and calcifications. On the other hand, IVUS is not able to detect lipids and the relatively low resolution (200 μm) avoid the quantification of smaller plaque components and cap thickness. To overcome the inability of IVUS to detect lipids in atherosclerotic plaque

combined near-infrared spectroscopy (NIRS)-IVUS catheters were introduced, allowing to identify plaques containing a lipid-rich necrotic core.

Optical coherence tomography

OCT (**Figure 1.6C**) is another invasive catheter-based imaging technique which use low-coherence light to capture high spatial resolution (10 μm) optical scatter media such biological tissues. This allows in atherosclerotic coronary arteries a precise quantification of the fibrous cap thickness, a risk factor for plaque rupture, and plaque microstructures. Moreover, OCT is able to detect lipids and microcalcifications due to its nature. The main issue related to this technique is related to the limited penetration depth, avoiding the quantification of plaque components in large atherosclerotic plaques.

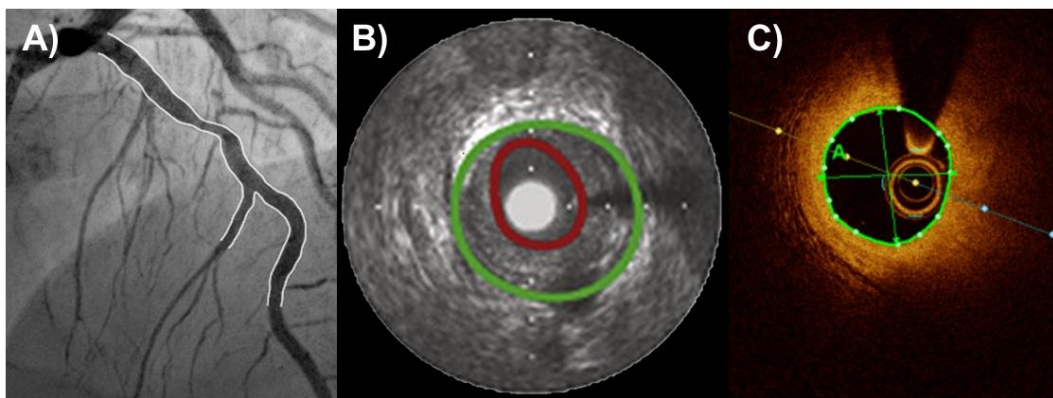


Figure 1.6. Techniques for invasive anatomical assessment of CAD. A) Invasive coronary angiography (ICA); B) intravascular ultrasound (IVUS); C) optical coherence tomography.

Coronary computed tomography angiography

CCTA is a non-invasive imaging technique which is gaining a great interest in the field of coronary interventions providing three-dimensional information about lesion length, severity, and plaque characteristic, allowing the selection of the correct size for stenting procedure. Moreover from the analysis of plaque characteristics enable the identification of high-risk plaque allowing the discrimination of non-calcified plaques, plaques with spotty calcifications or plaques with positive remodelling⁴⁴.

1.4.1 Functional assessment of CAD

Parallelly to anatomical lesion assessment some indices based on the measurement of blood flow, such as coronary flow reserve (CFR) and pressure, such as FFR and instantaneous wave-free ratio (iFR). More recently more advanced techniques to virtually compute FFR were introduced aiming to reduce time and costs of functional assessment of CAD.

Coronary flow reserve

CFR concept is based on the measure of baseline and hyperemic flow. The flow rate can be measured with different techniques which can be invasive, e.g., Doppler flow and continuous thermodilution, or non-invasive, e.g., positron emission tomography (PET) and magnetic resonance imaging (MRI)⁴⁵. CFR is defined as the ratio between maximal flow ($Q_{\text{Hyperemic}}$), inducing maximal hyperemia, and normal flow (Q_{Rest}) in resting condition:

$$\text{CFR} = \frac{Q_{\text{Hyperemic}}}{Q_{\text{Rest}}} \quad (1.20)$$

CFR measures the capacity of major resistance components represented by epicardial coronary arteries and microvascular bed. A CFR lower than 2 is associated to higher risk CAD⁴⁶. This measure presents some limitations:

1. it does not discriminate between epicardial and microvascular disease.
2. It can be altered by factors influencing the stability of resting conditions, e.g., volume loading conditions, contractility, tachycardia, and clinical conditions of the patient.

Fractional flow reserve

FFR is an invasive pressure-derived measure. It is defined as the ratio between the coronary pressure measured distally to a stenosis (P_d) and the aortic pressure (P_a) in condition of maximal hyperemia⁴⁷:

$$\text{FFR} = \frac{P_d^{\text{Hyperemic}}}{P_a^{\text{Hyperemic}}} \quad (1.20)$$

The condition of maximal hyperemia is achieved with drugs such as adenosine and allows to obtain a linear relationship between coronary flow and pressure representing a surrogate measure of the relative reduction of flow caused by an epicardial stenosis. In healthy vessel the FFR is theoretically equal to 1 while values lower than 0.75 are associated to ischemia suggesting to proceed with revascularization interventions^{48,49}. FFR resulted superior to the anatomical evaluation of coronary stenosis in clinical decision-making, preventing unnecessary stent implantation enhancing the clinical outcome of the patient⁴³.

Instantaneous wave free ratio

iFR is a recently proposed physiological index allowing to assess the functional significance of coronary lesion avoiding the use of hyperemia. This index is based on wave intensity analysis which allows the identification of a particular temporal window in the cardiac cycle called wave free period in which flow and pressure are linearly related so that the pressure ratio between distal and aortic pressure represent the flow impairment caused by the coronary stenosis:

$$iFR = \frac{P_d^{Wave\ free}}{P_a^{Wave\ free}} \quad (1.21)$$

Like FFR an iFR equal to 1 indicate a non-significant lesion while revascularization is suggested for lesion with iFR lower than 0.9. The main advantage of iFR with respect to FFR is that is a drug-free measurement. Moreover latest clinical trials reported an equivalence between iFR and FFR guided revascularization^{50,51}.

Virtual functional assessment of CAD

While FFR and iFR has become the standard of care in the evaluation of CAD functional significance its use is limited because of the increase of time and costs in the cathlab. For these reasons virtual alternatives to FFR were proposed by many companies (e.g., QFR from Medis Medical Imaging or vFFR from Pie Medical Imaging). While it is possible to use CFD simulations

to compute virtual FFR reconstructing the three-dimensional geometry of the vessel starting from two angiographic projections⁵², the commercially available solutions to speed-up the virtual FFR computation provides a surrogate measure applying analytical fluid dynamics law (i.e., Bernoulli's and Poiseuille's equations)⁵³. An alternative technique to virtually assess FFR is based on the coupling of non-invasive imaging (i.e., CCTA) and CFD simulations, called FFR_{CT} (HeartFlow Inc.) which represents the first widespread clinical application of CFD simulation⁵⁴ showing positive and promising results in the improvement of patients' care and significant CAD diagnosis⁵⁵. Moreover, a novel tool, called FFR_{CT} planner simulates the outcome of percutaneous coronary intervention (PCI) in terms of post-PCI FFR given to cardiologist the possibility of predict the benefit of PCI strategy applied to a specific lesion⁵⁶.

Even if the introduction of functional assessment of CAD had led to an improvement of lesion treatment some mechanisms which lead to plaque rupture and subsequent myocardial infarction still need to be elucidated to further improve the clinical decision-making.

1.5 Thesis objectives and outline

Computational methods and algorithms are promising tools in the improvement of CAD diagnosis, understanding and improvement of treatment. In this context, the thesis is divided in 2 parts: In the first part the potential and applicability of CFD simulations to improve diagnosis and understanding of CAD was investigated while in the second part the pressure pullback signal, a hemodynamic measure derived *in vivo*, was analyzed to improve CAD treatment. The objectives of this thesis project can be summarized as follows:

Part 1: Potential and applicability of CFD simulations to improve CAD diagnosis and understanding

1. To test the usefulness of endothelial shear stress as a potential clinical biomarker in the diagnosis of coronary atherosclerotic plaques at risk of rupture and prone to cause myocardial infarction.

2. Understand the relationship between atherosclerotic plaque phenotype, cellular gene expression, and endothelial shear stress pattern.
3. Quantify uncertainties in computational fluid dynamics simulations related to inflow boundary conditions to boost the clinical translation of computational hemodynamic-based descriptors.

Part 2: Improve CAD treatment analyzing pressure pullback signal

4. Improve CAD treatment with percutaneous coronary interventions analyzing the hyperemic automatic pressure pullback signal to redefine the concept of diseased length.

To address the above-mentioned hypotheses, the objectives of this thesis are elaborated in the next chapters as follows:

Part 1

Chapter 2 - Risk of Myocardial Infarction based on Endothelial Shear Stress Analysis Using Coronary Angiography

The identification of lesions prone to rupture is of paramount importance for medical management of patients with CAD. In clinical practice CAD evaluation was performed with an anatomical, and a functional assessment. Coronary atherosclerotic plaques experience a variety of hemodynamic stimuli and characteristic WSS features synthesized by means of WSS-based descriptors derived with CFD simulations may prove to have predictive capability for MI stronger than the traditional methods. To this aim 188 lesions (80 culprit for MI and 108 non-culprit for MI) were retrospectively selected and analyzed comparing the performance of three-dimensional quantitative coronary angiography (3D-QCA), vFFR, and WSS-based descriptors in the prediction of MI.

Chapter 3 - Coronary Artery Plaque Rupture and Erosion: Role of Wall Shear Stress Profiling and Biological Patterns in Acute Coronary Syndromes

Coronary atherosclerotic plaques might evolve to different phenotypes with a distinct morphology, plaque composition, and cellular gene expression.

On the other hand, local hemodynamics, and especially WSS, act on coronary plaques as a biomechanical stressor and is also involved in coronary artery plaque pathological mechanisms and modulation of gene expression. However, its relationship with coronary artery plaque phenotype and molecular patterns has not been investigated in acute coronary syndromes (ACS). In this chapter a comprehensive hemodynamic and biological description of unstable (intact-fibrous-cap, IFC, and ruptured-fibrous-cap, RFC) and stable (chronic coronary syndrome, CCS) plaques is provided. 24 CCS and 25 Non-ST Elevation Myocardial Infarction-ACS patients were enrolled, with IFC (n=11) and RFC (n=14) culprit lesions according to OCT analysis. A real-time PCR primer array was performed on for 17 different molecules whose expression is linked to WSS. CFD simulations were performed in high-fidelity 3D-coronary artery anatomical models reconstructed fusing ICA and OCT for 3 patients per group.

Chapter 4 - Does the inflow velocity profile influence physiologically relevant flow patterns in computational hemodynamic models of left anterior descending coronary artery?

Patient-specific CFD simulations are a powerful tool for investigating the hemodynamic risk in coronary arteries. Proper setting of flow boundary conditions in computational hemodynamic models of coronary arteries is one of the sources of uncertainty weakening the findings of *in silico* experiments, in consequence of the challenging task of obtaining *in vivo* 3D flow measurements within the clinical framework. Accordingly, in this chapter the influence of assumptions on inflow velocity profile shape on coronary artery hemodynamics is investigated. To do that, 10 left anterior LAD geometries were reconstructed from clinical angiography, and 11 velocity profiles with realistic 3D features such as eccentricity and differently shaped (single- and double-vortex) secondary flows were generated analytically and imposed as inflow boundary conditions. WSS and helicity-based descriptors obtained prescribing the commonly used parabolic velocity profile were compared with those obtained with the other velocity profiles to quantify the uncertainties related to the choice of velocity profile shape in patient-specific CFD simulations in coronary arteries.

Chapter 5 - Modelling coronary flows: impact of differently measured inflow boundary conditions on vessel-specific computational hemodynamic profiles

The translation of hemodynamic quantities based on WSS or intravascular helical flow into clinical biomarkers of coronary atherosclerotic disease is still hampered by the assumptions/idealizations required by the CFD simulations of the coronary hemodynamics. In the resulting budget of uncertainty, inflow boundary conditions (BCs) play a primary role. Accordingly, in this chapter the impact of the approach adopted for *in vivo* coronary artery blood flow rate assessment on personalized CFD simulations where blood flow rate is used as inflow BC was investigated. Therefore, CFD simulations were carried out on coronary angiograms by applying personalized inflow BCs derived from four different techniques assessing *in vivo* surrogates of flow rate: continuous thermodilution, intravascular Doppler, frame count-based 3D contrast velocity, and diameter-based scaling law. The impact of inflow BCs on coronary hemodynamics was evaluated in terms of WSS- and helicity-based quantities.

Part 2

Chapter 6 - Mismatch between morphological and functional assessment of the length of coronary artery disease

Anatomical evaluation of coronary lesion length is a paramount step during invasive assessment of CAD. Likewise, the extent of epicardial pressure losses can be measured using longitudinal vessel interrogation with fractional flow reserve FFR pullbacks redefining the CAD length using a functional definition. This chapter aims to quantify the mismatch in lesion length between morphological (i.e., based on quantitative coronary angiography, QCA, or optical coherence tomography, OCT) and functional evaluations (i.e., based on pressure pullback signal). This measure, called functional-anatomical mismatch (FAM) may be predictive of PCI outcome.

Chapter 7 - Conclusions and future works

In this last chapter final remarks of each previous chapter and possible future research applications are given.

Chapter 2

Risk of Myocardial Infarction based on Endothelial Shear Stress Analysis Using Coronary Angiography

A version of this chapter has been published in:

Atherosclerosis, Vol. 342, February 2022

Risk of Myocardial Infarction based on Endothelial Shear Stress Analysis Using Coronary Angiography

Alessandro Candreva, Mattia Pagnoni, **Maurizio Lodi Rizzini**, Takuya Mizukami, Emanuele Gallinoro, Valentina Mazzi, Diego Gallo, David Meier, Toshiro Shinke, Jean-Paul Aben, Sakura Nagumo, Jeroen Sonck, Daniel Munhoz, Stephane Fournier, Emanuele Barbato, Ward Heggermont, Stephane Cook, Claudio Chiastra, Umberto Morbiducci, Bernard De Bruyne, Oliver Muller, and Carlos Collet.

2.1 Introduction

Myocardial infarction (MI) remains a life-threatening complication of coronary artery disease (CAD)⁵⁷. MI frequently arise from thrombosis of lesions with large plaque burden⁵⁸. Coronary arteries and atherosclerotic plaques experience a variety of mechanical forces linked to plaque progression and destabilization^{59,60}. Among them, high pressure gradients across epicardial lesions have been recognized as independent predictors of myocardial infarction (MI)⁶¹. The frictional force of the flowing blood acting on the endothelium, i.e. wall shear stress (WSS), is also a key mechanism translating hemodynamic signals to vascular biological phenomena^{62,63}. In addition, WSS has been associated with vulnerable transformation of atherosclerotic lesions: low WSS has been linked to atherosclerosis progression, whereas high WSS has been associated with platelet activation and plaque rupture^{64,65}. More recently, WSS-based descriptors able to characterize the contraction/expansion action of endothelial shear forces along the cardiac cycle were associated with vascular pathophysiological processes in coronary^{66,67} and extra-coronary territories^{36,37}. In particular, a recent longitudinal study on swine models showed that early atherosclerotic changes in coronary arteries are associated with the endothelium shear stress contraction/expansion variability along the cardiac cycle, captured by the WSS-based quantity topological shear variation index (TSVI)⁶⁶.

Identification of lesions prone to rupture may personalize medical management in patients with CAD. The combination of computational fluid dynamic (CFD) quantities that can be extracted in a conventional clinical framework may prove to have predictive capability for MI. Accordingly, the present study aims to evaluate the usefulness of a comprehensive anatomical and hemodynamic assessment based on conventional coronary angiography, integrated by CFD simulations, for the identification of lesions prone to cause MI.

2.2 Methods

2.2.1 Study design

This is a case-control multicenter study including three European centers (OLV clinic, Aalst, Belgium; University of Lausanne, Switzerland; Fribourg Cantonal Hospital, Switzerland) designed to identify predictors of MI. Study protocol conforms to the ethical guidelines of the 1975 Declaration of Helsinki and has been approved by the Institution's ethics committee. Written informed consent was obtained from each patient included in the study.

2.2.2 Study population

Patients presenting with acute MI admitted for invasive coronary angiography were screened to identify those who:

1. had a previous coronary angiography (here forth referred as baseline angiography) performed between 1 month and 5 years before the index event
2. Had the visually identifiable mild lesion ($\leq 50\%$ visual diameter stenosis) culprit for the future MI at the baseline angiography.
3. Had at the baseline angiography at least one additional non-culprit lesion (NCL) in at least one of the other two major epicardial vessels.

Therefore, each patient served as its own control. Patient exclusion criteria were post-coronary artery bypass graft (CABG) status, MI as result of in-stent restenosis or thrombosis, MI in absence of angiographically identifiable coronary lesions, ostial lesions or lesions involving a coronary bifurcation with a side branch diameter ≥ 2 mm. In case of multiple coronary angiographies before the acute event, the latest angiography was selected for analysis.

Lesion selection (for both future culprit lesions, FCL, and NCL) was performed blinded to the MI information. Subsequently, three-dimensional geometries derived from coronary angiography of both FCL and NCL were generated for blood flow simulations.

2.2.3 Coronary angiography and blood flow simulations

The workflow of the study is presented in **Figure 2.1**.

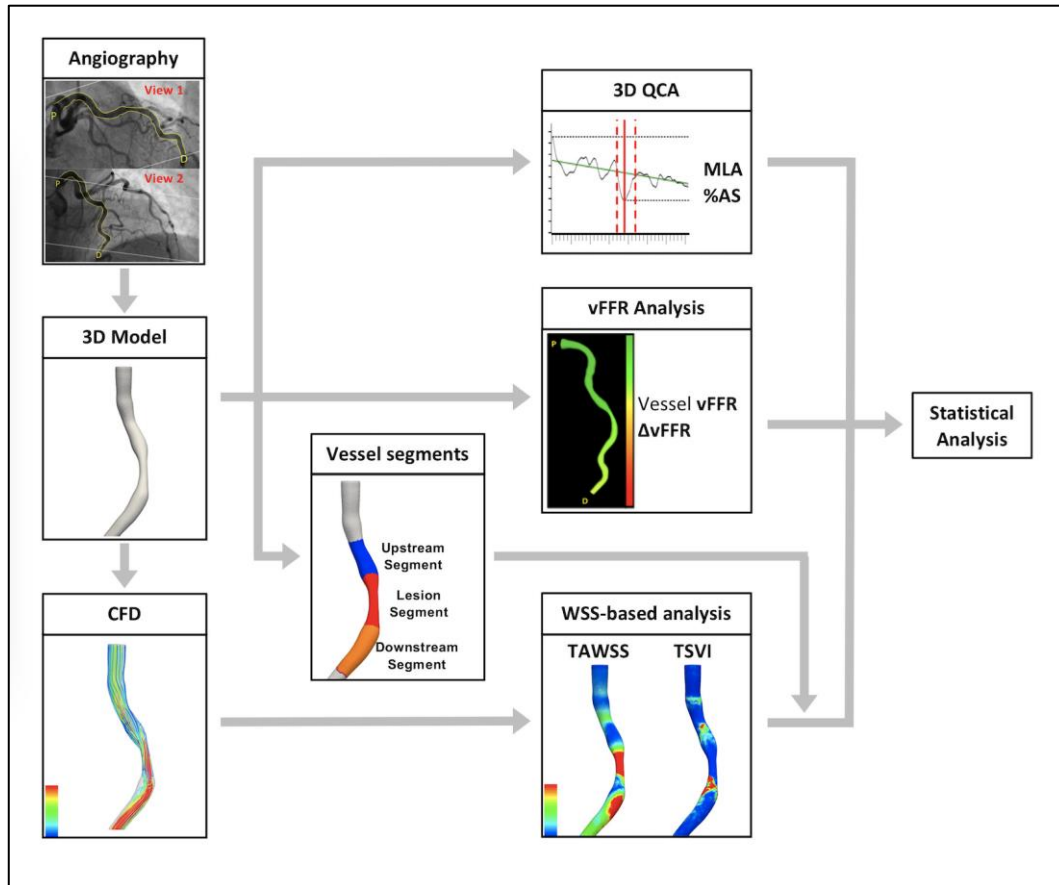


Figure 2.1. Workflow of the study. The geometrical information of the three-dimensional vessel reconstruction is exploited to compute in parallel quantitative coronary angiography (QCA) analysis as well as virtual fractional flow reserve (vFFR) and computational fluid dynamic (CFD)-derived wall shear stress (WSS) simulations.

Three-dimensional quantitative coronary angiography (3DQCA) reconstructions were performed using two angiographic end-diastolic frames at least 30 degrees apart using the CAAS Workstation WSS software (Pie Medical Imaging, Maastricht, the Netherlands). Automated lumen contour detection was enabled, and manually corrected when needed. Three-dimensional coronary reconstruction included at least 20 mm proximally and 20 mm distally from the minimal lumen diameter (MLD). Using the three-dimensional coronary reconstruction, transient CFD simulations to quantify WSS distribution along the cardiac cycle under resting conditions were carried out with two approaches:

1. the *clinical CFD*, using a finite element-based code (CAAS Workstation WSS software, Pie Medical Imaging, Maastricht, the Netherlands) with simulations performed by clinicians within a standard clinical framework.
2. The *expert CFD*, using a finite volume-based code with simulations performed by a CFD expert team with a greater accuracy and resolution to verify the reliability of clinical CFD.

Details about discretization and simulations setting are reported below.

In the clinical CFD setting the reconstructed three-dimensional fluid domain was discretized by means of NETGEN⁶⁸, using P1-P1 tetrahedral elements, according to a radius-based approach and 3 near-wall tetrahedral layers. The governing equations of fluid motion were solved in their discretized form under unsteady-state conditions by applying the finite element code Kratos⁶⁹, implemented in the CAAS Workstation WSS software (Pie Medical Imaging, Maastricht, the Netherlands). Blood was assumed as a homogeneous, incompressible, and Newtonian fluid with a density ρ equal to 1060 Kg/m³ and a dynamic viscosity μ equal to 0.0035 Pa·s. Vessel walls were assumed to be rigid and no-slip condition was applied at wall boundaries. Concerning boundary condition, since in vivo measured data were not available, generic Doppler curves were used for the left anterior descending (LAD), left circumflex (LCX), and right coronary arteries (RCA) (**Figure 2.2**). These curves were made patient-specific using a scaling law based on the individual diameter of the inlet cross-section, as proposed elsewhere⁷⁰. The resulting inlet flow rates were then prescribed in terms of parabolic velocity profiles at the inlet⁷¹. Concerning the outlet boundary conditions, a reference pressure was imposed at the outlet section. The settings used to perform CFD simulations go in the direction of a balance between the accuracy of the results and a computational time compatible with the clinical use of the software.

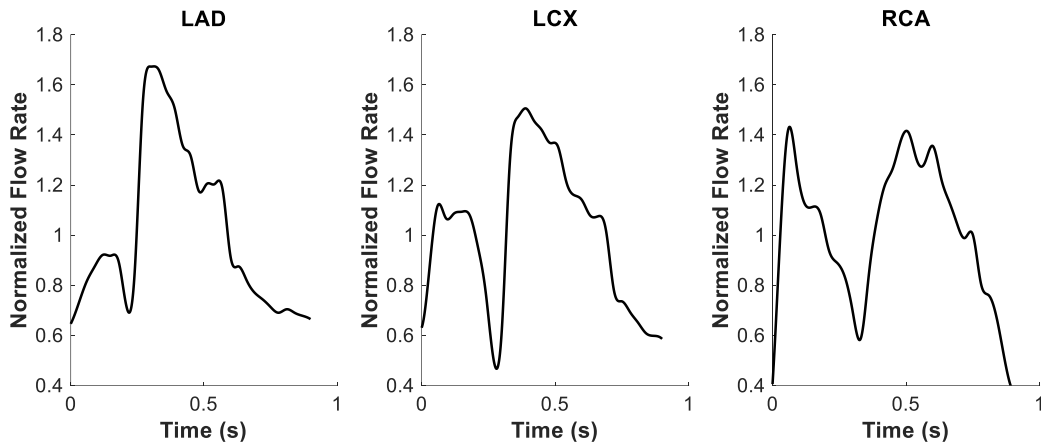


Figure 2.2. Normalized flow rate waveforms. Generic Doppler-based normalized flow rate curves typical for left anterior descending (LAD), left circumflex (LCX), and right coronary arteries (RCA), from left to right.

In the expert CFD setting the 3D vessel geometries were discretized using the software ICEM CFD (ANSYS Inc., Canonsburg, PA, USA), generating tetrahedral meshes with element edge size in the bulk ranging from 0.04 to 0.16 mm, a curvature-based refinement and five layers of prismatic elements close to the wall. The parameters were derived from grid independence analysis performed in a previous study⁷². The governing equations of fluid motion were solved in their discretized form under unsteady-state conditions using a commercial code based on the finite volume method (Fluent, ANSYS Inc.). In the expert CFD approach the rheological properties of blood were more realistically modelled than in the clinical CFD approach (where blood was considered as a Newtonian fluid). In detail, blood was considered as a continuous, incompressible ($\rho=1060$ kg/m³), non-Newtonian fluid implementing the Carreau model ($\mu_{\infty} = 0.0035$ kg/(m·s), $\mu_0 = 0.25$ kg/(m·s), $\lambda=25$ s, $n=0.25$)⁷³. Vessel walls were assumed to be rigid and no-slip condition was applied at wall boundaries. The applied boundary conditions were the same as the clinical CFD approach, detailed in the previous section. Regarding the applied numerical scheme, second-order accuracy was prescribed for both momentum and pressure equations, coupled using the full implicit Coupled pressure–velocity coupling scheme with explicit relaxation factors equal to 0.75 for pressure and momentum. The second order backward Euler implicit scheme was adopted for time integration, with a fixed time increment equal to 0.01 s. Convergence was

achieved when the maximum mass and momentum residuals fell below 10^{-5} .

3DQCA and the angiography-derived virtual fractional flow reserve (vFFR) were obtained using the CAAS Workstation vFFR software (Pie Medical Imaging) on the same angiographic projections selected for three-dimensional vessels reconstruction. Anatomical descriptors included percentage area stenosis (%AS), percentage diameter stenosis, minimal lumen area (MLA) and diameter, reference vessel diameter, lesion length and distance of MLA from the ostium. The distal vFFR, the translesional vFFR difference (Δ vFFR), and the absolute pressure drop in millimeters of mercury (mmHg) at the distal part of the vessel, i.e., distal pressure gradient, were extracted as detailed elsewhere⁷⁴.

2.2.4 Wall shear stress descriptors

The quantitative characterization of endothelial shear forces included the following WSS-based descriptors (**Table 2.1**): time-averaged wall shear stress (TAWSS); oscillatory shear index (OSI)²⁵; relative residence time (RRT)²⁶; transverse WSS (transWSS)²⁷; TAWSS axial component (TAWSS_{ax}) and secondary component (TAWSS_{sc})²⁹.

Table 2.1 WSS-based hemodynamic descriptors

| | |
|---|---|
| Time Averaged Wall Shear Stress (TAWSS) | $\text{TAWSS} = \frac{1}{T} \int_0^T \mathbf{WSS} dt$ |
| Oscillatory Shear Index (OSI) | $\text{OSI} = 0.5 \left[1 - \left(\frac{\left \int_0^T \mathbf{WSS} dt \right }{\int_0^T \mathbf{WSS} dt} \right) \right]$ |
| Relative Residence Time (RRT) | $\text{RRT} = \frac{1}{\text{TAWSS} \cdot (1 - 2 \cdot \text{OSI})} = \frac{1}{\frac{1}{T} \left \int_0^T \mathbf{WSS} dt \right }$ |
| Transverse WSS (transWSS) | $\text{transWSS} = \frac{1}{T} \int_0^T \left \mathbf{WSS} \cdot \left(\mathbf{n} \times \frac{\int_0^T \mathbf{WSS} dt}{\left \int_0^T \mathbf{WSS} dt \right } \right) \right dt$ |
| Time-Averaged WSS _{ax} (TAWSS_{ax}) | $\text{TAWSS}_{ax} = \frac{1}{T} \int_0^T \mathbf{WSS}_{ax} dt$ |

Time-Averaged WSS_{sc} (**TAWSS_{sc}**)

$$TAWSS_{sc} = \frac{1}{T} \int_0^T |WSS_{sc}| dt$$

WSS is the time-varying wall shear stress vector; T is the cardiac cycle duration; \mathbf{n} is the unit vector normal to the arterial surface at each element; **WSS_{ax}** is the WSS projection along the direction of the tangent to the vessel centerline; **WSS_{sc}** is the WSS projection along the direction perpendicular to the tangent of the vessel centerline.

In addition, the endothelial contraction/expansion regions were mathematically identified analyzing the WSS topological skeleton through a recently proposed Eulerian method³⁵ accounting for the local values of the divergence of the WSS unit vector field (DIV_{WSS}) defined as:

$$DIV_{WSS} = \nabla \cdot \left(\frac{WSS}{|WSS|} \right) \quad (2.1)$$

Negative/positive values of DIV_{WSS} identifies contraction/expansion regions, respectively (**Figure 2.3A**).

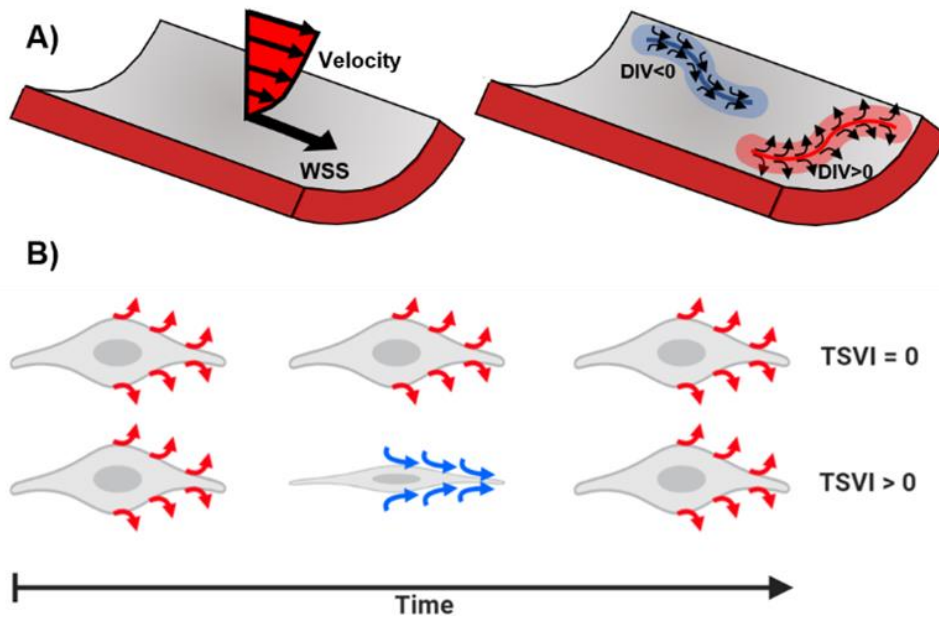


Figure 2.3. Action of the wall shear stress (WSS) at the blood-endothelium interface. A) Schematic representation of wall shear stress (WSS) at the luminal surface (left) and its push/pull action on the endothelial cells (right), as identified by the divergence of the WSS unit vector field (DIV_{WSS}). **B)** The variability of WSS contraction/expansion action on endothelial cells during the cardiac cycle is captured by the topological shear variation index (TSVI).

The variability of DIV_{WSS} along the cardiac cycle can be measured using the WSS-based quantity $TSVI$ ^{36,37,66} (**Figure 2.3B**), defined as the root mean

square deviation of the instantaneous divergence of the unit WSS vector field with respect to its average over the cardiac cycle:

$$\text{TSVI} = \left\{ \frac{1}{T} \int_0^T [\text{DIV}_{\text{WSS}} - \overline{\text{DIV}_{\text{WSS}}}]^2 dt \right\}^{1/2} \quad (2.2)$$

where T is the duration of the cardiac cycle, and the overbar denotes a cycle-average quantity.

The WSS-based descriptors are presented as averaged or maximum and minimum values over three distinct vessel segments (**Figure 2.4**):

1. lesion, defined as the segment including the MLA and delimited proximally and distally by the intersection of the QCA diameter function line with the interpolated reference line, defined as the linear interpolation of diameter curve to simulate the trend of a healthy vessel.
2. upstream segment with a length of three times the diameter of the proximal boundary of the lesion.
3. downstream segment with a length of three times the diameter of the distal boundary of the lesion.

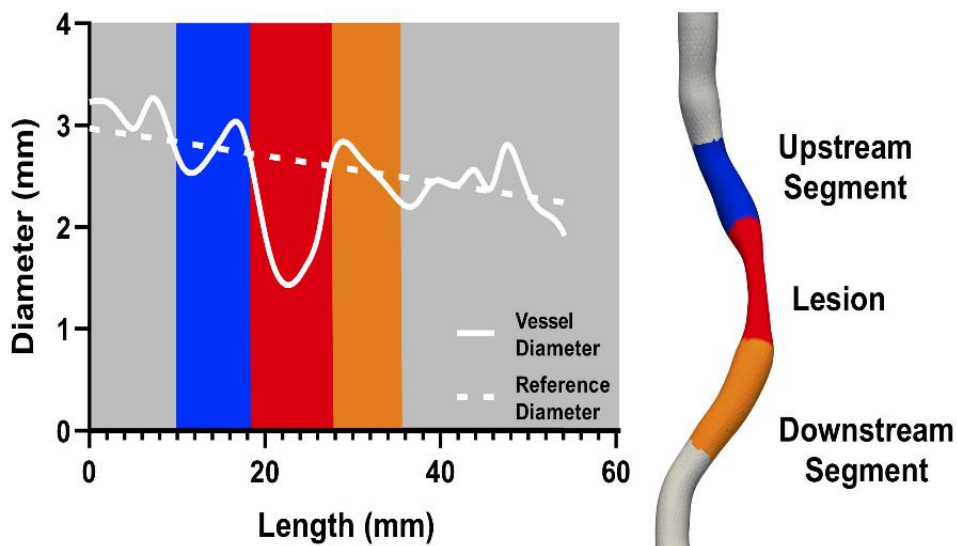


Figure 2.4. Relative anatomical lesion subdivision. The lesion segment included the minimal lumen area (MLA) and was limited by a proximal and a distal edge. Lesion segment edges were located at the intersection between the measured vessel diameter and the interpolated vessel line upstream and downstream the MLA. The upstream and downstream region extended three times the respective lesion edge diameter upstream and downstream to the lesion segment, to ensure a consistent spatial extent across all cases.

2.2.5 Statistical analysis

All statistical analyses were performed on a per-lesion basis to compare FCL and NCL characteristics. Continuous variables with normal distribution are presented as mean \pm standard deviation (SD) and non-normally distributed variables as median (inter-quartile range [IQR]). Categorical variables are presented as percentages. Chi-squared test was used for comparing categorical variables, while Student's tests (or Mann-Whitney tests as appropriate) for continuous ones. A p -value <0.05 was considered significant. The predictive capacity of QCA-, vFFR- and WSS-based descriptors was assessed using C-statistics. Receiving operator characteristic (ROC) curve were compared using the DeLong method⁷⁵. To determine the net reclassification index (NRI) and relative integrated discrimination improvement (IDI) for each model, continuous variables were dichotomized according to optimal cut-off values from the ROC curves. Three models were defined: the anatomical model (based on %AS) (**model 1**), the anatomical and pressure model (based on %AS and Δ vFFR) (**model 2**), and a third model based on %AS, Δ vFFR and a WSS descriptor (**model 3**). Time-to-event data are presented as Kaplan-Meier estimates. Anatomical and functional variables presenting a univariate relationship with future MI entered the multivariate Cox proportional-hazards regression models. Associated risk for discrete increments was assessed with odds ratio (OR) derived from binary logistic regression. WSS-based quantities reproducibility was assessed with intraclass correlation coefficients (ICC). All analyses were performed using R statistical software (R Foundation for Statistical Computing, Vienna, Austria).

2.3 Results

2.3.1 Patients selection

From January 2008 to December 2019, 6885 patients underwent coronary catheterization for acute MI in the three participating centers, 775 (11.26%) patients had a previous angiography, among which 80 (vessel $n=188$; 2.37 ± 0.47 vessel/patient) were included (the sequential screening steps for clinical and analytical exclusion criteria are summarized in **Figure 2.5**).

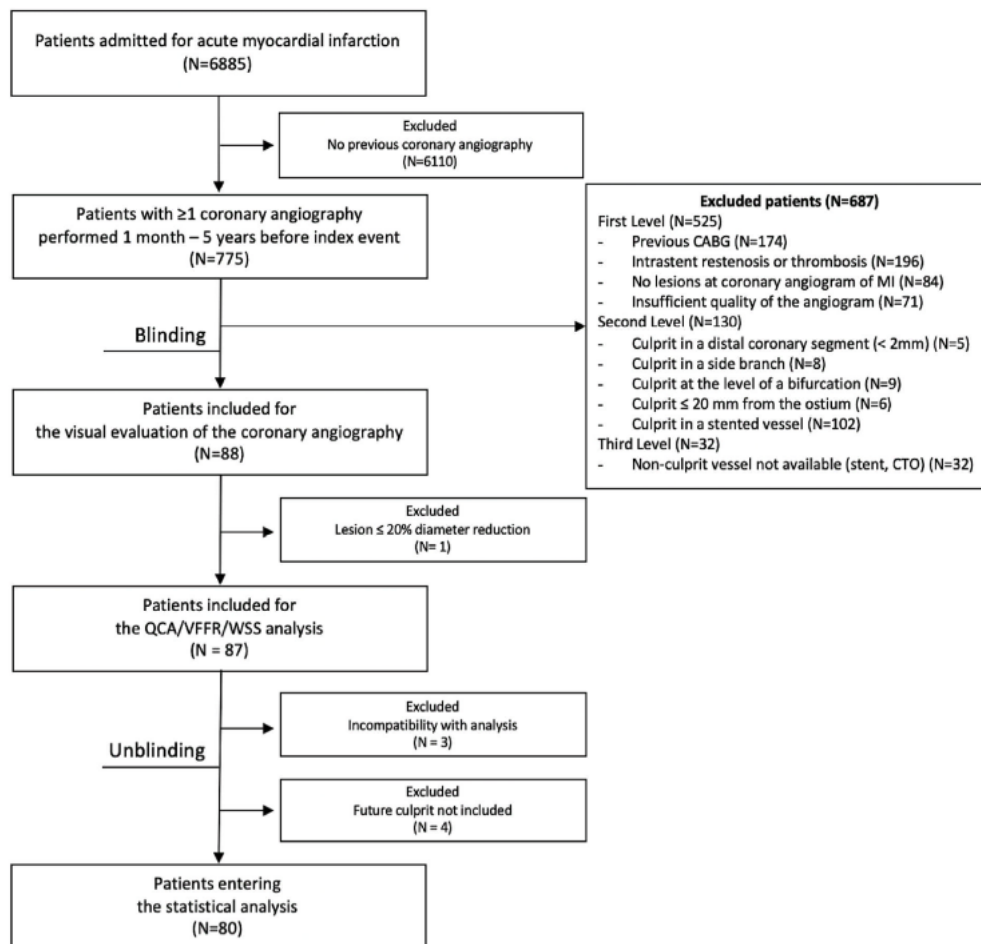


Figure 2.5. Flowchart of the patients included in the study. Sequential screening steps for clinical and analytical exclusion criteria allowed the selection of ca. 1% of the original queried patients, who met all the study assumptions and whose baseline angiography was successfully postprocessed. From the initial 6885 admitted with MI, only 775 patients had a previous angiography and only 88 met the study inclusion criteria. One case was excluded at the visual evaluation of the baseline coronary angiography for not having identifiable lesions, while three for incompatibility (low pixel number) to run the postprocessing analysis. Finally, after unblinding, four patients were excluded since their FCL were previously excluded. Thus, a total of 80 (1.2%) patients were included in the final analysis.

Clinical characteristics of the selected patients are summarized in **Table 1**. At the time of the MI, mean age of patients was 70.3 ± 12.7 years, 28.75% were female and 76.25% were on Aspirin and 90.0% on statins. Non-ST elevation myocardial infarction (NSTEMI) and STEMI were reported in 65% and 35% of the studied patients, respectively. Percutaneous coronary intervention was performed in 97.50% (78/80) of cases. The culprit lesion was located in the LAD in 43.75% of cases, in the LCX in 28.75% of cases and in the RCA in 27.50% of cases. Median time between baseline and

index angiography was 25.9 (IQR 21.9-29.8) months. The angiography-based analysis of QCA, vFFR and WSS was equally feasible in 98.90% of vessels (188 vessels, of which FCL n=80, NCL n=108).

Table 2.2. Clinical characteristics (N= 80)

| | |
|--|------------------|
| Age | 70.3 ±12.7 years |
| Female | 23 (28.75%) |
| Type of MI | |
| NSTEMI | 52 (65.00%) |
| STEMI | 28 (35.00%) |
| Treatment | |
| PCI | 78 (97.50%) |
| CABG | 1 (1.25%) |
| Medical | 1 (1.25%) |
| Time from baseline ICA | |
| Months | 25.9 ± 17.7 |
| 1 ICA before MI, n (%) | 67 (83.70%) |
| ≥ 2 ICA before MI, n (%) | 13 (16.30%) |
| Hypertension, n (%) | 61 (76.25%) |
| Hyperlipidemia, n (%) | 63 (78.75%) |
| Diabetes mellitus, n (%) | 20 (25.00%) |
| Insulin therapy, n (%) | 7 (8.75%) |
| Smoking, n (%) | 21(26.25%) |
| LVEF < 55%, n (%) | 18 (22.50%) |
| Reduced kidney function*, n (%) | 18 (22.50%) |
| Prior PCI, n (%) | 37 (46.25%) |
| Prior stroke, n (%) | 13 (16.25%) |
| Prior PVD, n (%) | 18 (22.50%) |
| Aspirin, n (%) | 61 (76.25%) |
| Statin, n (%) | 72 (90.00%) |
| P2Y12 inhibitors, n (%) | 15 (18.75%) |

Clinical characteristics of the studied population at the time of the acute myocardial infarction (index event). Coronary artery bypass graft (CABG); Invasive coronary angiography (ICA); Left ventricle ejection fraction (LVEF); Myocardial infarction (MI); non-ST segment elevation myocardial infarction (NSTEMI); Percutaneous coronary intervention (PCI); Peripheral vascular disease (PVD); ST segment elevation myocardial infarction (STEMI). * eGFR < 60 ml/min/1.73 m².

2.3.2 Anatomical and functional parameters and risk for MI

Percent AS was significantly higher in the FCL group (63.1±12.4 vs. 55.8±12.5, $p<0.001$). Distal vFFR was lower in FCL compared to NCL (0.84

(IQR 0.75-0.90) vs. 0.86 (IQR 0.82-0.92), $p=0.009$); whereas $\Delta vFFR$ was higher in FCL compared to NCL (0.08 (IQR 0.04-0.13) vs. 0.05 (IQR 0.03-0.08), $p=0.002$) with a pressure drop across the lesion of 14.5 (IQR 9.0-22.5) mmHg in FCL vs. 12.0 (IQR 8.0-16.0) mmHg in NCL ($p=0.012$; **Table 2.3**).

| Table 2.3 Results of QCA and vFFR analysis (Vessel N = 188) | | | |
|--|-------------------------------|--------------------------------|----------------|
| | FCL (Vessel N = 80) | NCL (Vessel N = 108) | p-value |
| Vessel category, n (%) | | | |
| RCA | 22 (27.5%) | 30 (27.8%) | 0.928 |
| LAD | 35 (43.8%) | 35 (32.4%) | 0.184 |
| LCX | 23 (28.7%) | 43 (39.8%) | 0.207 |
| Area stenosis, % | 63.1±12.4 | 55.8±12.5 | < 0.001 |
| Diameter stenosis, % | 40.2±10.6 | 34.3±9.66 | < 0.001 |
| Diameter stenosis, n (%) | | | |
| <30% | 15 (18.8%) | 31 (28.7%) | 0.118 |
| ≥30% and ≤50% | 48 (60.0%) | 72 (66.7%) | 0.350 |
| >50% | 17 (21.2%) | 5 (4.6%) | < 0.001 |
| Minimal lumen area (MLA), mm² | 2.31±1.24 | 2.64±1.23 | 0.064 |
| Minimal lumen diameter (MLD), mm | 1.65±0.46 | 1.78±0.43 | 0.045 |
| Reference vessel diameter, mm | 2.78±0.63 | 2.74±0.62 | 0.668 |
| Lesion length, mm | 17.1 (IQR 11.8-26.0) | 15.6 (IQR 10.3-28.3) | 0.526 |
| Distance MLA from ostium, mm | 38.1 (IQR 25.2- 54.3) | 36.8 (IQR 23.7-55.7) | 0.643 |
| Distal pressure drop, mmHg | 14.5 (IQR 9.0-22.5) | 12.0 (IQR 8.0- 16.0) | 0.012 |
| Distal vFFR | 0.84 (IQR 0.75-0.90) | 0.86 (IQR 0.82-0.92) | 0.009 |
| Distal vFFR ≤ 0.80, n (%) | 27 (33.8%) | 10 (9.3%) | <0.001 |
| ΔvFFR | 0.08 (IQR 0.04-0.13) | 0.05 (IQR 0.03-0.08) | 0.002 |
| Contour correction, % | 9.5 (IQR 5.5-14.75) | 10.2 (IQR 6.0-14.75) | 0.486 |

Output of the quantitative coronary angiography (QCA) and virtual fractional flow reserve (vFFR) according to the a priori known clinical classifier (culprit or non-culprit). Interquartile range (IQR). $\Delta vFFR$, translesional vFFR difference.

%AS and $\Delta vFFR$ emerged as moderate independent predictors for MI (%AS AUC 0.65, 95% CI 0.57-0.73, $p<0.001$ and $\Delta vFFR$ AUC 0.63, 95% CI 0.55-0.71, $p<0.001$), with best cut-off values derived from ROC curves analysis equal to 55.5% for %AS and 0.05 for $\Delta vFFR$ (**Table 2.4**).

Table 2.4 Results of the univariate prediction models (C-stat) for QCA and vFFR analysis (Vessel N = 188)

| Descriptor | Segment | AUC (Lower-Upper CI) | Threshold | Specificity | Sensitivity | p-value |
|---------------|---------|----------------------|-----------|-------------|-------------|---------|
| %AS | Lesion | 0.65 (0.57-0.73) | 55.5% | 0.52 | 0.72 | <0.001 |
| $\Delta vFFR$ | Lesion | 0.63 (0.55-0.71) | 0.05 | 0.56 | 0.70 | <0.001 |

Results of the univariate prediction models for FCL with percentage area stenosis (%AS), translesional virtual fractional flow reserve difference ($\Delta vFFR$).

2.3.3 Wall shear stress descriptors and risk for MI

On average, the computational time per clinical CFD-based WSS analysis was 10.8 ± 1.41 min.

Differences in the distribution of WSS-based quantities between the FCL and NCL groups at the lesion level are reported in **Supplemental Figure 5**.

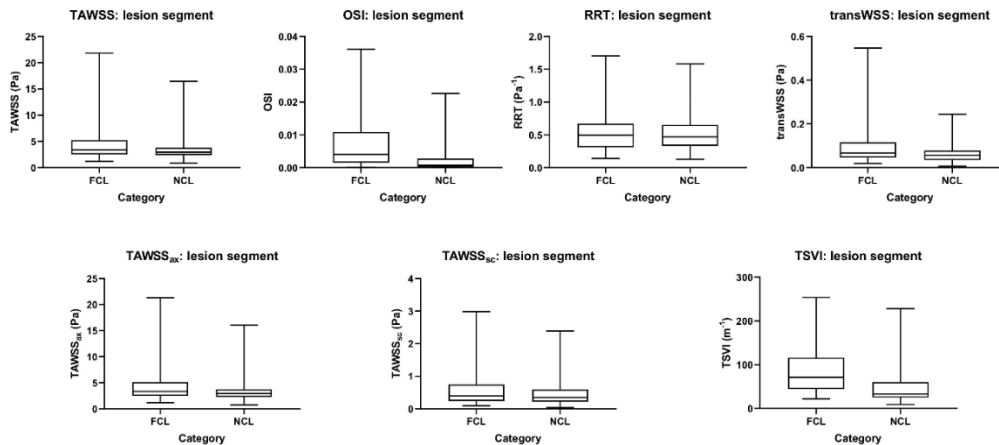


Figure 2.6. Box plots of WSS-based descriptors in FCL and NCL. Box plots of WSS-based descriptors averaged over the lesion segment in FCL and NCL. The median, the interquartile range, and the extreme values of the distribution (minimum and maximum) are represented. Time-averaged wall shear stress (TAWSS); oscillatory shear index (OSI); relative residence time (RRT); transverse WSS (transWSS); time-averaged axial component of WSS (TAWSS_{ax}); time-averaged secondary direction of WSS (TAWSS_{sc}); topological shear variation index (TSVI).

The comparison of the p-values heatmaps, representing the statistically significant differences between FCL and NCL obtained with Mann-Whitney test of all WSS-based descriptors obtained from the two CFD approaches are presented in **Figure 2.7**.

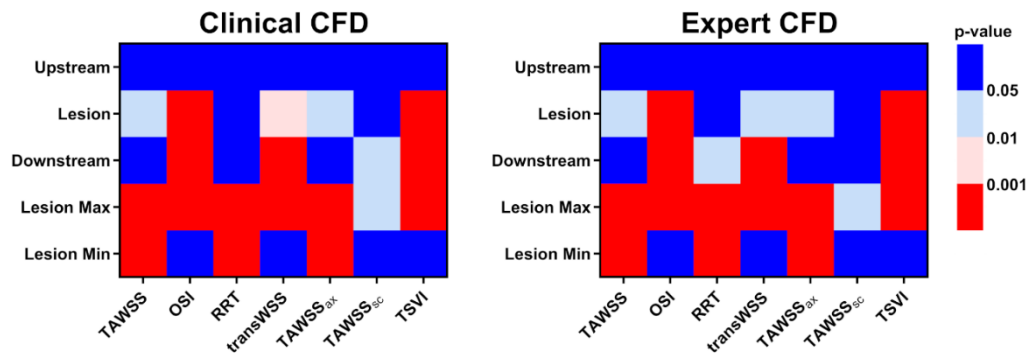


Figure 2.7. Heat maps for clinical vs. expert CFD simulations. Statistically significant differences between FCL and NCL assessed with Mann-Whitney test for WSS-based descriptors: time-averaged wall shear stress (TAWSS), oscillatory shear index (OSI), relative residence time (RRT), transverse WSS (transWSS), time-averaged axial component of WSS (TAWSS_{ax}), time-averaged secondary direction of WSS (TAWSS_{sc}), and topological shear variation index (TSVI) obtained with clinical and expert CFD. The color bar ranges from blue (not significant differences, $p > 0.05$) to red ($p < 0.001$).

The same statistically significant differences were observed for clinical and expert CFD, except for transWSS at lesion level, and RRT and TAWSS_{sc} in the downstream segment. This confirms the reliability of clinical CFD in the discrimination between FCL and NCL, justifying its use for the further analysis. Moreover, although OSI present a strong discriminatory capacity, at the same level of TSVI, it can be observed that OSI averaged values at lesion level were a scale factor of ten lower than the OSI upper bound value (by construction, $0.00 \leq \text{OSI} \leq 0.50$, **Figure 2.6**), and on average approximated zero. For this reason, OSI was not considered, and the further analyses were focused on TAWSS and TSVI.

Both TAWSS and TSVI values were significantly higher in the FCL group at the level of the lesion segment (4.58 Pa in FCL vs. 3.38 Pa in NCL, $p = 0.003$ and 89.00 m^{-1} in FCL vs 49.10 m^{-1} in NCL, $p < 0.001$, respectively). Results of the univariate analysis for TAWSS and TSVI are reported in **Table 2.5**. The analysis shows that TAWSS and TSVI, evaluated at the lesion level, present a moderate and high, respectively, predictive capacity for MI (TAWSS AUC 0.61, 95% CI 0.53-0.69, $p = 0.003$, TSVI AUC 0.77, 95% CI 0.71-0.84, $p < 0.001$). The best cut-off values were to 5.01 Pa and 40.50 m^{-1} for TAWSS and TSVI, respectively.

Table 2.5 Results of the univariate prediction models (C-stat) for TAWSS and TSVI (Vessel N = 188)

| Descriptor | Segment | AUC (Lower-Upper CI) | Threshold | Specificity | Sensitivity | p-value |
|------------|---------|----------------------|------------------------|-------------|-------------|---------|
| TAWSS | Lesion | 0.61 (0.53-0.69) | 5.01 Pa | 0.89 | 0.34 | 0.003 |
| | US | 0.53 (0.44-0.61) | 1.27 Pa | 0.64 | 0.51 | 0.745 |
| | DS | 0.51 (0.42-0.6) | 2.49 Pa | 0.67 | 0.44 | 0.413 |
| | Maximum | 0.69 (0.61-0.76) | 7.30 Pa | 0.58 | 0.73 | <0.001 |
| | Minimum | 0.67 (0.59-0.75) | 0.49 Pa | 0.55 | 0.77 | 0.999 |
| TSVI | Lesion | 0.77 (0.71-0.84) | 40.52 m ⁻¹ | 0.66 | 0.86 | <0.001 |
| | US | 0.58 (0.50-0.66) | 38.03 m ⁻¹ | 0.60 | 0.55 | 0.036 |
| | DS | 0.72 (0.65-0.79) | 105.2 m ⁻¹ | 0.79 | 0.58 | <0.001 |
| | Maximum | 0.78 (0.72-0.85) | 1266.5 m ⁻¹ | 0.67 | 0.79 | <0.001 |
| | Minimum | 0.54 (0.46- 0.63) | 1.40 m ⁻¹ | 0.34 | 0.77 | 0.85 |

Results of the univariate prediction models for FCL with time-averaged wall shear stress (TAWSS) and topological shear variation index (TSVI). TAWSS and TSVI were analyzed according to the adopted vessel subdivision: lesion, upstream (US), and downstream (DS) segments. Maximum and minimum nodal values are also reported. Area under the curve (AUC); confidence interval (CI).

The capacity of TSVI to predict the clinical outcome MI was markedly higher than TAWSS. This was also confirmed when evaluating predictive capacity separately for NSTEMI (TAWSS AUC 0.63, 95% CI 0.53-0.73, $p=0.007$; TSVI AUC 0.74, 95% CI 0.66-0.83, $p<0.001$) and STEMI (TAWSS AUC 0.58, 95% CI 0.44-0.72, $p=0.131$; TSVI AUC 0.83, 95% CI 0.73-0.93, $p<0.001$) (Figure 2.8).

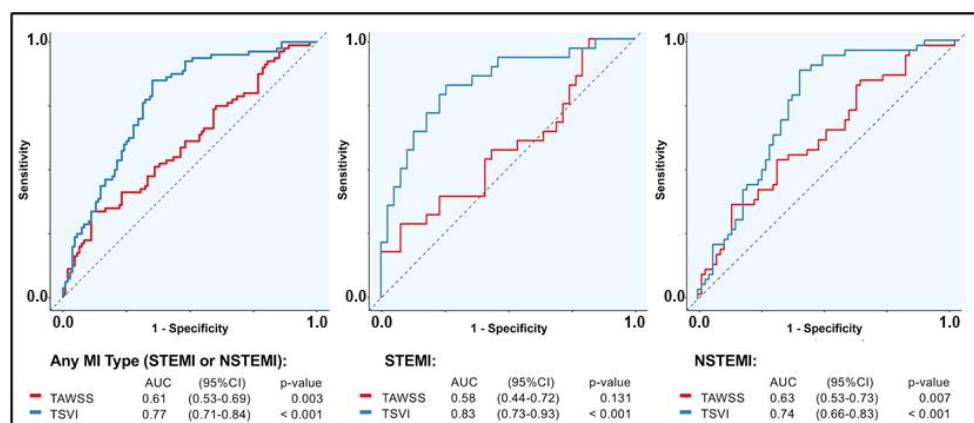


Figure 2.8. ROC curves of the adopted wall shear stress descriptors. Topological shear variation index (TSVI) resulted in a good predictive capacity for any type of myocardial infarction (MI), which was significantly superior to the time-averaged wall shear stress (TAWSS). The best performance of TSVI was found in ST segment elevation myocardial infarction (STEMI).

2.3.4 Multivariable predictive models for MI

Compared with the anatomical model with %AS (**model 1**), the inclusion of $\Delta v\text{FFR}$ (**model 2**), while not adding predictive capacity (**model 1**: AUC 0.65, 95% CI 0.57-0.73; **model 2**: AUC 0.66, 95% CI 0.58-0.74; $p=0.460$), led to a significant improvement in the reclassification and in the discrimination capacity (NRI 0.53, 95% CI 0.25-0.80, $p<0.001$; relative IDI 0.03, 95% CI 0.001-0.05, $p=0.020$) for the identification of lesions culprit of subsequent MI. Similarly, the addition of TAWSS (**model 3 based on TAWSS**) led to a non-significant increase in the predictive capacity of the model for detecting FCL (**model 2**: AUC 0.66, 95%CI 0.58-0.74; **model 3 based on TAWSS**: AUC 0.69, 95% CI 0.61-0.76; $p=0.099$, **Figure 2.9**) with a significant improvement in the reclassification capacity and discriminatory gain (NRI 0.45, 95% CI 0.21-0.69, $p<0.001$; relative IDI 0.04, 95% CI 0.01-0.07, $p=0.008$, **Table 2.6**).

On the contrary, the addition of TSVI to the anatomical and pressure model, led to a significant increase in predictive capacity for MI (**model 2**: AUC 0.66, 95% CI 0.58-0.74; **model 3 based on TSVI**: AUC 0.77, 95% CI 0.70-0.84; $p<0.001$, **Figure 2.9**) with incremental reclassification and discriminatory capacity (NRI 1.04, 95% CI 0.81-1.27, $p<0.001$; relative IDI 0.22, 95% CI 0.16-0.27, $p<0.001$, **Table 2.6**).

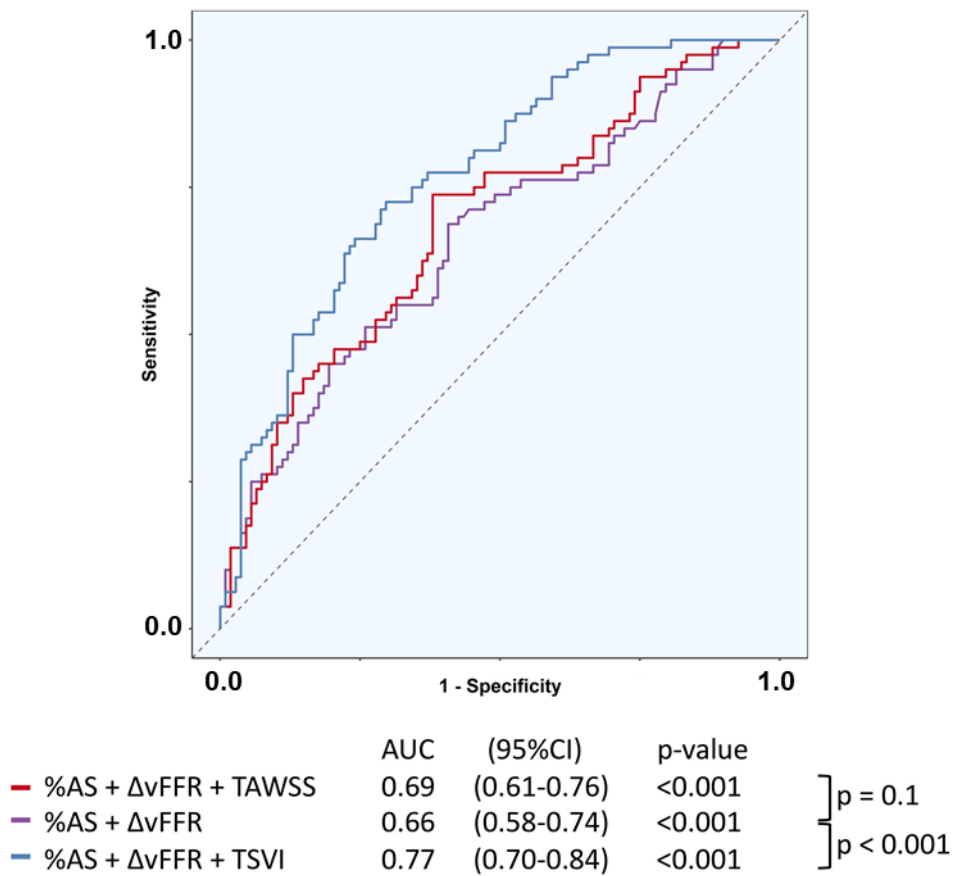


Figure 2.9. ROC curves of the multivariate models. A non-significant incremental predictive capacity was obtained by adding time-averaged wall shear stress (TAWSS) to a prediction model with percentage area stenosis (%AS) and translesional difference in virtual fractional flow reserve (Δ vFFR) (Δ AUC +0.03, $p=0.1$). On the contrary, adding topological shear variation index (TSVI) to the model with %AS and Δ vFFR added significant gain in predictive capacity (Δ AUC +0.11, $p<0.001$).

Among 60 lesions with %AS, lesion vFFR and TSVI above the threshold values, 45 (75%) evolved into a MI. Likewise, lesions with low %AS, vFFR and TSVI carried adverse prognosis in less than 8% of the cases (**Figure 2.10**).

**Table 2.6 Comparison of the predictive models for MI
(Vessel N = 188)**

| Initial model | Updated model | NRI | p-value (NRI) | IDI | p-value (IDI) |
|---------------------|------------------------------------|------------------------|---------------|------------------------|---------------|
| %AS | %AS + $\Delta vFFR$ | 0.53 (0.25 to 0.80) | < 0.001 | 0.03 (0.0 to 0.05) | 0.020 |
| %AS + vFFR | %AS + $\Delta vFFR$ + lesion TAWSS | 0.45 (0.21 to 0.69) | <0.001 | 0.04 (0.01 to 0.07) | 0.008 |
| %AS + $\Delta vFFR$ | %AS + $\Delta vFFR$ + lesion TSVI | 1.04 (0.81 to 1.27) | <0.001 | 0.22 (0.16 to 0.27) | <0.001 |

Results of the model-to-model comparison underlying the significant incremental predictive capacity of topological shear variation index (TSVI) at the lesion level when added to percental area stenosis (%AS) and translesional virtual fractional flow reserve difference ($\Delta vFFR$) (**model 3**). Integrated discrimination improvement, IDI; Net reclassification index, NRI; Time-averaged wall shear stress, TAWSS.

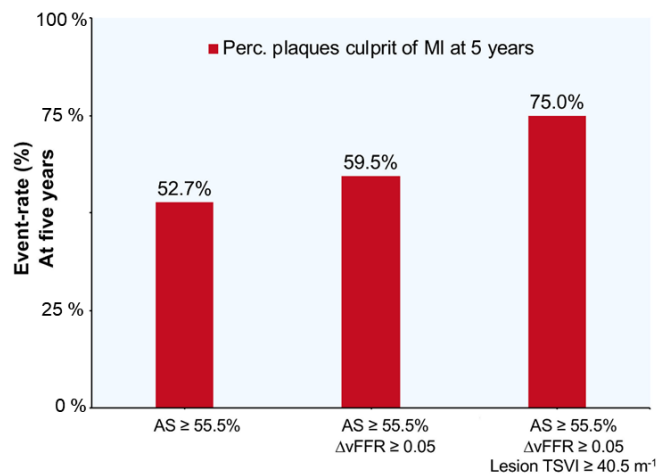


Figure 2.10 Percentage of event rate at 5 years. Lesions with percentage area stenosis (AS), translesional virtual fractional flow reserve difference ($\Delta vFFR$) and topological shear variability index (TSVI) above empirical thresholds resulted in the studied population in clinically overt myocardial infarction (MI) in 75% of cases within 5 years from the baseline angiography.

2.3.5 Time-to-event analysis

Event-free probabilities were investigated for %AS, $\Delta vFFR$, TAWSS and TSVI as single continuous variables (**Figure 2.11**). Lesion-averaged TAWSS resulted the weakest single predictor of MI (HR 1.71, 95% CI 1.06-2.74, $p=0.03$), while TSVI at the lesion level resulted the strongest predictor of MI (HR 5.11, 95% CI 2.70-9.68, $p<0.0001$) surpassing the performances of the classical clinically used %AS (HR 2.25, 95% CI 1.37-3.69, $p=0.001$), and $\Delta vFFR$ (HR 2.25, 95% CI 1.51-3.99, $p<0.001$). An increment of TSVI of 100 m^{-1} was associated with six-fold increased odds for a future MI (OR 5.97, 95% CI 2.94-13.5).

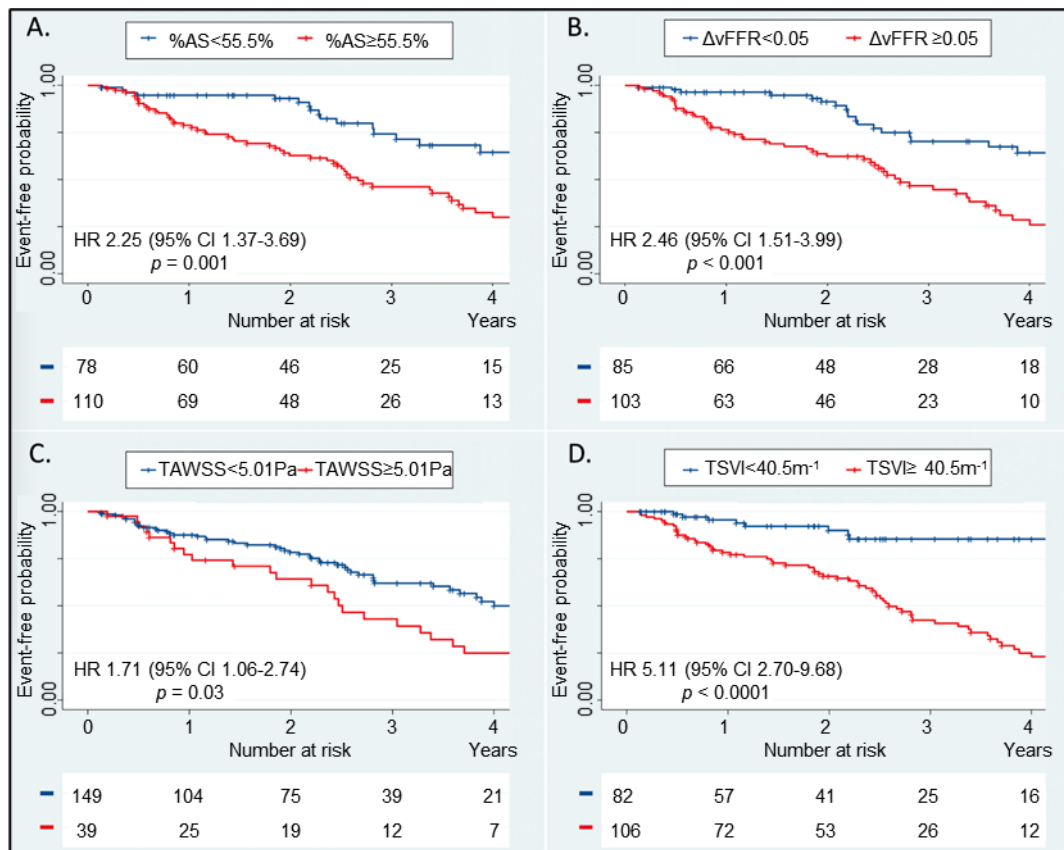


Figure 2.11. Time-to-event curves. Significantly divergent Kaplan-Meier curves for future MI are represented at 4-year follow-up for percentage area stenosis (%AS, panel A), translesional difference in virtual fractional flow reserve ($\Delta vFFR$, panel B), lesion time-averaged wall shear stress (TAWSS, panel C) and lesion topological shear variation index (TSVI, panel D). Red and blue curves refer to values above or below the threshold values obtained from the ROC analysis, respectively. Hazard ratio (HR) refers to the whole follow-up time interval (i.e., 5 years).

2.4 Discussion

The present study investigated the utility of a comprehensive approach integrating conventional coronary angiography and CFD evaluation for the identification of lesions culprit of future MI in a conventional clinical framework. The main findings can be summarized as:

1. culprit lesions had a higher area stenosis, higher pressure gradients, and higher TAWSS and TSVI than non-culprit lesions.
2. A predictive model integrating anatomical stenosis severity, pressure gradients and WSS-based descriptors showed improved discriminatory and reclassification capacity in identifying lesions culprit of future MI compared with a model based on anatomy and pressure gradients alone.
3. An easy-to-use QCA-based software able to provide in few minutes reliable WSS simulations from standard angiographic images proved to be useful in identifying lesions at risk of rupture.
4. A recently introduced WSS-based descriptor, which describe WSS topological skeleton features, the TSVI, showed the strongest predictive capacity for future MI.

2.4.1 A multidimensional approach to plaque vulnerability

Plaque vulnerability, defined as the propensity of an atherosclerotic plaque to cause an MI, has been the focus of extensive research over the last three decades⁷⁶. Early observations linked plaque vulnerability to lipid-rich atheromatous plaque and thin-cap fibroatheroma (TCFA)⁷⁷. Studies based on intravascular imaging led to the identification of several markers of vulnerability such as TCFA, plaque burden $\geq 70\%$ (PB) and MLA under 4mm^2 as predictors of major adverse cardiovascular events^{78,79}. Near-infrared spectroscopy (NIRS) integrating lipid-core burden showed also to carry prognostic information for the occurrence of MI⁸⁰. IVUS-based intracoronary elastography described high-strain regions surrounded by low-strain ones as site of plaque vulnerability⁸¹. Nevertheless, despite the association between plaque adverse characteristics and MI, the vast majority of these *high-risk plaques* become quiescent over time, thus

challenging the vulnerable plaque concept⁷⁸. On the other hand, since mild lesions outnumber severe stenoses, a sizable proportion of MI occur at the site of mild lesions^{82,83}. Using coronary computed tomography angiography (CCTA), a modality able to assess both plaque characteristic with hemodynamic factors such as pressure drop and shear stress, the EMERALD study demonstrated the added value of the integration of hemodynamic features to identify lesions prone to rupture⁸⁴. The present study combined luminal and hemodynamic information aiming at understanding the contribution of fluid shear and pressure stimuli applied to the endothelium on the risk of plaque rupture and subsequent MI. Lesions were classified as culprit and non-culprit according to an overt clinical event, and NCL served as internal control, thus accounting for the intrinsic biological variability. In contrast to previous studies, the culprit criterion referred to a clinically relevant endpoint (i.e. MI), thus, minimizing biases related to softer endpoints such as anatomical plaque progression or target vessel revascularization^{85,86}.

2.4.2 Applicability and reliability of CFD simulations based on conventional angiography

Based on recent studies confirming the reliability of angiographically-derived WSS⁸⁷, the present work nurtured from the combination of conventional coronary angiography and CFD algorithms, allowing for a multidimensional lesion evaluation. Despite this complexity, a remarkable clinical implication of the present study is that all analyses were obtained by a clinician in 10.8 ± 1.41 minutes from conventional angiography using a standard computer. Hence, the methodological approach offered in the present study brings WSS and derived quantities closer to the clinical environment, where otherwise CFD simulations require substantial computational efforts, and in most cases mandate the support of experts.

To further legitimate the clinical application of the investigated clinical CFD approach, the reliability for WSS calculation was tested against simulations with higher resolution and numerical robustness carried out by experts in computational hemodynamics. The reliability of the clinical CFD approach was tested in terms of statistical significance rather than as reproducibility

at the single-node level of computational grids. The comparison of the heat maps of WSS-based quantities as obtained from the two CFD approaches (**Figure 2.7**) highlighted that the clinical CFD is adequately robust to replicate the results obtained using expert CFD, in terms of MI predictivity. The clinical CFD allowed for a WSS calculation in shorter times without substantial loss in WSS predictive strength of MI.

2.4.3 Computational hemodynamics for MI prediction

Anatomical lesion severity (%AS) and the pressure drop across the lesions (lesion vFFR) had a significant albeit modest capacity in detecting lesions culprit of future MI (**Table 2.4**). Furthermore, this study investigated the action of fluid forces at the blood-endothelium interface. Shear forces transmitted by the flowing blood to the intraluminal surface of the endothelial cells play a central role in regulating local homeostasis, triggering pro-inflammatory plaque phenotypes associated with plaque destabilization and activation of platelets and von Willebrand factor⁸⁸. Previous studies have shown that low TAWSS (<1.5 Pa) was associated with endothelial dysfunction and plaque progression⁶⁴, while high TAWSS (> 4.71 Pa) in the proximal segments of the atherosclerotic plaque was predictive of plaque disruption and MI⁶⁵. More recently, a maximal TAWSS above 4.95 Pa over 3 mm vascular segment was found to independently predict major adverse cardiovascular events requiring revascularization⁸⁷. A significant association between TAWSS and the occurrence of MI was confirmed also in this study, where lesions evolving into culprit lesions presented higher TAWSS (4.58 Pa vs. 3.38 Pa, $p=0.011$), and in line with previous findings, TAWSS emerged to significantly predict acute MI, albeit weakly (TAWSS AUC 0.61, 95% CI 0.53 to 0.69, $p=0.003$). Moreover, the TAWSS cut-off (i.e., 5.01 Pa) supports previous reports⁶⁵. However, in contrast with the EMERALD study and the FAME 2 WSS sub-analysis^{65,84}, the present study cohort had a lower functional lesion severity as depicted by the proportion of hemodynamically significant lesions (19.7% vs. 49% vs. 100% in the current study, EMERALD and FAME 2, respectively). Finally, it has been recently reported that in vessels with borderline negative FFR values (range 0.81-0.85) lesions with %AS < 58% and maximum TAWSS < 7.69 Pa presented with a long term prevalence of lesion-oriented events below 6%⁸⁹.

Our study confirmed the predictive role of %AS with a similar cutoff (55.5%) and found also maximum TAWSS values highly different in FCL and NCL groups with a similar cutoff equal to 7.30 Pa. However, it is worth noting that the maximum nodal value is a very focal measure, more sensitive to local CFD inaccuracies ascribable to e.g., geometry reconstruction, optimization, and discretization than its averaged value, thus potentially hampering accuracy, and precision of the CFD-based analysis. The same considerations hold true for the minimum values.

These findings highlight the potential usefulness of the current approach in stratifying mild lesions and therefore tailoring preventive and therapeutic strategies in patients without hemodynamic significant lesions.

2.4.4 Emerging role of TSVI

WSS topological skeleton features, such as TSVI, identify blood flow stagnation, recirculation and separation regions (**Figure 2.12**), previously identified as flow disturbances promoting atherosclerosis¹⁹.

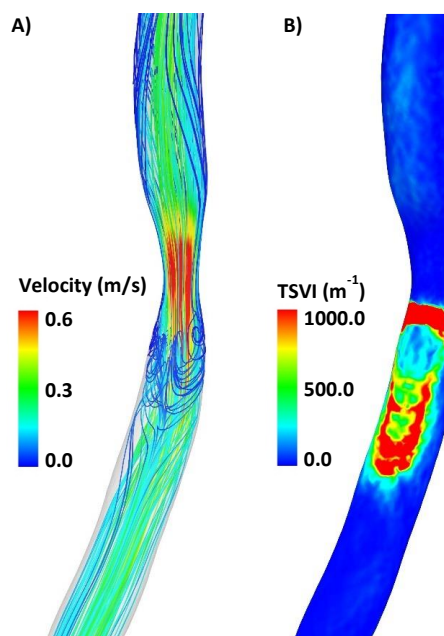


Figure 2.12 Explanatory case of flow patterns and TSVI. A) Streamlines of time averaged velocity vector field; B) TSVI luminal distribution.

Among WSS topological skeleton features, TSVI was linked to the development of long-term restenosis after carotid endarterectomy³⁷, to the degradation of mechanical properties of the aneurysmal ascending aorta³⁶, and early atherosclerotic changes in coronary arteries in swine models⁶⁶. Of note, high TSVI not only co-localized with higher wall thickness, but also predicted wall thickening longitudinally⁶⁶. These studies further demonstrated that TSVI represents a different hemodynamic signal with respect to TAWSS, consistently with the findings of the present study, where TSVI showed stronger predictive capacity than TAWSS.

This is the first study investigating the link between TSVI and MI. More specifically, TSVI quantifies the variability in the contraction/expansion action exerted by fluid forces on the vessel wall, i.e. the variations of the push/pull action exerted by the WSS on the endothelium along the cardiac cycle^{35,37}. Translating this into mechanistic implications, the variability of the contraction/expansion action exerted by shear forces on endothelial cells within the time scale of a cardiac cycle reflects on intracellular⁹⁰ as well as on intercellular tension variability, e.g. promoting junctions inclination variability, responsible for propagation of tension from cell to cell^{91,92}. This intra- and intercellular tension variability in turn may impact on shrinking/widening of cellular gaps, ultimately leading to aggravating biological events⁹³. Here we suggest that high temporal variation of WSS contraction/expansion action on the endothelium (quantified by TSVI), combined with area stenosis (%AS) and the pressure drop across the lesion ($\Delta vFFR$) may with time result in fibrous cap fragility, accelerated disease progression, up to plaque rupture with impact on clinical outcomes^{62,94}. As observed in this study the addition of TSVI to %AS and $\Delta vFFR$ enhanced discrimination for plaques vulnerable to rupture or, conversely, prone to senescence (**Figures 2.9** and **2.10**) providing the foundations for future clinical studies addressing different therapeutics strategies in this subgroup of patients. Of note, the best predictive performance was achieved by TSVI in predicting STEMI at 5 years (AUC 0.83, 95% CI 0.73 to 0.93, $p < 0.001$).

This hypothesis, although warranting further investigation, is grounded on the highest predictive capacity of TSVI at the lesion level, i.e., where also %AS and lesion vFFR were extracted. However, the highest TSVI values

were found downstream of the lesion, where TSVI but not TAWSS exhibited statistically significant predictive capacity for MI (TSVI AUC 0.72, 95% CI 0.65 to 0.79, $p < 0.001$, TAWSS AUC 0.52, 95% CI 0.42 to 0.60, $p = 0.413$). Moreover, the added value of plaque characteristics either derived from intravascular imaging or CCTA on top of anatomical, pressure and WSS characteristics remains to be elucidated.

2.4.5 Limitations

This study has several limitations. First, the limited number of included patients that represents approximately 1% of the initially screened population. This could be explained by the selection criteria of the retrospective screening; nevertheless, we cannot exclude possible selection biases, e.g., presence of at least two visually identifiable lesions, interaction with preexistent medications, exclusion of ostial lesion or lesion at bifurcations. The present results need to be confirmed in patients with single vessel disease, not under medical treatment with aspirin or statin and with ostial lesions or at bifurcations. Second, the retrospective design of the study limited our ability of controlling for potential confounding factors, such as administration of intracoronary nitroglycerine at the time of the baseline angiography. Third, given that all simulations were based on conventional angiography, no information concerning plaque burden or composition was available. Furthermore, the intrinsic limitations associated with the QCA-based three-dimensional vessel reconstruction⁹⁵ may impact the WSS calculation. However, although intravascular imaging allows for more detailed three-dimensional vessel reconstruction, several studies have shown a satisfactory agreement between the hemodynamic results obtained from conventional imaging such as angiography or coronary computed tomography angiography as compared to those reconstructed from intravascular imaging^{95,96}. Fourth, the uncertainties, assumptions and idealizations inherent in the modelling process might influence the considered WSS-based descriptors. However, previous sensitivity studies^{19,70,71} and the strength of the emergent correlations suggests that the generality of the results could be affected only modestly by the modelling approximations.

2.5 Conclusions

The present study, assessing the value of CFD derived from standard coronary angiography and performed in a conventional clinical framework, demonstrated the capability of WSS-based quantities to detect lesions culprit for future MI.

Angiography-derived anatomical lesion severity and pressure drop along the vessel showed modest capacity in identifying coronary lesions leading to MI. The extension of the functional evaluation to include angiographic derived endothelial shear stress features (TAWSS and TSVI) improved the predictive capacity for MI. TAWSS, the most common WSS-based descriptor, was able to identify culprit lesions of a future MI, but with a modest predictive capacity. In contrast, high TSVI, a descriptor of the time- and space-dependent WSS variability, showed to portray a five-fold increase in the risk for MI. Further clinical trials are justified to translate these concepts into clinical practice.

Chapter 3

Coronary Artery Plaque Rupture and Erosion: Role of Wall Shear Stress Profiling and Biological Patterns in Acute Coronary Syndromes

A version of this chapter is submitted to:

International Journal of Cardiology

Coronary Artery Plaque Rupture and Erosion: Role of Wall Shear Stress Profiling and Biological Patterns in Acute Coronary Syndromes

Giulio Russo, Daniela Pedicino, Claudio Chiastra, Ramona Vinci, **Maurizio Lodi Rizzini**, Lorenzo Genuardi, Mohammad Sarraf, Alessia d’Aiello, Marco Bologna, Cristina Aurigemma, Alice Bonanni, Antonio Bellantoni, Fabrizio D’Ascenzo, Pellegrino Ciampi, Aniello Zambrano, Luca Mainardi, Myriana Ponzio, Carlo Trani, Massimo Massetti, Diego Gallo, Francesco Migliavacca, Francesco Maisano, Amir Lerman, Umberto Morbiducci, Francesco Burzotta, Filippo Crea, Giovanna Liuzzo

3.1 Introduction

Pathophysiologic mechanisms underlying acute coronary syndromes (ACS) have not been fully identified, yet^{97,98}. In most cases, ACS represents the final clinical presentation and might be caused by alternative mechanisms leading to different culprit plaque morphologies: plaque rupture, plaque erosion and calcified nodules^{83,99–101}. Plaque rupture is the most common etiology for ACS followed by plaque erosion that accounts for at least one third of ACS cases while calcified nodules accounts for only 5-8%. However, due to pharmacological therapies including intense lipid lowering strategies, a gradual shift in the histological features of unstable plaques, from rupture to erosion, has been observed^{102,103}. So far, cross-sectional histopathology studies and, more recently, optical coherence tomography (OCT), have provided a detailed description of coronary artery plaques, thus allowing differentiation of plaque phenotypes and a definition of vulnerable plaques^{104–106}.

Alongside morphological features of plaques prone to rupture, different biological signatures for plaque erosion and plaque rupture have been described¹⁰⁷. Such data suggested that:

1. similar clinical presentations in ACS might have not only different morphological features as shown by OCT, but also different molecular mechanisms.
2. Some molecules might represent useful tools for the differential diagnosis between eroded and ruptured plaques. However, the triggers underpinning the evolution towards the different fates of coronary plaques are not well defined, yet.

Molecular mediators are only responsible for the sequence of events leading to different culprit plaque phenotypes, and other factors might be involved. Local alteration of wall shear stress (WSS) has been proposed as a biomechanical trigger predisposing to endothelial cell damage and detachment in plaque erosion¹⁰². Postmortem and in vivo studies suggested that both erosions and ruptures occur more frequently in the proximal and mid segments of the coronary arteries, with a prevalence of erosion in the

left anterior descending artery and coronary bifurcation, and a prevalence of rupture in the right coronary artery^{108,109}. These differences were ascribed to local flow disturbances, which therefore might precede and/or influence the progression and fate of atherosclerotic plaques.

In this perspective, image-based computational fluid dynamics (CFD) has enriched the available arsenal of tools for intracoronary analysis over the last few years. The addition of WSS data has contributed to better understanding some pathophysiological mechanisms underlying early and advanced phases of atherosclerosis^{66,67}. Indeed, several studies have suggested a role for WSS in plaque progression, composition and destabilization in coronary arteries^{110–115}, where the local hemodynamics may affect cell morphology, metabolism and inflammatory phenotype through signal transduction and endothelium-dependent gene and protein expression¹¹⁶. To complete the picture, several blood-circulating molecules have been demonstrated to be tightly regulated by WSS conditions including mediators of inflammation, cellular adhesion, thrombus formation, immunomodulation and vasomotility.

So far, only a few studies have investigated the relationship between WSS and different plaques phenotypes whereas WSS and biological characteristics have been mostly described with in vitro or animal models. Currently, in vivo combined description of hemodynamic and biological features in human eroded (intact fibrous cap, IFC) and ruptured (ruptured fibrous cap, RFC) plaques is lacking. Therefore, this study aims to describe the WSS and molecular patterns of stable (chronic coronary syndromes, CCS) and unstable (IFC and RFC) human coronary artery plaques, and to investigate whether any relationship between coronary WSS and biological data is present in the context of Non-ST Elevation Myocardial Infarction (NSTEMI-ACS).

3.2 Methods

3.2.1 Study design and population

This is a single-center, prospective study (**Figure 3.1**). Two groups of patients were consecutively enrolled:

1. patients with CCS defined by symptoms of stable effort angina lasting more than 12 months, angiographically confirmed coronary artery disease, no previous acute coronary events, and no overt ischemic episodes during the previous 48 hours (n=24).
2. Patients admitted to our Coronary Care Unit (CCU) with the first diagnosis of ACS presenting with NSTEMI confirmed at coronary angiography (n=25)^{117,118}.

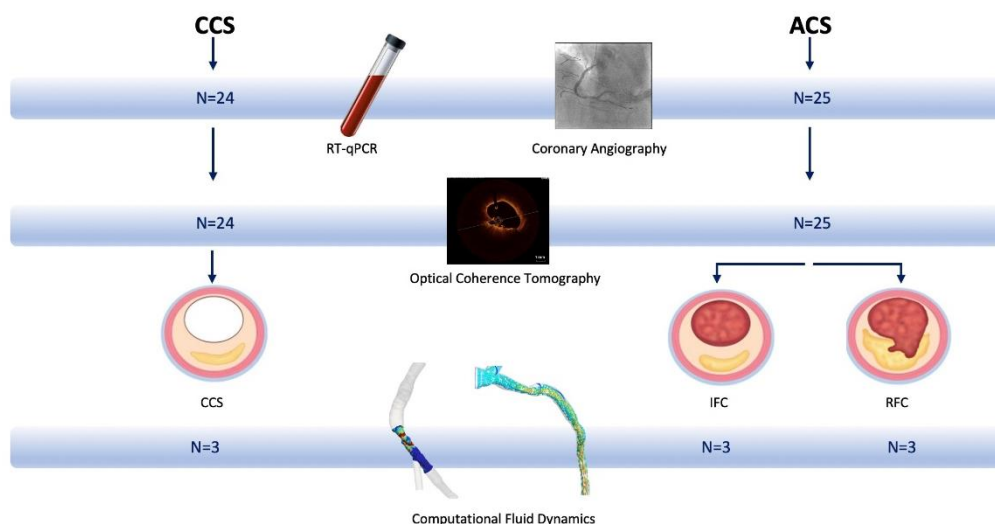


Figure 3.1 Study design. CCS: chronic coronary syndrome; IFC: intact fibrous cap; RFC: ruptured fibrous cap

Clinical features were carefully recorded, including demographic data, cardiovascular risk factors, cardiological history, comorbidities, angiographic and echocardiographic findings, and medical treatment at the time of enrollment (**Table 3.1**). The study complies with the Declaration of Helsinki. All patients gave their written informed consent. The Ethics Committee of the *Fondazione Policlinico Universitario "A. Gemelli" IRCCS - Catholic University of Sacred Heart of Rome* approved the study.

Table 3.1 Baseline characteristics of the study population

| | SA N=24 | IFC N=11 | RFC N=14 | p-value |
|--------------------------------|--------------------|---------------------|---------------------|----------------|
| Age, mean±SD | 69±9 | 59±11 | 58±13 | 0.005 ** |
| Gender, M/F | 20/4 | 9/2 | 12/2 | 0.964 |
| CV Risk Factors, n (%) | | | | |
| Smoke | 10 (42) | 8 (73) | 5 (36) | 0.141 |
| Diabetes | 5 (21) | 0 (0) | 5 (36) | 0.089 |
| Hypertension | 21 (88) | 6 (55) | 10 (71) | 0.100 |
| Dyslipidaemia | 18 (75) | 5 (46) | 6 (43) | 0.087 |
| Family history | 10 (42) | 3 (27) | 6 (43) | 0.672 |
| Medical Therapy, n (%) | | | | |
| DAPT | 9 (39) | 5 (55) | 5 (36) | 0.602 |
| ASA | 22 (96) | 5 (55) | 7 (50) | 0.003 ** |
| Clopidogrel | 7 (30) | 3 (27) | 1 (7) | 0.243 |
| Prasugrel | 1 (4) | 1 (9) | 1 (7) | 0.855 |
| Ticagrelor | 1 (4) | 4 (36) | 3 (21) | 0.055 |
| Anticoagulants | 1 (4) | 1 (9) | 1 (7) | 0.855 |
| Beta-Blockers | 18 (78) | 5 (46) | 4 (29) | 0.009 ° |
| Diuretics | 6 (26) | 2 (18) | 2 (14) | 0.672 |
| ACE-I | 6 (26) | 2 (18) | 4 (29) | 0.826 |
| ARBs | 11 (48) | 3 (27) | 6 (43) | 0.521 |
| Statins | 20 (87) | 5 (46) | 5 (36) | 0.003 ** |
| Ca-antagonists | 2 (9) | 3 (27) | 2 (14) | 0.356 |
| Nitrates | 3 (13) | 0 (0) | 0 (0) | 0.176 |
| Insulin | 2 (9) | 0 (0) | 0 (0) | 0.322 |
| Oral antidiabetic | 2 (9) | 0 (0) | 2 (14) | 0.438 |
| Lab Values, mean±SD | | | | |
| Tn I, ng/ml | 0.02±0.06 | 787±1970 | 511±1062 | 0.134 |
| Hb, g/dl | 14.2±1.6 | 13.9±1.5 | 14.5±1.9 | 0.651 |
| WBC, x10 ³ /ml | 7.1±2.0 | 8.7±4.2 | 8.4±3.6 | 0.247 |
| Platelet, x10 ³ /ml | 217±49 | 222±47 | 227±43 | 0.409 |

| | | | | |
|----------------------------------|---------|----------|---------|----------|
| Lymphocytes, x10 ⁹ /l | 2.3±2.0 | 1.9±1.0 | 2.0±1.3 | 0.814 |
| Glycemia, mg/dl | 106±26 | 104±26 | 117±32 | 0.447 |
| Creatinine, mg/dl | 0.9±0.1 | 0.9±0.4 | 0.7±0.3 | 0.205 |
| Cholesterol, mg/dl | 153±33 | 160±30 | 167±60 | 0.642 |
| LDL, mg/dl | 82±28 | 103±28 | 108±45 | 0.122 |
| HDL, mg/dl | 48±16 | 36±11 | 37±8 | 0.060 |
| Triglycerides, mg/dl | 114±46 | 135±25 | 143±40 | 0.174 |
| ESR, mm/h | 10±8 | 10±8 | 35±25 | 0.003 ° |
| hs-CRP, mg/l | 1.9±3.0 | 10.0±7.4 | 9.7±5.2 | 0.001 ** |

Data refer to the time of patient enrollment and blood withdrawal. SA: stable angina; IFC: intact fibrous cap; RFC: ruptured fibrous cap; CV: cardiovascular; DAPT: dual antiplatelet therapy; ASA: aspirin; ACE-I: ACE inhibitors; ARBs: angiotensin II receptor blockers; WBC: white blood cell; ESR: erythrocyte sedimentation rate; CRP: C-reactive protein. * SA vs IFC: p≤0.05; ° SA vs RFC: p≤0.05.

3.2.2 Optical coherence tomography

OCT images were acquired (after intracoronary administration of nitroglycerine) using a commercially available catheter (Dragonfly Optis; Abbott Vascular, Abbott Park, IL, USA) and system (Optis System; Abbott Vascular, Abbott Park, Illinois, USA)¹¹⁹. Unstable (NSTEMI-ACS) patients (n=25) were sub-grouped into Intact Fibrous Cap (IFC, n=11) and Ruptured Fibrous Cap (RFC, n=14) according to OCT characteristics. Plaque erosion was defined by the presence of thrombus overlying a plaque with IFC or by the presence of luminal surface irregularity at the culprit lesion in the absence of thrombus. RFC was defined by the presence of fibrous cap discontinuity with a cavity formed inside the plaque or with direct communication between the lumen and inner core of a plaque.

3.2.3 Biological Analysis

Blood samples were collected at the time of patient admission for routine hematological tests. Total and differential leukocyte count was performed on fresh blood samples using automated cytochemistry in flow (Bayer H*3-hematology analyzer, Leverkusen, Germany). Serum cardiac troponin I (cTnI) was determined at the time of hospital admission as routine measurement by high sensitivity Single Molecule Counting technology

(ADVIA Centaur, Siemens, Erlangen, Germany, Roche Diagnostics, Mannheim, Germany). A value of 0.04 ng/mL (99th percentile in control subjects) represented the minimum detectable concentration. Furthermore, high-sensitive-C-reactive protein (hs-CRP) was recorded using a high-sensitivity latex-enhanced nephelometric assay (Latex/BN II, Dade Behring, Marburg, Germany).

Venous blood samples were collected at the time of patient enrollment, within 24 hours from symptom onset. Peripheral blood mononuclear cells (PBMCs) were isolated from fresh whole blood EDTA samples by density gradient centrifugation method (Lympholyte ®-H Cell Separation Media, CEDARLANE, Burlington, Canada). PBMCs were washed in Dulbecco's Phosphate-buffered saline (DPBS) solution (Invitrogen, Carlsbad, CA, USA). Cell concentration was performed by using automated cell counter (Nucleocounter, ChemoMetec, Allerød, Denmark). Dried PBMCs were stored at -80°C.

Total RNA was obtained from stored PBMCs with RNeasy Plus Extraction Kit (QIAGEN GmbH, Hilden, Germany) and RNA quantitation and purity analyses were performed (Multiskan™ GO Microplate Spectrophotometer, Thermo Fisher Scientific, Waltham, MA, USA). First-strand cDNA synthesis was obtained via reverse transcription (iScript cDNA synthesis kit, Bio-Rad, Hercules, CA, USA). cDNA samples were pooled (n = 10 per group) in order to perform the gene expression array. The PrimePCR array (Bio-Rad, Hercules, CA, USA) was custom designed and performed on pooled samples for evaluating the expression of 17 different molecules using the real-time polymerase chain reaction (RT-PCR) (IQ5 Multicolor Detection System iCycler, Bio-Rad, Hercules, CA, USA). We followed manufacturer's instructions for PrimePCR cycling protocol. Relative gene expression was calculated, presented as percentage of the relevant baseline, using the $2^{-\Delta\Delta Cq}$ (quantification cycle) method (CFX Manager™ Software, Bio-Rad, Hercules, CA, USA). **Table 3.2** shows the function of the selected molecules and the effects of different WSS conditions on their expression/function according to the current literature.

Table 3.2 Effect of WSS on selected genes

| GENE | Specific Function | Effect of WSS |
|-------------------------------|---|--|
| ADAMTS13 | Cleavage of vWF; regulation of blood clotting | Up-regulated under high and very high WSS ¹²⁰ |
| CD31 | Leukocyte migration, angiogenesis, immunomodulation, mechano-transduction | Activated by WSS ¹²¹ |
| CD44 | Cell-cell interactions, cell adhesion and migration, hyaluronan receptor | Increased hyaluronan binding under WSS ¹²² |
| EDN1 | Vasomotility, vasoconstriction | Down-regulated under high WSS ^{123,124} |
| GPX1 | Antioxidant enzyme; redox-balancer | Up-regulated under high WSS ¹²⁵ |
| ICAM1 | Cell proliferation, differentiation, trafficking, apoptosis and tissue architecture | Up-regulated under high WSS ¹²⁶ |
| LGALS8 | Cell adhesion, cell-matrix interaction, growth, apoptosis, and RNA splicing | Activated under high WSS ¹²⁷ |
| MMP1 | ECM and molecule degradation | Up-regulated under high WSS ^{128,129} |
| MMP9 | ECM and molecule degradation; leukocyte migration; inflammation | Up-regulated under high WSS ^{130,131} |
| NOS3 | Vascular smooth muscle relaxation | Up-regulated under high WSS ¹³²⁻¹³⁴ |
| PI16 | Inhibition of cardiomyocyte growth, MMP inhibition | Up-regulated under high WSS ¹³⁵ |
| PLA2G7 | Modulation of platelet-activating factor (PAF) activity | Up-regulated under high WSS ^{136,137} |
| SOD1 | Destruction of superoxide anion radicals | Down-regulated under oscillatory SS ¹³⁸ |
| TFRC | Erythropoiesis and neurologic development | NA |
| TIMP1 | Cell proliferation and potential an anti-apoptotic function, MMP inhibition | Up-regulated under high WSS ^{128 9} |
| TNFα | Apoptosis, proliferation, differentiation, lipid metabolism, and coagulation | Up/down-regulated under high WSS ¹³⁹⁻¹⁴¹ |
| VEGF | Proliferation and migration of vascular endothelial cells, angiogenesis | Up-regulated under low WSS ^{142,143} |

ADAM metallopeptidase with thrombospondin type1 motif13, ADAMTS13; Cluster of differentiation, CD; Extracellular matrix, ECM; Endotelin-1, EDN1; Glutathione peroxidase1, GPX1; Intercellular Adhesion Molecule1, ICAM1; Galectin8, LGALS8; Matrix metalloprotease, MMP; Nitric oxide synthase3, NOS3; Peptidase inhibitor16, PI16; Phospholipase A2 Group VII, PLA2G7; Superoxide dismutase1, SOD1; Transferrin Receptor, TFRC; Tissue inhibitor of metalloproteinases 1, TIMP1; Tumor necrosis factor α , TNF α ; Vascular Cell Adhesion Molecule 1; VEGF; von-Willebrand Factor, vWF.

Gene validations was executed for the following molecules: ADAMTS13, CD31, CD44, EDN1, GPX1, ICAM1, LGALS8, MMP1, MMP9, NOS3, PI16, PLA2G7, SOD1, TFRC, TIMP1, TNF, VEGFA.

Gene expression analysis was performed using RT-PCR through CFX96 Touch Real-Time PCR Detection System (Bio-Rad, Hercules, CA, USA). Relative gene expression was calculated, presented as percentage of the

relevant baseline, using the $2^{-\Delta\Delta Cq}$ (quantification cycle) method (CFX Manager™ Software, Bio-Rad, Hercules, CA, USA). Non-template and positive controls were included in each 96-well PCR reaction, and dissociation curve analysis was performed at the end of each run to confirm the specificity of the reaction. We used beta 2-microglobulin (B2-m) as internal reference gene.

The amplification protocol used a step of 95°C for 3 minutes (min) followed by 40 cycles of 95°C for 10 seconds (sec) and 60°C for 30 sec and a plate read. Melting curves were generated by heating from 65 to 95°C with either 0.5°C increments, 5 seconds dwell time, and a plate read at each temperature.

Primers were designed from nucleotide sequences identified using NCBI BLAST and were ordered from Bio-Fab Research (Rome, Italy) with their certificates of analysis.

3.2.4 Wall shear stress profiling

A total of nine cases (three for each plaque category) with both biological and suitable coronary imaging data (i.e., two X-ray angiographic projections at least 25° apart and the OCT pullback) were retrospectively included for the CFD analysis.

High-fidelity three-dimensional (3D) geometrical models of coronary artery were reconstructed using a previously developed method based on the fusion of angiographic and OCT images^{144–146} (**Figure 3.2**).

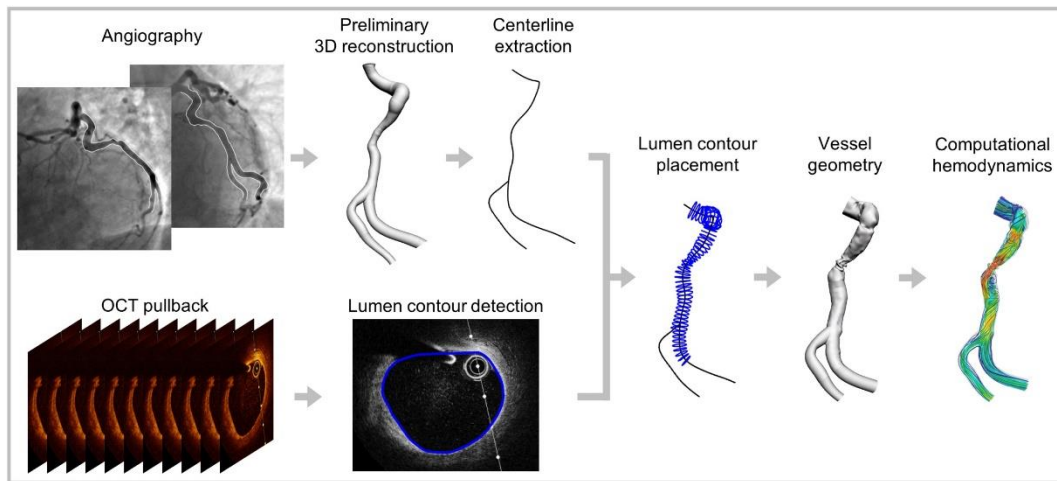


Figure 3.2 Angiography-OCT fusion. High-fidelity 3D vessel reconstruction of coronary artery models by fusion of angiographic and Optical Coherence Tomography (OCT) images: workflow for 3D reconstruction.

The reconstruction process was characterized by the following steps:

1. extraction of the vessel centerline from a preliminary 3D vessel reconstruction obtained from two angiographic views with QAngio XA (Medis Medical Imaging Systems, Leiden, Netherlands).
2. Detection of the lumen contours on the OCT images using an in-house automatic segmentation method¹⁴⁷.
3. Placement of the OCT lumen contours orthogonal to the main vessel centerline and orientation using the side branches as landmarks.
4. generation of the final 3D vessel geometry by smooth connection of the aligned OCT lumen contours and merging with the side branches, previously reconstructed from angiography.

The final 3D vessel reconstructions included all the side branches visible in the OCT pullback with a diameter larger than 1 mm¹⁴⁸.

The 3D vessel models were discretized using the software ICEM CFD (ANSYS Inc., Canonsburg PA, USA). In detail, tetrahedral meshes with curvature-based refinement and five layers of prismatic elements close to the wall were generated⁷³. Higher mesh density was assigned to the vessel regions presenting ruptured fibrous cap to better capture the local hemodynamic features.

On discretized models, steady-state flow simulations were performed by means of the finite volume-based code Fluent (ANSYS Inc., Canonsburg PA, USA). Patient-specific flow-rates, estimated from angiography using the frame count method, were applied as inflow boundary conditions¹⁴⁹. A diameter-based scaling law was adopted to impose a realistic flow-split at the outflow boundaries⁷⁰. The no-slip condition was prescribed at the luminal wall, which was considered as rigid. Blood was modeled as homogeneous, incompressible, non-Newtonian fluid. Exhaustive details about the solver settings are reported elsewhere¹⁵⁰.

The fluid dynamics in the coronary artery models was analyzed in terms of WSS. Both the distribution of WSS and the surface area exposed to low and high WSS values were computed. According to previous studies, the 10th and 90th percentiles of the overall distribution of WSS, obtained by pooling together the WSS data of all models, were used as thresholds to define low and high WSS⁴¹. The WSS analysis was performed at the following two levels:

1. global level, by considering the whole lesion.
2. segmental level, by considering three segments within the lesion and two segments adjacent to the lesion.

Specifically, the lesion region was identified according to quantitative coronary angiography standards^{151,152}. Then, the lesion was divided into three segments using the 50% of the minimum lumen diameter as relative threshold for the division and denoted as proximal, mid, and distal lesion segments. Furthermore, two additional segments were identified along the vessel models, one upstream and one downstream of the lesion. The length of those segments was defined as three times the proximal and distal diameter of the lesion, respectively for the upstream and downstream segments⁶⁷ (**Figure 2.4**).

3.2.4 Wall shear stress profiling

According to the distributions, continuous variables were presented as mean with standard deviation (SD) or median with interquartile range (IQR). Categorical variables were presented as numbers and percentages. As

appropriate, continuous variables were evaluated using a parametric test (ANOVA and Student's t-test) or a non-parametric test (Kruskal-Wallis test and Mann-Whitney test). Categorical variables were evaluated using χ^2 test or Fisher's exact test, as appropriate. For each plaque category (i.e., CCS, IFC, RFC), the WSS data of the identified lesions were pooled together. The lumen area exposed to low and high WSS was expressed as percentage \pm SD. Jarque-Bera test was used to test the normality of the WSS distributions. Correlation between WSS and biological results within groups was performed with bivariate Spearman's Rho correlation analysis. A 2-tailed, p -value <0.05 was established as the level of statistical significance. All statistical analyses were performed using SPSS software v25.0 (IBM Corporation, Armonk, NY, USA).

3.3 Results

3.2.1 Biological Analysis

Target gene validation showed significantly different expression across the three groups for the following 13 molecules: ADAMTS13, EDN1, GPX1, LGALS8, MMP1, MMP9, NOS3, PLA2G7, PI16, SOD1, TFRC, TIMP1, TNF α . No significant differences were observed for CD31, CD44, ICAM1, VEGF gene expression.

A total of nine genes were significantly overexpressed in the unstable plaque patients as compared to CCS patients, with no differences between IFC and RFC group: GPX1 (Kruskal-Wallis test: $p=0.001$, CCS vs. IFC: $p<0.001$, and CCS vs. RFC: $p=0.004$), MMP1 (Kruskal-Wallis test: $p=0.019$, CCS vs. IFC: $p<0.001$, and CCS vs. RFC: $p=0.032$), MMP9 (Kruskal-Wallis test: $p=0.011$, CCS vs. IFC: $p=0.007$, and CCS vs. RFC: $p=0.004$), NOS3 (Kruskal-Wallis test: $p<0.001$, CCS vs. IFC: $p<0.001$, and CCS vs. RFC: $p<0.001$), PLA2G7 (Kruskal-Wallis test: $p=0.029$, CCS vs. IFC: $p=0.002$, and CCS vs. RFC: $p=0.036$), PI16 (Kruskal-Wallis test: $p<0.001$, CCS vs. IFC: $p<0.001$, and CCS vs. RFC: $p<0.001$), SOD1 (Kruskal-Wallis test: $p<0.001$, CCS vs. IFC: $p<0.001$, and CCS vs. RFC: $p<0.001$), TIMP1 (Kruskal-Wallis test: $p<0.001$, CCS vs. IFC: $p<0.001$, and CCS vs. RFC: $p<0.001$).

$p < 0.001$), and TFRC (Kruskal-Wallis test: $p = 0.009$, CCS vs. IFC: $p = 0.008$, and CCS vs. RFC: $p = 0.004$) (**Figure 3.3**).

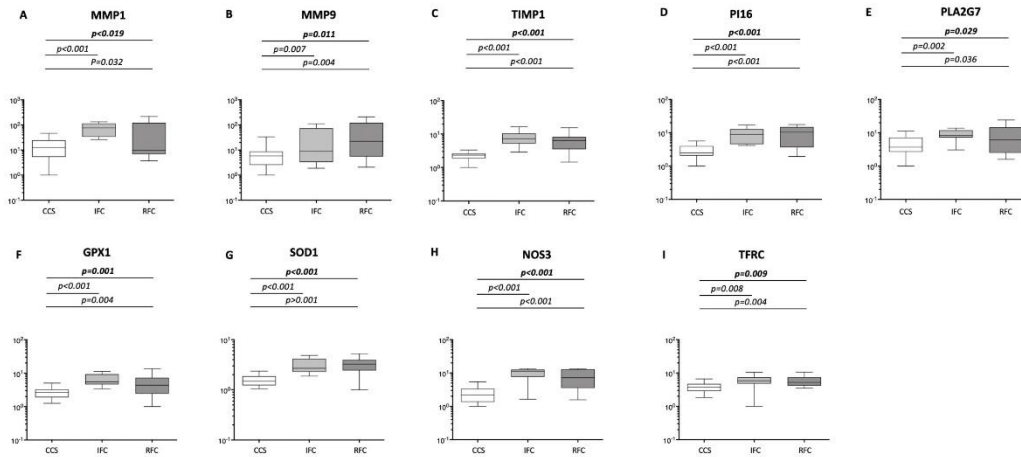


Figure 3.3. Gene expression: CCS vs. unstable plaques. Box plots showing the gene expression of MMP1 (A), MMP9 (B), TIMP1 (C), PI16 (D), PLA2G7 (E), GPX1 (F), SOD1 (G), NOS3 (H) and TFRC (I) on PBMCs assessed by RT-qPCR in stable (CCS), intact fibrous cap (IFC) and ruptured fibrous cap (RFC) groups. Distribution, median and interquartile range are displayed for each group.

IFC patients showed the highest gene levels of LGALS8 if compared to both CCS ($p < 0.001$) and RFC ($p = 0.032$), with RFC expressing also higher gene levels of the molecule if compared to CCS ($p < 0.001$) and $p < 0.001$ for three groups comparison (**Figure 3.4A**). Moreover, IFC expressed significantly higher levels of EDN1 if compared to both CCS ($p = 0.002$) and RFC ($p = 0.050$), with no differences between CCS and RFC ($p = 0.002$ for three groups comparison) (**Figure 3.4B**). As regards RFC, a significantly higher gene expression of ADAMTS13 was found if compared to both CCS ($p < 0.001$) and IFC ($p = 0.040$) ($p < 0.001$ for three groups comparison) (**Figure 3.4C**), and a significantly lower gene expression of $\text{TNF}\alpha$ if compared to both CCS ($p = 0.016$) and IFC ($p = 0.050$), with no difference between CCS and IFC ($p = 0.002$ for three groups comparison) (**Figure 3D**). Median and IQR for the investigated molecules are reported in **Table 3.3**.

Table 3.3 Biological results for gene expression

| GENE | SA | IFC | RFC | p-value |
|----------|----------------------|----------------------|----------------------|-----------|
| | N=24 Median (IQR) | N=11 Median (IQR) | N=14 Median (IQR) | |
| EDN1 | 6.24 (5.08) | 17.6 (29.2) | 6.02 (8.74) | 0.002*§ |
| ICAM1 | 3.84 (4.32) | 4.95 (2.76) | 1.20 (2.19) | 0.079 |
| TFRC | 3.79 (1.85) | 5.89 (2.66) | 5.24 (3.34) | 0.009° |
| VEGFA | 4.06 (4.16) | 6.54 (7.29) | 4.79 (3.97) | 0.542 |
| TNF | 22.17 (22.60) | 26.21 (37.06) | 2.30 (2.88) | 0.044*§ |
| CD31 | 3.13 (1.74) | 2.40 (1.36) | 3.46 (3.26) | 0.149 |
| LGALS8 | 2.04 (1.19) | 6.57 (2.99) | 4.41 (2.79) | <0.001*°§ |
| MMP9 | 5.83 (6.16) | 8.79 (70.31) | 22.22 (115.37) | 0.011*° |
| TIMP1 | 2.35 (0.71) | 7.27 (5.31) | 6.44 (4.59) | <0.001*° |
| GPX1 | 2.69 (1.31) | 5.51 (4.62) | 4.35 (4.89) | 0.001*° |
| PLA2G7 | 3.70 (4.50) | 8.41 (4.63) | 6.16 (11.95) | 0.029° |
| MMP1 | 12.60 (19.09) | 76.33 (81.82) | 9.63 (113.74) | 0.019° |
| PI16 | 2.48 (1.91) | 8.93 (8.37) | 10.36 (11.22) | <0.001*° |
| SOD1 | 1.48 (0.64) | 2.68 (1.89) | 3.25 (1.51) | <0.001*° |
| NOS3 | 2.16 (2.02) | 11.35 (4.99) | 7.23 (9.35) | <0.001*° |
| ADAMTS13 | 0.92 (0.37) | 0.99 (1.11) | 3.06 (2.89) | <0.001*§ |
| CD44 | 1.01 (0.61) | 0.70 (0.49) | 0.76 (0.59) | 0.127 |

*: p<0.05 for the comparison CCS vs IFC °: p<0.05 for the comparison CCS vs RFC §: p<0.05 for the comparison IFC vs RFC.

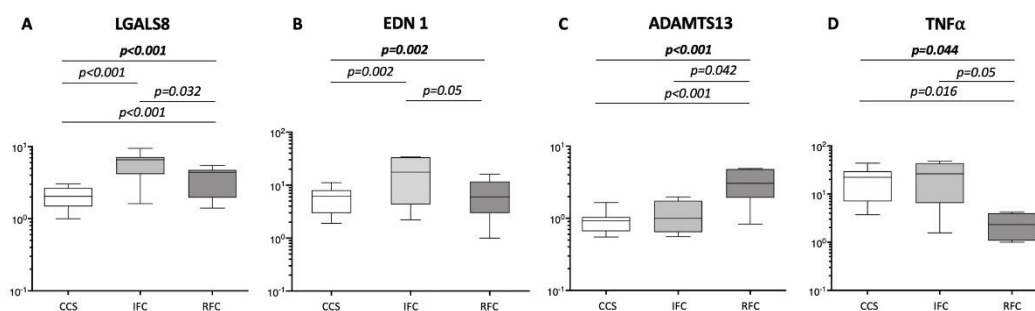


Figure 3.4. Gene expression: IFC vs. RFC. Box plots showing the gene expression of LGALS8 (A), EDN1 (B), ADAMTS13 (C) and TNF α (D) on PBMCs assessed by RT-qPCR in stable CCS, intact fibrous cap (IFC) and ruptured fibrous cap (RFC) groups. Distribution, median and interquartile range are displayed for each group.

3.2.2 Wall shear stress profiling

The WSS distribution assessed on the entire lesion segment was significantly different among the three plaques categories ($p < 0.001$, **Figure 3.5A**). In particular, the RFC group presented a higher WSS median value as compared to the other two groups (3.3 Pa for the RFC lesions versus 1.9 Pa and 2.5 Pa for the CCS and IFC lesions, respectively, $p < 0.001$ in the pairwise analysis) (**Figure 3.5A**). Furthermore, the RFC group exhibited a larger WSS IQR (7.6 Pa for the RFC lesions versus 2.4 Pa and 3.0 Pa for the CCS and IFC lesions, respectively), suggesting that the lumen was locally exposed to a wider and more heterogeneous distribution of WSS values (**Figure 3.5A**).

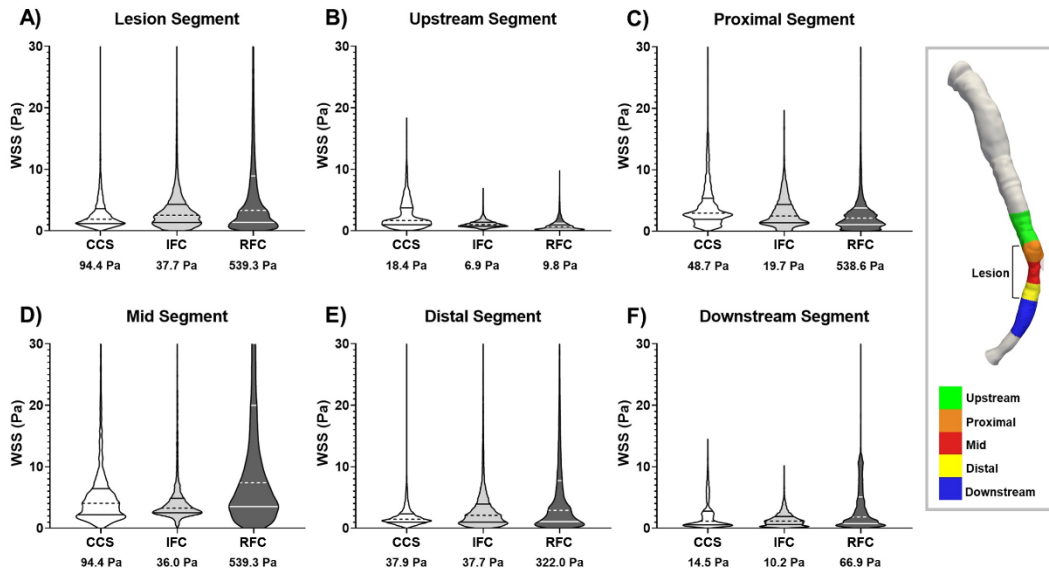


Figure 3.5. Wall shear stress magnitude. Violin plots illustrating the distribution of wall shear stress (WSS) along the (A) whole lesion, (B) upstream, (C) proximal, (D) mid, (E) distal, and (F) downstream segment of the lesion for the cases characterized by stable (CCS), intact fibrous cap (IFC) and ruptured fibrous cap (RFC) lesion. The number below each group represent the maximum value of WSS. The panel on the right illustrates the subdivision of the vessel lumen into five segments of interest.

At the segmental level (**Figure 3.5B-F**), the RFC group presented WSS values higher than CCS and IFC groups in the lesion's mid, distal, and downstream segments. Marked differences were observed at the mid segment of the lesion where the RFC cases presented the highest WSS

median value and the largest IQR with respect to the other two categories (7.4 Pa (IQR: 16.5 Pa) for the RFC lesions versus 4.0 Pa (IQR: 4.2 Pa) and 3.3 Pa (IQR: 2.4 Pa) for the CCS and IFC lesions, respectively, $p < 0.001$). Furthermore, the RFC cases were characterized by the maximum WSS value as compared to CCS and IFC groups (539.3 Pa versus 94.4 Pa and 36.0 Pa, respectively).

Although plaque morphology was different among the three groups, not significantly different area stenosis and minimum lumen area was observed (Figure 3.6 and Table 3.4).

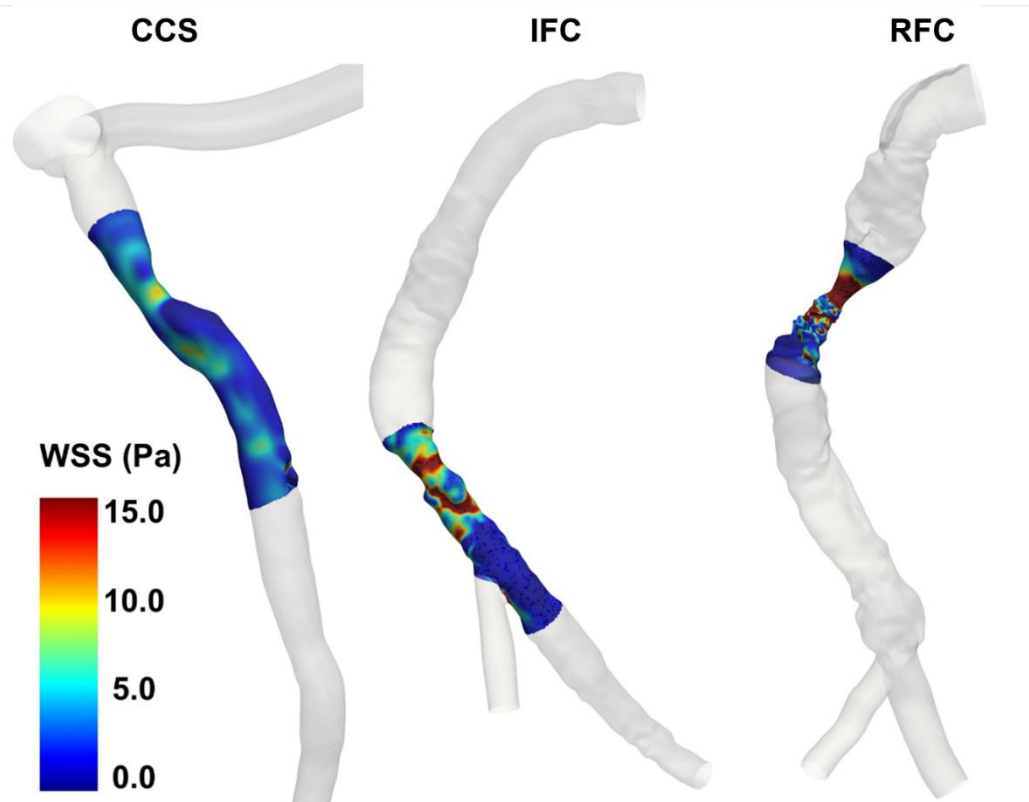


Figure 3.6 Wall shear stress luminal distribution. Color maps of wall shear stress (WSS) magnitude luminal distribution along the lesion for one explanatory case with chronic coronary syndrome (CCS), intact fibrous cap (IFC), and ruptured fibrous cap (RFC) lesions.

Table 3.4 Optical coherence tomography analysis results

| | SA | IFC | RFC | <i>p</i> -value |
|-----------------------------|-----|-----|-----|-----------------|
| MLA (mm²) | 1.7 | 2.5 | 1.6 | 0.19 |
| Area Stenosis (%) | 80 | 55 | 80 | 0.25 |

Minimum lumen area (MLA) and percentage of area stenosis measured from optical coherence tomography (OCT) images.

Differences between the three plaque morphologies also emerged from the analysis of the lumen areas exposed to low or high WSS (**Figures 3.7 and 3.8**, respectively). At a global level, the RFC lesions presented a larger lumen area exposed to low WSS compared to the other lesion categories, with a value of $5.8 \pm 1.4\%$ for the RFC lesions versus $1.9 \pm 1.4\%$ and $3.9 \pm 3.0\%$ for the CCS and IFC lesions, respectively (**Figure 3.7A**). A similar trend emerged at the segmental level (**Figures 3.7B-F**), except for the segment downstream of the lesion, which presented similar values for all lesion categories (**Figure 3.7E**).

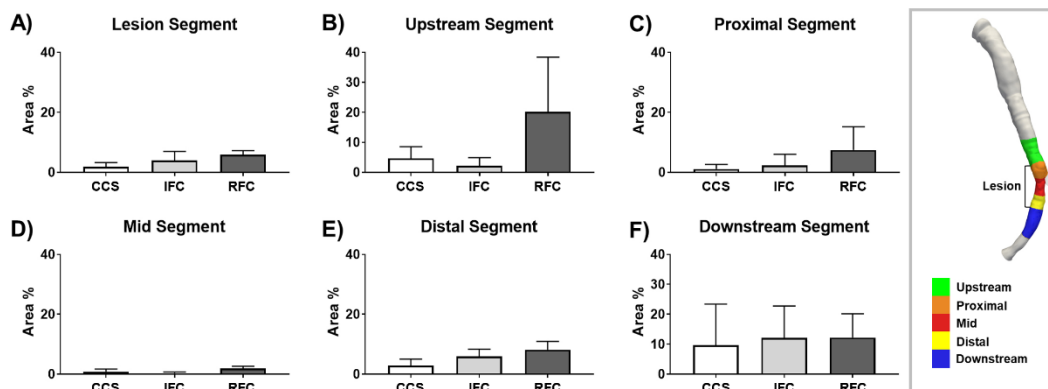


Figure 3.7 Surface area exposed to low wall shear stress magnitude. Bar diagrams of the percentage lumen areas exposed to low wall shear stress (WSS) averaged along the (A) whole lesion, (B) upstream, (C) proximal, (D) mid, (E) distal, and (F) downstream segment of the lesion for the cases presenting stable (CCS), intact fibrous cap (IFC) and ruptured fibrous cap (RFC) lesion. The panel on the right illustrates the subdivision of the vessel lumen into five segments of interest.

Of note, the RFC lesions presented also a higher percentage of area exposed to high WSS ($22.4\% \pm 10.3\%$) as compared to the other lesion categories ($10.3\% \pm 15.5\%$ and $5.5\% \pm 8.0\%$ for the CCS and IFC lesions, respectively, as reported in **Figure 3.8A**). This trend was confirmed also at

the segmental level, in particular, in the mid, distal and downstream segments (**Figures 3.8D-F**).

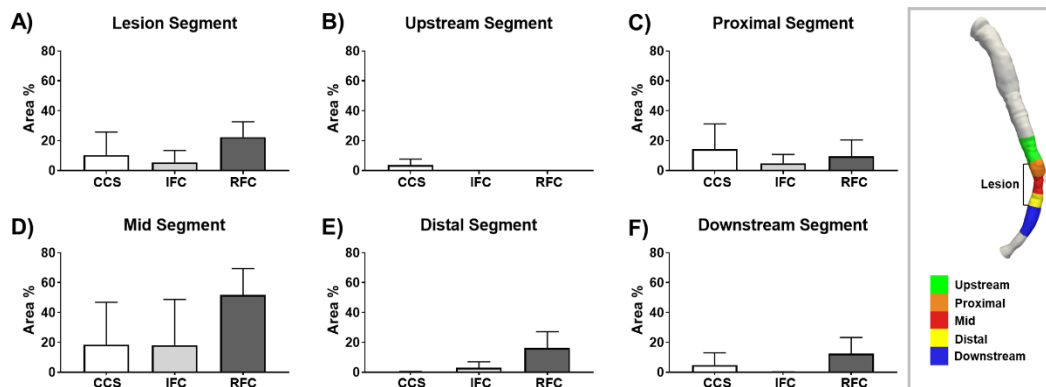


Figure 3.8. Surface area exposed to high wall shear stress magnitude. Bar diagrams of the percentage lumen areas exposed to high wall shear stress (WSS) averaged along the (A) whole lesion, (B) upstream, (C) proximal, (D) mid, (E) distal, and (F) downstream segment of the lesion for the cases presenting stable (CCS), intact fibrous cap (IFC) and ruptured fibrous cap (RFC) lesion. The panel on the right illustrates the subdivision of the vessel lumen into five segments of interest.

3.2.3 Link between biology and wall shear stress profiling

The trends emerging from the analysis of biological and WSS patterns suggest that some genes are differently expressed in patients with unstable and CCS plaques, depending on different (high or low) WSS distributions at the luminal surface. Within unstable patients (IFC and RFC), biological results hint at an overexpression of ADAMTS13 under higher WSS conditions (RFC) while LGALS8, EDN1 and TNF α expression is higher under lower WSS values, as observed in the IFC group. Such qualitative observations might be limited by the lack of univocal definition of low and high WSS cut-off and by the susceptibility of some molecules to both low and high WSS. Bearing in mind the limited number of patients with CFD data available (n=9), a significant correlation was found in the RFC group between WSS and TNF α ($p < 0.001$), EDN1 ($p = 0.036$) and MMP9 ($p = 0.005$), while no correlation was found in the CCS and IFC groups, thus suggesting a possible role of coronary patterns of WSS in the molecular pathways of ACS patients presenting with plaque rupture.

3.4 Discussion

This is the first study investigating:

1. WSS and molecular patterns among stable patients and unstable (NSTEMI-ACS) patients with different plaque morphologies.
2. A possible link between coronary WSS and molecular patterns in patients with three different plaque phenotypes (CCS, IFC, RFC).

The findings of this study indicates that WSS is different among the CCS, IFC and RFC plaques, with the latter showing higher levels of WSS and IFC plaques having an intermediate WSS value, between CCS and RFC. The segmental analysis confirms such results, and although the most significant differences are concentrated at the mid-segment (corresponding to the minimum lumen area), the distal and the downstream segments show higher WSS in the RFC plaques compared to CCS and IFC. Of interest, considering the plaque area exposed to low and high WSS, the patients belonging to RFC are the most subject to both low and high WSS with the widest, heterogeneous range of values as compared to IFC and CCS plaques. Indeed, more than 50% of the RFC plaque area is exposed to high WSS in the mid segment, compared to less than 20% of CCS and IFC plaques areas.

The effect of WSS on coronary artery plaques has been widely investigated over the last years and the greatest attention has been drawn to low WSS. It has been associated to plaque thickening, progression, increase in plaque and necrotic core area, thinner fibrous cap, endothelial dysfunction, negative remodeling and pro-inflammatory state^{20,85,110,113,153–156}.

Less well defined is the role of high WSS, although it has recently gained interest and has been involved in several pathological mechanisms, including plaque rupture^{67,157–160}. Multiple factors may be responsible for plaque rupture, including blood pressure and local geometry. Alongside, plaque tissue composition is another key determinant for cap strength and plaque resistance. Indeed, the thinnest areas of the fibrous cap are strictly correlated with the highest WSS areas and co-localize with macrophages

infiltration, lipid accumulation, intra-plaque hemorrhage and microcalcifications^{161–164}. In this perspective, high WSS might be closely involved in plaque rupture as an active actor playing two different roles: on one side acting as a direct biomechanical stressor against the plaque, on the other side it acts indirectly making the plaque more vulnerable by changing its composition. Accordingly, our data suggest that the detection of high WSS over a plaque might improve its identification as a vulnerable plaque prior to its rupture. Therefore, independently from WSS thresholds, the co-localization of high WSS and low plaque strength might be considered as a novel marker for the identification of vulnerable plaques. Consequently, WSS profiling in addition to commonly used intracoronary imaging techniques might play a crucial role in the differential diagnosis of culprit lesions and in the guidance of therapeutic strategies^{58,165}. These results corroborate and expand the recent results from the EROSION III trial (<https://clinicaltrials.gov/ct2/show/NCT03571269>), showing the important clinical implications of different therapeutic strategies for IFC and RFC plaques.

In addition to morphological and fluid dynamic features, detailed biological investigations might help to complete the plaque identikit. In this regard, the role of genetic to predict the risk of coronary artery disease has been widely studied and some genetic risk loci have been described^{166,167}. Moreover, recent data by our group have already demonstrated biological differences between IFC and RFC¹⁰⁷. In the present study, as much as thirteen genes have a significant different expression in the three groups of patients (CCS, IFC and RFC). The genes coding for proteins involved in matrix breakdown (MMP1, MMP9) are more expressed in unstable patients as compared to the stable ones, suggesting that the WSS pattern might be directly involved in plaque composition and fate¹⁶⁸. At the same time, unstable patients have also a greater systemic expression of genes involved in antioxidant functions (GPX1, NOS3, SOD1) and other counter-regulatory mechanisms, such as the inhibition of platelet activation (PLA2G7) and of matrix degradation (TIMP, PI16). Moreover, four genes show significantly different expressions between IFC and RFC plaques: LGALS8, EDN-1, ADAMTS13 and TNF α , responsible for cell-matrix interaction and cell adhesion (LGALS8), vasoconstriction (EDN1), regulation of blood clotting

(ADAMTS13) and inflammatory response ($TNF\alpha$), respectively. The different expression of these molecules in relation to different WSS reflects the existing data derived from animal and *in vitro* studies^{120,123,124,139–141,169,170}.

These data suggest that WSS might be involved in the unbalance of the molecular mechanisms leading to extracellular matrix remodeling, cap thinning and plaque instability (**Figure 3.9**).

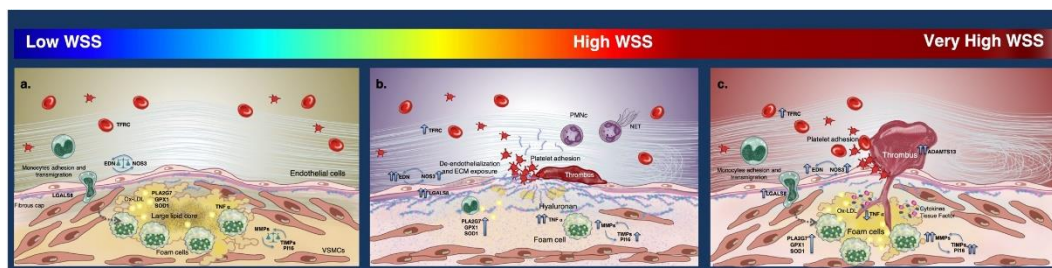


Figure 3.9 Biomechanical and molecular patterns of atherosclerotic plaques. Panels showing stable coronary plaque (CCS, a), intact fibrous cap unstable plaque (IFC, b) and ruptured fibrous cap unstable plaque (RFC, c). The figure summarizes the driving hypotheses that derive from both the existing literature and the data emerging from this experimental study. WSS influences plaque fate through multiple mechanisms: 1) it acts as a direct mechanical force on the arterial wall; 2) it affects plaque composition; 3) it up-/down-regulates gene expression. Molecular expression might vary in response to both levels, characteristics, and duration of WSS. Higher WSS values (panels b and c) are usually associated with increased expression of molecules involved in matrix breakdown (MMPs), cell-matrix interaction and cell adhesion (Galectin-8, LGALS8), vasoconstriction (EDN1) and inflammation ($TNF\alpha$). Alongside, the increased WSS is also responsible for the activation of counter regulatory mechanisms such as: 1) the activation of the lipoprotein-associated phospholipase A2 (LpPLA2, gene PLA2G7) and ADAMTS13 involved in platelet inhibition and regulation of blood clotting; 2) the increased release of nitric oxide, antioxidant molecules (SOD1, GPX1) and matrix degradation inhibitors (TIMP, PI16); 3) the inhibition of $TNF\alpha$ function and production for high and very high WSS values. The unbalance between these mechanisms together with mechanical forces acting on the plaque and the activation of specific molecular pathways represent the main triggers leading to plaque instability and thrombus formation.

In general, the significant differences among the selected genes, known to be influenced by WSS, support the hypothesis of a close link between coronary WSS and molecular pathways and suggest that the identification of biological markers, such as those associated with increased matrix degradation, represents an adjunctive tool for ACS patient's characterization. Finally, the significant association between WSS data and $TNF\alpha$, MMP9 and EDN1 gene expression in RFC group further strengthen our hypothesis: despite the small sample size, our findings suggest a prominent role of high WSS in the pathogenesis of plaque rupture, while in

CCS and IFC also other molecular as well as biomechanical mechanisms and triggers should be taken into account, confirming recent findings¹⁷¹.

Taken together, our data demonstrate a close and complex relationship between WSS and molecular patterns for different types of unstable plaque. However, which is the *primum movens* is still to be defined: biological signatures might be responsible for plaque phenotype and, in turn, for fluid shear stresses or, alternatively, plaque phenotype might be the consequence of the mechanical forces acting on endothelial cells. Most likely, a highly complex and dynamic interplay exists among the pathological processes leading to unstable plaques, wall remodeling and the underlying hemodynamics, which evolves as the pathology progresses. In this sense, the continuous arterial wall remodeling, influenced by flow disturbances, reshapes the local blood flow, which contributes to reshaping the lesion, giving rise to a pathological feedback loop. Following the architectural and design motto "*forms follow flow*", the hypothesis that the conformation of the plaque and its vulnerability is the result of mechanical forces acting on the arterial wall and that the molecular signature detectable at peripheral level is the result of counter-regulatory pathways activated as response of an altered WSS, is based upon the fact that most of the upregulated molecules in ACS belong to antioxidant, antithrombotic and anti-inflammatory enzymes. Of note, our findings suggest that the WSS might have a pathogenetic role in plaque rupture, where higher WSS values are related to mediators responsible for plaque inflammation and rupture in humans¹⁷².

3.5 Conclusions

In conclusion, this study demonstrates that different coronary plaques have different WSS and different molecular patterns, and that there might be a close link between them. Further studies are needed to better define the complex interaction between WSS and biology in the setting of ACS. Our data pave the way to a multiparametric approach aimed at identifying and treating ACS patients, in which morphological characteristics obtained by OCT imaging techniques should be integrated with molecular and hemodynamic features and with important implications for therapeutic strategies in the era of personalized medicine.

Chapter 4

Does the inflow velocity profile influence physiologically relevant flow patterns in computational hemodynamic models of left anterior descending coronary artery?

A version of this chapter is published in:

Medical Engineering & Physics, Vol. 82, August 2020

Does the inflow velocity profile influence physiologically relevant flow patterns in computational hemodynamic models of left anterior descending coronary artery?

Maurizio Lodi Rizzini, Diego Gallo, Giuseppe De Nisco, Fabrizio D'Ascenzo, Claudio Chiastra, Pier Paolo Bocchino, Francesco Piroli, Gaetano Maria De Ferrari, Umberto Morbiducci

4.1 Introduction

The marked predisposition to develop atherosclerosis makes coronary arteries of paramount clinical relevance. Although atherosclerosis initiation and progression results from the interplay of many systemic factors¹⁷³, its development at specific, geometrically predisposed locations such as branching and bifurcations¹⁷⁴ suggested the involvement of local hemodynamics^{18,175}. In particular, the role of wall shear stress (WSS) was extensively investigated over the last years^{20,112,113,176}, while more recently the role of intravascular helical patterns on coronary atherosclerosis initiation and progression was demonstrated^{72,177}. In this context, the combined use of medical imaging and computational fluid dynamics (CFD) has proven to be a valuable tool in the study of possible associations between local hemodynamics and coronary artery disease as it makes available highly resolved hemodynamic flow patterns inside anatomically realistic, patient-specific geometries^{178–180}. However, *in silico* methods require assumptions that introduce uncertainties, weakening CFD findings at a level that could limit their translation to clinics^{181–187}. As recently highlighted, the uncertainties in cardiovascular modelling should not compromise its added value with respect to standard clinical measurement and therefore they should be carefully assessed.

While anatomically realistic geometries can be reconstructed with satisfactory accuracy using *in vivo* imaging tools, acquiring non-defective patient-specific boundary conditions, as required to perform reliable computational hemodynamics, is not always feasible. This is particularly true for the coronary arteries, for which:

1. the measurable (whenever possible) inflow rates can be imposed only in terms of idealized velocity profiles.
2. The possibility to use realistic three-dimensional (3D) velocity profiles measured directly *in vivo* as inflow boundary condition is still challenging, due to issues related to resolution and cardiac motion¹⁸⁸.

To be clearer, when only the integral quantity flow rate is available, its translation to inflow Dirichlet boundary condition in terms of 3D velocity

profiles in CFD applications necessarily undergoes an idealization process based on a priori hypotheses to fill the gap of information. For these reasons, most of the previous computational studies on coronary arteries, including those accounting for the presence of coronary stents, starting from *in vivo* flow rate measurements/estimations, prescribed the inflow boundary conditions in terms of flat^{64,146,189,190} or fully developed^{145,191–194} velocity profiles. Such a priori hypotheses on the velocity profiles to be used as conditions at inflow boundaries represent a source of uncertainty in the estimation of helical and WSS patterns¹⁹⁵, potentially masking their relationship with atherosclerosis initiation and progression. Moreover, *in vitro* and *in silico* hemodynamic studies revealed the presence of skewed velocity profiles in the left coronary artery^{196–198}, with a not negligible presence of secondary flows in the entire coronary tree, as it can be expected by considering the vessel tortuosity and the presence of bifurcations and branching.

In this context, the aim of this study was to evaluate the budget of uncertainty associated with assumptions on the shape of the velocity profiles imposed as inflow boundary conditions in coronary artery CFD models. To this end, a framework was developed enabling the generation of artificial velocity profiles by means of generalized analytical formulations able to:

1. generate 3D velocity profiles with secondary flows.
2. Fit the non-circular cross-section of blood vessels.

The developed framework was then applied to left anterior descending (LAD) coronary artery models to evaluate the impact that the shape of inflow velocity profiles used as inlet boundary condition has on WSS distribution at the luminal surface and intravascular flow features, focusing on helical flow patterns.

4.2 Methods

4.2.1 Image data collection and 3D vessel reconstruction

Ten subjects (8 males and 2 females, age = 58.6 ± 6.5) that underwent invasive coronary cineangiography after heart transplant with no sign of atherosclerosis were selected for this study. Clinical images were acquired at Città della Salute e della Scienza hospital (Turin, Italy) with the monoplane X-ray system Allura Xper (Philips Medical Systems, Amsterdam, The Netherlands). Two cranial, end-diastolic angiographic projections, with a minimum angle of 25° between them were used to reconstruct the geometry of the LAD coronary arteries using the commercial software QAngio XA Bifurcation RE (Medis medical imaging systems, Leiden, The Netherlands). The study complies with the Declaration of Helsinki on human research and was approved by the Città della Salute e della Scienza hospital. All patients gave written informed consent.

Given the importance of side branches for hemodynamic characterization of coronary arteries^{189,199–201}, each side branch with a diameter greater than 1 millimetre was reconstructed and merged to form the LAD geometry using VTK (Kitware, Inc., Clifton Park, NY, USA) and VMTK (Orobix, Bergamo, Italy) libraries. Technically, the main vessel was segmented and reconstructed considering one side branch at a time, repeating this operation for all side branches (**Figure 1A**). Then, the Voronoi diagrams computed over each bifurcation were combined into a single diagram to obtain the complete 3D geometry including all side branches. The result of the 3D LAD geometry reconstruction process is presented in **Figure 1B**. Given the huge anatomical variability in coronary arteries the patients were properly selected so that all LAD geometries present two diagonal branches and one septal branch.

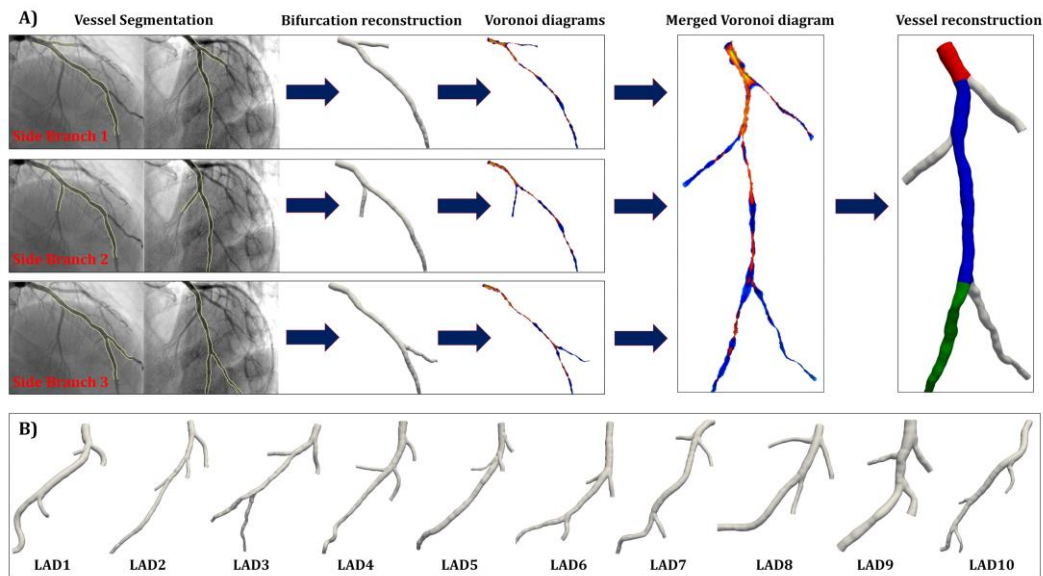


Figure 4.1. Three-dimensional vessel reconstruction. A) Workflow for the three-dimensional reconstruction of left anterior descending (LAD) coronary artery geometries from two angiographic projections. From left to right: single bifurcation segmentation, single bifurcation reconstruction, Voronoi diagrams computation, Voronoi diagrams merging, and geometry reconstruction. Proximal, mid, and distal segments are color coded (red, blue, and green, respectively) according to American Heart Association classification. B) The ten reconstructed LAD coronary artery geometries.

4.2.2 Computational hemodynamics and boundary conditions

The governing equations of fluid motion were solved in their discretized form under steady-state conditions using the finite volume method with the general purpose CFD software Fluent (Ansys Inc., Canonsburg, PA). The fluid domain was discretized by means of the meshing software ICM CFD (Ansys Inc., Canonsburg, PA, USA) using tetrahedral elements with curvature-based refinement and 5 near-wall prismatic layers. The same meshing parameters derived from a previous grid independence analysis were adopted^{72,177}, resulting in a mesh cardinality ranging between 1.7 and 5.5 million elements, depending on vessel total volume and local curvature. The blood was assumed as a homogeneous, incompressible fluid with a density ρ equal to 1060 Kg/m³. The blood non-Newtonian behaviour was modelled using the Carreau model ($\mu_{\infty} = 0.0035$ Pa·s, $\mu_0 = 0.25$ Pa·s, $\lambda = 25$ s, and $n=0.25$)⁷³. The vessel walls were assumed to be rigid and no-slip condition was applied at wall boundaries. Details on CFD settings are

extensively described elsewhere⁷³. Concerning the inlet and outlet boundary conditions, since *in vivo* measured data were not available, inlet flow rates were obtained using a scaling law based on the hydraulic diameter of the inlet cross-section⁷⁰. The resulting inlet flow rates (mean = 43.12 mL/min, range: 30.73 to 70.99 mL/min) were prescribed in terms of 3D velocity profiles at the inlet, as detailed in the following section. As for outlets, the flow split at each bifurcation was estimated using a scaling law based on the ratio of the hydraulic diameter of the daughter branches⁷⁰, and imposed as outflow boundary condition.

4.2.3 3D velocity profiles generation: analytical formulation

The 3D velocity profile on a generic cross-section of a vessel can be described as a combination of:

1. a principal, through-plane (TP) component, in the direction of the axis of the vessel.
2. A secondary, in-plane (IP) component, lying on the plane orthogonal to the axis of the vessel.

To test the impact of the velocity profile on the hemodynamics of LAD coronary arteries, different 3D velocity profiles were generated using analytical formulations based on previous observations demonstrating the presence of secondary flows in coronary arteries^{196,198}.

To deal with realistic non-circular cross-section of vessels, a generalized polar coordinate system was here introduced. More in detail, starting from the polar coordinate system (r, ϑ) defined on a generic vessel cross-section, a new generalized polar coordinate system (r', ϑ') was defined on the inflow section of each LAD vessel as:

$$\begin{cases} r' = \frac{r}{R(\vartheta)} \\ \vartheta' = \vartheta \end{cases} \quad (4.1)$$

where $R(\vartheta)$ is the variable radius of the inlet surface depending on angular coordinate. By construction, r' can assume values in the range $[0, 1]$. Once

the new coordinate system has been defined, the TP component was obtained using a generalized formulation of parabolic velocity profile:

$$\mathbf{v}_{TP}(r', \vartheta') = [1 - r'^2 + Kr'(r'^2 - 1) \cos(\vartheta')] \mathbf{u}_n \quad (4.2)$$

where K is a constant regulating the displacement of peak velocity from the geometric centre of the inlet cross-section, and \mathbf{u}_n is the unit vector in the vessel axis direction. Two differently shaped TP velocity profiles were built prescribing $K = 0$ and $K = 1$, to obtain a parabolic and a skewed velocity profile (i.e., with the $\mathbf{v}_{TP}(r', \vartheta')$ maximum value dislodged from vessel axis), respectively (**Figure 2A**).

Secondary flows as part of the 3D velocity profile were incorporated considering two possible configurations, namely the single-vortex and the Dean-like double-vortex configurations. The first configuration was obtained by generalizing the equation previously proposed to describe axially symmetric flow rotations²⁰² as follows:

$$\begin{cases} \mathbf{v}_{\vartheta'}(r', \vartheta') = r'(1 - r'^2) \mathbf{u}_{\vartheta'} \\ \mathbf{v}_{r'}(r', \vartheta') = 0 \cdot \mathbf{u}_{r'} \end{cases} \quad (4.3)$$

where $\mathbf{u}_{\vartheta'}$ and $\mathbf{u}_{r'}$ are the unit vectors in angular and radial directions, respectively. The second configuration was obtained generalizing the Dean theory for secondary flows in curved pipes²⁰³ as follows:

$$\begin{cases} \mathbf{v}_{\vartheta'}(r', \vartheta') = (1 - r'^2)(4 - 23r'^2 + 7r'^4) \cos \vartheta' \mathbf{u}_{\vartheta'} \\ \mathbf{v}_{r'}(r', \vartheta') = (1 - r'^2)^2(4 - r'^2) \sin \vartheta' \mathbf{u}_{r'} \end{cases} \quad (4.4)$$

The IP velocity vector was scaled with respect to the TP component as follows:

$$\mathbf{v}_{IP}(r', \vartheta') = C \frac{\mathbf{v}_{\vartheta'}(r', \vartheta') + \mathbf{v}_{r'}(r', \vartheta')}{|\mathbf{v}_{\vartheta'}(r', \vartheta') + \mathbf{v}_{r'}(r', \vartheta')|} \overline{(\mathbf{v}_{TP} \cdot \mathbf{u}_n)} \quad (4.5)$$

where C is a scaling factor. In this study, we imposed $C = \pm 0.25$, corresponding to an IP velocity component equal to the 25% of TP velocity component. The sign of constant C was used to generate secondary flows that differ in the direction of rotation, while a scaling factor $C = 0$ was used to

generate purely TP velocity profiles. Ten different inflow velocity profiles were generated combining all the TP and IP configurations mentioned above and imposed as inflow boundary conditions to the ten LAD models. The analysis was completed by prescribing a flat velocity profile, corresponding to plug flow and representing the simplest boundary condition to be imposed, resulting in a total number of 110 simulations.

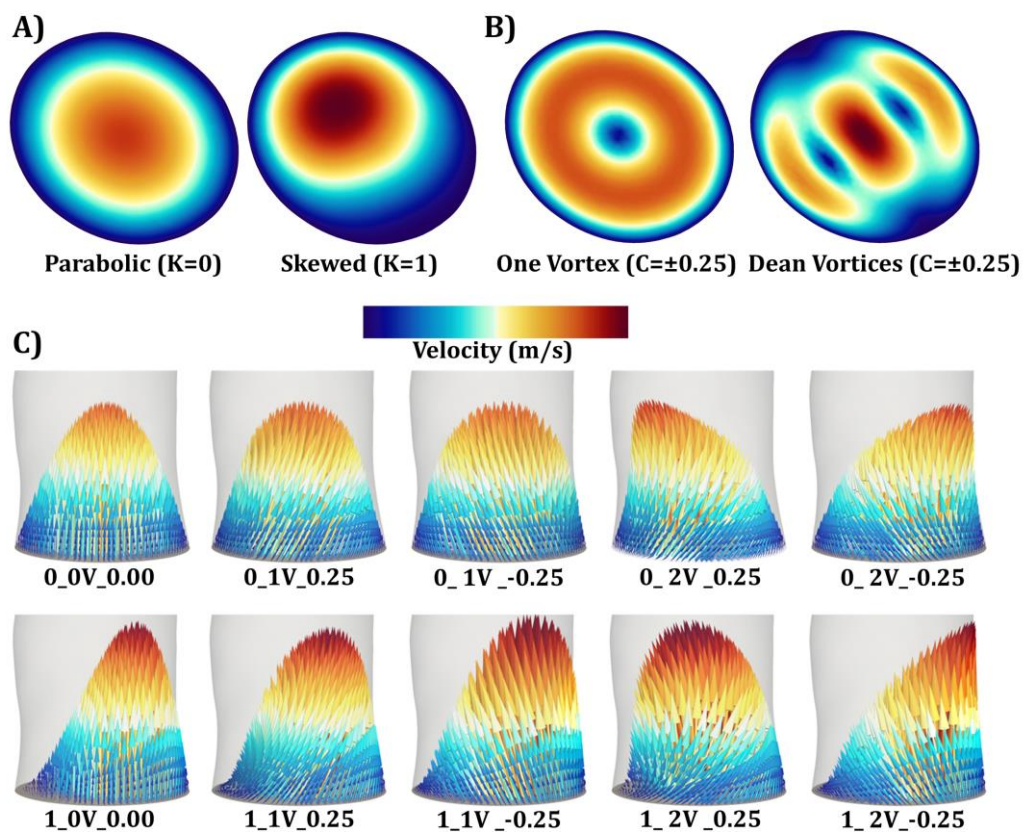


Figure 4.2. Generated velocity profiles. A) Colour maps of the through-plane (TP) velocity component coloured according to TP velocity magnitude; B) colour maps of the in-plane (IP) velocity component coloured according to IP velocity magnitude; C) three-dimensional velocity profile scaled vectors, coloured according to velocity magnitude.

In the followings, the generated velocity profiles are identified according to a code composed by the applied value of constant K, the number of vortices characterizing the secondary flows, and the value of constant C (e.g., 0_1V_0.25 for a parabolic velocity profile, with single-vortex IP component rotating in counter-clockwise direction). The differently shaped generated velocity profiles are displayed in **Figure 2C**.

4.2.4 Hemodynamic descriptors

The impact of the shape of inflow velocity profiles on LAD blood flow was evaluated in terms of near-wall and intravascular hemodynamic descriptors. In general, the quantitative comparison was carried out assuming as reference case the purely TP parabolic (0_0V_0.00) velocity profile^{191,193,194}.

Near-wall hemodynamics was investigated in terms of wall shear stress magnitude ($|\mathbf{WSS}|$) distribution over the luminal surface. In addition, for each simulation the surface averaged $|\mathbf{WSS}|$ value (AWSS) was computed as follows:

$$AWSS = \frac{1}{S} \int_S |\mathbf{WSS}(\mathbf{x})| dS \quad (4.6)$$

where \mathbf{x} is the position vector and S is the generic luminal surface. Here, four regions were considered as integration surface: the whole main vessel, the LAD proximal, mid and distal segments (**Figure 1A**), delimited by diagonal branches and defined in accordance with the American Heart Association classification²⁰⁴. To quantify the distance downstream of the inflow section of the LAD model where the shape of the inflow velocity profile still influences near-wall hemodynamics, the cross-section averages of the local $|\mathbf{WSS}|$ values were analysed moving along the centreline of the vessel. Then, impact length of the inflow velocity profile shape was defined as the distance from the LAD inflow section at which differences in cross-sectional average $|\mathbf{WSS}|$ values fall below 5%, when compared to the cross-sectional average $|\mathbf{WSS}|$ values obtained imposing the reference velocity profile. Such distance was expressed in terms of cross-sectional hydraulic diameter of the LAD inflow section. The velocity profile shape length of influence was then compared with the theoretical “entrance length”, calculated for each LAD model according to the formulation valid for fully developed laminar flows in cylindrical pipes²⁰⁵:

$$L = 0.05 \cdot Re \quad (4.7)$$

where L is expressed in terms of number of hydraulic diameters of the inflow section, and Re is the Reynolds number characterizing the flow field in the LAD model.

The impact of the shape of the inflow velocity profile on physiologically relevant intravascular flow features was also investigated. Motivated from very recent findings demonstrating the atheroprotective role of helical flow in coronary arteries^{72,177}, here the fluid mechanic quantity helicity was considered and helicity-based descriptors proposed elsewhere were analysed^{21,39,41}. In particular, helical flow was visualized in terms of local normalized helicity (LNH) isosurfaces^{39,206}. Briefly, LNH is a measure of the alignment between velocity and vorticity vectors and is defined as:

$$\text{LNH}(\mathbf{x}) = \frac{\mathbf{v}(\mathbf{x}) \cdot \boldsymbol{\omega}(\mathbf{x})}{|\mathbf{v}(\mathbf{x})||\boldsymbol{\omega}(\mathbf{x})|} \quad (4.8)$$

where \mathbf{v} and $\boldsymbol{\omega}$ are velocity and vorticity vectors, respectively. A quantitative description of helical flow was provided considering two helicity-based descriptors⁴¹, namely the volume-average helicity intensity (h_2), and the unsigned balance of counter-rotating helical structures (h_4), derived in steady-state form as:

$$h_2 = \frac{1}{V} \int_V |\mathbf{v}(\mathbf{x}) \cdot \boldsymbol{\omega}(\mathbf{x})| dV \quad (4.9)$$

$$h_4 = \frac{|\int_V \mathbf{v}(\mathbf{x}) \cdot \boldsymbol{\omega}(\mathbf{x}) dV|}{\int_V |\mathbf{v}(\mathbf{x}) \cdot \boldsymbol{\omega}(\mathbf{x})| dV} \quad 0 \leq h_4 \leq 1 \quad (4.10)$$

where V is the integration volume. h_4 measures the strength of relative rotation of helical fluid structures in the fluid domain. It is a non-dimensional quantity ranging between 0 and 1: its value equals 1 when only left-handed or right-handed helical structures are present in the integration volume, and it is equal to 0 in case of reflectional symmetry. Four volumes of integration were defined, namely the whole main vessel, the volume of the proximal, mid, and distal segments, following the same approach adopted for the computation of AWSS.

4.3 Results

4.3.1 Near-wall hemodynamics

The impact that the shape of the inflow velocity profile has on WSS was firstly evaluated in terms of AWSS percentage differences with respect to

the reference (TP-only parabolic) velocity profile. In the box plot of **Figure 3**, the analysis is presented aggregating AWSS data from all the 10 LAD models on the basis of the specific velocity profile used as inflow boundary condition and considering the whole vessel and its division in three segments.

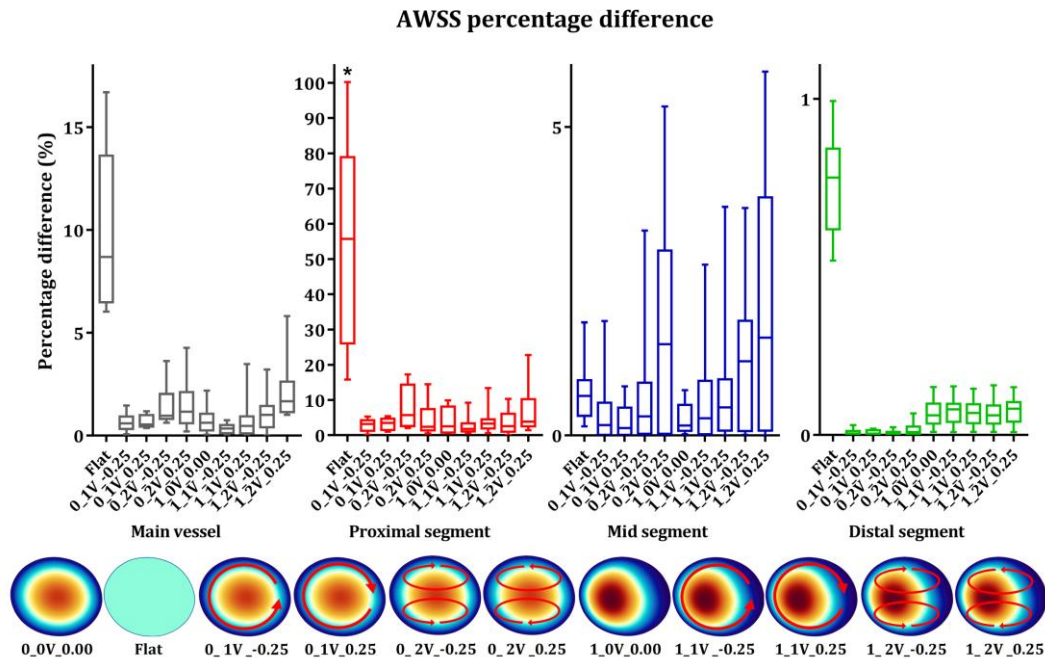


Figure 4.3 Surface averaged wall shear stress magnitude percentage difference. From left to right: percentage differences of surface averaged |WSS| (AWSS) between the reference (0_0V_0.00) and the other velocity profiles in the main vessel, proximal, mid and distal segments. Statistically significant differences are indicated with * (p-value<0.001).

Overall, the largest percentage differences from the reference TP-only parabolic velocity profile were observed in the proximal segment (median values range = [1.76%, 55.70%]), where they rose up to 100.24% in the case of the flat velocity profile (median value = 55.70%). The impact of the shape of the other inflow velocity profiles in the proximal segment was lower than 22.74% (velocity profile 1_2V_0.25 in geometry LAD8), with median value range = [1.76%, 5.71%] (**Figure 4.3**). In the mid segment, the maximum AWSS percentage differences from the reference case were reduced to 5.84% (velocity profile 1_2V_0.25 in geometry LAD8), with median value range = [0.01%, 0.96%] (**Figure 4.3**). AWSS percentage differences, came down to less than 1.00% in the distal segment, with a

median value range = [0.00%, 0.77%] (**Figure 4.3**). Focusing on the whole vessel, the AWSS percentage differences from the reference (TP-only parabolic) velocity profile reflected the observed differences in the proximal LAD segment. In detail, the maximum percentage difference (16.70% for geometry LAD9) was observed for flat velocity profile, while for the other velocity profiles percentage differences were lower than 5.81% (velocity profile 1_2V_0.25 in geometry LAD8), with a median value range = [0.34%, 1.67%]. Single cases percentage difference values are detailed in **Table 4.1**. For the sake of completeness, it is also reported that statistically significant differences in AWSS values emerged only in the proximal segment, and only between the reference (TP-only parabolic) velocity profile and the flat one (p -value<0.001, non-parametric Kruskal-Wallis test).

Table 4.1 Percentage difference values of AWSS

| Profiles | LAD1 | LAD2 | LAD3 | LAD4 | LAD5 | LAD6 | LAD7 | LAD8 | LAD9 | LAD10 |
|------------------------|-------|-------|-------|-------|-------|-------|-------|-------|--------|-------|
| Main Branch | | | | | | | | | | |
| <i>Flat</i> | 9.27 | 7.63 | 8.49 | 8.89 | 12.82 | 6.03 | 6.29 | 16.01 | 16.70 | 6.55 |
| <i>0_1V_-0.25</i> | 0.60 | 0.60 | 0.75 | 0.06 | 0.88 | 0.52 | 0.34 | 1.06 | 1.46 | 0.26 |
| <i>0_1V_0.25</i> | 1.12 | 0.46 | 0.47 | 0.56 | 0.80 | 0.52 | 0.37 | 1.17 | 0.95 | 0.38 |
| <i>0_2V_-0.25</i> | 3.63 | 0.84 | 0.81 | 1.86 | 1.04 | 0.90 | 0.62 | 1.20 | 2.51 | 0.80 |
| <i>0_2V_0.25</i> | 0.65 | 1.36 | 2.16 | 0.20 | 1.75 | 0.96 | 0.52 | 4.26 | 2.10 | 0.63 |
| <i>1_0V_0</i> | 2.19 | 0.86 | 0.60 | 0.21 | 0.90 | 0.65 | 0.31 | 0.04 | 1.50 | 0.27 |
| <i>1_1V_-0.25</i> | 0.16 | 0.49 | 0.12 | 0.12 | 0.05 | 0.33 | 0.57 | 0.35 | 0.75 | 0.42 |
| <i>1_1V_0.25</i> | 0.03 | 0.11 | 0.08 | 0.71 | 0.55 | 0.21 | 0.92 | 3.48 | 0.38 | 0.95 |
| <i>1_2V_-0.25</i> | 1.88 | 1.04 | 0.97 | 3.21 | 1.22 | 0.42 | 0.35 | 1.30 | 0.42 | 0.02 |
| <i>1_2V_0.25</i> | 1.18 | 1.61 | 2.75 | 1.74 | 2.58 | 1.28 | 1.01 | 5.81 | 2.31 | 1.04 |
| Proximal Branch | | | | | | | | | | |
| <i>Flat</i> | 45.76 | 63.45 | 73.92 | 47.95 | 64.18 | 18.43 | 28.58 | 93.90 | 100.24 | 15.77 |
| <i>0_1V_-0.25</i> | 2.82 | 3.85 | 4.61 | 0.14 | 3.45 | 1.42 | 1.42 | 5.28 | 4.14 | 0.66 |
| <i>0_1V_0.25</i> | 3.76 | 3.48 | 4.67 | 2.70 | 3.51 | 1.43 | 1.50 | 5.36 | 4.90 | 0.95 |
| <i>0_2V_-0.25</i> | 17.26 | 7.73 | 13.72 | 3.94 | 5.85 | 2.45 | 2.61 | 5.57 | 16.05 | 2.05 |
| <i>0_2V_0.25</i> | 0.54 | 6.82 | 8.95 | 1.40 | 5.18 | 2.62 | 2.16 | 14.47 | 1.15 | 1.60 |
| <i>1_0V_0</i> | 9.89 | 5.59 | 7.76 | 0.79 | 3.19 | 1.75 | 1.55 | 0.63 | 8.98 | 0.73 |
| <i>1_1V_-0.25</i> | 1.89 | 1.63 | 1.04 | 3.82 | 0.64 | 0.92 | 2.62 | 3.19 | 9.22 | 1.11 |
| <i>1_1V_0.25</i> | 0.58 | 2.67 | 4.43 | 3.08 | 4.33 | 0.60 | 3.53 | 13.38 | 4.49 | 2.39 |
| <i>1_2V_-0.25</i> | 9.59 | 4.35 | 0.34 | 10.34 | 2.93 | 1.17 | 1.70 | 4.86 | 2.17 | 0.01 |
| <i>1_2V_0.25</i> | 2.03 | 9.22 | 13.16 | 3.76 | 9.00 | 3.54 | 3.89 | 22.74 | 1.44 | 2.62 |
| Mid Branch | | | | | | | | | | |
| <i>Flat</i> | 0.14 | 0.64 | 0.33 | 0.28 | 0.55 | 0.99 | 0.80 | 0.86 | 1.83 | 0.64 |
| <i>0_1V_-0.25</i> | 0.02 | 0.28 | 0.28 | 0.06 | 0.57 | 0.01 | 0.00 | 0.51 | 1.85 | 0.01 |
| <i>0_1V_0.25</i> | 0.69 | 0.00 | 0.13 | 0.11 | 0.25 | 0.01 | 0.00 | 0.79 | 0.37 | 0.01 |
| <i>0_2V_-0.25</i> | 0.03 | 0.56 | 1.19 | 3.32 | 0.40 | 0.03 | 0.01 | 0.74 | 0.21 | 0.01 |
| <i>0_2V_0.25</i> | 1.11 | 1.41 | 1.57 | 1.54 | 2.22 | 0.03 | 0.00 | 5.32 | 5.33 | 0.02 |
| <i>1_0V_0</i> | 0.29 | 0.16 | 0.45 | 0.12 | 0.73 | 0.02 | 0.09 | 0.63 | 0.16 | 0.03 |
| <i>1_1V_-0.25</i> | 0.53 | 0.62 | 0.02 | 2.77 | 0.17 | 0.01 | 0.09 | 0.39 | 1.69 | 0.02 |
| <i>1_1V_0.25</i> | 0.35 | 0.52 | 0.90 | 0.38 | 0.93 | 0.00 | 0.09 | 3.70 | 0.85 | 0.04 |
| <i>1_2V_-0.25</i> | 0.31 | 1.20 | 1.47 | 3.69 | 1.91 | 0.01 | 0.08 | 1.20 | 1.84 | 0.03 |
| <i>1_2V_0.25</i> | 1.49 | 1.46 | 1.68 | 3.20 | 2.48 | 0.00 | 0.09 | 5.84 | 5.90 | 0.03 |
| Distal Branch | | | | | | | | | | |
| <i>Flat</i> | 0.80 | 0.93 | 0.52 | 0.82 | 0.64 | 0.99 | 0.82 | 0.55 | 0.73 | 0.63 |
| <i>0_1V_-0.25</i> | 0.00 | 0.01 | 0.00 | 0.03 | 0.01 | 0.00 | 0.01 | 0.02 | 0.00 | 0.00 |
| <i>0_1V_0.25</i> | 0.00 | 0.00 | 0.01 | 0.01 | 0.02 | 0.00 | 0.00 | 0.02 | 0.00 | 0.00 |
| <i>0_2V_-0.25</i> | 0.00 | 0.01 | 0.00 | 0.01 | 0.02 | 0.01 | 0.01 | 0.00 | 0.00 | 0.00 |
| <i>0_2V_0.25</i> | 0.00 | 0.01 | 0.02 | 0.06 | 0.01 | 0.00 | 0.01 | 0.04 | 0.00 | 0.00 |
| <i>1_0V_0</i> | 0.08 | 0.14 | 0.07 | 0.04 | 0.05 | 0.02 | 0.07 | 0.14 | 0.05 | 0.01 |
| <i>1_1V_-0.25</i> | 0.08 | 0.14 | 0.08 | 0.08 | 0.05 | 0.02 | 0.08 | 0.13 | 0.05 | 0.01 |
| <i>1_1V_0.25</i> | 0.08 | 0.14 | 0.08 | 0.04 | 0.05 | 0.02 | 0.08 | 0.13 | 0.05 | 0.01 |

| | | | | | | | | | | |
|------------|------|------|------|------|------|------|------|------|------|------|
| 1_2V_-0.25 | 0.08 | 0.15 | 0.07 | 0.04 | 0.04 | 0.02 | 0.08 | 0.12 | 0.04 | 0.01 |
| 1_2V_0.25 | 0.08 | 0.14 | 0.08 | 0.09 | 0.05 | 0.02 | 0.08 | 0.13 | 0.05 | 0.01 |

Percentage difference values of AWSS between the reference (0_0V_0.00) and the other velocity profiles in the main vessel, proximal, mid and distal segments.

The impact of the shape inflow velocity profile on the distribution of the **|WSS|** on the LAD luminal surface can be appreciated by visual inspection of **Figure 4.4**, where the contour maps of the local percentage difference with respect to the reference (TP-only parabolic) velocity profile are displayed for two explanatory models, LAD7 and LAD8, presenting, respectively, the lowest and the highest maximum AWSS percentage difference, between the reference (TP-only parabolic) and the other velocity profiles (excluding the flat one) in the whole main vessel.

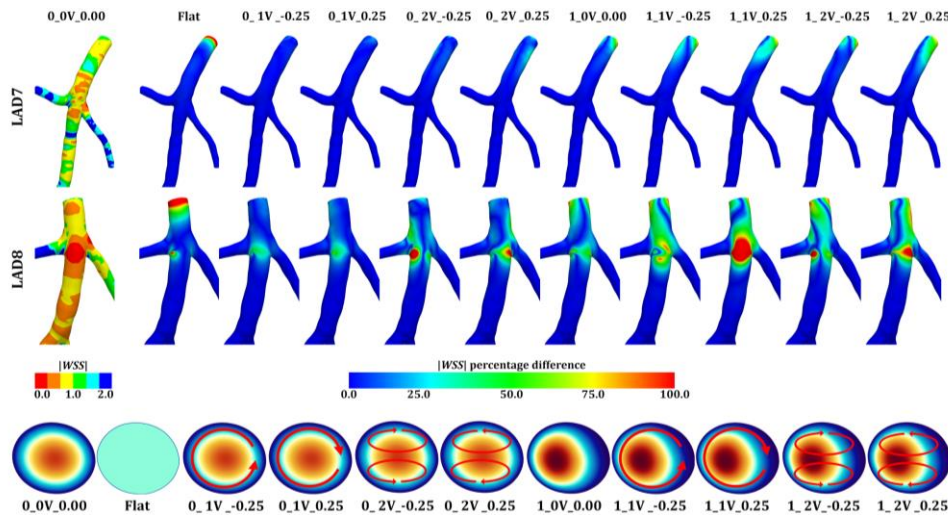


Figure 4.4 Distribution of $|WSS|$ and percentage difference at the luminal surface: explanatory cases. On the left: distribution of $|WSS|$ at the luminal surface for the reference velocity profile (0_0V_0.00); on the right: distribution of $|WSS|$ percentage differences between the reference and the other velocity profiles. Two explanatory cases are reported (i.e. the models with the lowest and the highest AWSS difference in the main vessel, namely LAD7 and LAD8, respectively). A magnified view of the vessels is presented for a clearer visualization of the results.

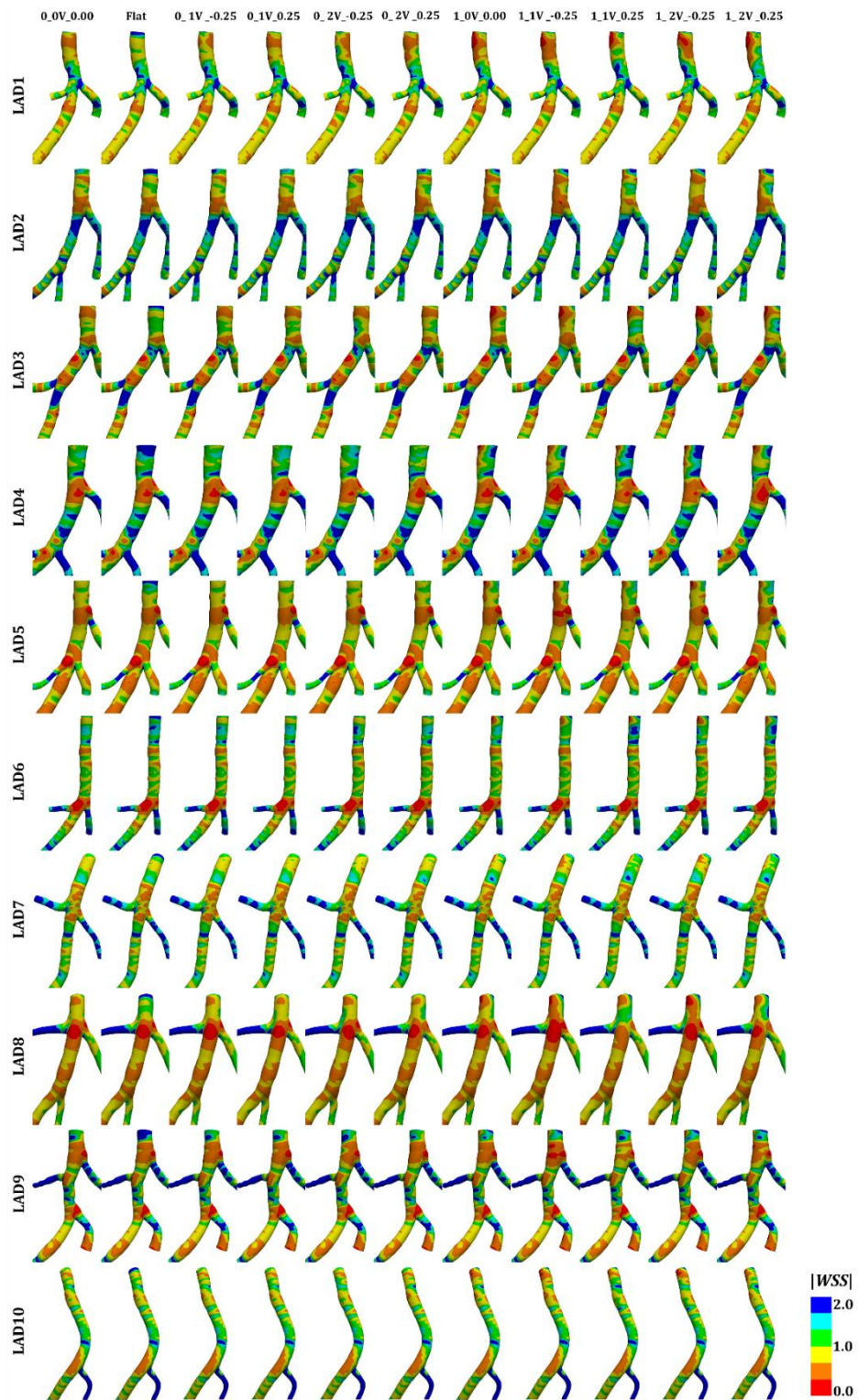


Figure 4.5 Distribution of $|WSS|$ at the luminal surface. From top to bottom the ten LAD geometries, from left to right the 11 simulated velocity profiles.

The highest percentage differences from the reference WSS magnitude distribution were always located in the proximal segment. High differences ($>100.00\%$) were observed also in the region of the first bifurcation only for model LAD8. However, this effect of the shape of the inflow velocity profile could be mainly ascribed to the fact that WSS magnitude values were lower than 0.5 Pa in a large part of this area (**Figure 4.4**), so that very small variations could give rise to high percentage differences. The **|WSS|** distribution on the luminal surface of the ten LAD models are presented in **Figure 4.5**.

The length of influence of the shape of the inflow velocity profile on near-wall hemodynamics, evaluated both in terms of maximum impact length and theoretical entrance length (**Table 4.2**), is visualized over each LAD model in **Figure 4.6**. It emerges that the theoretical entrance length evaluated using equation 4.7 was always longer than the maximum impact length (with the only exception of model LAD1). Therefore, the effects of the shape of the inflow velocity profile on the average WSS magnitude over each vessel cross-section vanished within a few diameters, and within a distance that was shorter than the one predicted by the theory in straight cylindrical conduits (**Figure 4.6**).

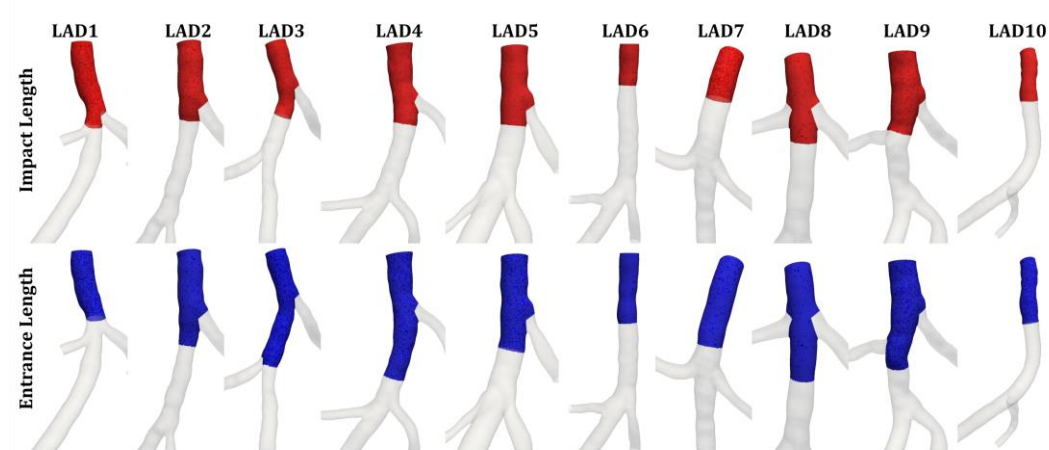


Figure 4.6 Theoretical vs. real entrance length. Upper panel: impact length is highlighted in red for each model. Lower panel: theoretical entrance length is highlighted in blue for each model. A magnified view of the vessels is presented for a clearer visualization of the results.

| Table 4.2 Entrance length | | |
|---------------------------|-------------------|---------------------------------|
| | Impact length (D) | Theoretical entrance length (D) |
| LAD1 | 5.6 | 4.4 |
| LAD2 | 3.2 | 3.9 |
| LAD3 | 3.8 | 5.9 |
| LAD4 | 3.1 | 5.0 |
| LAD5 | 3.0 | 3.6 |
| LAD6 | 2.2 | 3.8 |
| LAD7 | 2.1 | 3.7 |
| LAD8 | 3.1 | 4.2 |
| LAD9 | 3.0 | 3.9 |
| LAD10 | 3.3 | 4.1 |

Impact length vs theoretical entrance length

4.3.1 Intravascular hemodynamics

The impact of the shape of the inflow velocity profile on intravascular flow was quantified in terms of helicity intensity h_2 and counter-rotating helical patterns balance h_4 . Their values, integrated over each one of the ten LAD models main vessel, are presented in **Figure 4.7**. As a general, observations, expectedly the three-dimensionality of the inflow velocity profile (i.e., the presence of an IP velocity component) was associated with higher h_2 values in the vessel, while counter-rotating helical structures were markedly unbalanced (higher h_4) when a single-vortex IP velocity component was present in the imposed inflow velocity profile.

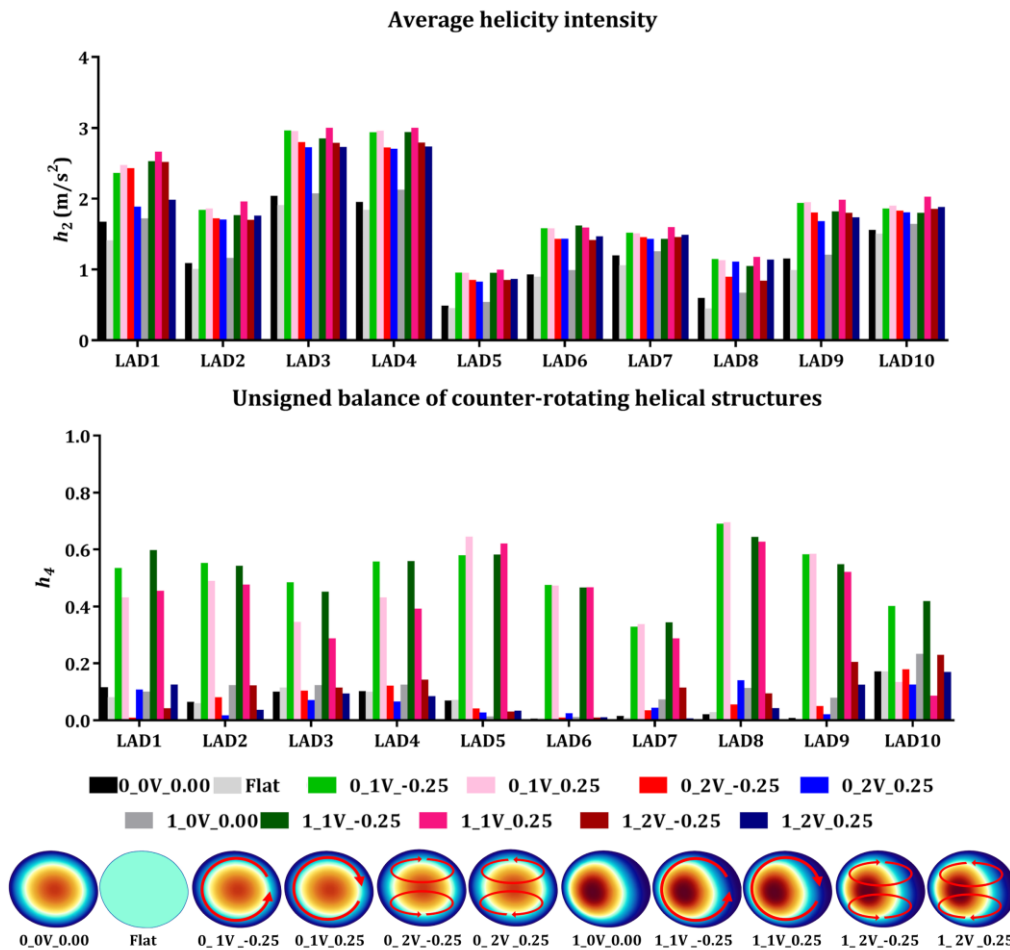


Figure 4.7 Helical flow descriptors. Upper panel: average helicity intensity (h_2) values in the main vessel grouped by geometry and coloured by velocity profile. Lower panel: unsigned balance of counter-rotating structures (h_4) values in the main vessel grouped by geometry and coloured by velocity profile.

Here the impact of the shape of the inflow velocity profile was firstly evaluated in terms of h_2 percentage difference and h_4 absolute difference with respect to the reference (TP-only parabolic) velocity profile. In **Figure 4.8**, the analysis is presented aggregating h_2 and h_4 data from all the 10 LAD models based on the specific velocity profile used as inflow boundary condition and considering the whole vessel and its division in three segments.

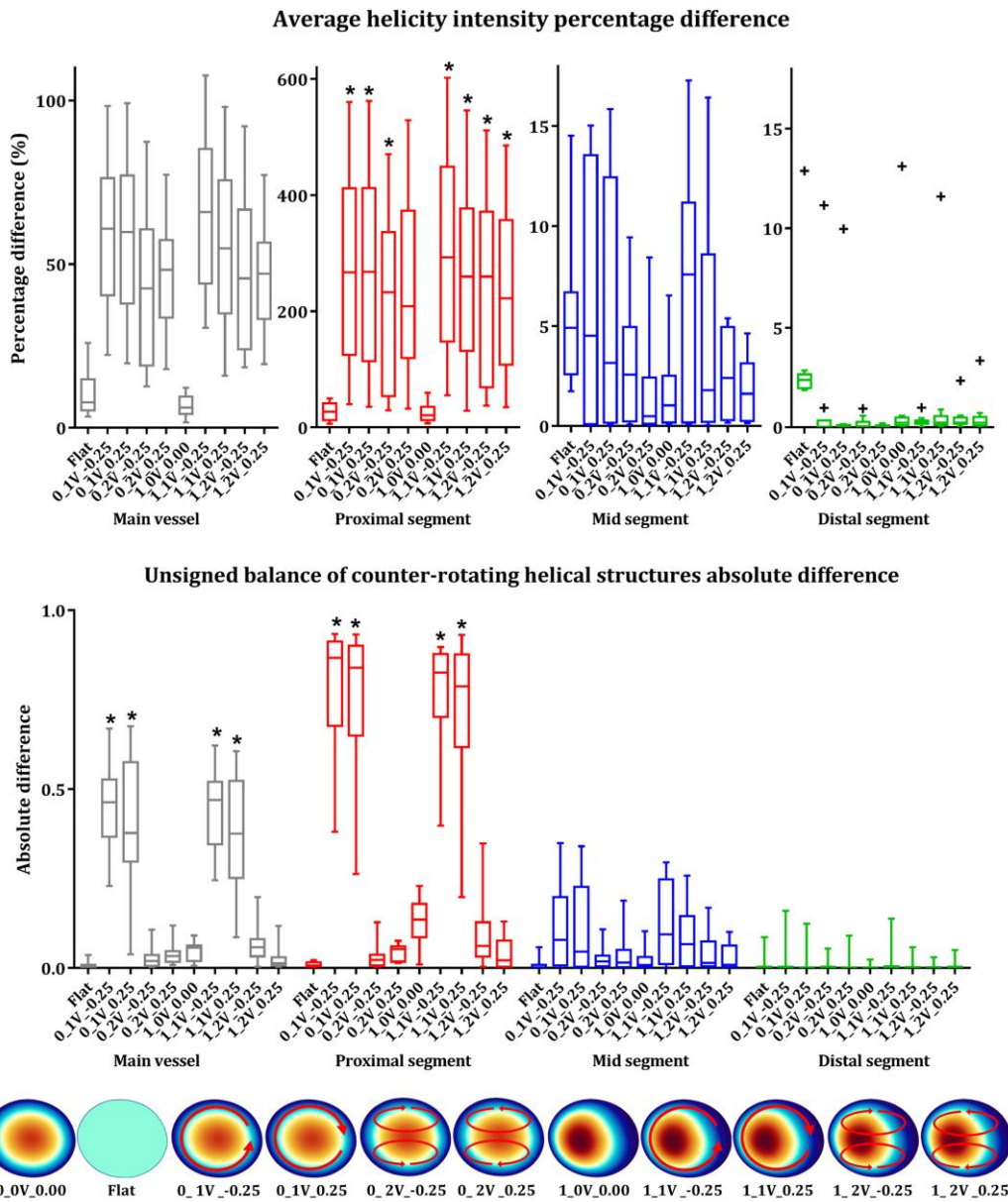


Figure 4.8. Helical flow descriptors: percentage differences. Upper panel: from left to right, average helicity intensity (h_2) percentage differences between the reference (0_0V_0.00) and the other velocity profiles in the main vessel, proximal, mid, and distal segments. Lower panel: from left to right, unsigned balance of counter-rotating structures (h_4) absolute differences between the reference (0_0V_0.00) and other velocity profiles in the main vessel, proximal, mid, and distal segments. Statistically significant differences are indicated with * (p-value<0.001).

Also for helical flow, the largest differences from the reference (TP-only parabolic) velocity profile for h_2 (maximum percentage difference of 602.27% profile 1_1V_-0.25 in geometry LAD5; median values range =

[20.72%, 292.79%]) and for h_4 (maximum absolute difference of 0.93 profile 0_1V_-0.25 in geometry LAD3; median values range = [0.01, 0.87]) were observed in the proximal segment. In the mid segment, the maximum h_2 percentage differences decreased to 17.28% (profile 1_1V_-0.25 in geometry LAD5) with a median values range = [0.49%, 7.58%], while h_4 maximum absolute difference was reduced to 0.35 (median values range = [0.00, 0.09]). In the distal segment, h_2 percentage differences became lower than 2.84% (median values range = [0.01%, 2.37%]), except for geometry LAD8, which presented differences up to 18.13% (velocity profile 0_2V_0.25). In the distal segment h_4 presented the smallest absolute differences from the case of the reference velocity profile, lower than 0.16 (observed in model LAD8, profile 0_1V_-0.25), and with median values lower than 0.001. As for the whole main vessel, h_2 and h_4 differences from the reference (TP-only parabolic) velocity profile reflected the observed differences in the proximal LAD segment. In detail, the h_2 percentage differences presented a median values range = [6.12%, 65.88%] and maximum percentage differences lower than 107.64% (model LAD5, velocity profile 1_1V_-0.25). Regarding h_4 absolute differences, a median values range = [0.003, 0.470] and a maximum value of 0.68 (profile 0_1V_0.25 in geometry LAD8) were observed. A case-by-case summary of the differences for the reference (TP-only parabolic) velocity profile is reported in **Table 4.3** and **Table 4.4**. For the sake of completeness, it is also reported that statistically significant differences (p -value<0.001) in h_2 values emerged only in the proximal segment with all velocity profiles that present the IP component (except for 0_2V_0.25 velocity profile), while for h_4 statistically significant differences (p -value<0.001) emerged in the proximal segment and in the whole main vessel, when velocity profiles with a single-vortex were imposed.

Table 4.3 Percentage difference values of average helicity intensity

| Profiles | LAD1 | LAD2 | LAD3 | LAD4 | LAD5 | LAD6 | LAD7 | LAD8 | LAD9 | LAD10 |
|--------------------|-------|-------|-------|-------|--------|-------|-------|-------|-------|-------|
| Main Branch | | | | | | | | | | |
| <i>Flat</i> | 16.00 | 7.96 | 6.45 | 5.75 | 7.47 | 3.75 | 11.61 | 25.91 | 14.32 | 3.42 |
| <i>0_1V_-0.25</i> | 48.07 | 71.36 | 45.12 | 52.05 | 98.35 | 70.93 | 26.41 | 90.91 | 69.63 | 22.28 |
| <i>0_1V_0.25</i> | 41.53 | 69.69 | 45.54 | 50.90 | 99.17 | 71.40 | 27.08 | 94.03 | 68.73 | 19.65 |
| <i>0_2V_-0.25</i> | 12.69 | 56.83 | 33.82 | 38.96 | 72.08 | 54.85 | 19.90 | 87.39 | 46.13 | 16.19 |
| <i>0_2V_0.25</i> | 45.47 | 58.67 | 37.52 | 39.77 | 77.32 | 54.68 | 21.97 | 51.02 | 56.87 | 17.89 |
| <i>1_0V_0</i> | 2.76 | 6.68 | 1.59 | 9.08 | 10.76 | 6.60 | 4.98 | 12.19 | 4.63 | 5.65 |
| <i>1_1V_-0.25</i> | 59.42 | 80.83 | 47.39 | 54.16 | 107.64 | 72.33 | 34.06 | 98.39 | 72.52 | 30.57 |
| <i>1_1V_0.25</i> | 51.56 | 62.54 | 39.99 | 51.03 | 98.04 | 75.31 | 19.75 | 76.62 | 58.15 | 15.87 |
| <i>1_2V_-0.25</i> | 18.44 | 61.98 | 33.98 | 40.57 | 80.61 | 58.66 | 24.96 | 92.14 | 50.65 | 20.92 |

| | | | | | | | | | | |
|------------------------|--------|--------|--------|--------|--------|--------|-------|--------|--------|-------|
| 1_2V_0.25 | 50.89 | 56.53 | 36.86 | 43.29 | 77.24 | 52.84 | 22.23 | 41.33 | 56.75 | 19.39 |
| Proximal Branch | | | | | | | | | | |
| Flat | 39.06 | 22.89 | 35.37 | 14.46 | 25.83 | 6.15 | 28.77 | 49.22 | 49.77 | 7.63 |
| 0_1V_-0.25 | 141.14 | 363.81 | 554.93 | 291.16 | 560.08 | 214.48 | 76.71 | 242.72 | 334.54 | 40.29 |
| 0_1V_0.25 | 126.05 | 363.81 | 562.35 | 291.80 | 556.85 | 215.85 | 78.30 | 243.95 | 340.26 | 35.59 |
| 0_2V_-0.25 | 43.70 | 306.32 | 470.61 | 262.34 | 426.57 | 165.62 | 57.38 | 242.95 | 222.70 | 29.24 |
| 0_2V_0.25 | 138.20 | 305.51 | 528.90 | 252.17 | 475.54 | 165.06 | 63.52 | 156.05 | 338.94 | 32.35 |
| 1_0V_0 | 7.08 | 31.67 | 22.96 | 47.47 | 59.57 | 19.89 | 13.67 | 21.54 | 17.45 | 10.14 |
| 1_1V_-0.25 | 164.49 | 401.14 | 593.00 | 318.69 | 602.27 | 218.64 | 98.54 | 266.89 | 367.82 | 55.19 |
| 1_1V_0.25 | 157.21 | 331.64 | 512.35 | 294.83 | 546.12 | 227.52 | 56.20 | 203.25 | 291.76 | 28.66 |
| 1_2V_-0.25 | 61.49 | 334.32 | 511.58 | 260.26 | 482.53 | 177.26 | 71.58 | 259.09 | 260.32 | 37.74 |
| 1_2V_0.25 | 153.98 | 289.78 | 485.43 | 284.96 | 459.06 | 159.64 | 63.83 | 123.09 | 322.86 | 35.00 |
| Mid Branch | | | | | | | | | | |
| Flat | 6.22 | 4.97 | 4.57 | 5.07 | 4.86 | 2.47 | 2.62 | 14.53 | 8.06 | 1.74 |
| 0_1V_-0.25 | 3.44 | 4.16 | 4.88 | 10.77 | 13.12 | 0.10 | 0.07 | 15.02 | 14.81 | 0.04 |
| 0_1V_0.25 | 0.40 | 1.60 | 4.73 | 8.64 | 15.41 | 0.12 | 0.17 | 15.85 | 11.45 | 0.05 |
| 0_2V_-0.25 | 4.40 | 1.51 | 1.50 | 3.63 | 4.83 | 0.23 | 0.24 | 5.28 | 9.44 | 0.08 |
| 0_2V_0.25 | 0.61 | 1.56 | 2.29 | 0.38 | 0.03 | 0.27 | 0.13 | 2.84 | 8.42 | 0.03 |
| 1_0V_0 | 0.88 | 1.19 | 0.19 | 2.84 | 1.87 | 0.07 | 0.44 | 6.53 | 2.41 | 0.13 |
| 1_1V_-0.25 | 12.34 | 8.02 | 4.13 | 7.13 | 17.28 | 0.18 | 0.08 | 10.79 | 9.28 | 0.18 |
| 1_1V_0.25 | 1.25 | 0.03 | 2.35 | 8.13 | 16.43 | 0.26 | 0.71 | 9.07 | 8.42 | 0.06 |
| 1_2V_-0.25 | 4.87 | 1.61 | 5.18 | 0.32 | 3.79 | 0.19 | 0.50 | 3.20 | 5.39 | 0.15 |
| 1_2V_0.25 | 0.27 | 2.95 | 0.93 | 2.30 | 4.63 | 0.20 | 0.37 | 2.41 | 3.70 | 0.14 |
| Distal Branch | | | | | | | | | | |
| Flat | 2.16 | 2.59 | 2.43 | 1.86 | 1.98 | 2.84 | 2.49 | 12.87 | 2.30 | 1.91 |
| 0_1V_-0.25 | 0.02 | 0.00 | 0.96 | 0.04 | 0.13 | 0.01 | 0.00 | 11.15 | 0.06 | 0.00 |
| 0_1V_0.25 | 0.00 | 0.01 | 0.15 | 0.01 | 0.10 | 0.01 | 0.05 | 9.96 | 0.04 | 0.01 |
| 0_2V_-0.25 | 0.00 | 0.01 | 0.93 | 0.07 | 0.17 | 0.01 | 0.05 | 0.58 | 0.04 | 0.01 |
| 0_2V_0.25 | 0.01 | 0.00 | 0.02 | 0.02 | 0.19 | 0.01 | 0.05 | 18.13 | 0.01 | 0.00 |
| 1_0V_0 | 0.22 | 0.45 | 0.58 | 0.20 | 0.11 | 0.05 | 0.32 | 13.10 | 0.20 | 0.03 |
| 1_1V_-0.25 | 0.23 | 0.45 | 0.97 | 0.22 | 0.23 | 0.07 | 0.29 | 0.22 | 0.20 | 0.02 |
| 1_1V_0.25 | 0.23 | 0.44 | 0.89 | 0.14 | 0.22 | 0.06 | 0.27 | 11.60 | 0.15 | 0.03 |
| 1_2V_-0.25 | 0.23 | 0.45 | 0.59 | 0.23 | 0.21 | 0.06 | 0.28 | 2.33 | 0.20 | 0.03 |
| 1_2V_0.25 | 0.23 | 0.44 | 0.71 | 0.10 | 0.10 | 0.07 | 0.28 | 3.34 | 0.19 | 0.03 |

Percentage difference values of h_2 between the reference (0_0V_0.00) and the other velocity profiles in the main vessel, proximal, mid, and distal segments.

Table 4.4 Absolute difference values of counter-rotating structures balance

| Profiles | LAD1 | LAD2 | LAD3 | LAD4 | LAD5 | LAD6 | LAD7 | LAD8 | LAD9 | LAD10 |
|------------------------|------|------|------|------|------|------|------|------|------|-------|
| Main Branch | | | | | | | | | | |
| Flat | 0.04 | 0.00 | 0.01 | 0.00 | 0.00 | 0.00 | 0.01 | 0.01 | 0.00 | 0.00 |
| 0_1V_-0.25 | 0.42 | 0.49 | 0.38 | 0.46 | 0.51 | 0.47 | 0.31 | 0.67 | 0.58 | 0.23 |
| 0_1V_0.25 | 0.32 | 0.42 | 0.24 | 0.33 | 0.57 | 0.47 | 0.32 | 0.67 | 0.58 | 0.04 |
| 0_2V_-0.25 | 0.11 | 0.02 | 0.00 | 0.02 | 0.03 | 0.00 | 0.02 | 0.03 | 0.04 | 0.01 |
| 0_2V_0.25 | 0.01 | 0.05 | 0.03 | 0.04 | 0.04 | 0.02 | 0.03 | 0.12 | 0.01 | 0.05 |
| 1_0V_0 | 0.02 | 0.06 | 0.02 | 0.02 | 0.06 | 0.01 | 0.06 | 0.09 | 0.07 | 0.06 |
| 1_1V_-0.25 | 0.48 | 0.48 | 0.35 | 0.46 | 0.51 | 0.46 | 0.33 | 0.62 | 0.54 | 0.25 |
| 1_1V_0.25 | 0.34 | 0.41 | 0.19 | 0.29 | 0.55 | 0.46 | 0.27 | 0.61 | 0.51 | 0.09 |
| 1_2V_-0.25 | 0.07 | 0.06 | 0.01 | 0.04 | 0.04 | 0.00 | 0.10 | 0.07 | 0.20 | 0.06 |
| 1_2V_0.25 | 0.01 | 0.03 | 0.01 | 0.02 | 0.04 | 0.01 | 0.01 | 0.02 | 0.12 | 0.00 |
| Proximal Branch | | | | | | | | | | |
| Flat | 0.02 | 0.01 | 0.01 | 0.01 | 0.01 | 0.00 | 0.01 | 0.02 | 0.00 | 0.01 |
| 0_1V_-0.25 | 0.69 | 0.90 | 0.93 | 0.84 | 0.90 | 0.77 | 0.63 | 0.91 | 0.93 | 0.38 |
| 0_1V_0.25 | 0.64 | 0.89 | 0.93 | 0.80 | 0.88 | 0.76 | 0.65 | 0.88 | 0.93 | 0.26 |
| 0_2V_-0.25 | 0.13 | 0.00 | 0.01 | 0.01 | 0.05 | 0.00 | 0.02 | 0.03 | 0.02 | 0.03 |
| 0_2V_0.25 | 0.06 | 0.02 | 0.02 | 0.05 | 0.06 | 0.03 | 0.05 | 0.08 | 0.01 | 0.06 |
| 1_0V_0 | 0.03 | 0.14 | 0.17 | 0.10 | 0.17 | 0.01 | 0.13 | 0.21 | 0.23 | 0.11 |
| 1_1V_-0.25 | 0.73 | 0.90 | 0.88 | 0.81 | 0.86 | 0.75 | 0.62 | 0.85 | 0.88 | 0.40 |
| 1_1V_0.25 | 0.63 | 0.83 | 0.93 | 0.74 | 0.84 | 0.74 | 0.59 | 0.86 | 0.93 | 0.20 |
| 1_2V_-0.25 | 0.09 | 0.02 | 0.04 | 0.03 | 0.06 | 0.00 | 0.18 | 0.07 | 0.35 | 0.11 |
| 1_2V_0.25 | 0.05 | 0.08 | 0.00 | 0.00 | 0.08 | 0.01 | 0.03 | 0.00 | 0.13 | 0.01 |
| Mid Branch | | | | | | | | | | |
| Flat | 0.06 | 0.01 | 0.01 | 0.00 | 0.00 | 0.00 | 0.00 | 0.01 | 0.00 | 0.00 |
| 0_1V_-0.25 | 0.12 | 0.09 | 0.15 | 0.07 | 0.00 | 0.01 | 0.01 | 0.35 | 0.33 | 0.00 |
| 0_1V_0.25 | 0.06 | 0.09 | 0.03 | 0.25 | 0.00 | 0.00 | 0.00 | 0.34 | 0.22 | 0.00 |

| | | | | | | | | | | |
|----------------------|------|------|------|------|------|------|------|------|------|------|
| 0_2V_-0.25 | 0.02 | 0.03 | 0.02 | 0.02 | 0.00 | 0.01 | 0.01 | 0.11 | 0.05 | 0.00 |
| 0_2V_0.25 | 0.05 | 0.03 | 0.00 | 0.04 | 0.00 | 0.00 | 0.00 | 0.19 | 0.06 | 0.00 |
| 1_0V_0 | 0.01 | 0.03 | 0.00 | 0.01 | 0.00 | 0.01 | 0.01 | 0.10 | 0.04 | 0.00 |
| 1_1V_-0.25 | 0.25 | 0.08 | 0.11 | 0.11 | 0.00 | 0.01 | 0.01 | 0.30 | 0.26 | 0.00 |
| 1_1V_0.25 | 0.09 | 0.12 | 0.05 | 0.26 | 0.00 | 0.01 | 0.01 | 0.22 | 0.10 | 0.00 |
| 1_2V_-0.25 | 0.07 | 0.02 | 0.03 | 0.00 | 0.00 | 0.01 | 0.01 | 0.17 | 0.09 | 0.00 |
| 1_2V_0.25 | 0.08 | 0.06 | 0.01 | 0.05 | 0.00 | 0.00 | 0.00 | 0.10 | 0.01 | 0.00 |
| Distal Branch | | | | | | | | | | |
| Flat | 0.00 | 0.00 | 0.00 | 0.00 | 0.00 | 0.00 | 0.00 | 0.09 | 0.00 | 0.00 |
| 0_1V_-0.25 | 0.00 | 0.00 | 0.00 | 0.00 | 0.00 | 0.00 | 0.00 | 0.16 | 0.00 | 0.00 |
| 0_1V_0.25 | 0.00 | 0.00 | 0.00 | 0.00 | 0.00 | 0.00 | 0.00 | 0.12 | 0.00 | 0.00 |
| 0_2V_-0.25 | 0.00 | 0.00 | 0.00 | 0.00 | 0.00 | 0.00 | 0.00 | 0.06 | 0.00 | 0.00 |
| 0_2V_0.25 | 0.00 | 0.00 | 0.00 | 0.00 | 0.00 | 0.00 | 0.00 | 0.09 | 0.00 | 0.00 |
| 1_0V_0 | 0.00 | 0.00 | 0.00 | 0.00 | 0.00 | 0.00 | 0.00 | 0.02 | 0.00 | 0.00 |
| 1_1V_-0.25 | 0.00 | 0.00 | 0.00 | 0.00 | 0.00 | 0.00 | 0.00 | 0.14 | 0.00 | 0.00 |
| 1_1V_0.25 | 0.00 | 0.00 | 0.00 | 0.00 | 0.00 | 0.00 | 0.00 | 0.06 | 0.00 | 0.00 |
| 1_2V_-0.25 | 0.00 | 0.00 | 0.00 | 0.00 | 0.00 | 0.00 | 0.00 | 0.03 | 0.00 | 0.00 |
| 1_2V_0.25 | 0.00 | 0.00 | 0.00 | 0.00 | 0.00 | 0.00 | 0.00 | 0.05 | 0.00 | 0.00 |

Absolute difference values of h_4 between the reference (0_0V_0.00) and the other velocity profiles in the main vessel, proximal, mid, and distal segments.

Finally, to better appreciate the impact of the shape of the inflow velocity profile on LAD intravascular flow, LNH isosurfaces are visualized in **Figure 4.9**. For the sake of synthesis, the cases characterized by the minimum and the maximum percentage difference in h_2 with respect to the reference parabolic velocity profile (LAD10 and LAD5, respectively) are reported in **Figure 4.9**, while all geometries are shown in **Figure 4.10**.

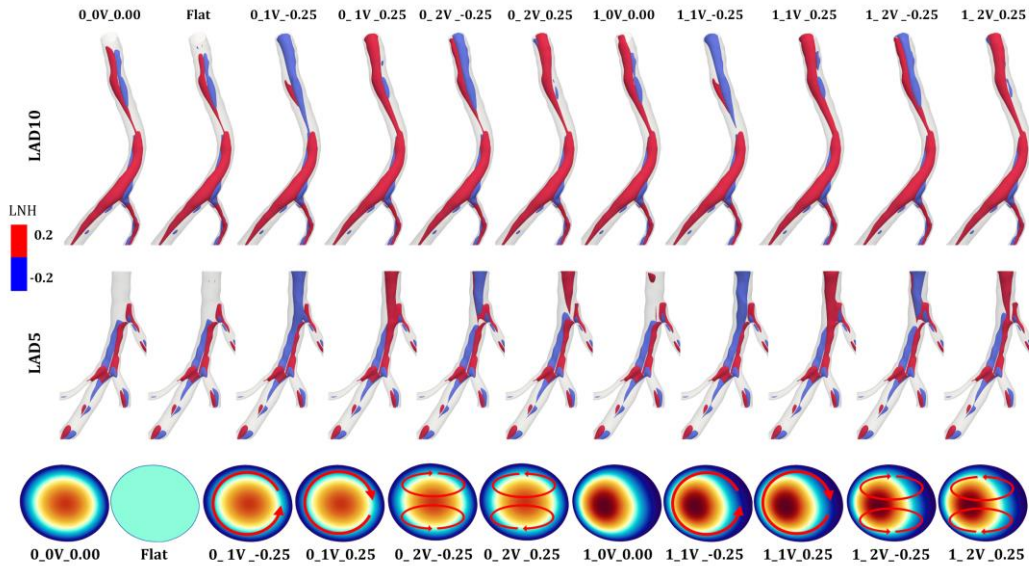


Figure 4.9. LNH isosurfaces visualization: explanatory cases. Visualization of intravascular local normalized helicity (LNH) isosurfaces for two explanatory cases (i.e. the models with the lowest and the highest h_2 percentage difference in the main vessel: LAD10 and LAD5, respectively). Right-handed helical structures are associated with positive LNH values (red colour) and left-handed helical structures are associated with negative LNH values (blue colour). A magnified view of the vessels is presented for a clearer visualization of the results.

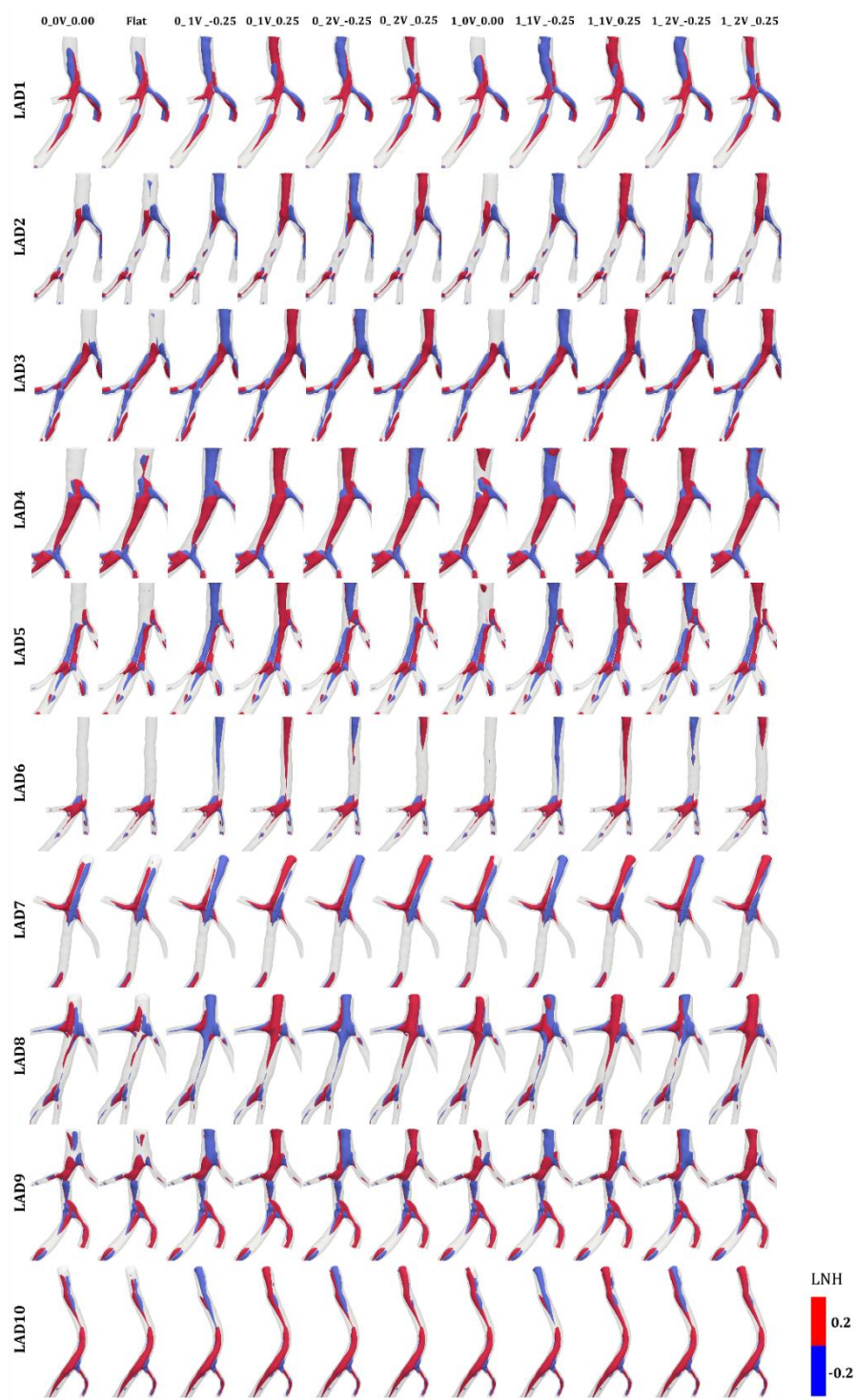


Figure 4.10. LNH isosurfaces visualization. Visualization of intravascular local normalized helicity (LNH) isosurfaces. Right-handed helical structures are associated with positive LNH values (red colour) and left-handed helical structures are associated with negative LNH values (blue colour). From top to bottom the ten LAD geometries, from left to right the 11 simulated velocity profiles.

The LNH-based visualization confirms that, in general, the presence of an IP component on the inflow velocity profile enriched helical flow in the LAD proximal segment. Moreover, the structure of the IP velocity component (i.e., single- or double-vortex shape) dictated the arrangement of helical flow patterns in one or two counter-rotating structures (cases denoted by 1V and 2V in **Figure 4.9**, respectively).

4.4 Discussion

In computational hemodynamics, when dealing with patient-specific models, the imposition of *in vivo* measured 3D velocity profiles as inflow boundary condition leads to more realistic simulations. However, velocity profiles are often not measurable *in vivo*, and their idealized versions, based upon assumptions needed to fill a gap of knowledge, are prescribed to model blood flow.

In coronary arteries, blood flow velocity values can be derived *in vivo* from Doppler flow velocity or thermodilution measurements^{207,208}. Nevertheless, these techniques are uncommon in the clinical practice, and provide an estimation of blood velocity averaged over the vessel cross-section. Consequently, as information on the three components of the velocity profile is not available, idealized velocity profiles need to be assumed a priori to turn the defective boundary data problem into a classic Dirichlet problem. Such an assumption can influence the numerical solution, potentially weakening the findings of the *in silico* experiments. In this regard, the uncertainty associated with the use of idealized velocity profiles as inflow boundary condition in computational hemodynamics has been investigated in, e.g., carotid arteries^{209,210} and ascending aorta^{195,211,212}, where 3D velocity profiles can be measured *in vivo*, but not in coronary arteries.

Motivated by this, ten LAD geometries were reconstructed from two angiographic projections, using a new reconstruction method that allows obtaining multiple branches in the LAD geometries. To evaluate the impact of assumptions on the shape of the inflow velocity profiles on coronary hemodynamics, a novel framework to generate 3D velocity profiles on non-circular shaped blood vessels cross-sections was developed by

generalizing analytical formulations. The impact of inflow velocity profiles was tested in terms of near-wall and intravascular physiologically relevant hemodynamic quantities.

Using the widely adopted inflow parabolic velocity profile as reference profile, here we found that, in terms of AWSS, all the investigated cases present percentage differences <5.80%, except for the flat velocity profile, presenting differences up to 16.70%. The highest percentage differences were observed in the proximal segment of the vessel models, while moderate-to-negligible differences were observed in mid and distal segments (**Figure 4.3**). These findings are consistent with those previously observed in a simplified computational model of right coronary artery²¹³ when comparing idealized, only TP flat, parabolic and Dean-like inflow velocity profiles. Also in that study, the impact of the velocity profile on WSS was limited to the proximal part of vessel²¹³.

As expected, it emerged that the presence of secondary flow (IP) component in the inflow velocity profile has a marked impact on helical flow. Such marked differences, dictated by the shape of the inflow velocity profile, are mainly located in the proximal segment (up to 602.27%), where the imposition of TP-only velocity profiles leads to a production of helicity intensity h_2 smaller than 3D velocity profiles. In the mid and distal segments, maximum differences in helical flow intensity decreases to values lower than 18.13% confirming the main role played by geometry in the dispersal of the imposed inlet velocity profile and in the production/disruption of laminar helicity intensity⁷³. The impact that the presence of IP components in the inflow velocity profiles has on helical flow patterns downstream configuration emerges also by the analysis of h_4 , highlighting how the presence of one main or two balanced counter-rotating helical flow patterns in the proximal segment is dictated by the single- or double-vortex shape of the IP component of the inflow velocity profile. Interestingly, in the proximal segment h_4 values in the TP-only velocity profiles are low, suggesting that the production of almost balanced counter-rotating bi-helical blood flow patterns is dictated by the arterial geometry. Moreover, as a consequence of a double-vortex IP configuration at the inlet the bi-helical flow patterns in the proximal segment are almost balanced by construction and therefore

present low h_4 values (as in the TP-only velocity profile cases). On the opposite, in the case of inflow velocity profiles with single-vortex IP component h_4 values are close to 1 indicating that one helical direction of rotation predominates in the flow field. In the mid and distal coronary segments, the impact of the presence of IP components in the imposed inflow velocity profile on helical structures balance vanishes, and vessel geometry mainly dictates blood flow arrangement in helical patterns.

Overall, the findings of this study suggest that the influence of the shape of the velocity profile imposed at the inflow section in computational hemodynamics models of LAD coronary arteries is limited to few diameters downstream. Taking into consideration the importance of the entrance length, also highlighted elsewhere²¹³, a more realistic hemodynamic picture in proximal LAD coronary arteries could be obtained extending the reconstruction upstream, including the left main coronary artery or even the aortic root. However, the advantage coming from the reconstruction of the geometry up to the aortic root, which assures a minor dependence of the proximal LAD simulated hemodynamics on inflow boundary conditions, cannot be exploited using the here adopted, routine invasive coronary angiography, which is the most convenient clinical modality²¹⁴.

This study presents limitations that might weaken the current findings. The lack of the real, *in vivo* measured 3D velocity profiles in the LAD enforced the generation of velocity profiles (1) based upon analytical formulations, and (2) with an arbitrary amount of secondary flows, deemed as representative of the real situation. However, the proposed approach has the advantage of generating velocity profiles in a tightly controlled manner, allowing to test differently shaped inflow velocity patterns. Moreover, steady-state simulations were carried out, neglecting the pulsatile nature of coronary flow. This choice was based on previous computational studies and further discussed in the next chapter, demonstrating that for flow regimes characterized by low Reynolds numbers, like those of coronary arteries, the difference between time averaged **WSS** and the steady-state **|WSS|** is negligible^{65,215}. It is also worth noting that the steady flow assumption reduced sensibly the computational cost, given reliable results meeting clinical time constraints. Lastly, the idealization of velocity profiles

as inflow boundary condition in LAD coronary arteries represents just one source of uncertainty that nonlinearly pile-up with other uncertainties regarding:

1. the flow rate estimation⁷⁰.
2. The assumption of rigid wall ²¹⁶, even if recent findings suggest a negligible impact of wall deformability on WSS in coronary arteries²¹⁷.
3. The cardiac motion and coronary displacement, here not considered even if not univocal conclusions are reported^{218,219}.

All these assumptions could affect the results. However, here we focused on a single source of uncertainty to link the observed differences to unambiguous causes.

4.5 Conclusions

In this study, the impact of the shape of blood velocity profiles, prescribed as inflow boundary conditions in image-based computational models of LAD coronary arteries, on local hemodynamics was evaluated. Our findings highlighted that the hemodynamic impact of considering realistic 3D features, such as eccentricity and differently shaped secondary flows, as a part of the inflow velocity profile is limited to the proximal LAD segment. Furthermore, the findings suggested that the problem of the paucity of information affecting the imposition of as realistic as possible velocity profiles as inflow boundary condition in LAD models can be satisfactorily overcome by applying idealized inflow parabolic velocity profiles, as long as the proximal LAD segment is not considered in the evaluation of the results. As a pragmatic rule of thumb, a conservative estimation of the length of influence of the shape of the inflow velocity profile on LAD local hemodynamics can be given by the theoretical entrance length, in general longer than the maximum impact length.

The strategy proposed here to manage inflow boundary conditions, which emerged studying healthy, image-based LAD models, may be translated to diseased or stented coronary vessels, given that the reconstructed coronary artery geometry upstream of the lesion or of the stent is sufficiently extended.

Chapter 5

Modelling coronary flows: impact of differently measured inflow boundary conditions on vessel-specific computational hemodynamic profiles

A version of this chapter is published in:

Computer Methods and Programs in Biomedicine, Vol. 221, June 2022

Modelling coronary flows: impact of differently measured inflow boundary conditions on vessel-specific computational hemodynamic profiles

Maurizio Lodi Rizzini, Alessandro Candreva, Claudio Chiastra, Emanuele Gallinoro, Karol Calò, Fabrizio D'Ascenzo, Bernard De Bruyne, Takuya Mizukami, Carlos Collet, Diego Gallo, Umberto Morbiducci

5.1 Introduction

In the last years, substantial evidence has established the role of local hemodynamics at the blood-endothelium interface in the onset and progression of atherosclerotic plaques¹⁸. In coronary arteries, on one hand specific wall shear stress (WSS) profiles were associated with early atherosclerosis^{62,113,220}, plaque vulnerability and risk of myocardial infarction^{65,221}. On the other hand, specific intravascular flow features, such as helical flow, were proven to play an atheroprotective role^{24,72}.

For the accurate estimation of local hemodynamic features, increasingly refined computational models of coronary blood flow have been developed^{222,223}. However, their clinical adoption is still hampered by the fact that patient-specific computational fluid dynamics (CFD) simulations, as all model-based strategies, require the inevitable use of assumptions and idealizations^{181–183,224,225}. These represent sources of uncertainty undermining the credibility, and the clinical applicability as well, of the resulting hemodynamic models. In this regard, a major source of uncertainty is related to the conditions to be prescribed at the inflow boundary^{71,226}, since intracoronary flow measurement is uncommon in the clinical practice and theoretical assumptions and/or idealizations are thus required for generating boundary conditions (BCs). Invasively, intracoronary flow velocity can be derived from Doppler recordings²²⁷ or from the Thrombolysis In Myocardial Infarction (TIMI) frame count method based on the contrast velocity propagation during angiographic acquisitions^{65,228,229}. From velocity, coronary blood flow rate is derived using information on the vessel diameter obtained from imaging^{65,227}. Alternatively, anatomy-based laws directly relating flow to the vessel diameter at specific locations have been formulated. These scaling laws have been first based on minimum energy hypothesis²³⁰ while later studies determined empirical power law flow-diameter relationships specifically for coronary arteries⁷⁰. More recently, the introduction of intracoronary continuous thermodilution has allowed the direct measurement of vessel-specific coronary blood flow rate and resistance in absolute terms (i.e. in ml/min and in Wood unit, respectively)²³¹ at rest as well as in hyperemia²³². However, application of continuous thermodilution in the clinical routine is for now limited²³³.

Alongside its importance as input of reliable patient-specific CFD simulations, from a clinical perspective coronary blood flow rate is a marker of coronary disease as it allows a direct assessment of coronary perfusion, it identifies the presence of flow-limiting epicardial stenosis and is a surrogate of myocardial ischemia²³⁴. In this sense, it is well established that a depressed coronary perfusion is a hallmark of poor patient outcome at the long term²³⁴. The clinical relevance of coronary perfusion has inevitably led to the development of several techniques assessing surrogates of flow rate in coronary arteries. Given that each technique uses a different theoretical and/or practical approach for measuring blood flow rate, perfect agreement amongst the different methods should not be expected.

In this scenario, a comparative analysis among the most relevant clinically available techniques is still lacking. With the final goal of obtaining reliable biomechanical markers of coronary disease from computational hemodynamics, here we compared the effect of deriving inflow BCs from four different *in vivo* techniques assessing clinical surrogates of flow rate on the results of angiography-based CFD simulations.

5.2 Methods

The workflow of the study, from image and flow-derived data acquisition to vessel geometry reconstruction, and from CFD to post-processing, is presented in **Figure 1**.

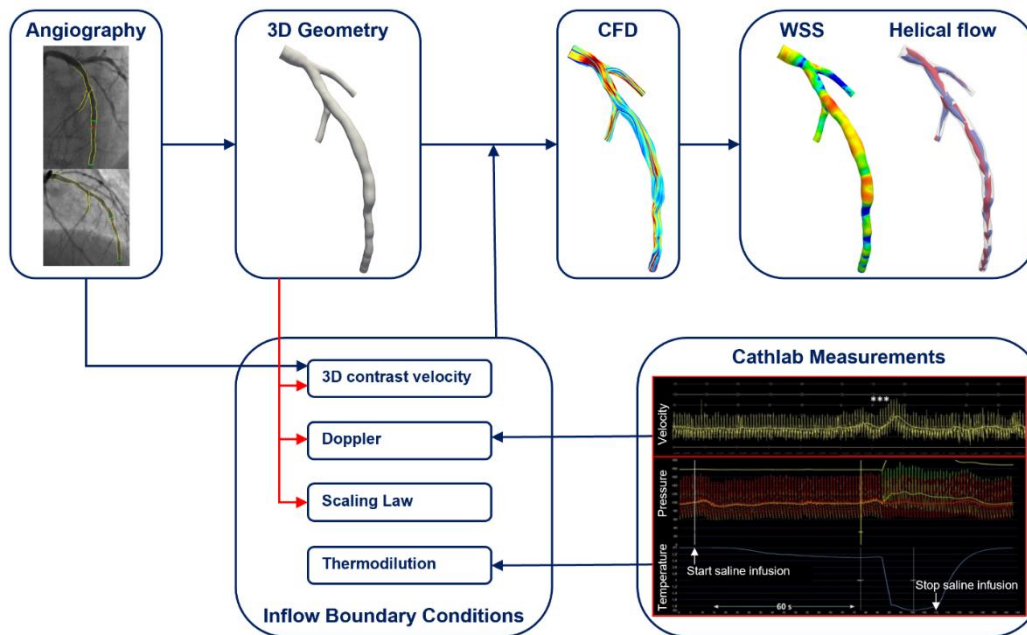


Figure 5.1. Workflow of the study. Coronary angiography was used to reconstruct 3D models of the coronary arteries and to assess contrast velocity-based flow rate. The diameter-based scaling law for flow rate assessment was applied directly to the 3D reconstructed geometries, while thermodilution and Doppler flow rate measurement were performed in the cathlab. The assessed flow rates were prescribed as inflow boundary conditions to computational fluid dynamics simulations to obtain wall shear stress and intravascular flow data.

5.2.1 Patients selection and 3D vessel reconstruction

Fourteen vessels (7 left anterior descending, LAD, and 7 right coronary arteries, RCA) from 14 patients (92.5% of male gender, mean age 63.2 ± 7.88 years) undergoing clinically indicated coronary angiography and invasive assessment of the coronary microcirculation underwent sequential intracoronary Doppler²²⁷ and continuous thermodilution measurements²³⁵. The study protocol is exhaustively detailed elsewhere²³². The study was approved by the Institutional Review Board at Cardiovascular Center Aalst (Aalst, Belgium) and conformed to the Helsinki Declaration on human research of 1975, as revised in 2000. Informed consent was obtained from the patients.

Invasive flow measurements were performed in vessels with estimated visual diameter stenosis below 30%. 3D coronary reconstructions were performed using two angiographic projections at least 25° apart combining a commercially available software (QAngio XA Bifurcation RE, Medis

medical imaging systems, Leiden, The Netherlands) and a custom-made algorithm¹⁴⁸. Side branches with diameter larger than 1 mm were included¹⁴⁸. The reconstructed 3D vascular models are presented in **Figure 5.2**.

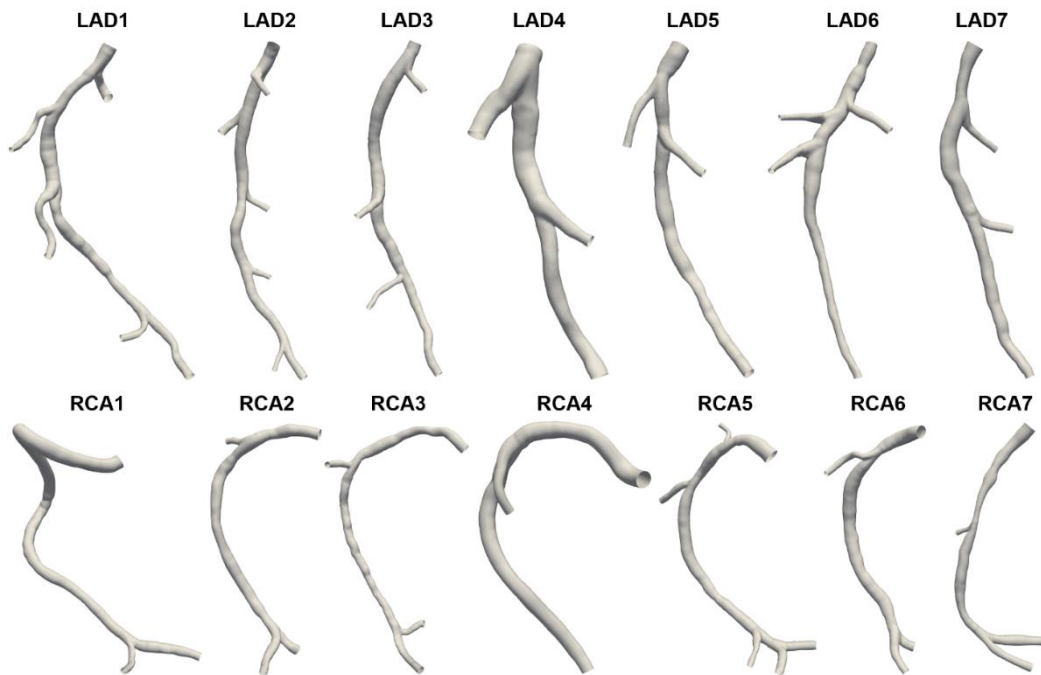


Figure 5.2. 3D vessel reconstructions. Three-dimensional reconstruction of the 14 coronary arteries under investigation. In the upper panel: 7 left anterior descending (LAD) coronary arteries. In the lower panel: 7 right coronary arteries (RCA).

5.2.2 Coronary flow rate estimation procedures

Coronary blood flow rate was assessed in resting conditions with four different techniques:

1. Continuous thermodilution^{231,235}.
2. Doppler ultrasound²²⁷.
3. 3D contrast velocity⁶⁵.
4. Diameter-based scaling law⁷⁰.

Intracoronary continuous thermodilution was performed using a dedicated infusion microcatheter with 4 lateral side holes (RayFlow™, Hexacath, Paris, France) loaded on the pressure/temperature wire (PressureWire™ X,

Abbott Vascular, Santa Clara, CA, USA) and connected to a 200 cc syringe of injector (Medrad® Stellant, Medrad Inc, Warrendale, PA, USA) filled with saline at room temperature (between 21 and 22°C) and placed in the first millimetres of the artery under investigation²³³. Distally, the saline was infused at an infusion rate of 10 mL/min during 60 to 90 seconds and the thermodilution-derived flow rate (Q_{thermo}) was estimated according to the formula²⁰⁸:

$$Q_{\text{thermo}} = \gamma \frac{T_i}{T} Q_i \quad (5.1)$$

where Q_i is the infusion rate of saline, T_i is the temperature of the infused saline, T is the temperature of the homogeneous mixture of blood and saline measured in the distal part of coronary artery with the pressure/temperature wire, and the quantity $\gamma=1.08$ accounts for the densities and specific heat of blood and saline²³³. Q_{thermo} unit of measure is expressed as mL/min.

Intravascular Doppler flow velocity estimation was performed using a dedicated coronary Doppler velocity wire (FloWire®, Philips/Volcano, San Diego, CA, USA) connected to a Doppler system (FlowMap®, Cardiometrics; Mountain View, CA, USA) and advanced in the distal part of the artery, at the same location as the pressure/temperature wire²³². Time-dependent Doppler signals were acquired using the physiologic tracings recorder (Mac-Lab™ Hemodynamic Recording System, GE Healthcare, Chicago, IL, USA). The cycle-average Doppler flow rate (Q_{Doppler}) at the inflow section of each vessel was estimated assuming a parabolic velocity profile²²⁷, according to the formula:

$$Q_{\text{Doppler}} = A \cdot \frac{APV}{2} \quad (5.2)$$

where A is the area of the inlet surface and APV is the cycle-Average Peak Velocity value from Doppler flow measurements.

The 3D contrast velocity method⁶⁵ for determining inlet flow rate is based on the number of angiographic frames required for contrast to travel from the vessel ostium to a standardized distal coronary landmark. In detail, using the number of frames (N) visually counted by an expert operator and

the distance (L) of the coronary landmark from the ostium as computed on the 3D anatomical reconstruction of the vessel, the average flow rate (Q_{CV}) can be estimated according to the formula:

$$Q_{CV} = A \cdot \frac{L \cdot f}{N} \quad (5.3)$$

where f is the frame rate of acquisition of the angiographic images.

The average coronary flow rate (Q_{SL}) was also estimated according to the anatomy-based scaling law:

$$Q_{SL} = \alpha \cdot d^\beta \quad (5.4)$$

where the volumetric flow rate Q_{SL} was expressed in m^3/s by van der Giessen et al.⁷⁰, being d the hydraulic diameter of the inflow section measured in m and the values of the parameters $\alpha = 1.43 m^{0.45}/s$ and $\beta=2.55$ ⁷⁰.

5.2.3 Steady-state CFD simulations

For each 3D coronary artery model, four steady-state CFD simulations were carried out, each of them testing one of the four estimated flow rate values as inflow boundary condition. A total of 56 steady-state CFD simulations was carried out. The estimated average flow rates were prescribed in terms of parabolic velocity profile at the inflow section of the fluid domain, as suggested by previous studies¹⁴⁸. The fluid domain was discretized combining tetrahedral elements with 5 near-wall prismatic layers using the software ICEM CFD (Ansys Inc., Canonsburg, PA, USA) and adopting meshing parameters derived from a grid independence analysis performed in a previous study⁷². The discretized governing equations of fluid motion, the Navier-Stokes equations, were then solved using the finite volume-based code Fluent (Ansys Inc.). Blood was assumed as a homogeneous and incompressible fluid (density $\rho=1060 \text{ kg/m}^3$), and its non-Newtonian behaviour was modelled using the Carreau model ($\mu_\infty=0.0035 \text{ Pa}\cdot\text{s}$, $\mu_0=0.25 \text{ Pa}\cdot\text{s}$, $\lambda=25 \text{ s}$, and $n=0.25$)⁷³. The coronary vessel wall was assumed to be rigid with no-slip conditions. The boundary conditions at the outflow were prescribed according to the widely adopted strategy of setting the flow split

at each coronary bifurcation according to a diameter-based scaling law⁷⁰. Steady-state simulations were performed adopting a second-order accuracy scheme for both momentum and pressure equations, coupled using the full implicit coupled pressure–velocity coupling scheme with explicit relaxation factors equal to 0.75 for pressure and momentum. Convergence was achieved when the maximum mass and momentum residuals fell below 10^{-5} .

5.2.4 Unsteady-state CFD simulations

The governing equations of fluid motion were solved in their discretized form under unsteady-state conditions using the commercial code based on the finite volume method Fluent (ANSYS Inc.). Blood was considered as a continuous, incompressible ($\rho=1060 \text{ kg/m}^3$) fluid and its non-Newtonian behaviour was modelled using the Carreau model⁷³ as in the steady-state simulations. Vessel walls were assumed to be rigid and no-slip condition was applied at wall boundaries. The same numerical scheme used for steady-state simulations was applied, while regarding the time integration, the second order backward Euler implicit scheme was adopted with a fixed time increment equal to 0.01 s. For each subject, the inflow boundary conditions were obtained by scaling the measured vessel-specific Doppler-based velocity waveform with the cycle-averaged flow rate obtained with the four estimation techniques (i.e., continuous thermodilution, Doppler, 3D contrast velocity, and scaling law) as reported for two explanatory cases (i.e., one right and one left anterior descending coronary artery) in **Figure 5.3**. The same scheme of flow repartition as in the steady-state simulations was prescribed at the outlets.

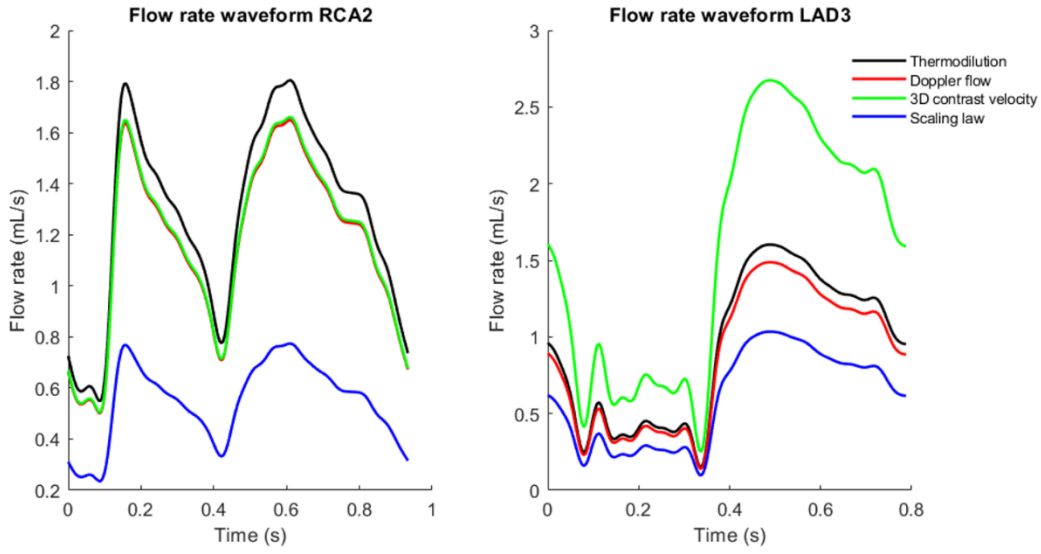


Figure 5.3. Flow rate waveforms. Two explanatory vessel-specific flow rate waveforms (one RCA, one LAD) scaled with thermodilution (black), Doppler (red), 3D contrast velocity (green), and scaling law (blue) cycle-average flow rate.

The impact of the adopted flow rate as inflow BC on CFD simulations was evaluated in terms of WSS distribution at the luminal surface and intravascular flow features. The flow rate from continuous thermodilution was assumed as reference since this technique provides a direct measurement of absolute flow rate, according to equation 5.1.

5.2.5 Steady-state WSS-based descriptors

Regarding steady-state simulations, the luminal distribution of the WSS magnitude and the absolute error in WSS direction (AEWSSD) were analysed: the former quantifies the local magnitude of the fluid shear stress at the blood-endothelium interface; the latter quantifies the inflow BC-dependent local misalignment of the WSS according to the formula^{236,237}:

$$AEWSSD = 1 - \frac{|\mathbf{WSS}_{\text{thermo}} \cdot \mathbf{WSS}_{\text{BC}}|}{|\mathbf{WSS}_{\text{thermo}}| \cdot |\mathbf{WSS}_{\text{BC}}|} \quad (5.5)$$

where $\mathbf{WSS}_{\text{thermo}}$ is the local WSS vector obtained when the reference flow rate Q_{thermo} is prescribed as inflow BC, and \mathbf{WSS}_{BC} is the WSS vector field obtained when Q_{Doppler} , Q_{CV} or Q_{SL} are prescribed. AEWSSD ranges from 0, indicating a perfect alignment between vectors, to 1, corresponding to an

angle of $\pm 90^\circ$ between the vectors. The impact of the inflow BC on WSS magnitude was also quantified in terms of luminal surface area exposed to low WSS, an indicator of hemodynamic risk in the early stages of the atherosclerotic process^{62,113,220}. Technically, on each vessel the low WSS surface area was assessed by calculating the percentage of luminal surface exposed to WSS magnitude values below the 10th percentile (WSS10)^{41,72} of the WSS magnitude distribution obtained pooling together data from the four simulations carried out over each vessel. On each vessel, the co-localization of WSS10 surface areas from Q_{Doppler} -based, Q_{CV} -based and Q_{SL} -based simulations with the Q_{thermo} -based one was assessed by applying the Jaccard similarity index (SI)²³⁸:

$$SI = \frac{2(WSS10_{\text{thermo}} \cap WSS10_{\text{BC}})}{WSS10_{\text{thermo}} \cup WSS10_{\text{BC}}} \quad (5.6)$$

where $WSS10_{\text{thermo}}$ is the luminal surface area exposed to low WSS magnitude when Q_{thermo} is prescribed as inflow BC and $WSS10_{\text{BC}}$ is the luminal surface area exposed to low WSS magnitude when Q_{Doppler} , Q_{CV} or Q_{SL} are prescribed. The SI of equation 5.6 ranges from 0 (no co-localization) to 1 (perfect co-localization). The inflow rate-dependent local WSS misalignment with respect to WSS_{thermo} was evaluated comparing probability density functions and the luminal surface AEWSSD profiles.

Based on theory, WSS magnitude in arteries can be markedly affected by the absolute flow rate value. As perfect agreement amongst the different methods for measuring blood flow rate should not be expected, here normalized WSS magnitude (normWSS) was also analysed. Normalized WSS was obtained by dividing the local absolute WSS magnitude values by WSS magnitude value as obtained applying the Hagen-Poiseuille theory at the inflow section of the model geometry (with dynamic viscosity derived from the adopted Carreau model for blood rheology, calculated at the characteristic shear rate corresponding to the inlet average velocity^{40,239}).

5.2.5 Unsteady-state WSS-based descriptors

The quantitative characterization of endothelial shear forces included the following WSS-based descriptors (**Table 5.1**): time-averaged wall shear

stress (TAWSS); oscillatory shear index (OSI)²⁵; transverse WSS (transWSS)²⁷; TAWSS axial component (TAWSS_{ax})²⁹; secondary component (TAWSS_{sc})²⁹ and topological shear variation index (TSVI)^{37,66}.

Table 5.1 Unsteady-state WSS-based descriptors

| | |
|---|---|
| Time Averaged Wall Shear Stress (TAWSS) | $\text{TAWSS} = \frac{1}{T} \int_0^T \mathbf{WSS} dt$ |
| Oscillatory Shear Index (OSI) | $\text{OSI} = 0.5 \left[1 - \frac{\left \int_0^T \mathbf{WSS} dt \right }{\int_0^T \mathbf{WSS} dt} \right]$ |
| Transverse WSS (transWSS) | $\text{transWSS} = \frac{1}{T} \int_0^T \left \mathbf{WSS} \cdot \left(\mathbf{n} \times \frac{\int_0^T \mathbf{WSS} dt}{\left \int_0^T \mathbf{WSS} dt \right } \right) \right dt$ |
| Time-Averaged WSS _{ax} (TAWSS_{ax}) | $\text{TAWSS}_{ax} = \frac{1}{T} \int_0^T \mathbf{WSS}_{ax} dt$ |
| Time-Averaged WSS _{sc} (TAWSS_{sc}) | $\text{TAWSS}_{sc} = \frac{1}{T} \int_0^T \mathbf{WSS}_{sc} dt$ |
| Topological shear variation index (TSVI) | $\text{TSVI} = \left\{ \frac{1}{T} \int_0^T [\nabla \cdot (\mathbf{WSS}_u) - \overline{\nabla \cdot (\mathbf{WSS}_u)}]^2 dt \right\}^{1/2}$ |

WSS is the time-varying wall shear stress vector; **T** is the cardiac cycle duration; **n** is the unit vector normal to the arterial surface at each element; **WSS_{ax}** is the WSS projection along the direction of the tangent to the vessel centerline; **WSS_{sc}** is the WSS projection along the direction perpendicular to the tangent of the vessel centerline. **WSS_u** is the **WSS** unit vector; $\nabla \cdot (\mathbf{WSS}_u) = \text{DIV}_{\text{WSS}}$ is the divergence of the WSS unit vector field; the overbar denotes a cycle-average quantity.

Also for unsteady-state WSS-based descriptors the impact of flow rate estimation technique was evaluated in terms of surface averaged values and surface exposed to disturbed shear (SA) considering low values of TAWSS, TAWSS_{ax}, and TAWSS_{sc}, and high values of OSI, transWSS, and TSVI by defining the BCs-specific thresholds with the 10th and 90th for low and high values, respectively, as done for steady-state WSS-based descriptors. The SA was quantified as percentage area, and its co-localization areas from Q_{Doppler}-based, Q_{CV}-based and Q_{SL}-based simulations with the Q_{thermo}-based one was assessed by applying the SI according to the equation 5.6.

Moreover, to verify if the WSS magnitude profiles obtained from steady-state simulations are representative of the WSS magnitude distribution also

under transient-flow conditions the distribution of time averaged wall shear stress (TAWSS), a well-established hallmark of coronary artery disease^{112,113,175}, was analysed and compared to steady-state WSS magnitude profiles.

5.2.6 Intravascular flow

Intravascular coronary flow was investigated in terms of helical flow patterns, which were visualized in terms of local normalized helicity (LNH), a measure quantifying the local alignment between velocity and vorticity vectors according to³⁹:

$$\text{LNH} = \frac{\mathbf{v}(\mathbf{x}) \cdot \boldsymbol{\omega}(\mathbf{x})}{|\mathbf{v}(\mathbf{x})||\boldsymbol{\omega}(\mathbf{x})|} = \cos \varphi(\mathbf{x}) \quad (5.7)$$

where \mathbf{v} and $\boldsymbol{\omega}$ are velocity and vorticity vectors, respectively, and φ is the angle between velocity and vorticity vectors. In addition, a quantitative description of helical flow features was provided considering four well-established helicity-based hemodynamic descriptors^{41,195}, namely the volume-average helicity (h_1), the volume-average helicity intensity (h_2), the signed balance of counter-rotating helical structures (h_3), and the unsigned balance of counter-rotating helical structures (h_4), derived in steady-state and unsteady form and reported in **Table 5.2**.

Table 5.2 Helicity-based descriptors

| | Steady-state CFD simulations | Unsteady-state CFD simulations |
|--------------------------------------|--|--|
| Volume-average helicity | $h_1^{\text{steady}} = \frac{1}{V} \int_V \mathbf{v}(\mathbf{x}) \cdot \boldsymbol{\omega}(\mathbf{x}) dV$ | $h_1^{\text{unsteady}} = \frac{1}{T} \frac{1}{V} \int_0^T \int_V \mathbf{v}(\mathbf{x}, t) \cdot \boldsymbol{\omega}(\mathbf{x}, t) dV dt$ |
| Volume-average helicity intensity | $h_2^{\text{steady}} = \frac{1}{V} \int_V \mathbf{v}(\mathbf{x}) \cdot \boldsymbol{\omega}(\mathbf{x}) dV$ | $h_2^{\text{unsteady}} = \frac{1}{T} \frac{1}{V} \int_0^T \int_V \mathbf{v}(\mathbf{x}, t) \cdot \boldsymbol{\omega}(\mathbf{x}, t) dV dt$ |
| Signed balance of helical structures | $h_3^{\text{steady}} = \frac{h_1^{\text{steady}}}{h_2^{\text{steady}}}$ | $h_3^{\text{unsteady}} = \frac{h_1^{\text{unsteady}}}{h_2^{\text{unsteady}}}$ |

| | | |
|---|---|---|
| Unsigned balance of helical structures | $h_4^{\text{steady}} = \frac{ h_1^{\text{steady}} }{h_2^{\text{steady}}}$ | $h_4^{\text{unsteady}} = \frac{ h_1^{\text{unsteady}} }{h_2^{\text{unsteady}}}$ |
|---|---|---|

\mathbf{v} and \mathbf{w} are the velocity and vorticity vectors, respectively; T is the cardiac cycle duration and V is the integration volume. h_3 ranges between -1 and 1, while h_4 ranges between 0 and 1. h_1 represents the average amount of helical flow and h_2 quantifies its intensity, while h_3 and h_4 measure the prevalence (identified by the sign) and the strength of relative rotations of helical flow structures, respectively.

To verify if the helical flow features obtained from steady-state simulations are representative of the average intravascular flow patterns also under transient-flow conditions cycle-average values of the helicity-based descriptors⁴¹ were analysed and compared to the steady-state ones listed in **Table 5.2**.

5.2.7 Statistical analysis

The Shapiro-Wilk test was applied to verify the normality of data distributions due to the small sample investigated. Parametric coupled t-tests or non-parametric Wilcoxon tests, as appropriate, were used for comparing continuous variable distributions. Continuous thermodilution was assumed as reference measurement procedure. Correlation between measurement procedures was assessed using Pearson or Spearman coefficients, as appropriate, while agreement between measurement procedures with the Bland-Altman method²⁴⁰. The significance threshold was set at 0.05. All statistical analyses were performed in Matlab (The MathWorks Inc., Natick, MA, USA).

5.3 Results

5.3.1 Coronary blood flow rate estimates

Coronary flow rate estimates and corresponding Reynolds numbers at the inflow section of each vessel are summarized in **Table 5.3**.

Table 5.3 Flow rate and Reynolds numbers

| ID | Thermodilution | | Doppler flow | | 3D contrast velocity | | Scaling law | |
|-------------|----------------|--------|--------------|--------|----------------------|--------|-------------|--------|
| | Q (mL/min) | Re | Q (mL/min) | Re | Q (mL/min) | Re | Q (mL/min) | Re |
| RCA1 | 80.05 | 114.30 | 66.85 | 95.46 | 121.35 | 173.28 | 88.96 | 127.03 |
| LAD1 | 88.40 | 160.77 | 47.10 | 85.67 | 86.05 | 156.50 | 47.99 | 87.29 |
| RCA2 | 76.54 | 161.61 | 69.91 | 147.62 | 70.42 | 148.69 | 32.82 | 69.30 |
| RCA3 | 46.42 | 101.12 | 32.84 | 71.54 | 71.77 | 156.34 | 29.90 | 65.15 |
| RCA4 | 87.10 | 179.48 | 38.99 | 80.35 | 78.25 | 161.25 | 34.91 | 71.94 |
| LAD2 | 54.68 | 138.16 | 21.36 | 53.98 | 45.01 | 113.73 | 20.22 | 51.09 |
| LAD3 | 55.47 | 113.17 | 51.49 | 105.05 | 92.59 | 188.89 | 35.81 | 73.05 |
| RCA5 | 37.20 | 62.89 | 40.88 | 69.12 | 124.11 | 209.82 | 57.74 | 97.62 |
| RCA6 | 70.05 | 134.78 | 36.83 | 70.86 | 80.41 | 154.70 | 40.83 | 78.55 |
| RCA7 | 45.90 | 96.14 | 31.08 | 65.10 | 78.26 | 163.92 | 33.35 | 69.85 |
| LAD4 | 74.67 | 155.10 | 76.77 | 159.45 | 57.01 | 118.42 | 34.12 | 70.86 |
| LAD5 | 59.66 | 114.45 | 60.85 | 116.75 | 111.19 | 213.33 | 41.89 | 80.36 |
| LAD6 | 66.34 | 188.23 | 27.85 | 79.01 | 32.24 | 91.49 | 15.31 | 43.43 |
| LAD7 | 98.28 | 211.86 | 73.37 | 158.17 | 57.42 | 123.78 | 30.20 | 65.10 |

Flow rates and Reynolds numbers at the inlet section for each investigated coronary artery model.

Continuous thermodilution-derived flow rate values Q_{thermo} (68.20 [52.61-81.81] mL/min) were significantly higher than Q_{Doppler} values (43.99 [32.40-67.62] mL/min; $p=0.0014$) and Q_{SL} values (34.51 [30.12-43.41] mL/min; $p=0.0023$) and lower than Q_{CV} (78.25 [57.32-97.24]; $p=0.2368$), **Figure 5.4A**. A moderate linear correlation emerged between Q_{thermo} and Q_{Doppler} ($r=0.54$, 95% CI 0.01 to 0.83, $p=0.0473$), **Figure 5.4B**.

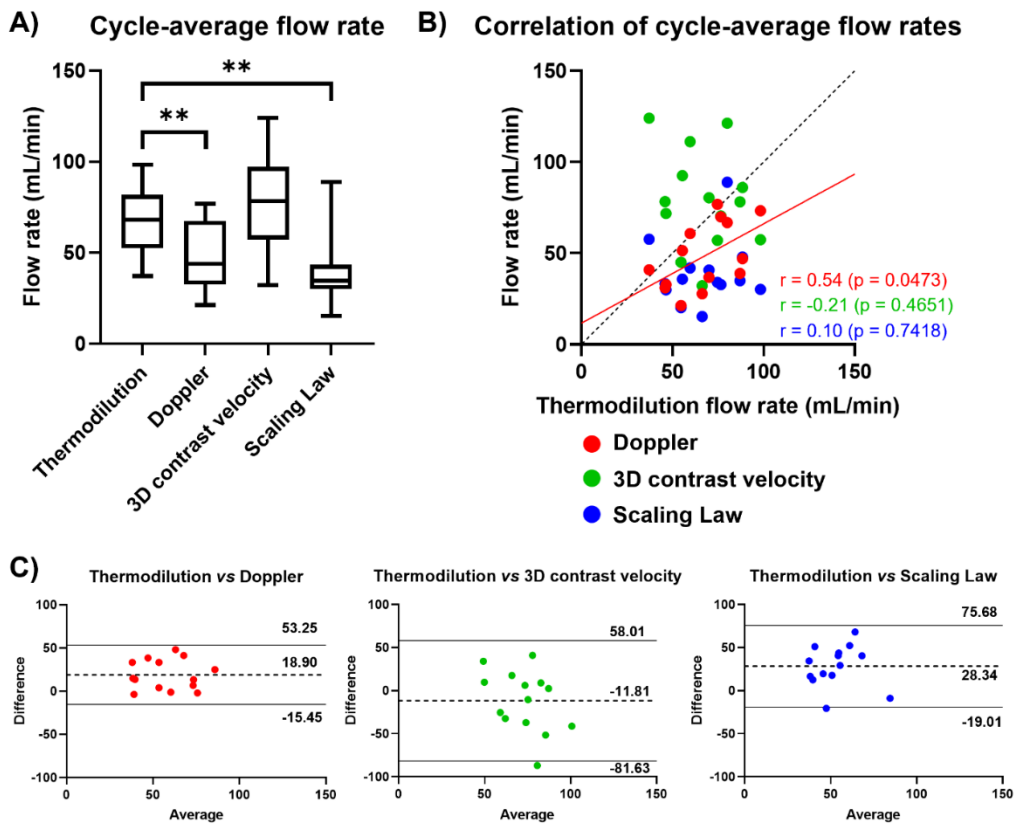


Figure 5.4. Flow rate analysis. (A) boxplot representation of the assessed cycle-average flow rate distributions per adopted technique. Statistically significant differences, evaluated between thermodilution and the other flow rate assessment techniques, are indicated with ** ($p < 0.01$); (B) scatter plot of thermodilution-based vs. Doppler-based, 3D contrast velocity-based and scaling law-based flow rate assessment. Linear regression line was reported only for Doppler-based flow rate due to the emerged significant linear correlation (as reported in figure). The black dotted line represents the identity line; (C) Bland-Altman plots of Doppler-based, 3D contrast velocity-based and scaling law-based vs. thermodilution-based flow rate values.

Results from the Bland-Altman analysis are presented in **Figure 5.4C**. Both scaling law- and Doppler-based procedures lead to an underestimation of the coronary blood flow measured with thermodilution (Q_{thermo} vs. Q_{Doppler} bias = 18.90 mL/min; Q_{thermo} vs. Q_{SL} bias = 28.34 mL/min), while an opposite trend emerged for 3D contrast velocity method (Q_{thermo} vs. Q_{CV} bias = -11.81 mL/min). The lowest data dispersion was found for Q_{thermo} vs. Q_{Doppler} (SD = 17.52 mL/min). No significant linear trend in terms of error was observed for Q_{Doppler} , Q_{CV} , and Q_{SL} vs. Q_{thermo} .

5.3.2 Impact of flow rate estimation on steady-state WSS

WSS magnitude distributions with the four different inflow BCs for the 14 coronary artery models are visually presented in **Figure 5.5**.

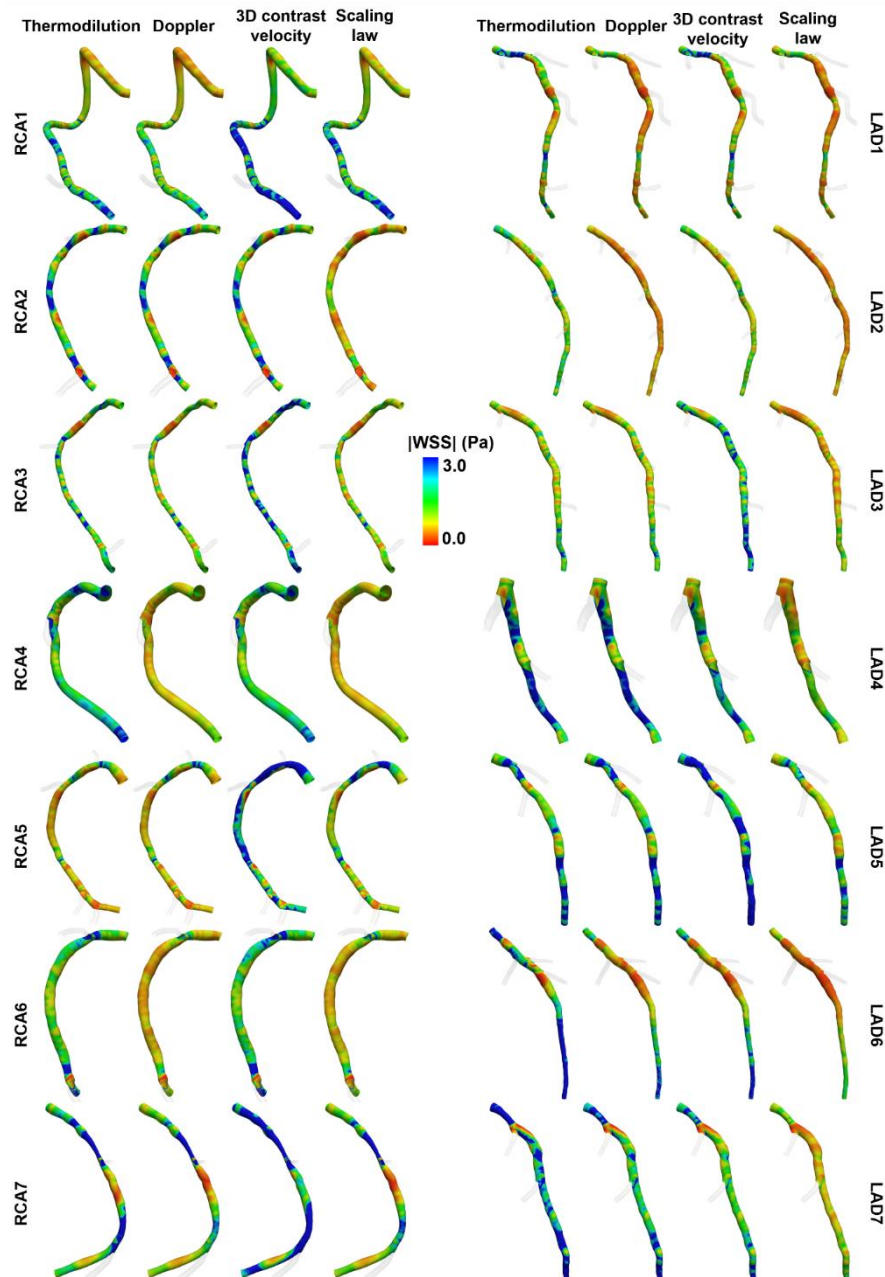


Figure 5.5. WSS magnitude luminal distribution. WSS color maps obtained prescribing the different flow rates as inflow boundary condition in each coronary model. Left panel: RCA; right panel: LAD.

Two explanatory coronary artery models (one RCA and one LAD) reflecting results common to all the 14 cases are displayed in **Figure 5.6**, where the WSS magnitude distribution at the luminal surface obtained prescribing Q_{thermo} is presented with the local percentage differences (absolute values) from it in terms of WSS magnitude, obtained when Q_{Doppler} , Q_{CV} , and Q_{SL} values are prescribed as inflow BC.

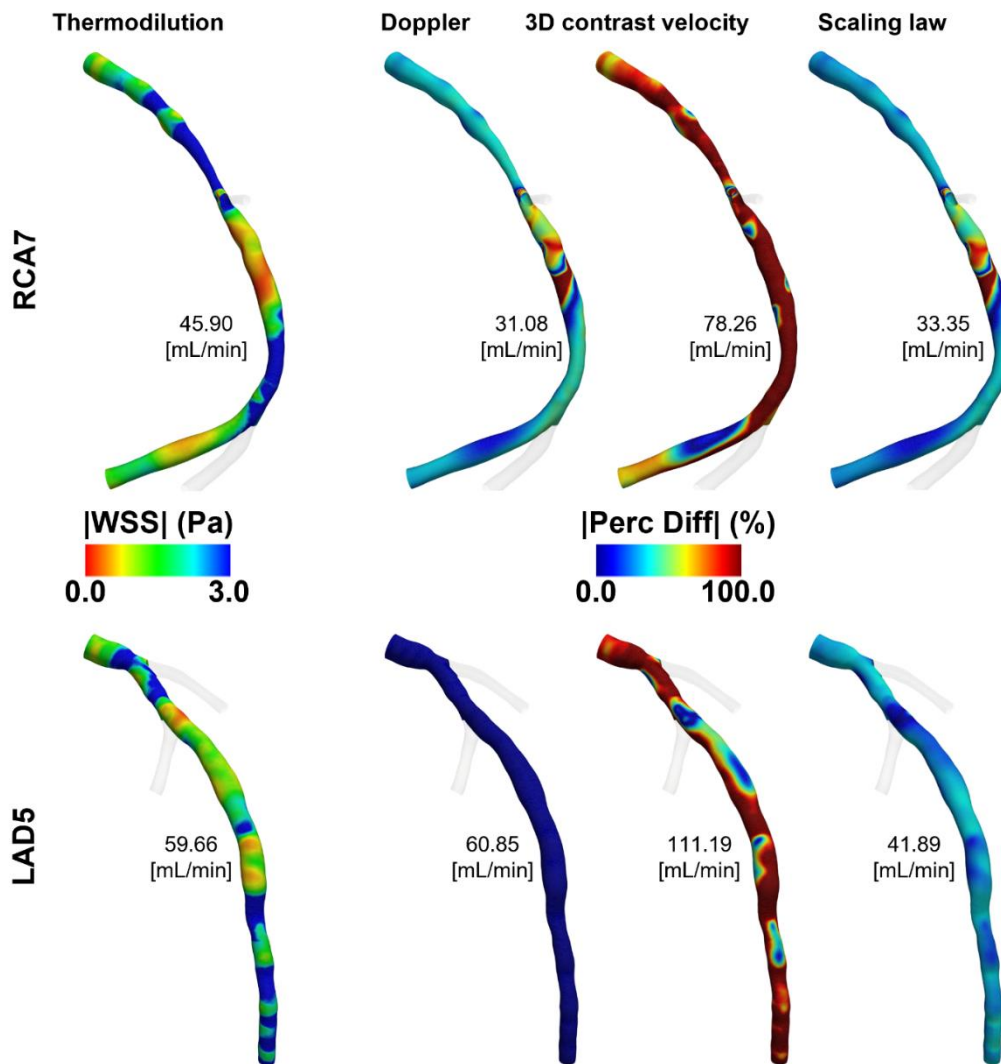


Figure 5.6. WSS magnitude luminal distribution: explanatory cases. WSS magnitude distribution at the luminal surface for the reference inflow boundary condition thermomodulation (left panel). Distribution of absolute values of WSS magnitude percentage differences of Doppler-based, 3D contrast velocity-based and scaling law-based vs. thermomodulation-based flow rate values (right panel). Two explanatory cases, one LAD and one RCA, are reported.

A significant difference in terms of luminal surface-averaged values of WSS magnitude emerged between simulations based on Q_{thermo} and Q_{Doppler} as inflow BC (1.69 [1.23-2.30] Pa and 1.05 [0.80-1.76] Pa, respectively; $p=0.0020$) and simulations based on Q_{thermo} and Q_{SL} (0.80 [0.70-1.40] Pa; $p=0.0008$) as inflow BC (**Figure 5.7A**). A significant linear correlation ($r=0.65$, 95% CI 0.18 to 0.88; $p=0.0119$) emerged between surface-averaged WSS magnitude median values derived from Q_{thermo} and Q_{Doppler} simulations (**Figure 5.7B**), in accordance with the emerged correlation between thermodilution and Doppler flow rate measurements (**Figure 5.4B**).

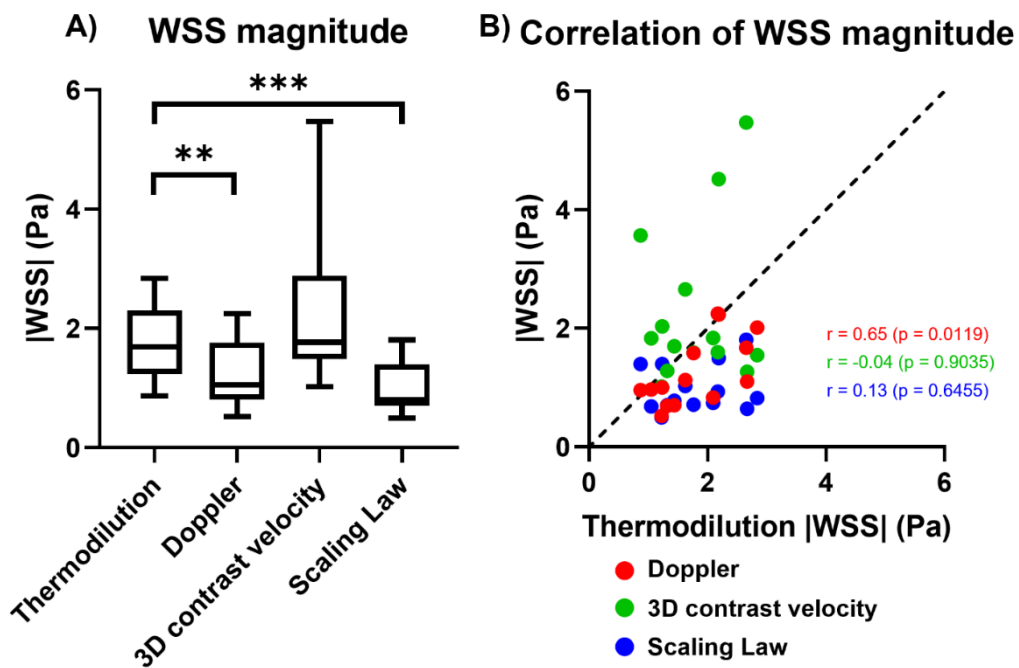


Figure 5.7. WSS magnitude quantitative analysis. (A) boxplot representation of luminal surface-averaged WSS magnitude values per adopted technique. Statistically significant differences between obtained from thermodilution-based flow rate assessment and the three other techniques are indicated with ** ($p < 0.01$) and *** ($p < 0.001$); (B) scatter plots of thermodilution-based luminal surface-averaged WSS magnitude values vs. Doppler-based, 3D contrast velocity-based and scaling law-based ones. The black dotted line represents the identity line.

As for the luminal surface areas exposed to low WSS magnitude, no significant differences emerged applying the different flow rate values as inflow BC (**Figure 5.8A**). Additionally, the analysis of WSS10 surface areas highlighted a satisfactory co-localization (**Figure 5.8B**) of the results from

Q_{thermo} -based simulations with Q_{Doppler} -based (SI = 0.67 [0.49-0.83]), Q_{CV} -based (SI = 0.64 [0.51-0.84]) and Q_{SL} -based (SI = 0.69 [0.39-0.79]) simulations. Explanatory WSS10 co-localization maps are presented in **Figure 5.8C**, where the two cases with the lowest and highest SI value are displayed.

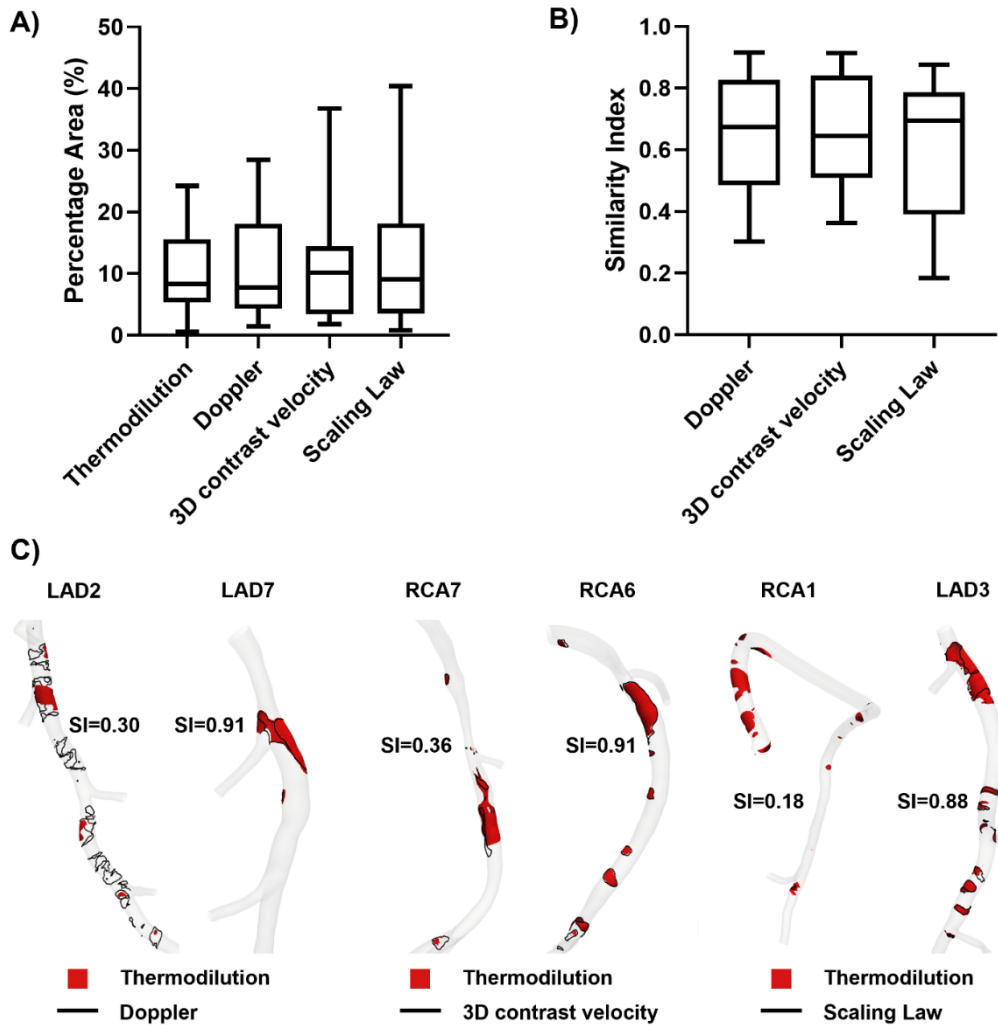


Figure 5.8. Low WSS magnitude surface area analysis. (A) boxplot representation of luminal surface percentage area exposed to low WSS per adopted technique; (B) boxplot representation of the luminal surface area exposed to low WSS magnitude of Doppler-based, 3D contrast velocity-based, and scaling law-based simulations co-localizing with low WSS magnitude surface area of thermodilution-based simulations, expressed in terms of similarity index (SI); (C) visual representation of the co-localization of the luminal surface areas exposed to low WSS magnitude in Doppler-based, 3D contrast velocity-based, and scaling law-based simulations with respect to thermodilution-based simulations. For each flow rate assessment technique, the two cases with highest and lowest SI, are presented.

When considering surface-averaged values of normalized WSS, significant albeit moderate differences emerged between simulations based on Q_{thermo} and Q_{Doppler} as inflow BC (1.18 [0.99 -1.81] and 1.07 [0.92-1.81], respectively; $p=0.0101$) and simulations based on Q_{thermo} and Q_{SL} (1.04 [0.89-1.93]; $p=0.0203$) as inflow BC (**Figure 5.9A**). Very strong linear correlations emerged between surface-averaged normalized WSS magnitude median values derived from Q_{Doppler} -based, Q_{CV} -based and Q_{SL} -based simulations and Q_{thermo} -based simulations ($r>0.97$ and $p<0.0001$ in all cases, **Figure 5.9B**).

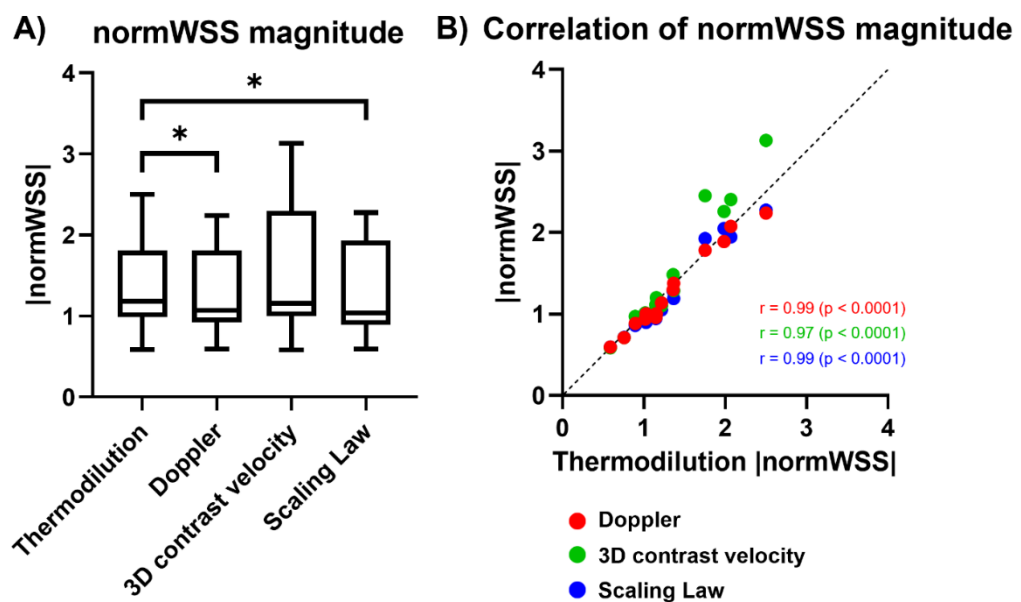


Figure 5.9. normWSS quantitative analysis. (A) boxplot representation of luminal surface-averaged normalized WSS magnitude values per adopted technique. Statistically significant differences between obtained from thermodilution-based flow rate assessment and the three other techniques are indicated with * ($p<0.05$); (B) scatter plots of thermodilution-based luminal surface-averaged normalized WSS magnitude values vs. Doppler-based, 3D contrast velocity-based and scaling law-based ones. The black dotted line represents the identity line.

The impact of the different flow rates adopted as inflow BCs on WSS directionality was overall low: the 90th percentile values of the AEWSSD values probability density function were equal to 0.0095, 0.0105, and 0.0194, for Q_{Doppler} -based, Q_{CV} -based, and Q_{SL} -based simulations, corresponding to local misalignments of WSS vectors from the reference (from Q_{thermo} -based simulations) equal to 0.5443°, 0.6016°, and 1.1116°, respectively (**Figure 5.10A**). By visual inspection of the AEWSSD luminal

surface distributions of two representative cases characterized by the absence/presence of regions of markedly different WSS misalignment, it was possible to observe that WSS misalignment was located close to the side branches, i.e., where the WSS deviation from the axial direction is more pronounced (model LAD6 in **Figure 5.10B**).

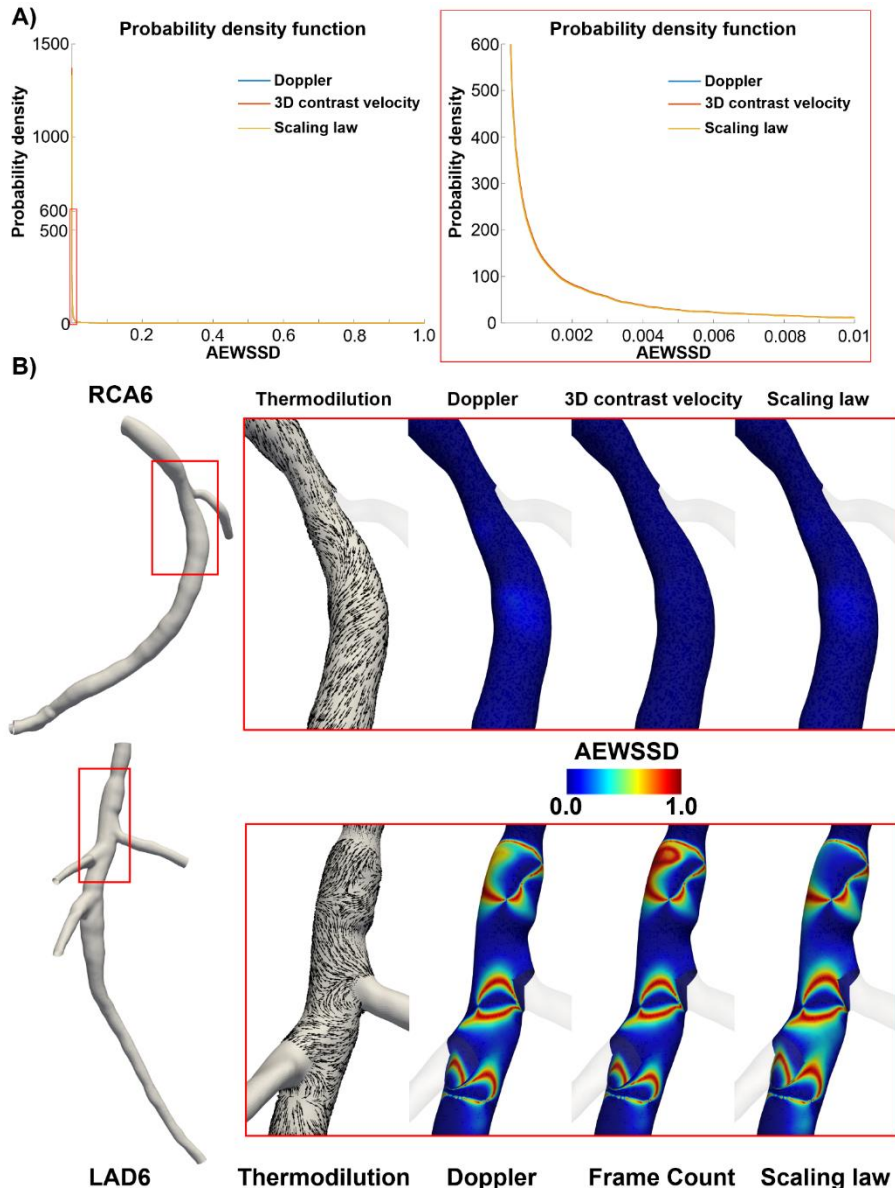


Figure 5.10. WSS directionality analysis. (A) probability density function of the absolute error in WSS direction (AEWSSD) with an inset zooming in AEWSSD values < 90th percentile; (B) zoomed visualizations (red box) of the WSS normalized vector field obtained from Doppler-based, 3D contrast velocity-based, and scaling law-based simulations with respect to the thermodilution-based one. Two explanatory cases, one with low and one with high AEWSSD values, are presented.

5.3.3 Impact of flow rate estimation on unsteady-state WSS

As observed in steady-state WSS magnitude, a significant difference in terms of luminal surface-averaged values of all unsteady-state WSS-based descriptors emerged between simulations based on Q_{thermo} vs. Q_{Doppler} and Q_{SL} as inflow BC while no statistically significant difference emerged between simulations based on Q_{thermo} vs. Q_{3DCV} . (Figure 5.11).

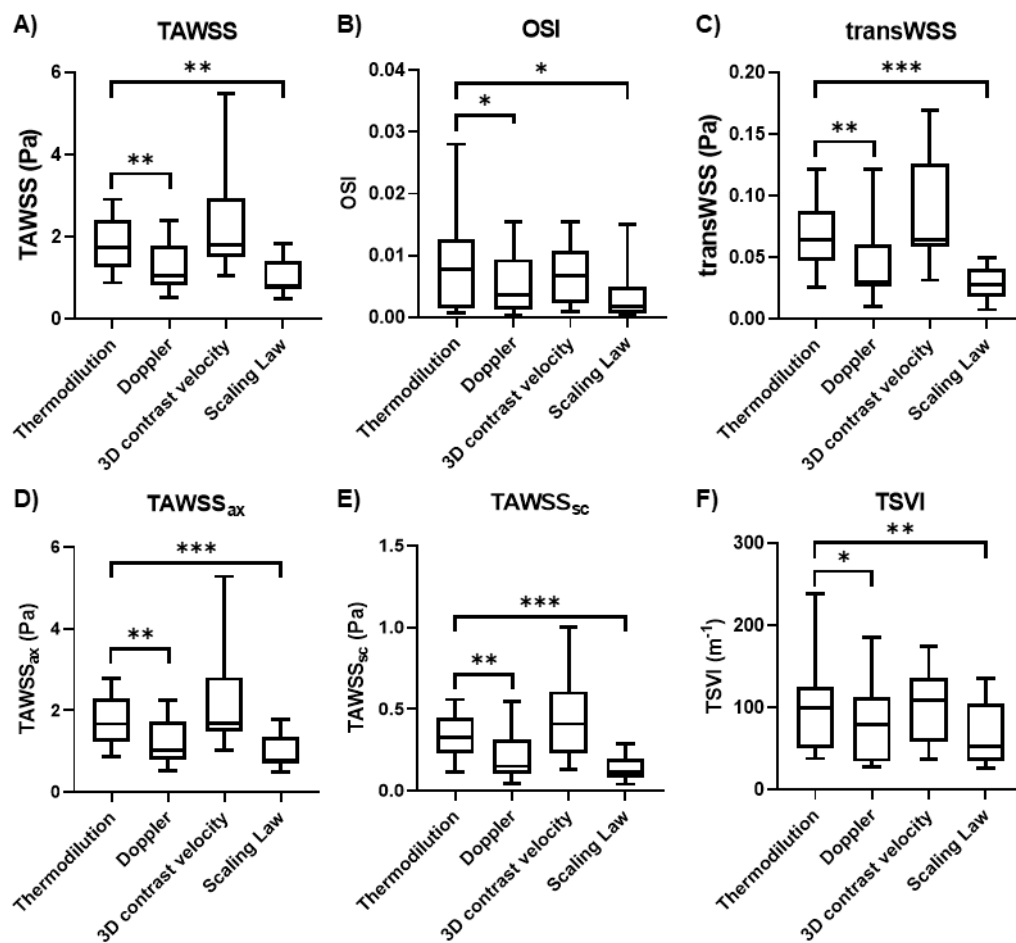


Figure 5.11. Surface averaged WSS-based descriptors. Boxplot representation of luminal surface-averaged unsteady-state WSS-based descriptors values per adopted technique. A) time averaged WSS (TAWSS); B) oscillatory shear index (OSI); C) transverse WSS (transWSS); D) TAWSS axial component (TAWSS_{ax}); E) TAWSS secondary component (TAWSS_{sc}); F) topological shear variation index (TSVI). Statistically significant differences between obtained from thermodilution-based flow rate assessment and the three other techniques are indicated with * ($p < 0.05$), ** ($p < 0.01$), and *** ($p < 0.001$).

Median value, IQR, and p -values for all surface averaged WSS-based descriptors are listed in **Table 5.4**.

| Table 5.4 WSS-based descriptors surface averaged values | | | | | |
|---|------------|---------------------|---------------------|----------------------|---------------------|
| WSS-based descriptor | | Thermodilution | Doppler | 3D contrast velocity | Scaling law |
| TAWSS (Pa) | Value | 1.741[1.272-2.415] | 1.062[0.813-1.778] | 1.794[1.517-2.941] | 0.803[0.714-1.421] |
| | p -value | | 0.0023 | 0.3575 | 0.0009 |
| OSI | Value | 0.008[0.002-0.013] | 0.004[0.001-0.009] | 0.007[0.002-0.011] | 0.002[0.001-0.005] |
| | p -value | | 0.0353 | >0.99 | 0.0107 |
| transWSS (Pa) | Value | 0.064[0.048-0.087] | 0.030[0.026-0.060] | 0.064[0.059-0.130] | 0.028[0.018-0.041] |
| | p -value | | 0.0017 | 0.3910 | 0.0009 |
| TAWSS _{ax} (Pa) | Value | 1.670[1.224-2.290] | 1.033[0.793-1.741] | 1.699[1.472-2.812] | 0.7857[0.699-1.362] |
| | p -value | | 0.0023 | 0.3575 | 0.0009 |
| TAWSS _{sc} (Pa) | Value | 0.328[0.232-0.450] | 0.151[0.103-0.314] | 0.410[0.230-0.610] | 0.116[0.082-0.196] |
| | p -value | | 0.0023 | 0.3910 | 0.0009 |
| TSVI (m ⁻¹) | Value | 99.33[49.99-125.70] | 79.96[57.96-112.20] | 109.5[57.96-135.60] | 52.50[34.63-105.30] |
| | p -value | | 0.0203 | 0.6257 | 0.0067 |

Surface averaged values and p -values for WSS-based descriptors. Time averaged WSS (TAWSS); oscillatory shear index (OSI); transverse WSS (transWSS); TAWSS axial component (TAWSS_{ax}); TAWSS secondary component (TAWSS_{sc}); topological shear variation index (TSVI).

As reported in **Figure 5.12**, a statistically significant correlation emerged between surface-averaged TAWSS ($r=0.65$, $p=0.0136$) and TAWSS_{ax} ($r=0.67$, $p=0.0113$) values derived from Q_{thermo} and Q_{Doppler} simulations accordingly to steady-state derived WSS magnitude. Interestingly a strong correlation was observed for OSI ($r=0.86$, $p=0.0002$) and TSVI ($r=0.80$, $p=0.0005$) derived from Q_{thermo} and Q_{Doppler} , while a moderate correlation was observed also between Q_{thermo} and Q_{3DCV} ($r=0.60$, $p=0.0274$ and $r=0.72$, $p=0.0036$ for OSI and TSVI, respectively). No statistically significant were observed for transWSS and TAWSS_{sc}. It is worth to notice that none of WSS-based descriptors obtained prescribing Q_{SL} as inflow BC resulted statistically significantly correlated with those obtained prescribing Q_{thermo} .

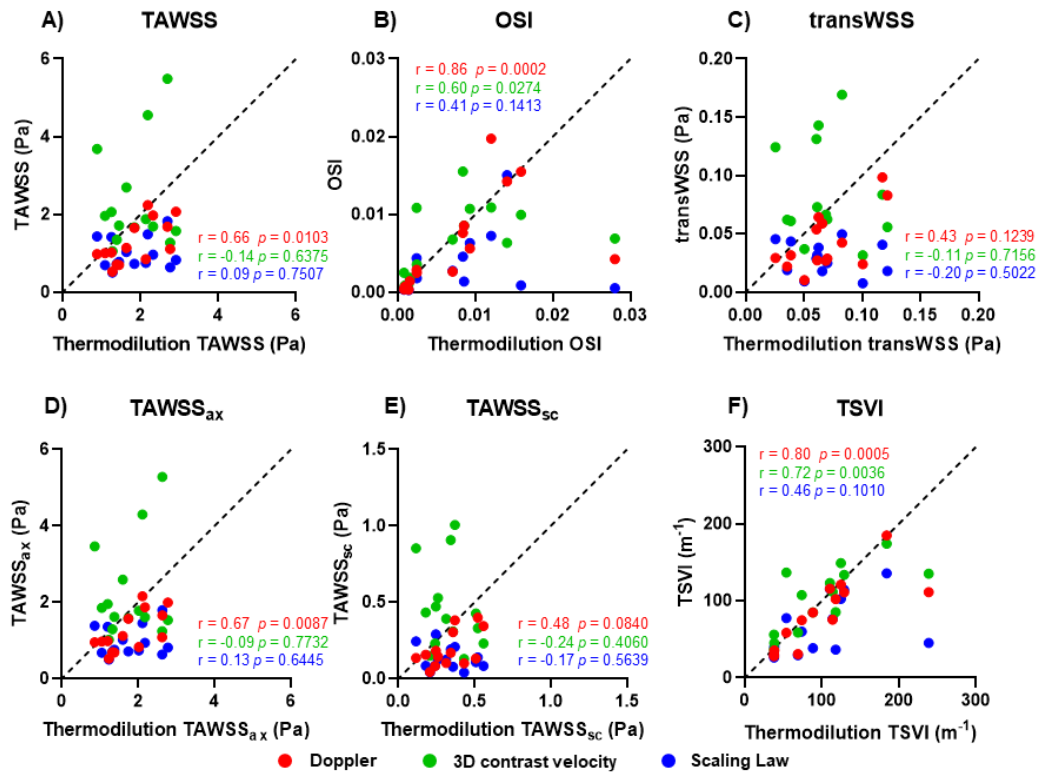


Figure 5.12. WSS-based descriptors correlation analysis. Scatter plots of thermodilution-based luminal surface-averaged WSS-based descriptors values vs. Doppler-based, 3D contrast velocity-based and scaling law-based ones. A) time averaged WSS (TAWSS); B) oscillatory shear index (OSI); C) transverse WSS (transWSS); D) TAWSS axial component (TAWSS_{ax}); E) TAWSS secondary component (TAWSS_{sc}); F) topological shear variation index (TSVI). The black dotted line represents the identity line.

As for SA, no significant differences emerged applying the different flow rate values as inflow BC for all WSS-based descriptors (**Figure 5.13**).

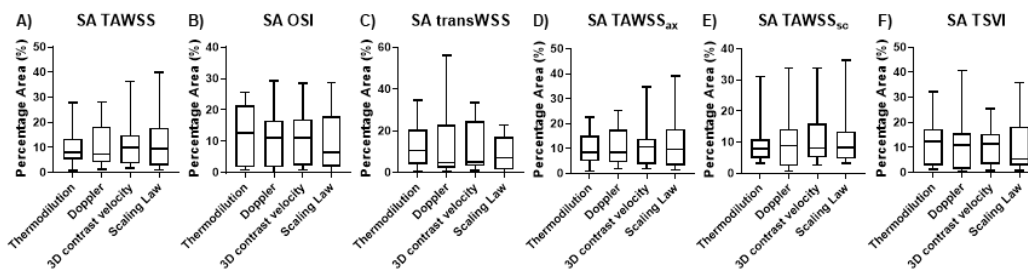


Figure 5.13. SA for all WSS-based descriptors. Boxplot representation of luminal surface percentage area exposed to disturbed flow per adopted technique. A) time averaged WSS (TAWSS); B) oscillatory shear index (OSI); C) transverse WSS (transWSS); D) TAWSS axial component (TAWSS_{ax}); E) TAWSS secondary component (TAWSS_{sc}); F) topological shear variation index (TSVI).

Additionally, the analysis of SA highlighted a satisfactory co-localization (**Figure 5.14**) of the results from Q_{thermo} -based simulations with Q_{Doppler} -based ones for TAWSS (SI = 0.67 [0.50-0.77]), OSI (SI = 0.76 [0.51-0.87]), TAWSS_{ax} (SI = 0.75 [0.55-0.83]), and TSVI (SI = 0.80 [0.62-0.85]), while was only modest for transWSS (SI = 0.55 [0.21-0.68]), and TAWSS_{sc} (SI = 0.56 [0.44-0.67]). Regarding the comparison of SA obtained from Q_{thermo} -based simulations with Q_{CV} -based ones a good co-localization was observed for TAWSS (SI = 0.62 [0.51-0.83]), OSI (SI = 0.75 [0.60-0.95]), TAWSS_{ax} (SI = 0.75 [0.62-0.89]), and TSVI (SI = 0.74 [0.62-0.84]), while also in this case was only modest for transWSS (SI = 0.45 [0.22-0.56]), and TAWSS_{sc} (SI = 0.59 [0.45-0.73]). Finally, comparing SA obtained from Q_{thermo} -based simulations with Q_{SL} -based ones a good co-localization was observed for TAWSS (SI = 0.67 [0.42-0.79]) and TAWSS_{ax} (SI = 0.75 [0.45-0.83]), while was only modest for OSI (SI = 0.60 [0.28-0.80]), transWSS (SI = 0.46 [0.10-0.72]), TAWSS_{sc} (SI = 0.47 [0.39-0.66]), and TSVI (SI = 0.58 [0.46-0.73]).

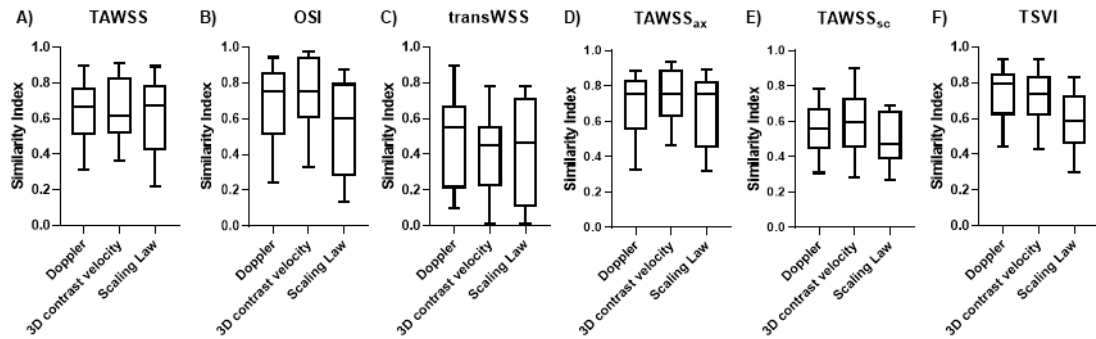


Figure 5.14. Similarity index for all WSS-based descriptors. Boxplot representation of the surface exposed to disturbed flow (SA) of Doppler-based, 3D contrast velocity-based, and scaling law-based simulations co-localizing with low WSS magnitude surface area of thermodilution-based simulations, expressed in terms of similarity index (SI).

The correlation between steady-state WSS magnitude profiles and TAWSS profiles from unsteady state simulations (**Figure 5.15**) was very strong ($r \geq 0.998$; $p < 0.0001$), proving that here analysed steady-state WSS magnitude values are representative of the cycle-average WSS magnitude.

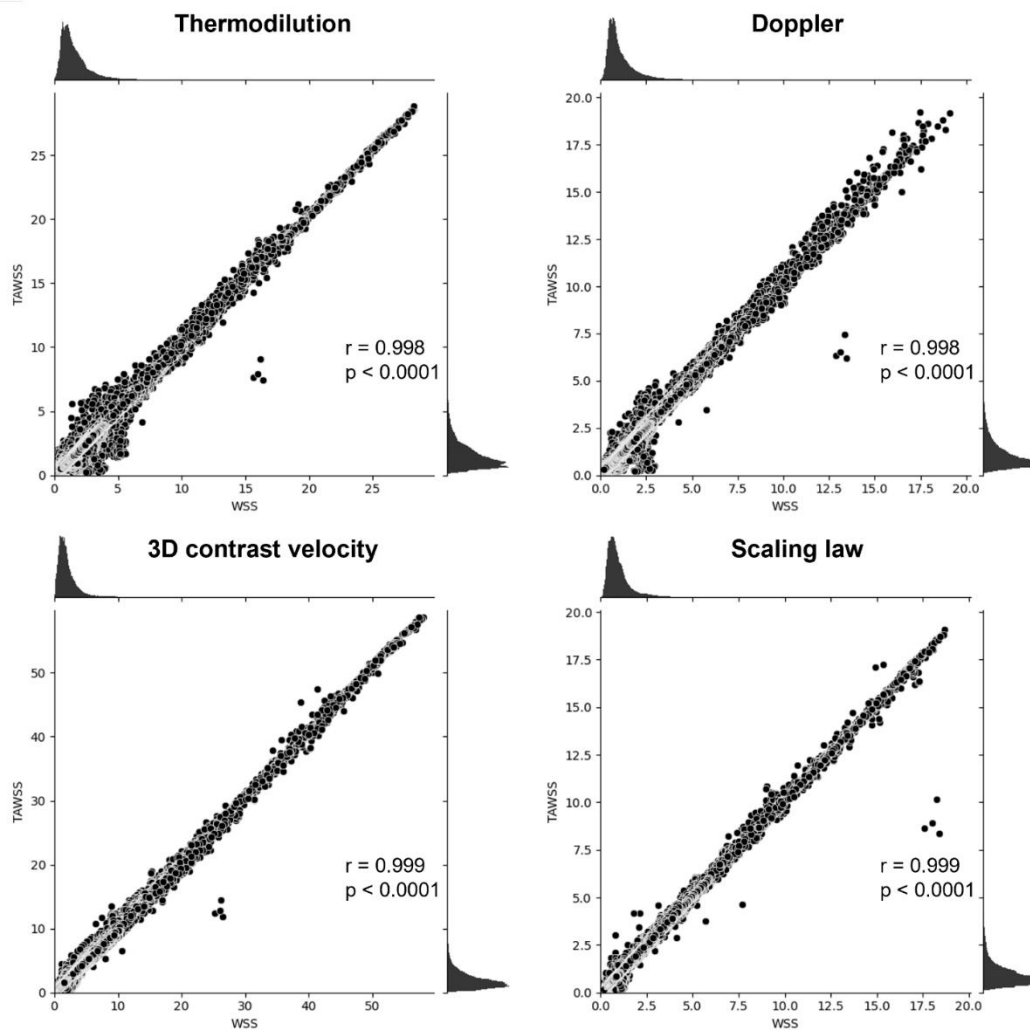


Figure 5.15. Steady-state WSS magnitude vs. unsteady-state TAWSS. Scatter plots of steady-state WSS magnitude vs. time averaged WSS (TAWSS) for each inflow boundary condition. r and p are the correlation coefficient and the p -value of the linear regression. The probability density functions of steady-state WSS magnitude and TAWSS are reported on the top and right axes, respectively.

5.3.4 Impact of flow rate estimation on unsteady-state WSS

Intravascular flow visualization using LNH isosurfaces highlighted the establishment of distinguishable counter-rotating helical blood flow patterns in the coronary models (**Figure 5.16**). In all cases, helical flow is topologically similar, independent of the flow rate estimate applied as inflow BC.

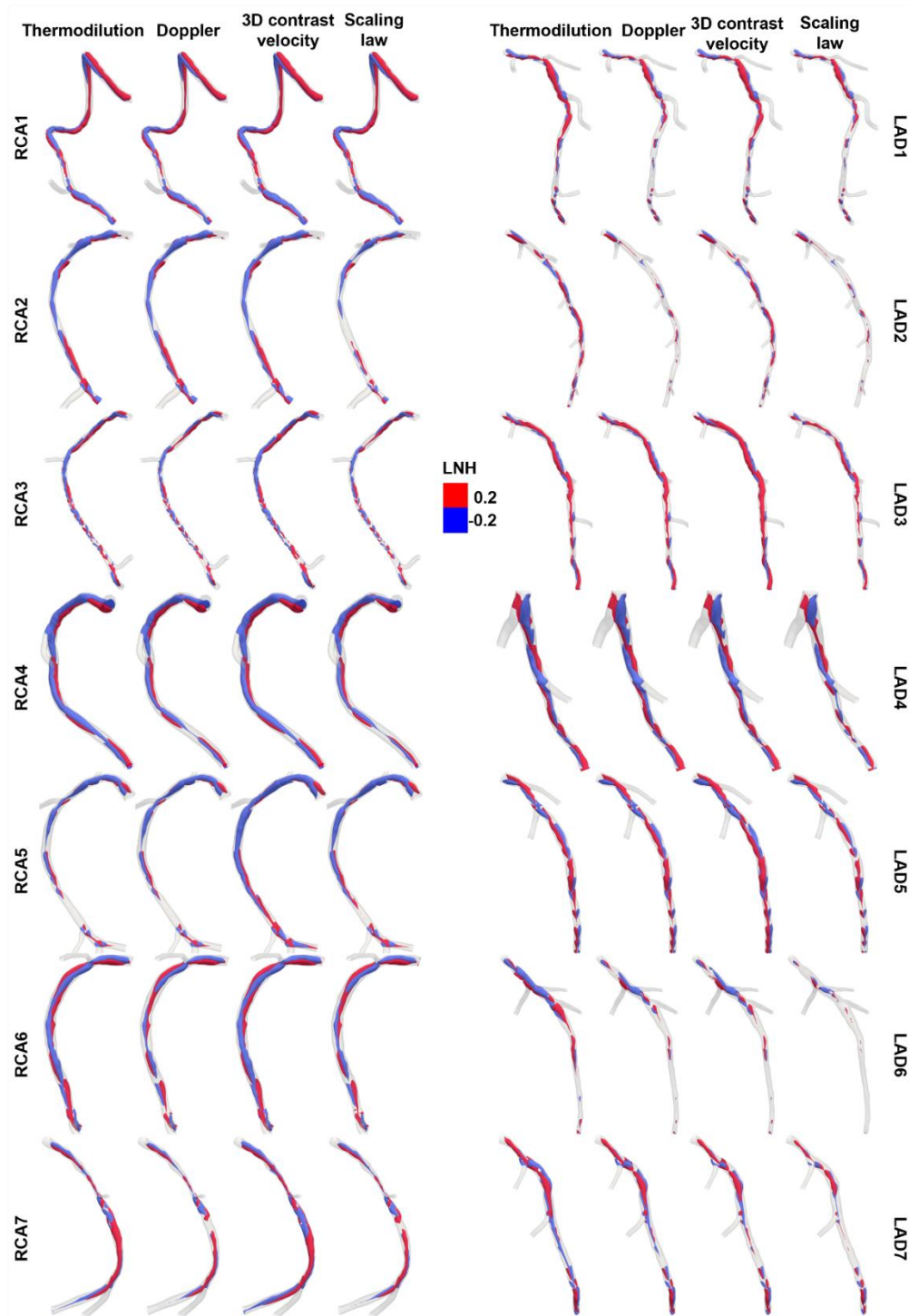


Figure 5.16. LNH isosurfaces visualization. Visualization of intravascular local normalized helicity (LNH) isosurfaces obtained prescribing the different flow rates as inflow boundary condition in each coronary model. Right-handed helical structures are associated with positive LNH values (red colour), and left-handed helical structures are associated with negative LNH values (blue colour). Left panel: RCA; right panel: LAD.

The impact of the different flow rate estimates prescribed as inflow BC on coronary helical flow features is quantified in **Figure 5.17A** and **Figure 5.17B** for steady-state and unsteady-state helicity-based descriptors, respectively.

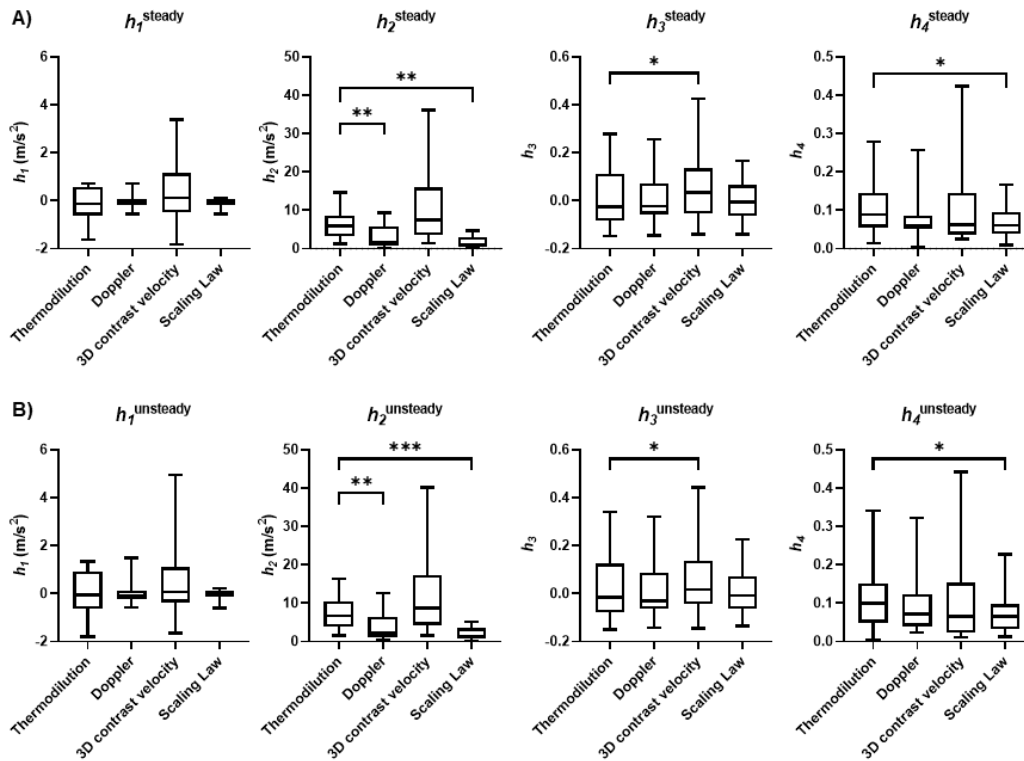


Figure 5.17. Helicity-based descriptors. (A) boxplot representation of steady-state helicity-based descriptors distributions per adopted technique. (B) boxplot representation of unsteady-state helicity-based descriptors distributions per adopted technique. Statistically significant differences, evaluated between thermodilution and the other flow rate assessment techniques, are indicated with * ($p < 0.05$), ** ($p < 0.01$) and *** ($p < 0.001$).

Helicity production intensity was sensitive to the inlet flow rate. Overall, Q_{CV} -based simulations presented the highest h_2 values as well as the largest range of variation ($h_2^{\text{steady}} = 7.48$ [3.56-15.89] m/s^2 and $h_2^{\text{unsteady}} = 8.71$ [4.29-17.29] m/s^2), although the differences with respect to the Q_{thermo} -based simulations were not significant ($h_2^{\text{steady}} = 5.87$ [3.23-8.66] m/s^2 and $h_2^{\text{unsteady}} = 6.71$ [3.86-10.46] m/s^2). Conversely, significant differences with respect to the Q_{thermo} -based simulations emerged for the Q_{Doppler} -based ($h_2^{\text{steady}} = 1.71$ [0.88-5.72] m/s^2 , $p=0.0023$ and $h_2^{\text{unsteady}} = 2.25$ [1.09-6.53] m/s^2 , $p=0.0023$) and Q_{SL} -based simulations ($h_2^{\text{steady}} = 1.09$ [0.62-3.00] m/s^2 ,

$p=0.0012$ and $h_2^{\text{unsteady}} = 1.35 [0.80-3.44] \text{ m/s}^2$, $p=0.0009$). Differences from Q_{thermo} -based simulations emerged also in terms bi-helical flow patterns balance, expressed in terms of h_3 and h_4 for both steady-state and unsteady-state simulations. In particular, a significant but weak difference was found between the simulations based on Q_{CV} and Q_{thermo} in terms of h_3^{steady} ($0.03 [-0.06-0.13]$ vs. $-0.02 [-0.08-0.11]$, respectively; $p=0.0273$) and h_3^{unsteady} ($0.02 [-0.05-0.14]$ vs. $-0.01 [-0.08-0.12]$, respectively; $p=0.0338$). A significant difference emerged also between the simulations based on Q_{SL} and Q_{thermo} in terms of h_4^{steady} ($0.06 [0.04-0.09]$ and $0.09 [0.06-0.14]$, respectively; $p=0.0183$) and h_4^{unsteady} ($0.06 [0.03-0.10]$ and $0.10 [0.05-0.15]$, respectively; $p=0.0158$). However, such differences in helical flow topological organization can be considered negligible, with h_3 and h_4 tending to be a simple affair round the zero value, the latter indicating perfect balance of counter-rotating helical flow patterns. As far as the whole helicity production (h_1^{steady} and h_1^{unsteady}) no significant differences from Q_{thermo} -based simulations emerged (**Figure 5.17**).

Results of the correlation analysis for the steady-state and unsteady-state helicity-based descriptors are presented in **Figure 5.18A** and **Figure 5.18B**, respectively. Descriptor h_1^{steady} from Q_{CV} -based and Q_{SL} -based simulations was correlated (even if not very strongly) with the same descriptor obtained from Q_{thermo} -based simulations ($r=0.60$, $p=0.0235$ and $r=0.55$, $p=0.0438$, respectively). Higher correlations were observed for h_1^{unsteady} from Q_{Doppler} -based and Q_{CV} -based simulations with the same descriptor obtained from Q_{thermo} -based simulations ($r=0.76$, $p=0.0024$ and $r=0.75$, $p=0.0027$, respectively). Regarding h_2 , a significant linear correlation between Q_{thermo} -based and Q_{Doppler} -based simulations ($r=0.53$, $p=0.0496$ and $r=0.57$, $p=0.0346$ for h_2^{steady} and h_2^{unsteady} , respectively) emerged. Descriptor h_3 from Q_{Doppler} -based, Q_{CV} -based and Q_{SL} -based simulations were strongly correlated with the same descriptors obtained from Q_{thermo} -based simulations ($r>0.88$ and $r>0.91$, for h_3^{steady} and h_3^{unsteady} , respectively, with $p<0.0001$ in all cases). Similar considerations, even if with weaker correlations can be made for h_4^{steady} and h_4^{unsteady} , confirming that different flow rate estimates applied as inflow BCs have a more marked impact on helicity intensity rather than on helical flow topological features.

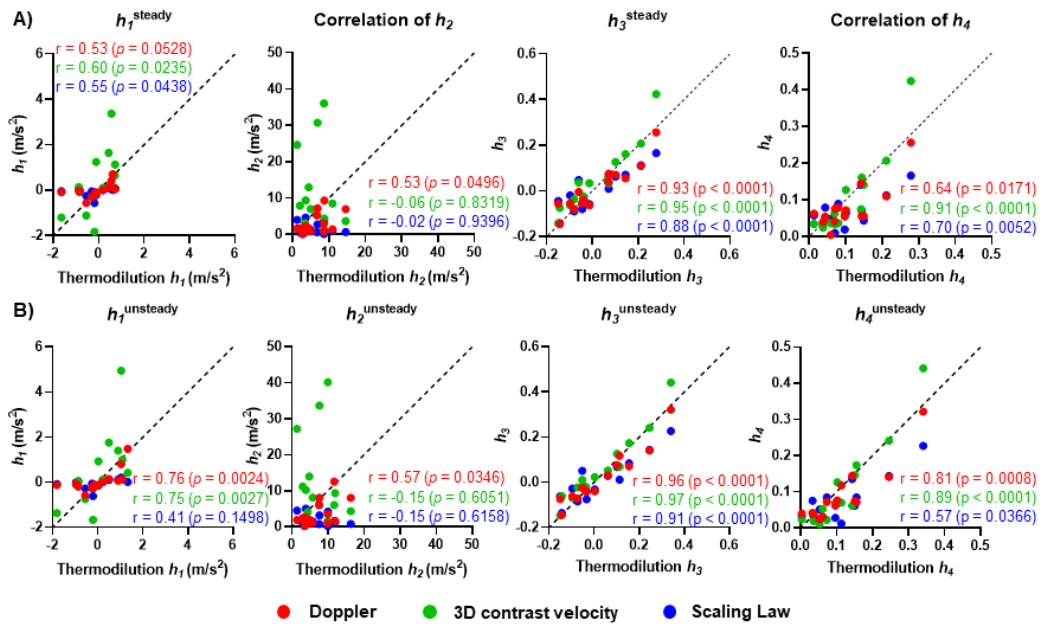


Figure 5.18. Helicity-based descriptors correlations. (A) scatter plots of steady-state helicity-based descriptors from thermodilution-based vs. Doppler-based, 3D contrast velocity-based and scaling law-based flow rate assessment; (B) scatter plots of unsteady-state helicity-based descriptors from thermodilution-based vs. Doppler-based, 3D contrast velocity-based and scaling law-based flow rate assessment. r and p are the correlation coefficient and the p -value of the linear regression, and the black dotted line represents the identity line.

In addition to the same statistically significant differences and correlations observed from steady-state and unsteady-state helicity-based descriptors the correlation between steady- and unsteady-state helicity-based descriptors (**Figure 5.19**) was very strong ($r \geq 0.952$; $p < 0.0001$), proving that steady-state helicity-based descriptors capture the main features of cycle-averaged helical flow patterns.

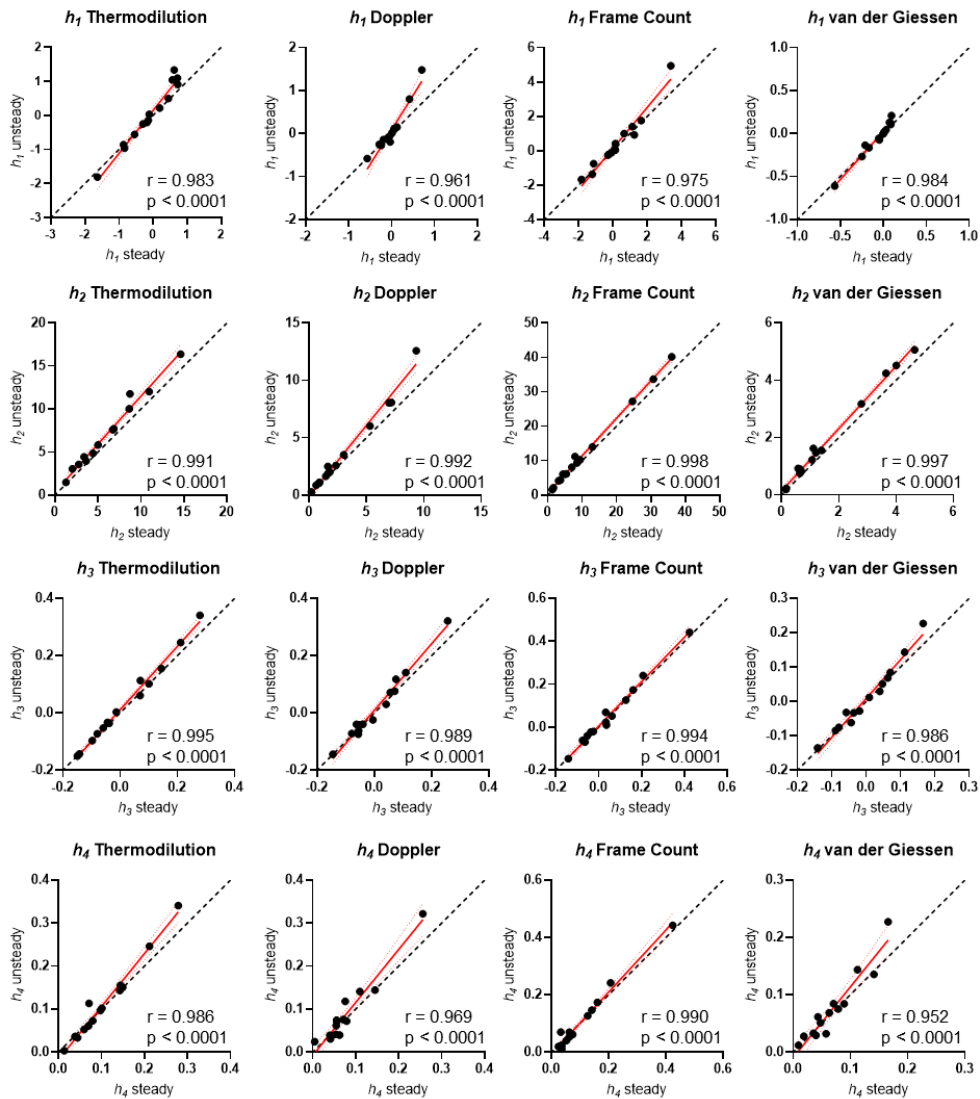


Figure 5.19. Steady-state and unsteady-state helicity-based descriptors correlation. Scatter plots of steady-state vs. unsteady-state helicity-based descriptors for each inflow boundary condition. r and p are the correlation coefficient and the p-value of the linear regression. The black dotted line represents the identity line.

5.4 Discussion

The present study performed a comparative analysis among four different techniques for the *in vivo* assessment of coronary blood flow rate, namely continuous thermodilution, intravascular Doppler flow, 3D contrast velocity and anatomy-based scaling law. The analysis was carried out in terms of assessed blood flow rate values, and angiography-based CFD simulations of the coronary hemodynamics with inflow BCs derived from the four different techniques.

The main findings of the present study can be summarised as follows:

1. coronary flow rate value may vary across *in vivo* measurement techniques, given that the clinically available techniques are based on different theories as well as practical approaches.
2. Differences in measured blood flow rates reflect into uncertainty on the prescribed inflow BCs for angiography-based CFD simulations, which in turn can impact both local WSS distribution and intravascular flow patterns, such as intracoronary helical flow, especially on descriptors based on WSS and velocity magnitude, such as steady-state WSS magnitude, TAWSS, TAWSS_{ax}, TAWSS_{sc}, transWSS, and h_2 .
3. WSS directionality and WSS-based descriptors based on it, rather than on WSS magnitude, such as OSI and TSVI, are less affected from inflow BC.
4. Surface exposed to disturbed flow is a more robust descriptor with respect to surface averaged values.

The rationale of this work lies in the evaluation of the endothelial shear stress based on the integration of patient data and CFD simulations. In the context of coronary atherosclerosis, endothelial shear stress promises to have a remarkable translational clinical impact, by virtue of its ability to identify e.g. coronary segments with endothelial dysfunction⁶⁴, intermediate coronary lesion prone to rupture^{65,89}, and site of subsequent myocardial infarction²²¹. To pursue the goal of using CFD models of coronary arteries to inform (and possibly enable) prognosis and preemptive treatment strategies, the available clinical information should be leveraged to

determine the conditions to be prescribed at the inflow boundaries, which represent a major source of uncertainty.

The here investigated clinically implementable approaches for flow rate assessment in coronary arteries are characterized by different levels of invasiveness, uncertainty, and costs. Among them, only continuous thermodilution provides a direct measurement of blood flow rate, independent of the 3D reconstruction of the vessel. Moreover, previous studies reported continuous thermodilution being less sensitive to loading conditions, wire position, and accounting for a lower interoperator variability with respect to e.g. Doppler flow measurements, which remain difficult to perform^{231,241,242}. These considerations motivated the adoption of continuous thermodilution as reference technique in the present analysis. Differently from the latter, the estimation of the blood flow rate values by the other three techniques might be affected also by the uncertainties related to the geometric reconstruction. As evident from equations 5.2, 5.3 and 5.4, all analysed techniques with the exception of continuous thermodilution require the estimation of the cross-sectional lumen area or the hydraulic diameter to obtain the blood flow rate value, with an associated budget of uncertainty ascribable to:

1. the quality of images recorded within the routine clinical framework.
2. The reconstruction methods (e.g. using two angiographic views)²⁴³.
3. The location where the cross section is considered, as local variations may be present due to tapering and geometric complexity.

Moreover, the conversion of the Doppler velocity measurement to flow rate values necessarily requires an assumption on the velocity profile (e.g., parabolic) that may affect the reliability of the estimated flow rate value^{227,244}. The 3D contrast velocity method and the anatomy-based scaling law represent the two most clinically convenient techniques since they make use of angiography alone. However, for the former the sensitivity of the estimated flow rate value to the angiographic images acquisition frame rate (i.e., parameter f in equation 5.3) might be remarkable. For the latter, the flow rate estimation depends on the local hydraulic diameter solely. Moreover, a previous comparison with intravascular Doppler

ultrasound measurements²⁴⁵ underlined how the application of the scaling law, represented by equation 5.4, leads to a general underestimation of both flow rate and WSS values, as also observed in the present study (**Figures 5.4 and 5.7**). Since equation 5.4 was derived from Doppler velocity measurements in angiographically normal bifurcations of patients presenting with coronary artery disease, it may not properly account for the influence of the resistance of the distal vascular bed, with a possible impact on the observed relationship between geometry and flow rate⁷⁰.

The here observed significant correlation between Q_{thermo} and Q_{Doppler} (**Figure 5.4C**) is consistent with recent studies on animals and humans reporting a satisfactory agreement between Doppler flow-based and thermodilution-based measurements of blood flow²³¹ or coronary flow reserve (CFR)^{246,247}, defined as the ratio of coronary flow in hyperemic conditions to resting coronary flow. Conversely, contradictory findings have been reported when comparing TIMI frame count-based and Doppler flow-based CFR^{248,249}.

Not unexpectedly, on one hand the differences here observed in the flow rate assessment are reflected on the WSS magnitude and unsteady-state WSS-based descriptors which account for it in their formulation (TAWSS, transWSS, TAWSS_{ax}, and TAWSS_{sc}) profiles (**Figures 5.4, 5.7, 5.11, and 5.12**), in agreement with previous studies^{245,250}. The significance of these differences decreased when considering normalized WSS values and unsteady state WSS-based descriptors not accounting for WSS magnitude (OSI and TSVI), while a very strong linear correlation with respect to the Q_{thermo} -based simulation emerged for all cases (**Figure 5.9B, 5.11, and 5.12**). This expands the previously reported lower sensitivity of normalized WSS with respect to absolute WSS values when comparing inflow BCs based on intravascular Doppler measurements vs. the anatomy-based scaling law adopted here²²⁶. This would seem to suggest that the use of normalized WSS would help increase standardization, although the biological and clinical implications of absolute vs. normalized WSS need to be elucidated, while the physiopathological role of the TSVI is emerging in different vascular regions^{36,37,66,67}. On the other hand, the surface area exposed to low WSS magnitude values and, in general to disturbed flow, is

less sensitive to the flow rate prescribed at the inlet section, as no significant differences in WSS10 and SA emerged among simulation with different inflow BCs (**Figure 5.8** and **Figure 5.13**). Recent evidence demonstrated that the adoption of a study-specific threshold to define low WSS, as done here, may not compromise the predictive power of WSS for coronary plaque progression²⁵¹. In this sense, the robustness of the surface area exposed to low WSS and disturbed flow could allow to reliably stratify subjects at risk of developing coronary atherosclerosis even when intravascular flow measurements are not available, such as in retrospective studies.

Regarding the impact of blood flow rate on coronary helical flow features with a recognized atheroprotective role^{24,72}, for both steady-state and unsteady-state helicity-based descriptors, the impact of the prescribed inflow BC is more relevant for the helicity intensity, quantified by h_2 . In detail, the results obtained from the statistical analysis of h_2 for the four analysed inflow BCs match what observed for the absolute flow rate and WSS magnitude. This can be explained by the established correlation between helicity intensity and WSS magnitude in coronary arteries⁷², and the dependence by construction of h_2 on the velocity magnitude (**Table 5.2**). Conversely, helical flow topology (**Figure 5.16**) appeared to be limitedly affected by the prescribed flow rate value applied as inflow BC, suggesting that coronary geometry is a more important determinant of helical flow topology than the inflow BC.

Finally, the strong correlation between steady-state WSS-magnitude profiles and TAWSS (**Figure 5.15**) or helicity-based descriptors (**Figure 5.19**) from unsteady state simulations proves that the findings on steady-state WSS magnitude are representative of the cycle-average quantities characterizing unsteady-state simulations.

Several limitations could weaken the findings of this study. The volume of saline infused for the continuous thermodilution measurements might influence the flow rate values. However, a previous study indicated that the infusion rate adopted here did not affect flow velocity²³². In this study, the flow rate values at the inflow section were imposed as a Dirichlet boundary condition in terms of a parabolic velocity profile. We reasonably expect a

limited effect of the inflow velocity profile on the simulated hemodynamics based on our previous findings demonstrating that the influence of the inlet velocity profile shape in LADs vanishes after a length equal to few inlet cross-section diameters¹⁴⁸. The adopted outflow boundary conditions based on a prescribed flow split at each coronary bifurcation according to a diameter-based scaling law might influence the simulated hemodynamics. However, at this stage of the investigation, the lack of measured patient-specific flow split does not entail the generality of the results.

5.5 Conclusions

In this study, different clinically applicable techniques for flow rate measurements in coronary arteries were compared and their impact on the results obtained when blood flow rate measurements are used to derive personalized inflow BCs in computational hemodynamics models was evaluated. Our findings indicate that the flow rate values provided by the different measurement techniques may reflect into different WSS profiles as well as helical blood flow intensity. However, such differences are not significant in terms of luminal surface area exposed to low WSS magnitude as well as in terms of helical flow topological features. Given the obtained results and the fact that it is uncommon to have patient-specific measured flow rates in the clinical practice, we refrain from a general recommendation for one coronary flow measurement technique, highlighting the uncertainty associated with assumptions related to inflow BCs. This suggests that particular attention should be given in analysing results obtained from patient-specific CFD simulations in coronary arteries and that a standardization would be desirable to provide comparable results among different studies, while waiting for the improvement and wider dissemination of non-invasive and precise flow rate measurement²⁵².

Chapter 6

Mismatch between morphological and functional assessment of the length of coronary artery disease

A version of this chapter has been published in:

International Journal of Cardiology, Vol. 334, July 2021

Mismatch between morphological and functional assessment of the length of coronary artery disease

Maurizio Lodi Rizzini, Sakura Nagumo, Diego Gallo, Jeroen Sonck, Takuya Mizukami, Fabrizio D'Ascenzo, Dimitri Buytaert, Umberto Morbiducci, Bernard De Bruyne, Claudio Chiastra, and Carlos Collet

6.1 Introduction

Invasive functional assessment of coronary artery disease (CAD) has been regarded as the standard of reference for decision making about revascularization in patients with chronic coronary syndromes. Guidelines advocate evaluating the reduction in coronary flow using pressure-derived indices to decide upon the need for revascularization^{117,118}. Intracoronary pressure measurements are typically performed in the distal segment of the coronary artery reflecting cumulative pressure losses along the epicardial vessel²⁵³. Focal narrowing can be entirely responsible for the pressure drops; nonetheless, diffuse functional deterioration can be also observed outside angiographic stenotic regions contributing to the total decrease in coronary perfusion pressure²⁵⁴.

Coronary angiography remains to date the most utilized method to guide stent implantation. The length of the lesion can be quantified by quantitative coronary angiography (QCA), or alternatively, and more precisely, using intravascular imaging. Both approaches aim to guide stent length selection to restore epicardial conductance and improve myocardial perfusion. In almost a third of patients, however, after an angiographically successful PCI, epicardial conductance remains suboptimal²⁵⁵. Patients with persistent low FFR after percutaneous revascularization appear to be at an increased risk of adverse events²⁵⁵.

A pullback maneuver during intracoronary pressure measurements identifies the presence, location, magnitude and extent of pressure drops²⁵⁴. Two factors, namely the magnitude of FFR drops and extension of functional CAD, are predictive of improvement in epicardial conductance after percutaneous revascularization²⁵⁴. Thus, quantifying the extent of functional CAD may have prognostic capability for post-PCI FFR.

Our aim was to quantify the mismatch in the extent of CAD between morphological and functional evaluations and to assess the impact of the morphological and functional mismatch on FFR after PCI.

6.2 Methods

6.2.1 Study design

This is a multicenter, prospective registry of patients undergoing clinically indicated coronary angiography in whom motorized FFR pullback evaluations were performed before PCI. Patients presenting with acute coronary syndromes, previous coronary artery bypass grafting, significant valvular disease, severe obstructive pulmonary disease or bronchial asthma, coronary ostial lesions, severe tortuosity, or severe calcification were excluded. Patients with adequate pressure tracings and pullback curves were included in this analysis. The study was approved by the Ethics Committee at each participating center. The study population is a combination of two prospective studies NCT03824600 and NCT03782688.

6.2.2 Coronary angiographic analysis

Angiographies were performed using a dedicated acquisition protocol. Two angiographic projections separated at least 30 degrees were obtained for each target lesion after the administration of intracoronary nitrates (**Figure 6.1A**). Angiograms were evaluated blinded to physiological and clinical data and were analyzed using three-dimensional quantitative coronary angiography (QCA) (QAngio XA, Medis Medical Imaging, Netherlands). Minimal lumen diameter (MLD), reference vessel diameter (RVD), and percentage diameter stenosis (%DS) were calculated. Acute gain was defined as the difference between post and pre-PCI MLD. Manual correction of anatomical lesion length was not allowed. Serial lesions were defined as the presence of at least two >50% visual diameter stenosis lesions within the same vessel, at a distance of at least three times the reference vessel diameter²⁵⁶. QCA-derived anatomical lesion length expressed in millimeters was calculated using the 3D QCA software and defined as the length where the reference diameter line intersects the diameter function line (**Figure 6.1B**).

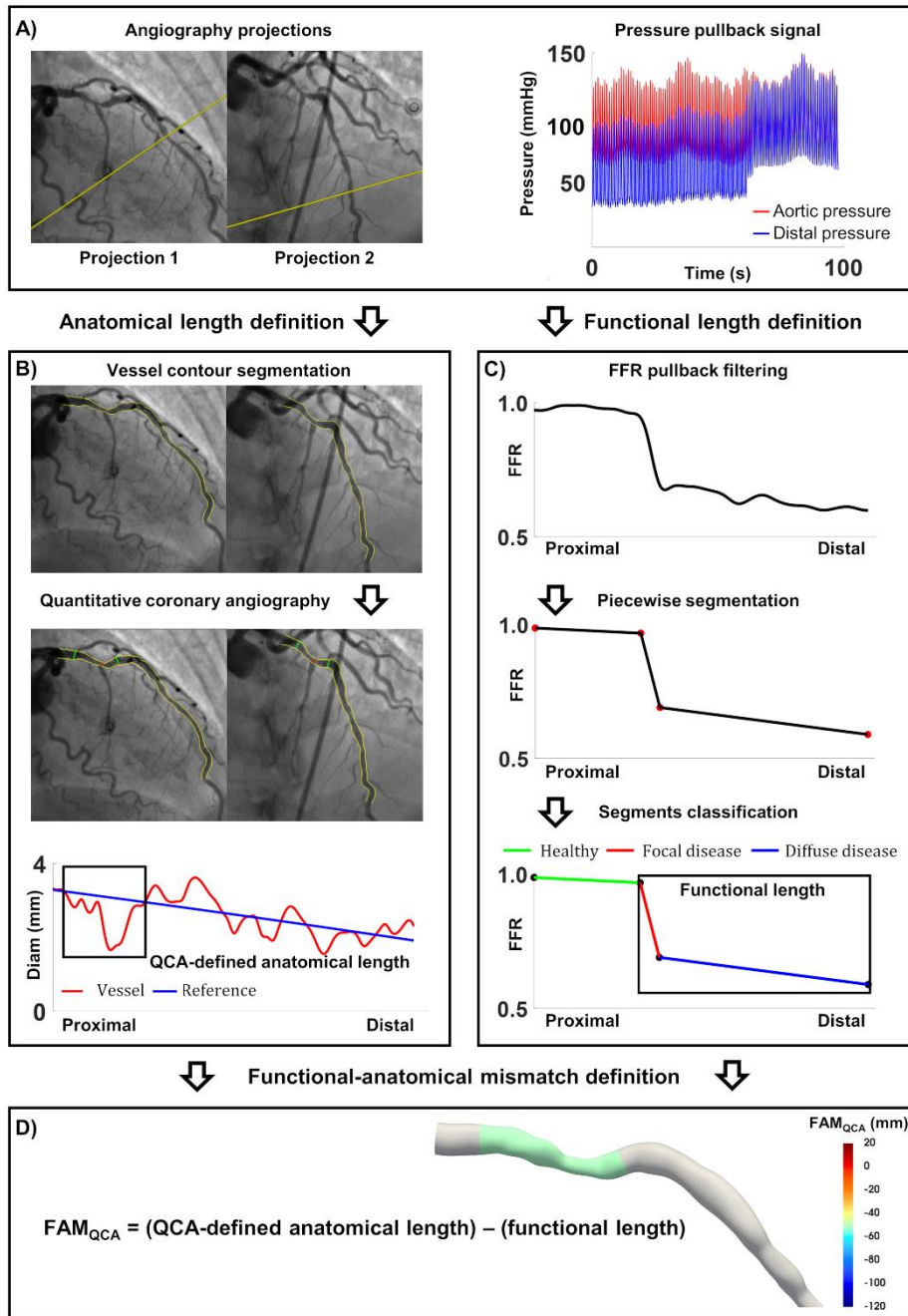


Figure 6.1. Workflow of the study. Definition of QCA-derived anatomical lesion length, functional lesion length and functional-anatomical mismatch (FAM_{QCA}). A): The QCA-derived anatomical lesion length was obtained starting from two angiographic projections for each target lesion. B): 3D quantitative coronary angiography algorithm was used to obtain the QCA-derived anatomical lesion length as the distance where the reference diameter line intersects with the curve describing the local vessel diameter value. C): The functional lesion length was obtained from analysis of the FFR pullback curve after smoothing and piece-wise linearization as the sum of the segments characterized by FFR deterioration. D): The FAM_{QCA} is defined as the difference between the QCA-derived anatomical lesion length minus the functional lesion length.

6.2.3 Optical Coherence Tomography

Examinations were performed using the OPTIS™ OCT systems (Abbott Vascular). OCT pullbacks at 36mm/s were acquired before pre-dilation if feasible. Stent diameter selection was based on the distal reference mean external elastic lamina (EEL)-based diameters rounded down to the nearest available stent size (usually in 0.25 mm increments) to determine stent diameter. If the EEL could not be adequately visualized, the stent diameter is chosen using the mean lumen diameter at the distal reference rounded up to the next stent size. Optimization of the device was performed based on OCT at operator discretion. OCT-derived anatomical lesion length expressed in millimeters was defined as the distance between the proximal and distal reference segments using the OCT automated lumen detection feature²⁵⁷.

6.2.4 Intracoronary pressure measurement and FFR pullback curve analysis

Fractional flow reserve (FFR) measurements were performed with the PressureWire X (Abbott Vascular, Chicago, IL, USA) that was connected to a motorized pullback device at a speed of 1 mm/s (R 100, Philips Volcano, San Diego, Ca, USA). Pressure pullback measurements were acquired at a sampling frequency of 100 Hz. A continuous intravenous adenosine infusion was given at a dose of 140 µg/kg/min via a peripheral or central vein to obtain steady-state hyperemia for at least 2 min²⁵³. The position of the pressure sensor was recorded with a contrast injection to identify the pullback initial position for co-registration purposes. In cases undergoing PCI, FFR measurements were repeated at the same anatomical location. FFR gain was defined as FFR post-PCI minus FFR pre-PCI. If FFR drift (>0.03) was observed, the FFR pullback was repeated.

The FFR curve along the vessel axis was reconstructed by applying a moving average filter with a window size of 10 s, followed by an infinite impulse response low pass elliptic filter (0.1 Hz cutoff frequency) for smoothing (**Figure 6.1C**). An automatic algorithm was developed for functional length quantification from FFR curves. The first step of the algorithm consisted in the piece-wise linearization of each FFR curve

(**Figure 6.1C**) by applying an automated change-points detection algorithm based on a penalized parametric global method. The implemented approach leads to a piece-wise linearization of FFR pullback curves based on a change points detection problem, where a change point is defined as a sample of the acquired FFR pullback curve at which an attribute of the curve suddenly changes.

Technically, a parametric global method already proposed elsewhere²⁵⁸ was implemented here in MATLAB environment (MathWorks, Natick, MA, US) for FFR pullback change points identification. The steps of the implemented algorithm leading to a single change point detection are the following:

1. the FFR pullback curve is divided into two segments.
2. On each segment, the empirical estimation of the statistical property of interest is computed.
3. On each point of each segment the deviation from the empirical estimation is computed.
4. The total residual error is obtained by summation of deviations of segments points.
5. The location of the change point is identified iteratively minimizing the cost function represented by the total residual error.

The problem expressed by points 1-5 can be translated into an algorithm as explained in the followings. Given a generic FFR pullback curve, $FFR = (FFR_1, FFR_2, \dots, FFR_N)$, where FFR_i is the FFR value at i -th sample of the curve and N the total number of samples, the problem consists in finding the k -th sample minimizing the cost function:

$$J(k) = \sum_{i=1}^{k-1} \Delta(FFR_i; \chi([FFR_1 \dots FFR_{k-1}])) + \sum_{i=k}^N \Delta(FFR_i; \chi([FFR_k \dots FFR_N])) \quad (6.1)$$

where χ is the empirical estimation of the statistical property of interest and Δ is the deviation measure. Since we are interested in highlighting changes in average value and slope along the FFR pullback curve, here a linear function was adopted as statistical property of interest. This is like to say that for a generic interval between points m and n along the FFR pullback

curve (**Figure 6.2**), the terms at the right-hand side of equation 6.1 can be expressed as:

$$\sum_{i=m}^n \Delta(\text{FFR}_i; \chi([\text{FFR}_m \dots \text{FFR}_n])) = (n - m + 1) \text{var}([\text{FFR}_m \dots \text{FFR}_n]) - \frac{(\sum_{i=m}^n (\text{FFR}_i; \mu([\text{FFR}_m \dots \text{FFR}_n])) (i - \mu([\text{FFR}_m \text{FFR}_{m+1} \dots \text{FFR}_n]))^2}{(n - m + 1) \text{var}([\text{FFR}_m \text{FFR}_{m+1} \dots \text{FFR}_n])} \quad (6.2)$$

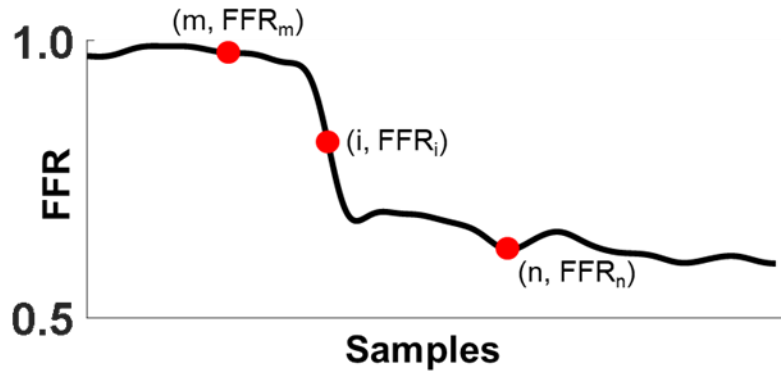


Figure 6.2. FFR pullback curve. Explanatory case of FFR pullback curve with the generic points (m, FFR_m) , (i, FFR_i) and (n, FFR_n) .

A generic FFR pullback curve might have several change points, the number of change points being unknown a priori. Since adding change points decreases the residual error, the overfitting of the FFR curve is avoided by adding a penalty term which is a linear function of the number of change points to the cost function, which can be expressed as²⁵⁹:

$$J(C) = \sum_{r=0}^C \sum_{i=k_r}^{k_{r+1}-1} \Delta(x_i; \chi([\text{FFR}_{k_r} \dots \text{FFR}_{k_{r+1}-1}])) + \beta C \quad (6.3)$$

where k_r and k_c are the first and the last sample of the FFR pullback curve, respectively, C is the number of change points, and β is the fixed penalty term (set equal to 0.1 in this study). The minimization of the cost function was obtained implementing an algorithm based on dynamic programming with early abandonment²⁵⁸.

Once the piece-wise linearization of FFR pullback curve has been carried out, each linearized segment of the curve was then characterized by two quantities (**Figure 6.3**): the FFR drop, defined as the difference between the FFR values at the distal and at the proximal point of the segment and the

segment length, defined as the distance along the vessel axis between the distal point of the segment and the proximal point of the segment. On each segment a third quantity, the segment slope, was defined as the ratio between FFR drop and segment length.

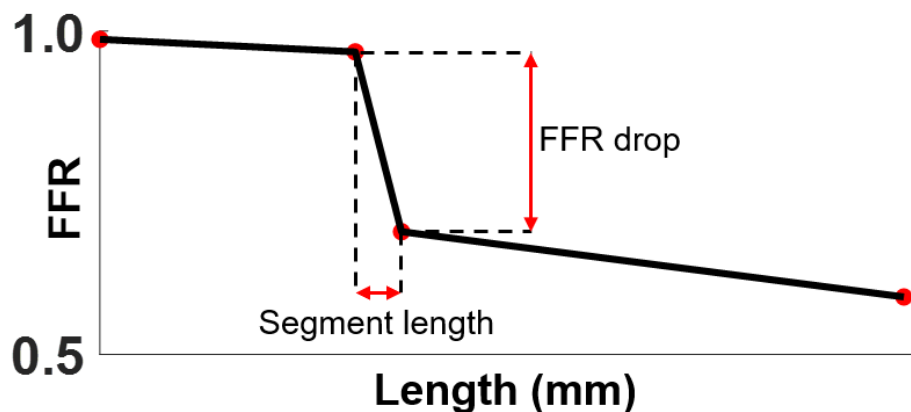


Figure 6.3. linearized FFR pullback curve. Explanatory case of piece-wise linearized FFR pullback curve with a graphical explanation of FFR drop and segment length.

The second step of the algorithm consisted in the automatic classification of the linearized FFR curve segments as *healthy* segments (i.e., without FFR deterioration), *focal* or *diffuse* disease segments (**Figure 6.1C**), based on their length and the associated FFR drop.

Two cohorts were defined to develop and validate the part of the algorithm performing automatic FFR segments classification. The derivation cohort consisted of patients with CAD defined as distal FFR < 0.90. For this cohort, only baseline (i.e., pre-PCI) FFR pullbacks were included. These were selected in a consecutive fashion from all patients included in the registry. The validation cohort included subsequent patients with CAD defined as a distal FFR ≤ 0.80 who underwent OCT-guided PCI and FFR measurement after stent implantation.

Two independent observers (observer 1 and observer 2) adjudicated by visual inspection each segment of the piece-wise linearized of FFR pullback curve as belonging to one of five segment phenotypes:

1. *healthy* segment.
2. *Focal* disease segment
3. *Diffuse* disease segment.
4. *Pressure recovery* segment.
5. *Artifact*.

The visual adjudication of the derivation cohort (81 patients, 216 segments) was used to develop the automatic classifier, based on a two-variables logistic regression. The two independent variables considered for the logistic regression were the length of the linearized segment and the associated FFR drop. Technically, the logistic regression model was built on segments which obtained the same adjudication from the two observers (216 segments), while segments manually classified as artefacts were not considered. Two independent variables were considered in the logistic regression model to discriminate the segments: FFR drop and segment length.

Since the logistic regression provides a binary separation, a two-steps approach was implemented for the piece-wise linearized FFR pullback curve segments automatic adjudication:

1. separation between *healthy* and all (grouping focal and diffuse) diseased segments.
2. separation between *focal* and *diffuse* diseased segments.

In the *healthy* segment phenotype, pressure recovery segments were identified as the ones meeting all the following criteria: they have a positive FFR drop, they are contiguous to a diseased segment, and they are shorter than 20 mm.

The performance of the automatic adjudication was evaluated by comparison with the manual adjudication by the two observers on piece-wise linearized FFR pullback curves belonging to the validation cohort (50 patients, 179 segments).

Functional length of CAD, expressed in millimeters, was defined as the length of the pressure pull-back curve with FFR deterioration. To calculate

functional length, an automatic piece-wise linearization and classification of the FFR curve segments was developed. In detail, the functional length of disease for each coronary artery was obtained as the summation of the length of all linearized FFR curve segments classified as diseased by the algorithm. In the presence of serial or multiple lesions (i.e., functionally diseased segments separated by functionally *healthy* segments), the functional length was considered as the sum of all (i.e., contiguous, and non-contiguous) diseased segments.

6.2.4 Functional-anatomical mismatch (FAM)

The difference between the anatomical and the functional length of CAD was defined as Functional Anatomical Mismatch (FAM) (**Figure 6.1D**). This quantity allows identifying two lesion endotypes:

1. functional disease circumscribed within the anatomical defined lesion (i.e., $FAM > 0$).
2. Functional disease extending beyond the anatomical defined lesion ($FAM < 0$).

A positive FAM represents focal CAD where the functional length of disease is restricted to the lesion length, whereas a negative FAM value points to the presence of functional disease outside the anatomical lesion.

As the anatomical length of CAD can be derived from QCA or OCT, two FAM values were calculated, namely FAM_{QCA} and FAM_{OCT} (**Figure 6.4**). In addition, the proportion of pressure loss contained within the anatomical lesion defined the FFR drop attributable to the QCA or OCT-derived anatomical lesion relative to the FFR drop of the entire vessel (i.e., FFR drop within QCA or OCT lesion, respectively).

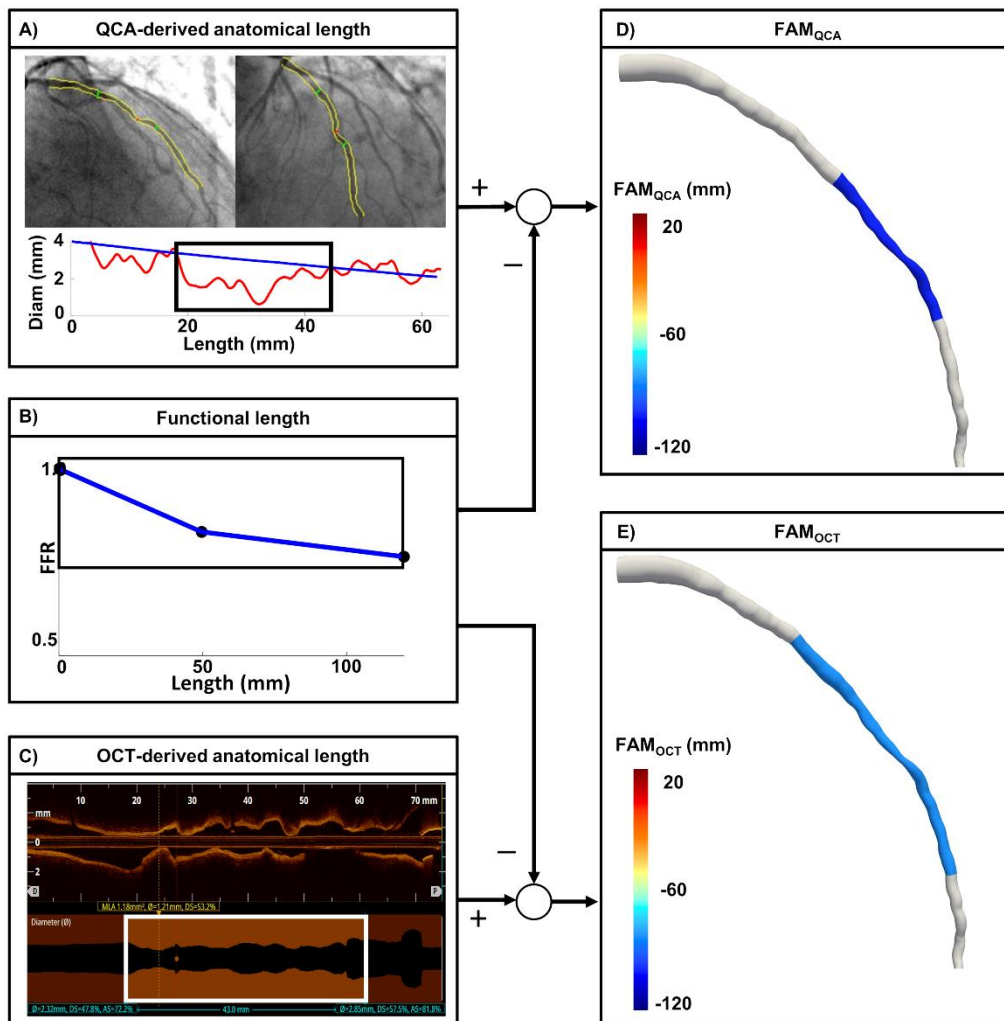


Figure 6.4. Angiography-derived vs. OCT-derived FAM. FAM Definition of QCA-derived anatomical length, OCT-derived anatomical length, FAM_{QCA} , and FAM_{OCT} . An example of vessel with functional diffuse disease is considered. FAM_{QCA} is defined as the difference between QCA-derived anatomical length (panel A) and functional length (panel B) while FAM_{OCT} is defined as the difference between OCT-derived anatomical length (panel C) and functional length (panel B). The anatomical lesion derived from QCA or OCT is represented on the 3D geometric vessel reconstruction and color-coded using FAM_{QCA} or FAM_{OCT} (panels D and E, respectively). In both cases, functional lesion length is longer than anatomical lesion length (i.e., negative FAM).

6.2.5 Procedure guidance and results

PCI was performed following standard of care guided by FFR and OCT, both executed before and after stent implantation. Intraprocedural PCI guidance or stent optimizations based on either physiology or imaging were left at operator's discretion. New generation DES were used in all cases. To

quantify the impact of PCI, the relative functional gain was defined as post PCI FFR minus pre-PCI FFR divided by 1 – pre-PCI FFR.

6.2.6 Statistical analysis

Continuous data are presented as mean (\pm SD) or median [25th – 75th percentiles]. Categorical data are presented as counts and proportions (%). Differences were evaluated using the univariate Mann–Whitney non-parametric U test. Spearman’s correlation coefficients were calculated to assess the relationship between FAM and post-PCI FFR. Agreement between observers was assessed by the intraclass correlation coefficient (ICC). The optimal cutoff values of FAM to predict relative functional gain were calculated using receiver operating characteristic (ROC) curves. The discriminant ability of FAM value to predict optimal post-PCI physiologic results was evaluated with area under curve (AUC). Optimal relative functional gain was defined as an increase in epicardial conductance greater than 50%.

6.3 Results

Clinical characteristics of patients are shown in **Table 6.1**. Overall, 117 patients (131 vessels) were included: 71 patients (81 vessels) in the derivation cohort and 48 patients (50 vessels) in the validation cohorts.

Table 6.1 Baseline clinical characteristics of the study population

| | All | Derivation Cohort | Validation Cohort |
|--|-----------------|-------------------|-------------------|
| Patients, n | 117 | 69* | 48 |
| Vessels, n | 131 | 81 | 50 |
| Age, mean \pm SD | 66.9 \pm 9.84 | 68.2 \pm 9.6 | 64.7 \pm 9.9 |
| Sex, male, n (%) | 86 (73.5) | 52 (73.2) | 36 (75.0) |
| BMI, kg/m ² , mean \pm SD | 26.8 \pm 3.53 | 26.7 \pm 3.52 | 26.8 \pm 3.32 |
| Hyperlipidemia, n (%) | 94 (80.3) | 57 (80.3) | 38 (79.2) |
| Hypertension, n (%) | 63 (53.8) | 36 (50.7) | 29 (60.4) |
| Diabetes Mellitus, n (%) | 26 (22.2) | 17 (23.9) | 9 (18.8) |
| Current smoking, n (%) | 20 (17.1) | 12 (16.9) | 9 (18.8) |
| Family history, n (%) | 17 (14.5) | 10 (14.1) | 8 (16.7) |
| Previous stroke, n (%) | 3 (2.6) | 3 (4.2) | 0 (0) |
| Prior PCI, n (%) | 32 (27.4) | 28 (39.4) | 4 (8.3) |

| | | | |
|----------------------------------|-----------------|-----------------|-----------------|
| LVEF, %, mean \pm SD | 58.0 \pm 8.06 | 58.1 \pm 9.28 | 58.0 \pm 5.57 |
| Creatinine, mg/dl, mean \pm SD | 0.98 \pm 0.22 | 0.99 \pm 0.24 | 0.96 \pm 0.18 |
| Symptomatic, n (%) | 91 (77.8) | 50 (70.4) | 43 (89.6) |
| Angina Class, CCS, n (%) | | | |
| 1 | 26 (28.6) | 15 (30.0) | 11 (25.6) |
| 2 | 61 (67.0) | 32 (64.0) | 31 (72.1) |
| 3 | 4 (4.4) | 3 (6.0) | 1 (2.3) |
| 4 | 0 (0) | 0 (0) | 0 (0) |

* In two patients, two vessels were analyzed, and one underwent PCI. For patient level characteristic these were included in the validation cohort. PCI Percutaneous coronary interventions, CCS Canadian classification society, LVEF Left ventricular ejection fraction, BMI Body mass index, SD Standard deviation.

In the validation cohort, QCA and OCT lesion lengths were available for 50 and 36 vessels, respectively (**Table 6.2**). FFR motorized pullbacks pre and post PCI were available in all cases.

6.3.1 FFR pullback curve automatic classifier

Anatomical, functional, and procedural characteristics of the derivation and validation cohort are presented in **Table 6.2**.

Table 6.2 Anatomical, functional, and procedural characteristics

| | All | Derivation Cohort | Validation Cohort |
|--|-----------------|-------------------|-------------------------|
| Target vessel, n (%) | | | |
| LAD | 99 (75.6) | 57 (70.4) | 42 (84.0) |
| LCX | 9 (6.9) | 6 (7.4) | 3 (6.0) |
| RCA | 23 (17.6) | 18 (22.2) | 5 (10.0) |
| Serial lesion, n (%) | 17 (13.0) | 9 (11.1) | 8 (16.0) |
| QCA-derived anatomical lesion length (mm), median [25th – 75th percentile] | NA | NA | 16.05[11.40 – 22.05] |
| OCT-derived anatomical lesion length (mm), median [25th – 75th percentile] | NA | NA | 28.00[16.63 – 38.00] |
| MLD (mm), median [25th – 75th percentile] | NA | NA | 1.34 [1.23 – 1.48] |
| DS (%), median [25th – 75th percentile] | NA | NA | 53.00[47.25 – 59.50] |
| RVD (mm), median [25th – 75th percentile] | NA | NA | 2.95 [2.57 – 3.20] |
| Functional lesion length (mm), median [25th – 75th percentile] | NA | NA | 67.12[25.38 – 91.37] |
| FAM _{QCA} (mm), median [25th – 75th percentile] | NA | NA | -47.59 [-73.22 – -8.08] |
| FAM _{OCT} (mm), median [25th – 75th percentile] | NA | NA | -37.47[-64.29 – -8.98] |
| Pre PCI FFR, median [25th – 75th percentile] | 0.78[0.71–0.86] | 0.82[0.73 – 0.88] | 0.74[0.67 – 0.77] |
| PCI, number | NA | NA | 54 |
| Stent per vessel, n (%) | NA | NA | 1.00 [1.00, 1.00] |

| | | | |
|---|----|----|---------------------|
| Stent length (mm) | NA | NA | 27.45 ± 11.52 |
| Stent diameter (mm) | NA | NA | 3.05± 0.43 |
| Post dilatation, n (%) | NA | NA | 46 (85.2) |
| OCT-guided PCI, n (%) | NA | NA | 42 (84.0) |
| MSA (mm ²), median [25th – 75th percentile] | NA | NA | 5.66[4.33 – 6.45] |
| Residual DS (%), median [25th – 75th percentile] | NA | NA | 7.00 [2.00 – 12.00] |
| Acute gain | NA | NA | 1.34 ± 0.54 |
| Post PCI FFR, median [25th – 75th percentile] | NA | NA | 0.86 [0.82 – 0.89] |
| Relative functional gain, median [25th – 75th percentile] | NA | NA | 0.49 [0.30 – 0.62] |

LAD left anterior descending artery. LCX left circumflex artery. RCA right coronary artery. FAM functional anatomical mismatch. PCI percutaneous coronary interventions. MLD minimal lumen diameter. QCA quantitative coronary angiography. FFR fractional flow reserve. DS diameter stenosis. OCT optical coherence tomography. RVD reference vessel diameter. NA not available.

From the FFR curves, 431 segments were extracted. In detail, 151 (observer 1) and 156 (observer 2) segments were visually assessed as healthy, 101 (observer 1) and 106 (observer 2) as focal disease, 146 (observer 1) and 147 (observer 2) as diffuse disease (**Figure 6.5**). In the validation cohort, the automatic classifier provided an excellent discrimination ability between *healthy* and *diseased* segments (AUC was 0.97, 95% CI 0.94 to 0.99 for observer 1, and 1.00, 95% CI 0.98 to 1.00 for observer 2). Concerning differentiation between *focal* and *diffuse*, the discriminatory capacity was also excellent (AUC was 0.93, 95% CI 0.86 to 0.97 for observer 1, and 0.96, 95% CI 0.91 to 0.99 for observer 2). The inter-observer agreement for the visual evaluation of the FFR curve was moderate (ICC 0.66, 95% CI 0.60 to 0.71), whereas the reproducibility for the automatic algorithm was excellent because the algorithm is based on a deterministic approach.

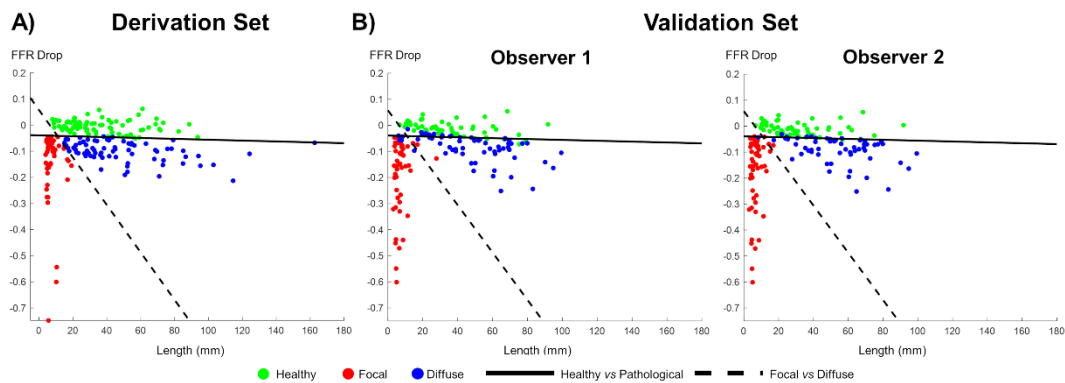


Figure 6.5. Automatic classifier visual performances. Development and performance of the automatic classifier. Healthy, focal disease and diffuse disease segments (green, red, and blue, respectively) in length vs. FFR drop plane. The visual adjudication by two independent observers (observer 1 and observer 2) in the derivation set was used to develop the automatic classifier able to discriminate among healthy, focal disease and diffuse disease segments (panel A). The automatic classifier was then applied to the validation set (panel B). The performance of the classifier was evaluated by comparing with the visual adjudication by the two independent observers.

More in detail, the ability of the proposed automatic adjudication method in discriminating *healthy*, *focal*, and *diffuse* disease segments clearly emerges (**Figure 6.6A**). Concerning the adjudication of *healthy vs. diseased* segments (**Figure 6.6B**), the automatic adjudication provided an excellent performance in terms of accuracy (87.7% for observer 1, 94.6% for observer 2) sensitivity (87.2% for observer 1, 92.8% for observer 2) and specificity (88.7% for observer 1, 98.2% for observer 2, respectively). Concerning the adjudication of *focal vs. diffuse* disease, (**Figure 6.6C**) the automatic adjudication performance was also outstanding in terms of accuracy (94.6% for observer 1, 96.4% for observer 2), sensitivity (91.9% for observer 1, 98.3% for observer 2) and specificity (93.6% for observer 1, 94.3% for observer 2).

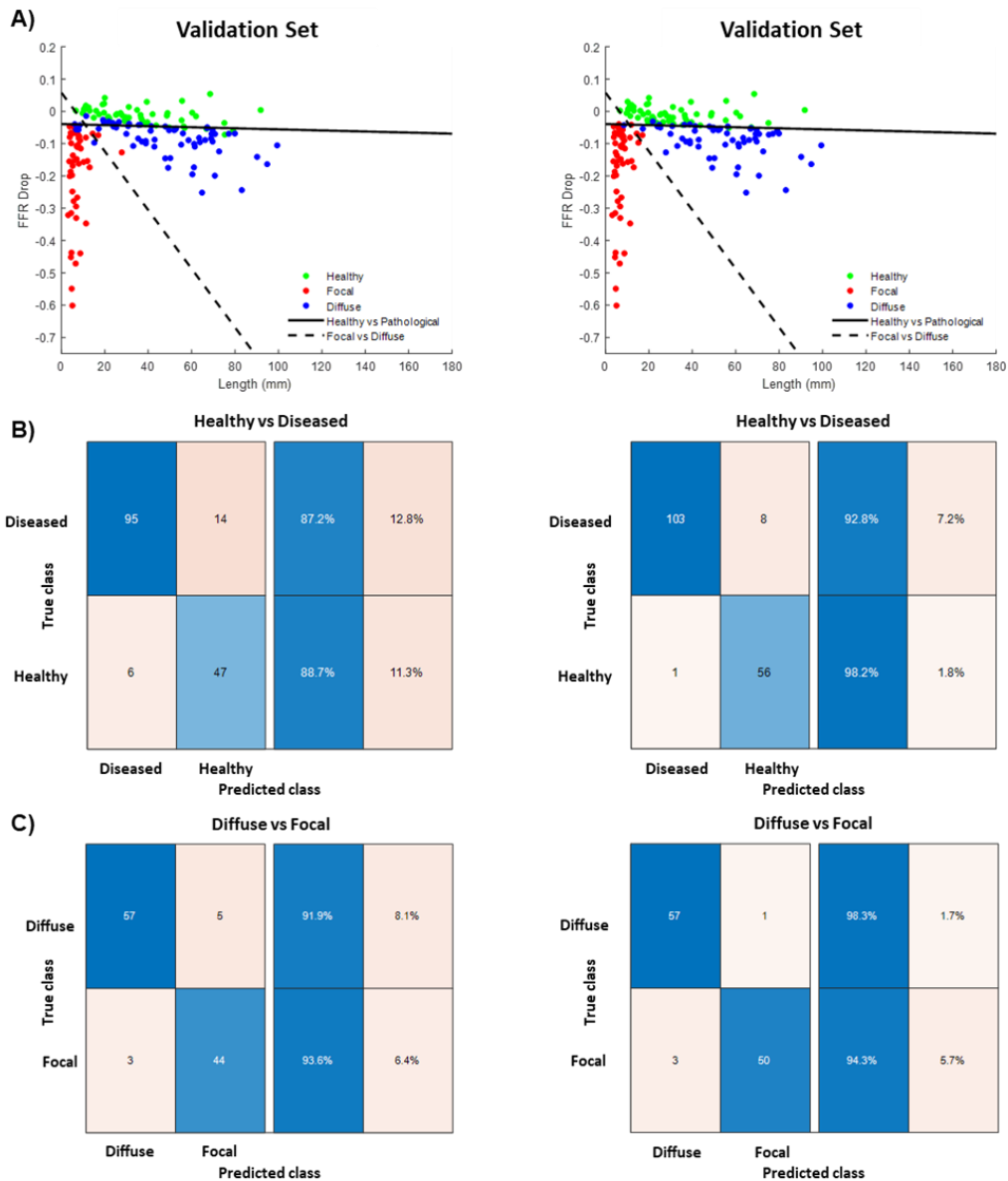


Figure 6.6. Automatic classifier performance analysis. Results on the left are relative to observer 1, on the right to observer 2. Panel A: Healthy, focal disease and diffuse disease segments (respectively, green, red, and blue) in length vs. FFR drop plane for the validation set. Panel B: confusion matrices of the classification healthy vs pathological segments. Panel C: confusion matrices of the classification focal vs diffuse disease segments.

6.3.2 Functional anatomical mismatch

PCI was performed in 50 vessels included in the validation cohort. Pre-PCI FFR was 0.74 [0.67 – 0.77] and diameters stenosis was 53.0 % [47.25 – 59.50]. Anatomical CAD length derived from QCA was 16.05 mm [11.40 –

22.05], anatomical CAD length derived from OCT was 28.0 mm [16.63 – 38.0] and functional CAD length was 67.12 mm [25.38 – 91.37] ($p < 0.001$). No correlation emerged between the extent of CAD derived from QCA and FFR pullback ($r = 0.124$, 95% CI 0.168 to 0.396, $p = 0.390$, **Figure 6.7A**). OCT-derived anatomical lesion length was correlated with functional CAD length ($r = 0.469$, 95% CI 0.156 to 0.696, $p = 0.004$, **Figure 6.7B**).

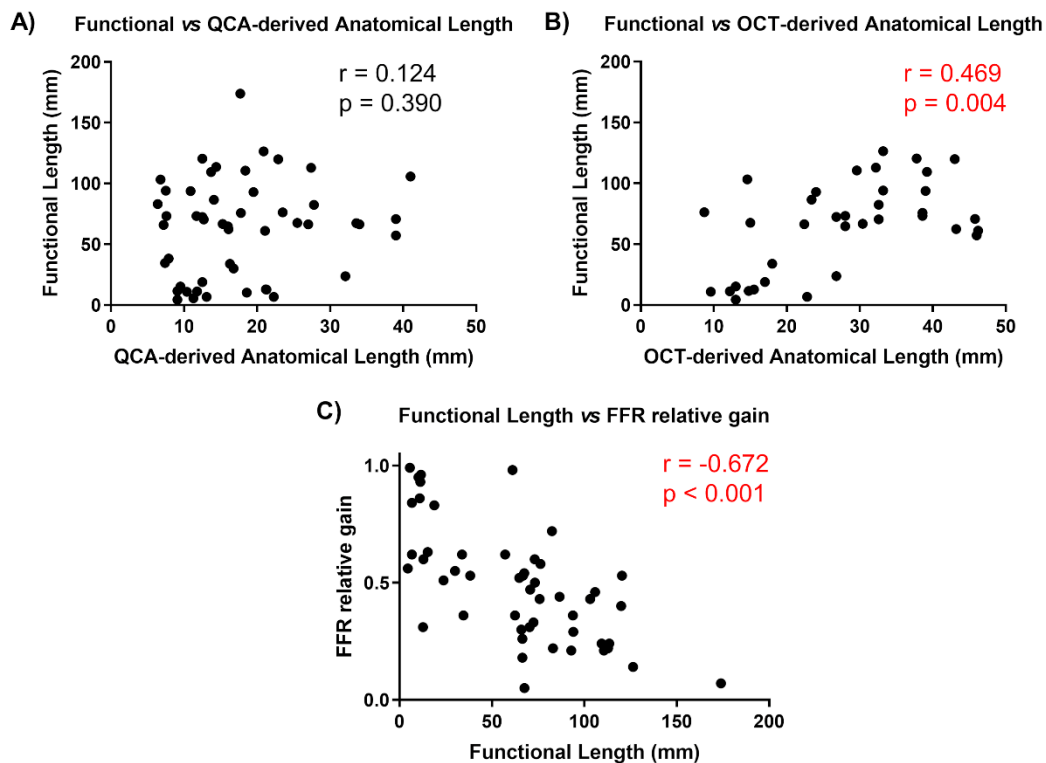


Figure 6.7. Functional-anatomical length correlations. Scatter plots illustrating the correlations among functional length and QCA-derived anatomical length, OCT-derived anatomical length and FFR relative gain. The QCA-derived anatomical length was not correlated with functional length (panel A). The OCT-derived anatomical length was correlated with the functional length (panel B). The functional disease length was inversely correlated with the FFR relative gain (panel C).

Mean stent length was 27.45 ± 11.52 mm. Mean post-PCI FFR was 0.86 [0.82 – 0.89]. An explanatory example visualizing vessels with positive and negative FAM that underwent PCI and post-PCI FFR measurement is presented in **Figure 6.8**. FAM_{QCA} was -47.59 [-73.22 – -8.08] mm and FAM_{OCT} was -37.47 [-64.29 – -8.98] mm ($p = 0.446$). The length of functional CAD was inversely correlated with relative functional gain ($r = -0.672$, 95%

CI -0.804 to -0.478, $p < 0.001$, **Figure 6.7C**) i.e., the longer the functional disease, the lesser the improvement in FFR with PCI.

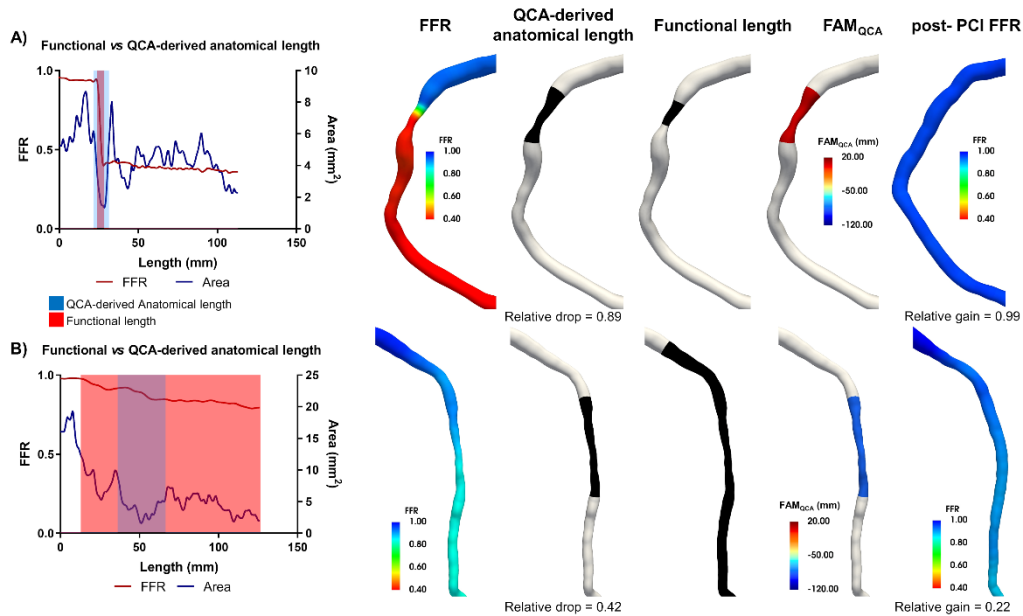


Figure 6.8. FAM three-dimensional visualization: explanatory cases. Positive vs. negative FAM_{QCA}. A): example of vessel with positive FAM_{QCA}, where the QCA-derived anatomical lesion length is longer than the functional lesion length, respectively blue and red shade in the area and FFR curves (left panel). From left to right, FFR is displayed as a color-coded map on the 3-dimensional geometric reconstruction of the vessel. The extension of the anatomical and functional length is displayed in black, with indication of the relative FFR drop within the QCA-derived anatomical lesion. FAM_{QCA} is displayed as a color-coded map: the red color underlines that the functional disease was circumscribed within the anatomical lesion. The percutaneous coronary intervention (PCI) restored epicardial conductance and resulted in high post-PCI FFR (right panel), with a relative gain equal to 0.99. B): example of vessel with negative FAM_{QCA}, where the anatomical lesion length is shorter than the functional lesion length, respectively blue and red shade in the area and FFR curves (left panel). From left to right, FFR is displayed as a color-coded map on the 3-dimensional geometric reconstruction of the vessel. The extension of the anatomical and functional length is displayed in black, with indication of the relative FFR drop within the anatomical lesion. FAM_{QCA} is displayed as a color-coded map: the blue color underlines that the functional disease extended beyond the anatomical lesion. The percutaneous coronary intervention (PCI) resulted in minor improvement of epicardial conductance and a low post-PCI FFR (right panel), with a relative gain equal to 0.22.

A strong association emerged between FAM_{QCA} and FFR relative gain after PCI ($r=0.647$, 95% CI 0.443 to 0.788, $p < 0.001$, **Figure 6.9A**), as well as between FAM_{OCT} and FFR relative gain after PCI ($r=0.630$, 95% CI 0.372 to 0.798, $p < 0.001$, **Figure 6.9B**). Patients in whom functional disease was confined within the anatomical lesion (i.e., FAM_{QCA} ≥ 0) had the strongest improvement in relative functional gain (FAM_{QCA} $\geq 0.701 \pm 0.235$ vs. FAM_{QCA} $< 0.441 \pm 0.225$, $p < 0.001$). FAM either derived from QCA or OCT predicted

functional gain (FAM_{QCA} AUC 0.84, 95% CI 0.71 to 0.93, $p < 0.001$ and FAM_{OCT} AUC 1.00, 95% CI 0.93 to 1.00, $p < 0.001$). The best FAM_{QCA} and FAM_{OCT} cut-off values predicting 50% gain in epicardial conductance were -57.64 mm and -37.19 mm, respectively. Percent FFR drops within the anatomical lesions either derived from QCA or OCT were strongly correlated with functional gain ($r = 0.792$, 95% CI 0.655 to 0.879, $p < 0.001$ for QCA and $r = 0.789$, 95% CI 0.615 to 0.890, $p < 0.001$ for OCT, **Figure 6.9C-6.9D**).

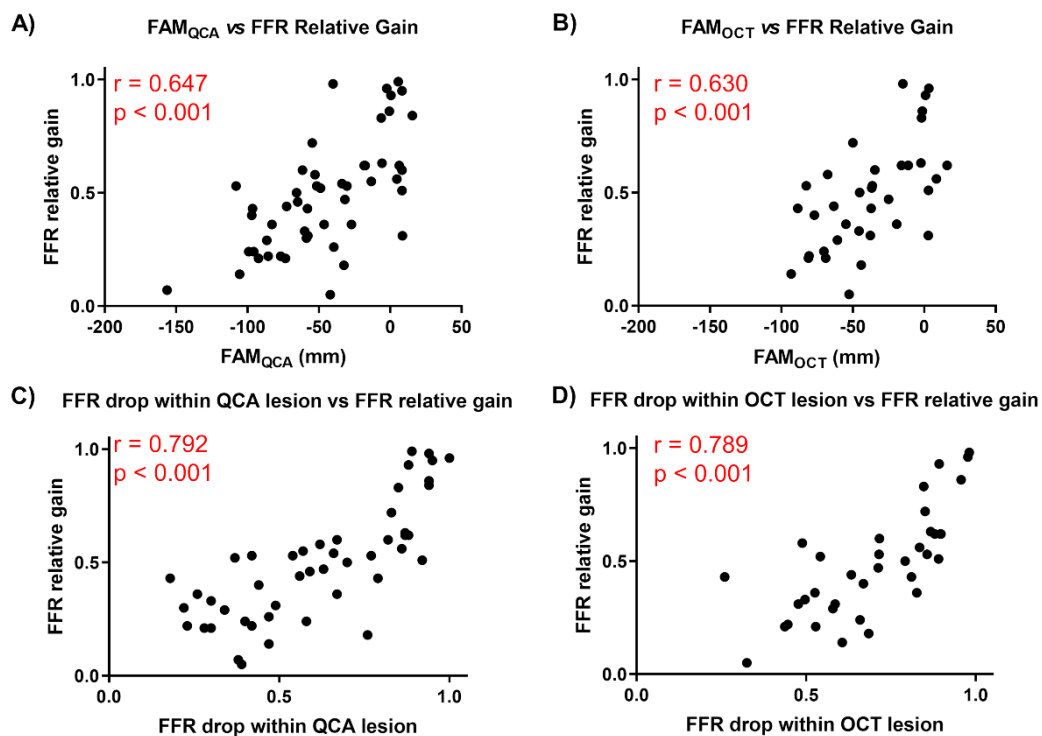


Figure 6.9. FAM correlations. Scatter plots illustrating the correlations among FAM, FFR relative gain and among the FFR drop within the anatomical lesion and FFR relative gain. A direct significant association was found between the FAM_{QCA} and the FFR relative gain after PCI, i.e., the larger the FAM the higher the functional relative gain after PCI (panel A). A direct significant association was also found between the FAM_{OCT} and the FFR relative gain after PCI (panel B). The FFR drop within the QCA-derived anatomical lesion was strongly correlated with the functional relative gain after PCI, i.e., the larger the drop is attributable to the anatomical lesion with respect to the functional lesion, the better the PCI outcome (panel C). The FFR drop within the OCT-derived anatomical lesion was strongly correlated with the functional relative gain after PCI (panel D).

A sensitivity analysis in the sub-group of serial lesions showed similar results (**Figure 6.10**). Sensitivity of FAM_{QCA} and FAM_{OCT} to serial lesions was tested with two approaches: 1) considering only the contiguous segment in functional length

definition and 2) excluding serial lesions from the analysis. Defining functional length considering only the contiguous segment both FAM_{QCA} and FAM_{OCT} are still correlated with FFR relative gain after PCI ($r=0.606$, 95% CI 0.387 to 0.760, $p<0.001$, **Figure 6.10A** and $r=0.560$, 95% CI 0.326 to 0.729, $p<0.001$, **Figure 6.10C**). Excluding serial lesions (10 cases excluded for QCA and 8 cases excluded for OCT) both FAM_{QCA} and FAM_{OCT} are still correlated with FFR relative gain after PCI ($r=0.708$, 95% CI 0.502 to 0.838, $p<0.001$, **Figure 6.10B** and $r=0.679$, 95% CI 0.400 to 0.8427, $p<0.001$, **Figure 6.10D**).

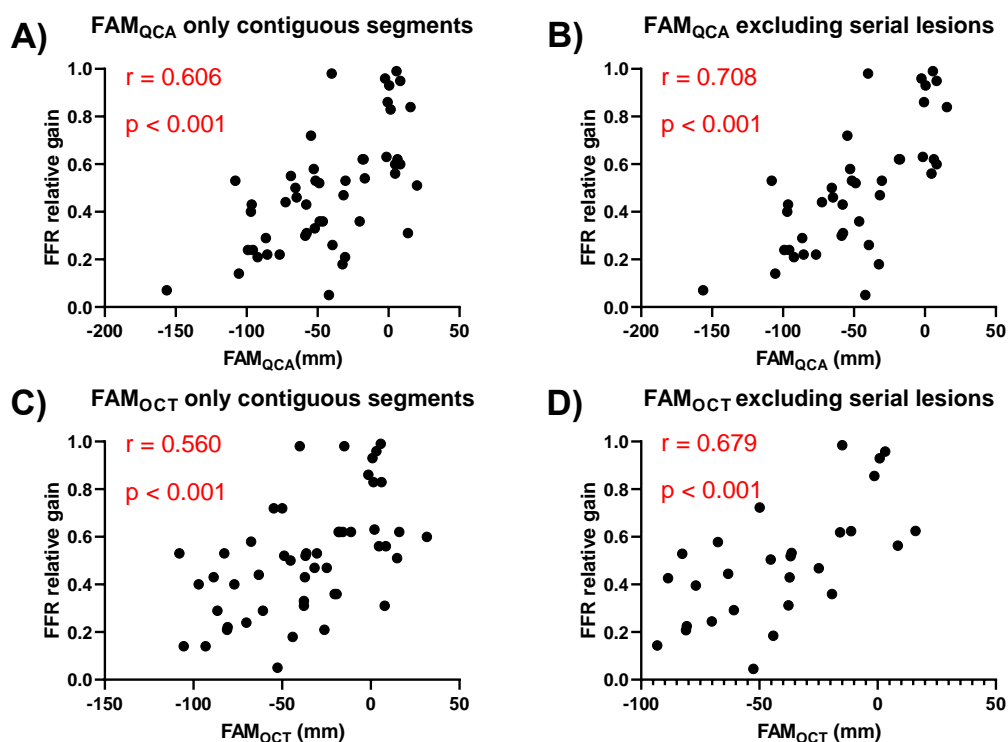


Figure 6.10. FAM sensitivity to serial lesions. Sensitivity analysis to serial lesions of FAM_{QCA} and FAM_{OCT} . Defining functional length considering only the contiguous segment, a direct significant association was found between the FAM_{QCA} and the FFR relative gain after PCI (panel A) and between the FAM_{QCA} and the FFR relative gain after PCI (panel C). Excluding serial lesions from analysis a direct significant association was found between the FAM_{QCA} and the FFR relative gain after PCI (panel B) and between the FAM_{QCA} and the FFR relative gain after PCI (panel D).

6.4 Discussion

The present study describes a novel approach for the quantification of the extension of functional CAD. This allowed to determine the mismatch in the extent of CAD between anatomical and physiological invasive evaluations

based on angiography, intravascular imaging, and intracoronary hyperemic pressure tracing pullbacks. The main findings can be summarized as:

1. the extent of functional disease derived from FFR pullback curves can be quantified using an automated algorithm.
2. In patients with hemodynamically significant coronary stenosis, lesion length based on QCA, and CAD length based on FFR pullbacks were not correlated. In contrast, CAD length derived from OCT correlated with functional CAD extent.
3. The mismatch between the length of anatomical and functional CAD (i.e., FAM, either derived from QCA or OCT) correlated with the improvement in epicardial conductance after percutaneous revascularization.

The discordance between anatomy and physiology regarding epicardial lesion severity has been widely recognized. In the FAME study, more than one-third of lesions with an angiographic 50% to 70% diameter stenosis demonstrated an FFR ≤ 0.80 whereas one-fifth of lesions with a 71% to 90% angiographic diameter stenosis demonstrated an FFR > 0.80 ²⁶⁰. Disconnection between anatomy and physiology goes beyond the assessment of lesion significance. The length of CAD also differs between anatomical and functional evaluations. In the present study, length of functional disease was greater than its anatomical equivalent either derived from QCA or OCT (i.e., those with FAM <0 , **Figure 6.9**). QCA is based on conventional angiography and identifies CAD length as the extent of the stenotic segment. On the other hand, OCT, possessing higher spatial resolution, derives lesion length from the selection of proximal and distal reference cross-sections without atherosclerotic plaques. Therefore, it is expected that CAD anatomical length derived from OCT will be equal or longer than the QCA-derived length. We observed that the anatomical length of CAD was shorter when derived from QCA compared to the one derived from OCT; still, FFR pullbacks derived CAD length was longer (**Figure 6.9**). This finding highlights the diffuse nature of atherosclerosis when assessed using coronary physiology. Interestingly, CAD extent derived from QCA, and functional length were not statistically correlated, whereas OCT-derived anatomical length and functional length exhibited a

moderate correlation. These results underline the suboptimal guidance offered by QCA in terms of the evaluation of lesion extension and confirms the usefulness of intravascular imaging for attaining functional complete revascularization.

Pressure pullbacks can show two distinct functional CAD endotypes, namely predominant focal or diffuse²⁵⁴. In the focal functional CAD, pressure drops are commonly restricted to anatomical stenosis. In this disease endotype, PCI restores epicardial conductance, results in higher post-PCI FFR, increases the likelihood of relieving patients from angina and is associated with improved clinical outcomes. In contrast, in patients with functional diffuse disease, PCI results in minor improvement in vessel physiology, low post-PCI FFR and higher likelihood of persistent angina²⁶¹. Several novel methods are available to assess the pattern of CAD aiming at predicting the results of PCI in terms of coronary physiology. The pullback pressure gradient (PPG) index (Coroventis Research, Uppsala, Sweden), instant wave-free ratio (iFR) co-registration system (Philips, Best, the Netherlands) and the FFR_{CT} revascularization planner (HeartFlow Inc, Redwood city, USA) are novel approaches that may further personalize clinical decision making and refine revascularization strategies in patients with chronic coronary syndromes^{262,263}. In the present study, we developed a complementary approach to predict the response to PCI by quantifying the extent of functional CAD from FFR pullbacks. The larger the functional length of CAD, the lower the functional gain obtained with PCI and the lower the likelihood of functional revascularization. With the current approach, the length of functional disease is computed based on an automated algorithm classifying the FFR curve segments as healthy or diseased. This approach may be less vulnerable to artefacts in the pullback curves compared to the application of a threshold. Moreover, the FAM concept by incorporating the anatomical length of the disease accounts for the interaction with PCI, thus assessing the functional contribution in the context of the segment to be treated.

Revascularization aims at restoring epicardial conductance to improve myocardial perfusion. Two factors influence the response of epicardial vessels to PCI in terms of coronary physiology: the functional contribution

of the treated lesion to the complete vessel pressure loss, i.e., in other words, the magnitude of the FFR curve step-up within the lesion relative to the overall reduction of FFR in the vessel and the presence of pressure losses outside the treated segment. FAM quantifies the mismatch between the anatomical and functional CAD length thereby stressing the impact of residual pressure losses outside the treated region on post PCI physiology. Moreover, the FAM approach is based on the presence and length of disease rather than on the magnitude of pressure drops, making this approach less influenced by the interaction in cases of serial lesions. Furthermore, the functional contribution of the treated lesion, reported in this study as relative FFR drop within the lesion, also correlated with functional gain (**Figure 6.9C-D**). The larger the delta lesion FFR, the larger the functional gain. Altogether, these findings further support pressure pullback strategies to guide PCI as a second level of decision making after the confirmation of hemodynamic lesion significance.

By identifying lesions with negative FAM where the functional extent of CAD is longer than the anatomical CAD, a dilemma is posed upon clinicians. Extending the treated region with longer stents covering the functional disease may improve post-PCI FFR but it may also lead to longer and more stents, which has been associated with higher rates of target vessel failure^{264,265}. Moreover, PCI in vessels with functional diffuse disease has been associated with more periprocedural complications²⁶². Therefore, the assessment of the functional pattern of CAD provides further risk stratification, may improve patient selection for PCI by avoiding stenting lesions without pullback step ups, reduce the risk of peri-procedural myocardial infarction and results in a net clinical benefit from revascularization. It can be hypothesized that patients with negative FAM, i.e., diffuse functional CAD, may be better treated with optimal medical therapy or coronary artery bypass grafting whereas patients with positive FAM are better treated with PCI. Further studies are required to assess the treatment strategies in patients with chronic coronary syndromes and diffuse CAD.

The present study has several limitations. First, the performance of FAM is presented based on its relationship with post PCI FFR and not directly with

clinical outcomes. Nonetheless, post-PCI FFR have identified as an independent predictor of adverse events after PCI. Second, the sample size of the study was relatively small; however, this is one of the most completely evaluated cohorts with motorized FFR pullbacks and OCT pre- and post-PCI. Third, we were able to validate the FAM concept internally; an external validation is still warranted.

6.5 Conclusions

Lesion length assessment differs between morphological and functional evaluations. The morphological functional mismatch in lesion length was frequent, often large, and influenced the results of PCI in terms of coronary physiology. Integration of the extent of pressure losses provides clinically relevant information that may be useful during PCI.

Chapter 7

Conclusions and future works

7.1 Summary and main contributions

The aim of this thesis work concerns the investigation of computational methods and algorithms for the improvement of diagnosis, understanding and treatment of CAD. In detail, the main objectives of this thesis work are listed below:

1. Exploring the potential of endothelial shear stress-based analysis derived from angiographic images as a clinical biomarker to improve the diagnosis of atherosclerotic plaques prone to cause MI. In particular, the analysis was performed using a novel software aiming to make CFD simulations available in a clinical setting focusing on different aspects of WSS vector field.
2. Improve the understanding of the relationship between cellular pathways, plaque morphology and endothelial shear stress.
3. Provide a quantification of the budget of uncertainty associated to inflow BCs focusing on the impact of inflow velocity profile shape and of the technique used to estimate the flow rate in coronary arteries to reliably translate CFD simulations in clinical practice.
4. Redefine the concept of diseased length in coronary arteries, to improve PCI analyzing the hyperemic pressure pullback signal to define the CAD functional length and its difference with respect to anatomical length assessed by means of clinical imaging.

In the first part of this thesis work the hemodynamic profile in coronary arteries was investigated by means of CFD simulations to improve the diagnosis and understanding of CAD. The clinical translation of computational hemodynamics is still hampered by:

1. Computational times and technicalities incompatible with clinical practice.
2. Lacking of a full understanding of the link between hemodynamics and adverse clinical events and *in vivo* cellular response to biomechanical stimuli.
3. Uncertainties in CFD obtained results due to necessarily introduced assumptions introduced modelling coronary hemodynamics.

The main contributions of this thesis to address these points are reported below:

Chapter 2 - Risk of Myocardial Infarction based on Endothelial Shear Stress Analysis Using Coronary Angiography

An analysis based on WSS estimated in a clinical setting was performed to improve the discrimination of atherosclerotic plaques prone to cause MI. It was found that WSS estimated with a prototype software (in times compatible with clinical practice (mean computational time equal to 15 minutes), i.e., clinical CFD, is robust enough with respect to expert CFD simulations to discriminate plaques prone to cause MI. Although already used clinical parameters based on anatomy and pressure gradients as well as the classical WSS-descriptor TAWSS resulted predictive for MI, a WSS-based descriptor, analyzing the variability of the expansion/contraction action of WSS vector field on the endothelium, namely the topological shear variation index (TSVI) showed a stronger predictive capacity for MI resulting very promising in the definition of vulnerable plaques.

Chapter 3 - Coronary Artery Plaque Rupture and Erosion: Role of Wall Shear Stress Profiling and Biological Patterns in Acute Coronary Syndromes

Aiming at bridging the gap of understanding of mechanisms underlying plaque erosion and rupture and their link with hemodynamics, a comprehensive analysis based on cellular gene expression, plaque morphology and WSS pattern was performed combining real time PCR, OCT, and CFD simulations. It emerged that different morphologies of atherosclerotic plaques, i.e., stable, eroded, and ruptured plaques show a different gene expression of inflammatory markers (TNF α , ADAMTS13, EDN1, LGALS8). Moreover, different WSS pattern, in terms of low shear area, high shear area, and variability of WSS magnitude were observed among stable, eroded and ruptured plaques. These *in vivo* findings confirm previous *in vitro* observations suggesting that a link between biomechanical stimuli and cellular gene expression exists, improving the understanding of the role of WSS in CAD.

Chapter 4 - Does the inflow velocity profile influence physiologically relevant flow patterns in computational hemodynamic models of left anterior descending coronary artery?

Obtain *in vivo* 3D flow measurements within the clinical framework is a challenging task due to the absence of proper imaging techniques in coronary arteries. This results in uncertainties which could weaken the findings of *in silico* experiments. In absence of a measured 3D velocity profile as a reference the dependence of computational hemodynamics results, in terms of WSS and helicity-based descriptors, on velocity profile shape was assessed comparing different analytical velocity profiles accounting for velocity peak displacement and secondary flows. The findings of this study clearly indicated that the imposition of parabolic velocity profiles as inflow BC is acceptable as long as the results of the proximal vessel segment are not considered, in coronary arteries. As a pragmatic rule of thumb, a conservative estimation of the length of influence of the shape of the inflow velocity profile on coronary local hemodynamics can be given by the theoretical entrance length for cylindrical conduits in laminar flow conditions.

Chapter 5 - Modelling coronary flows: impact of differently measured inflow boundary conditions on vessel-specific computational hemodynamic profiles

The analysis on the impact of inflow BCs in coronary arteries was completed studying the dependence of computational hemodynamic results on the approach adopted for *in vivo* coronary artery blood flow rate assessment. Inflow BCs were derived from four different techniques assessing *in vivo* surrogates of flow rate: continuous thermodilution, intravascular Doppler, frame count-based 3D contrast velocity, and diameter-based scaling law. The impact of inflow BCs on coronary hemodynamics was evaluated in terms of WSS- and helicity-based descriptors. As main findings we report that: (1) coronary flow rate values may differ based on the applied flow derivation technique, as continuous thermodilution provided higher flow rate values than intravascular Doppler and diameter-based scaling law; (2) such intrasubject differences in flow rate values lead to different surface-

averaged values of WSS magnitude and helical blood flow intensity; (3) luminal surface areas exposed to low WSS showed robustness to the flow rate values; (4) descriptors which does not account on WSS magnitude such as normalized WSS, OSI, and TSVI as well as helical flow topological features showed less dependence on inlet flow rate. Although the absence of a clinically applicable gold standard approach prevents a general recommendation for one coronary blood flow rate derivation technique, the findings of this indicate that the inflow BC may impact computational hemodynamic results, suggesting that a standardization would be desirable to provide comparable results among personalized CFD simulations of the coronary hemodynamics.

In the second part of this thesis an *in vivo* measured hemodynamic parameter, i.e., the hyperemic pullback pressure signal, was analyzed to improve the treatment of CAD. The main contribution of this thesis to address this point is reported below:

Chapter 6 - Mismatch between morphological and functional assessment of the length of coronary artery disease

In this study an automatic algorithm was applied to quantify the functional length of diseased coronary arteries aiming to improve CAD treatment foreseeing the result of PCI. The main findings of this study indicate that functional length based on hyperemic pressure pullback signal differs from anatomical lesion either quantified from 3D-QCA or OCT. Moreover, the mismatch between anatomical and functional length, namely the FAM, is well correlated with post-PCI FFR indicating a strong association with the improvement in vessel conductance after PCI. The integration of the extent of pressure losses provides clinically relevant information that may be useful for clinical decision-making concerning revascularization strategy.

7.2 Concluding remarks

Computational hemodynamics and the derived information have resisted translation to the clinic for different reasons.

Firstly, the most reliable method to obtain WSS estimations is based on computational modelling, but: (1) the process of creating a computational hemodynamic model from medical images is still cumbersome, especially if compared to current diagnostic imaging acquisitions; (2) it needs a high computational time or the use of clusters and supercomputers; (3) it still requires highly specialized users; (4) it produces a large amount of information that needs to be synthesized in simple and clinically relevant mechanistic criteria; and (5) it is affected by uncertainties linked to not measured/measurable data, consequently requiring assumptions and idealizations to construct the computational model. These issues have hampered the use of computational hemodynamics in large clinical studies, which in turn would be required to prove the utility of hemodynamic modelling, setting up a vicious cycle.

Second, the current consensus indicates low and oscillatory WSS as the principal hemodynamic factor involved in the initiation and development and the high WSS magnitude in the final stage of vascular disease. However, there are evidence that *“the low/oscillatory shear theory is less robust than commonly assumed”*²⁷. Recent findings report that low and oscillatory WSS is a significant but moderate (at best) and poorly specific predictor of lesions localization^{27,266} or endothelial dysfunction at the early stage²⁶⁷ suggesting that other WSS features may be involved in the atherosclerosis onset, progression, as well as in plaque erosion and rupture.

Overall, as discussed in the previous chapters and summarized in the previous paragraph, the results of the present thesis addressed many of the points reported above, presenting the potential of computational methods and algorithms in the improvement of CAD diagnosis, understanding and treatment with a view on its application in a clinical setting. This would

represent a step forward in the translation of computational tools from research laboratories to the bedside.

7.3 Future works

The promising results of TSVI as a predictor of MI, obtained in a clinical framework, encourages further studies on this topic. Since the presented study was performed on a very strictly selected population, consisting in 80 patients with 188 mild lesions (percent area stenosis lower than 50%), the natural extension of this work involves the inclusion of a higher number of patients with more heterogeneous coronary lesions, to confirm the reported findings. Moreover, the applicability of the adopted framework in a real-world clinical scenario needs to be tested with a perspective study including the on-site measurement of WSS directly in the cathlab.

Another step forward in the understanding of the role of hemodynamics in the prediction of MI consist in the study of the role of helical blood flow. While it was observed an atheroprotective behavior in the early stage of atherosclerosis^{24,72}, due to its link with higher WSS values, its role in a more advanced phase of the pathology need to be clarified.

Given the importance of reducing computational time to obtain reliable WSS values, a key point in its translation as a clinical biomarker, a further improvement on WSS computation in terms of time and accuracy may involve the coupling of CFD with reduced order modeling²⁶⁸ or the use of artificial intelligence (AI) based methods to speed up CFD simulations²⁶⁹ or directly compute WSS from three-dimensional geometry²⁷⁰.

Finally, given the increasing use of CFD simulations or computational algorithms to derive FFR with a less invasive approach at any point of coronary arteries, the virtually computed FFR may be easily used to derive a surrogate measure of functional diseased length extending the use of FAM avoiding the invasive measure of hyperemic pressure pullback signal.

References

1. Pick, B. P. Gray's Anatomy. *Br. Med. J.* **2**, 801 (1958).
2. Cerqueira, M. D. *et al.* Standardized myocardial segmentation and nomenclature for tomographic imaging of the heart: A Statement for Healthcare Professionals from the Cardiac Imaging Committee of the Council on Clinical Cardiology of the American Heart Association. *Circulation* vol. 105 539–542 (2002).
3. Klabunde, E. R. *Cardiovascular Physiology Concepts 2nd Edition. Cardiovascular Physiology Concepts 2nd Edition* (2012).
4. Chatzizisis, Y. S., Giannoglou, G. D., Parcharidis, G. E. & Louridas, G. E. Is left coronary system more susceptible to atherosclerosis than right?. A pathophysiological insight. *International Journal of Cardiology* vol. 116 7–13 (2007).
5. Giannoglou, G. D., Antoniadis, A. P., Koskinas, K. C. & Chatzizisis, Y. S. Difference in the Localisation of Coronary Artery Disease Between the Left and Right Coronary Artery System. *Eur. J. Cardiovasc. Med. I*, (2011).
6. Oskarsson, G., Pesonen, E., Munkhammar, P., Sandström, S. & Jögi, P. Normal coronary flow reserve after arterial switch operation for transposition of the great arteries: An intracoronary Doppler guidewire study. *Circulation* **106**, 1696–1702 (2002).
7. Akasaka, T. *et al.* Comparison of relation of systolic flow of the right coronary artery to pulmonary artery pressure in patients with and without pulmonary hypertension. *Am. J. Cardiol.* **78**, 240–244 (1996).
8. Heller, L. I., Silver, K. H., Villegas, B. J., Balcom, S. J. & Weiner, B. H. Blood flow velocity in the right coronary artery: Assessment before and after angioplasty. *J. Am. Coll. Cardiol.* **24**, 1012–1017 (1994).
9. Eurostat & European Statistical System. Deaths due to coronary heart diseases in the EU - Products Eurostat News - Eurostat.

<https://ec.europa.eu/eurostat/web/products-eurostat-news/-/edn-20200928-1> (2020).

10. Medina-Leyte, D. J. *et al.* Endothelial dysfunction, inflammation and coronary artery disease: Potential biomarkers and promising therapeutical approaches. *International Journal of Molecular Sciences* vol. 22 (2021).
11. Libby, P. Inflammation during the life cycle of the atherosclerotic plaque. *Cardiovascular Research* vol. 117 2525–2536 (2021).
12. Strong, J. P. *et al.* Prevalence and extent of atherosclerosis in adolescents and young adults: Implications for prevention from the pathobiological determinants of atherosclerosis in youth study. *J. Am. Med. Assoc.* **281**, 727–735 (1999).
13. Souilhol, C. *et al.* Endothelial responses to shear stress in atherosclerosis: a novel role for developmental genes. *Nature Reviews Cardiology* vol. 17 52–63 (2020).
14. Baeyens, N., Bandyopadhyay, C., Coon, B. G., Yun, S. & Schwartz, M. A. Endothelial fluid shear stress sensing in vascular health and disease. *Journal of Clinical Investigation* vol. 126 821–828 (2016).
15. Yia-Herttuala, S. *et al.* Evidence for the presence of oxidatively modified low density lipoprotein in atherosclerotic lesions of rabbit and man. *J. Clin. Invest.* **84**, 1086–1095 (1989).
16. Pasterkamp, G., Den Ruijter, H. M. & Libby, P. Temporal shifts in clinical presentation and underlying mechanisms of atherosclerotic disease. *Nature Reviews Cardiology* vol. 14 21–29 (2016).
17. Insull, W. The Pathology of Atherosclerosis: Plaque Development and Plaque Responses to Medical Treatment. *Am. J. Med.* **122**, S3–S14 (2009).
18. Morbiducci, U. *et al.* Atherosclerosis at arterial bifurcations: Evidence for the role of haemodynamics and geometry. *Thromb. Haemost.* **115**, 484–492 (2016).
19. Gijzen, F. *et al.* Expert recommendations on the assessment of wall shear stress in human coronary arteries: existing methodologies, technical considerations, and clinical applications. *Eur. Heart J.* **40**, 3421–3433 (2019).

20. Kwak, B. R. *et al.* Biomechanical factors in atherosclerosis: Mechanisms and clinical implications. *Eur. Heart J.* **35**, 3013–3020 (2014).
21. Morbiducci, U. *et al.* Mechanistic insight into the physiological relevance of helical blood flow in the human aorta: An in vivo study. *Biomech. Model. Mechanobiol.* **10**, 339–355 (2011).
22. Gallo, D., Steinman, D. A., Bijari, P. B. & Morbiducci, U. Helical flow in carotid bifurcation as surrogate marker of exposure to disturbed shear. *J. Biomech.* **45**, 2398–2404 (2012).
23. De Nisco, G. *et al.* The Atheroprotective Nature of Helical Flow in Coronary Arteries. *Ann. Biomed. Eng.* **47**, 425–438 (2019).
24. De Nisco, G. *et al.* The impact of helical flow on coronary atherosclerotic plaque development. *Atherosclerosis* **300**, 39–46 (2020).
25. Ku, D. N., Giddens, D. P., Zarins, C. K. & Glagov, S. Pulsatile flow and atherosclerosis in the human carotid bifurcation. Positive correlation between plaque location and low and oscillating shear stress. *Arteriosclerosis* **5**, 293–302 (1985).
26. Himburg, H. A. *et al.* Spatial comparison between wall shear stress measures and porcine arterial endothelial permeability. *Am. J. Physiol. - Hear. Circ. Physiol.* **286**, 1916–1922 (2004).
27. Peiffer, V., Sherwin, S. J. & Weinberg, P. D. Computation in the rabbit aorta of a new metric - the transverse wall shear stress - to quantify the multidirectional character of disturbed blood flow. *J. Biomech.* **46**, 2651–2658 (2013).
28. Mohamied, Y., Sherwin, S. J. & Weinberg, P. D. Understanding the fluid mechanics behind transverse wall shear stress. *J. Biomech.* **50**, 102–109 (2017).
29. Morbiducci, U. *et al.* A rational approach to defining principal axes of multidirectional wall shear stress in realistic vascular geometries, with application to the study of the influence of helical flow on wall shear stress directionality in aorta. *J. Biomech.* **48**, 899–906 (2015).
30. Arzani, A., Gambaruto, A. M., Chen, G. & Shadden, S. C. Wall shear stress exposure time: a Lagrangian measure of near-wall stagnation and concentration in cardiovascular flows. *Biomech. Model.*

- Mechanobiol.* **16**, 787–803 (2017).
31. Arzani, A. & Shadden, S. C. Wall shear stress fixed points in cardiovascular fluid mechanics. *J. Biomech.* **73**, 145–152 (2018).
 32. Farghadan, A. & Arzani, A. The combined effect of wall shear stress topology and magnitude on cardiovascular mass transport. *Int. J. Heat Mass Transf.* **131**, 252–260 (2019).
 33. Mahmoudi, M. *et al.* The Story of Wall Shear Stress in Coronary Artery Atherosclerosis: Biochemical Transport and Mechanotransduction. *J. Biomech. Eng.* **143**, (2021).
 34. Mazzi, V. *et al.* Wall shear stress topological skeleton analysis in cardiovascular flows: Methods and applications. *Mathematics* vol. 9 720 (2021).
 35. Mazzi, V. *et al.* A Eulerian method to analyze wall shear stress fixed points and manifolds in cardiovascular flows. *Biomech. Model. Mechanobiol.* **19**, 1403–1423 (2020).
 36. De Nisco, G. *et al.* Deciphering ascending thoracic aortic aneurysm hemodynamics in relation to biomechanical properties. *Med. Eng. Phys.* **82**, 119–129 (2020).
 37. Morbiducci, U. *et al.* Wall Shear Stress Topological Skeleton Independently Predicts Long-Term Restenosis After Carotid Bifurcation Endarterectomy. *Ann. Biomed. Eng.* **48**, 2936–2949 (2020).
 38. Mazzi, V. *et al.* Early Atherosclerotic Changes in Coronary Arteries are Associated with Endothelium Shear Stress Contraction/Expansion Variability. *Ann. Biomed. Eng.* **49**, 2606–2621 (2021).
 39. Morbiducci, U., Ponzini, R., Grigioni, M. & Redaelli, A. Helical flow as fluid dynamic signature for atherogenesis risk in aortocoronary bypass. A numeric study. *J. Biomech.* **40**, 519–534 (2007).
 40. Morbiducci, U. *et al.* On the importance of blood rheology for bulk flow in hemodynamic models of the carotid bifurcation. *J. Biomech.* **44**, 2427–2438 (2011).
 41. Gallo, D., Steinman, D. A., Bijari, P. B. & Morbiducci, U. Helical flow in carotid bifurcation as surrogate marker of exposure to disturbed

- shear. *J. Biomech.* **45**, 2398–2404 (2012).
42. Steitieh, D., Sharma, N. & Singh, H. S. How Technology Is Changing Interventional Cardiology. *Current Cardiovascular Risk Reports* vol. 16 1–10 (2022).
 43. Tonino, P. A. L. *et al.* Angiographic Versus Functional Severity of Coronary Artery Stenoses in the FAME Study. Fractional Flow Reserve Versus Angiography in Multivessel Evaluation. *J. Am. Coll. Cardiol.* **55**, 2816–2821 (2010).
 44. Bertolone, D. T. *et al.* Contemporary Management of Stable Coronary Artery Disease. *High Blood Pressure and Cardiovascular Prevention* (2022) doi:10.1007/s40292-021-00497-z.
 45. Wijntjens, G. W. M., Van Lavieren, M. A., Van De Hoef, T. P. & Piek, J. J. Physiological assessment of coronary stenosis: A view from the coronary microcirculation. *Interv. Cardiol.* **7**, 401–413 (2015).
 46. Ferrari, M., Schnell, B., Werner, G. S. & Figulla, H. R. Safety of deferring angioplasty in patients with normal coronary flow velocity reserve. *J. Am. Coll. Cardiol.* **33**, 82–87 (1999).
 47. Pijls, N. H. J. *et al.* Measurement of Fractional Flow Reserve to Assess the Functional Severity of Coronary-Artery Stenoses. *N. Engl. J. Med.* **334**, 1703–1708 (1996).
 48. Pijls, N. H. J. *et al.* Percutaneous Coronary Intervention of Functionally Nonsignificant Stenosis. 5-Year Follow-Up of the DEFER Study. *J. Am. Coll. Cardiol.* **49**, 2105–2111 (2007).
 49. Zimmermann, F. M. *et al.* Deferral vs. performance of percutaneous coronary intervention of functionally non-significant coronary stenosis: 15-year follow-up of the DEFER trial. *Eur. Heart J.* **36**, 3182–3188 (2015).
 50. Davies, J. E. *et al.* Use of the Instantaneous Wave-free Ratio or Fractional Flow Reserve in PCI. *N. Engl. J. Med.* **376**, 1824–1834 (2017).
 51. Götzberg, M. *et al.* Instantaneous Wave-free Ratio versus Fractional Flow Reserve to Guide PCI. *N. Engl. J. Med.* **376**, 1813–1823 (2017).
 52. Morris, P. D., Van De Vosse, F. N., Lawford, P. V., Hose, D. R. & Gunn, J. P. ‘virtual’ (Computed) Fractional Flow Reserve Current Challenges and Limitations. *JACC: Cardiovascular Interventions* vol.

- 8 1009–1017 (2015).
53. Masdjedi, K. *et al.* Validation of a three-dimensional quantitative coronary angiography-based software to calculate fractional flow reserve: The FAST study. *EuroIntervention* **16**, 591–599 (2021).
 54. Taylor, C. A., Fonte, T. A. & Min, J. K. Computational fluid dynamics applied to cardiac computed tomography for noninvasive quantification of fractional flow reserve: Scientific basis. *Journal of the American College of Cardiology* vol. 61 2233–2241 (2013).
 55. Patel, M. R. *et al.* 1-Year Impact on Medical Practice and Clinical Outcomes of FFRCT: The ADVANCE Registry. *JACC Cardiovasc. Imaging* **13**, 97–105 (2020).
 56. Bom, M. J. *et al.* Non-invasive procedural planning using computed tomography-derived fractional flow reserve. *Catheter. Cardiovasc. Interv.* **97**, 614–622 (2021).
 57. Roe, M. T. *et al.* Treatments, trends, and outcomes of acute myocardial infarction and percutaneous coronary intervention. *Journal of the American College of Cardiology* vol. 56 254–263 (2010).
 58. Stone, G. W. *et al.* Percutaneous Coronary Intervention for Vulnerable Coronary Atherosclerotic Plaque. *J. Am. Coll. Cardiol.* **76**, 2289–2301 (2020).
 59. Kok, A. M. *et al.* The influence of multidirectional shear stress on plaque progression and composition changes in human coronary arteries. *EuroIntervention J. Eur. Collab. with Work. Gr. Interv. Cardiol. Eur. Soc. Cardiol.* **15**, 692–699 (2019).
 60. Wentzel, J. J. *et al.* In vivo assessment of the relationship between shear stress and necrotic core in early and advanced coronary artery disease. *EuroIntervention J. Eur. Collab. with Work. Gr. Interv. Cardiol. Eur. Soc. Cardiol.* **9**, 989–995; discussion 995 (2013).
 61. De Bruyne, B. *et al.* Fractional flow reserve-guided PCI versus medical therapy in stable coronary disease. *N. Engl. J. Med.* **367**, 991–1001 (2012).
 62. Chatzizisis, Y. S. *et al.* Role of Endothelial Shear Stress in the Natural History of Coronary Atherosclerosis and Vascular Remodeling. Molecular, Cellular, and Vascular Behavior. *J. Am. Coll. Cardiol.* **49**,

2379–2393 (2007).

63. Puri, R. *et al.* Coronary artery wall shear stress is associated with endothelial dysfunction and expansive arterial remodelling in patients with coronary artery disease. *EuroIntervention J. Eur. Collab. with Work. Gr. Interv. Cardiol. Eur. Soc. Cardiol.* **10**, 1440–1448 (2015).
64. Kumar, A. *et al.* Low Coronary Wall Shear Stress Is Associated With Severe Endothelial Dysfunction in Patients With Nonobstructive Coronary Artery Disease. *JACC Cardiovasc. Interv.* **11**, 2072–2080 (2018).
65. Kumar, A. *et al.* High Coronary Shear Stress in Patients With Coronary Artery Disease Predicts Myocardial Infarction. *J. Am. Coll. Cardiol.* **72**, 1926–1935 (2018).
66. Mazzi, V. *et al.* Early Atherosclerotic Changes in Coronary Arteries are Associated with Endothelium Shear Stress Contraction/Expansion Variability. *Ann. Biomed. Eng.* **49**, 2606–2621 (2021).
67. Candreva, A. *et al.* Risk of myocardial infarction based on endothelial shear stress analysis using coronary angiography. *Atherosclerosis* **342**, 28–35 (2022).
68. Schöberl, J. NETGEN An advancing front 2D/3D-mesh generator based on abstract rules. *Comput. Vis. Sci.* **1**, 41–52 (1997).
69. Dadvand, P., Rossi, R. & Oñate, E. An Object-oriented Environment for Developing Finite Element Codes for Multi-disciplinary Applications. *Arch. Comput. Methods Eng.* **17**, 253–297 (2010).
70. van der Giessen, A. G. *et al.* The influence of boundary conditions on wall shear stress distribution in patients specific coronary trees. *J. Biomech.* **44**, 1089–1095 (2011).
71. Lodi Rizzini, M. *et al.* Does the inflow velocity profile influence physiologically relevant flow patterns in computational hemodynamic models of left anterior descending coronary artery? *Med. Eng. Phys.* **82**, 58–69 (2020).
72. De Nisco, G. *et al.* The Atheroprotective Nature of Helical Flow in Coronary Arteries. *Ann. Biomed. Eng.* **47**, 425–438 (2019).
73. Chiastra, C. *et al.* Healthy and diseased coronary bifurcation geometries influence near-wall and intravascular flow: A

- computational exploration of the hemodynamic risk. *J. Biomech.* **58**, 79–88 (2017).
74. Masdjedi, K. *et al.* Validation of a three-dimensional quantitative coronary angiography-based software to calculate fractional flow reserve: the FAST study. *EuroIntervention J. Eur. Collab. with Work. Gr. Interv. Cardiol. Eur. Soc. Cardiol.* **16**, 591–599 (2020).
 75. DeLong, E. R., DeLong, D. M. & Clarke-Pearson, D. L. Comparing the areas under two or more correlated receiver operating characteristic curves: a nonparametric approach. *Biometrics* **44**, 837–845 (1988).
 76. Samady, H. & Lee, J. M. Anatomy, Physiology, and Biomechanics: The Dream of Identifying Vulnerable Plaque Remains Alive. *JACC Cardiovasc. Imaging* **13**, 2220–2222 (2020).
 77. Richardson, P. D., Davies, M. J. & Born, G. V. Influence of plaque configuration and stress distribution on fissuring of coronary atherosclerotic plaques. *Lancet (London, England)* **2**, 941–944 (1989).
 78. Stone, G. W. *et al.* A Prospective Natural-History Study of Coronary Atherosclerosis. *N. Engl. J. Med.* **364**, 226–235 (2011).
 79. Toutouzas, K. *et al.* New insights by optical coherence tomography into the differences and similarities of culprit ruptured plaque morphology in non-ST-elevation myocardial infarction and ST-elevation myocardial infarction. *Am. Heart J.* **161**, 1192–1199 (2011).
 80. Koskinas, K. C., Ughi, G. J., Windecker, S., Tearney, G. J. & Räber, L. Intracoronary imaging of coronary atherosclerosis: validation for diagnosis, prognosis and treatment. *Eur. Heart J.* **37**, 524–35a-c (2016).
 81. Schaar, J. A., van der Steen, A. F. W., Mastik, F., Baldewsing, R. A. & Serruys, P. W. Intravascular palpography for vulnerable plaque assessment. *J. Am. Coll. Cardiol.* **47**, C86-91 (2006).
 82. Ambrose, J. A. *et al.* Angiographic progression of coronary artery disease and the development of myocardial infarction. *J. Am. Coll. Cardiol.* **12**, 56–62 (1988).
 83. Virmani, R., Burke, A. P., Farb, A. & Kolodgie, F. D. Pathology of the vulnerable plaque. *J. Am. Coll. Cardiol.* **47**, C13-8 (2006).

84. Lee, J. M. *et al.* Identification of High-Risk Plaques Destined to Cause Acute Coronary Syndrome Using Coronary Computed Tomographic Angiography and Computational Fluid Dynamics. *JACC. Cardiovasc. Imaging* **12**, 1032–1043 (2019).
85. Stone, P. H. *et al.* Regions of low endothelial shear stress are the sites where coronary plaque progresses and vascular remodelling occurs in humans: an in vivo serial study. *Eur. Heart J.* **28**, 705–710 (2007).
86. Samady, H. *et al.* Coronary artery wall shear stress is associated with progression and transformation of atherosclerotic plaque and arterial remodeling in patients with coronary artery disease. *Circulation* **124**, 779–788 (2011).
87. Bourantas, C. V *et al.* Shear Stress Estimated by Quantitative Coronary Angiography Predicts Plaques Prone to Progress and Cause Events. *JACC. Cardiovasc. Imaging* **13**, 2206–2219 (2020).
88. Shankaran, H., Alexandridis, P. & Neelamegham, S. Aspects of hydrodynamic shear regulating shear-induced platelet activation and self-association of von Willebrand factor in suspension. *Blood* **101**, 2637–2645 (2003).
89. Tufaro, V. *et al.* Wall shear stress estimated by 3D-QCA can predict cardiovascular events in lesions with borderline negative fractional flow reserve. *Atherosclerosis* **322**, 24–30 (2021).
90. Naruse, K. & Sokabe, M. Involvement of stretch-activated ion channels in Ca²⁺ mobilization to mechanical stretch in endothelial cells. *Am. J. Physiol.* **264**, C1037-44 (1993).
91. Dabagh, M., Jalali, P., Butler, P. J. & Tarbell, J. M. Shear-induced force transmission in a multicomponent, multicell model of the endothelium. *J. R. Soc. Interface* **11**, 20140431 (2014).
92. Melchior, B. & Frangos, J. A. Shear-induced endothelial cell-cell junction inclination. *Am. J. Physiol. Cell Physiol.* **299**, C621-9 (2010).
93. Lei, M., Kleinstreuer, C. & Truskey, G. A. A focal stress gradient-dependent mass transfer mechanism for atherogenesis in branching arteries. *Med. Eng. Phys.* **18**, 326–332 (1996).
94. Thondapu, V. *et al.* Biomechanical stress in coronary atherosclerosis: emerging insights from computational modelling. *Eur. Heart J.* **38**,

- 81–92 (2017).
95. Bourantas, C. V. *et al.* Angiographic derived endothelial shear stress: A new predictor of atherosclerotic disease progression. *Eur. Heart J. Cardiovasc. Imaging* **20**, 314–322 (2019).
 96. Toutouzas, K. *et al.* Accurate and reproducible reconstruction of coronary arteries and endothelial shear stress calculation using 3D OCT: Comparative study to 3D IVUS and 3D QCA. *Atherosclerosis* **240**, 510–519 (2015).
 97. Crea, F. & Liuzzo, G. Pathogenesis of acute coronary syndromes. *Journal of the American College of Cardiology* vol. 61 1–11 (2013).
 98. Yeh, R. W. *et al.* Population Trends in the Incidence and Outcomes of Acute Myocardial Infarction. *N. Engl. J. Med.* **362**, 2155–2165 (2010).
 99. DeWood, M. A. *et al.* Prevalence of Total Coronary Occlusion during the Early Hours of Transmural Myocardial Infarction. *N. Engl. J. Med.* **303**, 897–902 (1980).
 100. Falk, E. Unstable angina with fatal outcome: dynamic coronary thrombosis leading to infarction and/or sudden death. Autopsy evidence of recurrent mural thrombosis with peripheral embolization culminating in total vascular occlusion. *Circulation* **71**, 699–708 (1985).
 101. Virmani, R., Kolodgie, F. D., Burke, A. P., Farb, A. & Schwartz, S. M. Lessons from sudden coronary death: A comprehensive morphological classification scheme for atherosclerotic lesions. *Arterioscler. Thromb. Vasc. Biol.* **20**, 1262–1275 (2000).
 102. Franck, G. *et al.* Flow Perturbation Mediates Neutrophil Recruitment and Potentiates Endothelial Injury via TLR2 in Mice: Implications for Superficial Erosion. *Circ. Res.* **121**, 31–42 (2017).
 103. Bentzon, J. F. & Falk, E. Plaque Erosion: New Insights from the Road Less Travelled. *Circulation Research* vol. 121 8–10 (2017).
 104. Jang, I. K. *Cardiovascular OCT imaging*. *Cardiovascular OCT Imaging* (Springer International Publishing, 2015). doi:10.1007/978-3-319-10801-8.
 105. Ruggio, A. *et al.* Correlation between CD4 + CD28 null T lymphocytes,

regulatory T cells and plaque rupture: An Optical Coherence Tomography study in Acute Coronary Syndromes. *Int. J. Cardiol.* **276**, 289–292 (2019).

106. Romagnoli, E., Gatto, L. & Prati, F. The CLIMA study: Assessing the risk of myocardial infarction with a new anatomical score. *Eur. Hear. Journal, Suppl.* **21**, B80–B83 (2019).
107. Pedicino, D. *et al.* Alterations of Hyaluronan Metabolism in Acute Coronary Syndrome: Implications for Plaque Erosion. *J. Am. Coll. Cardiol.* **72**, 1490–1503 (2018).
108. Dai, J. *et al.* In vivo predictors of plaque erosion in patients with ST-segment elevation myocardial infarction: A clinical, angiographical, and intravascular optical coherence tomography study. *Eur. Heart J.* **39**, 2077–2085 (2018).
109. Jinnouchi, H., Virmani, R. & Finn, A. V. Are characteristics of plaque erosion defined by optical coherence tomography similar to true erosion in pathology? *European Heart Journal* vol. 39 2086–2089 (2018).
110. Costopoulos, C. *et al.* Impact of combined plaque structural stress and wall shear stress on coronary plaque progression, regression, and changes in composition. *Eur. Heart J.* **40**, 1411–1422 (2019).
111. Kumar, A. *et al.* High Coronary Shear Stress in Patients With Coronary Artery Disease Predicts Myocardial Infarction. *J. Am. Coll. Cardiol.* **72**, 1926–1935 (2018).
112. Wentzel, J. J. *et al.* Endothelial shear stress in the evolution of coronary atherosclerotic plaque and vascular remodelling: Current understanding and remaining questions. *Cardiovasc. Res.* **96**, 234–243 (2012).
113. Samady, H. *et al.* Coronary artery wall shear stress is associated with progression and transformation of atherosclerotic plaque and arterial remodeling in patients with coronary artery disease. *Circulation* **124**, 779–788 (2011).
114. Chatzizisis, Y. S. *et al.* Role of endothelial shear stress in the natural history of coronary atherosclerosis and vascular remodeling: molecular, cellular, and vascular behavior. *J. Am. Coll. Cardiol.* **49**, 2379–2393 (2007).

115. Stone, P. H. *et al.* Regions of low endothelial shear stress are the sites where coronary plaque progresses and vascular remodelling occurs in humans: An in vivo serial study. *Eur. Heart J.* **28**, 705–710 (2007).
116. Pan, S. Molecular mechanisms responsible for the atheroprotective effects of laminar shear stress. *Antioxid. Redox Signal.* **11**, 1669–1682 (2009).
117. Neumann, F. J. *et al.* 2019 ESC Guidelines for the diagnosis and management of chronic coronary syndromes. *European Heart Journal* vol. 41 407–477 (2020).
118. Collet, J. P. *et al.* 2020 ESC Guidelines for the management of acute coronary syndromes in patients presenting without persistent ST-segment elevation. *European Heart Journal* vol. 42 1289–1367 (2021).
119. Tearney, G. J. *et al.* Consensus standards for acquisition, measurement, and reporting of intravascular optical coherence tomography studies: A report from the International Working Group for Intravascular Optical Coherence Tomography Standardization and Validation. *J. Am. Coll. Cardiol.* **59**, 1058–1072 (2012).
120. Shida, Y. *et al.* Shear stress and platelet-induced tensile forces regulate ADAMTS13-localization within the platelet thrombus. *Res. Pract. Thromb. Haemost.* **3**, 254–260 (2019).
121. Conway, D. E. *et al.* Fluid shear stress on endothelial cells modulates mechanical tension across VE-cadherin and PECAM-1. *Curr. Biol.* **23**, 1024–1030 (2013).
122. Christophis, C. *et al.* Shear stress regulates adhesion and rolling of cd44+ leukemic and hematopoietic progenitor cells on hyaluronan. *Biophys. J.* **101**, 585–593 (2011).
123. Janke, D. *et al.* The ‘Artificial Artery’ as In Vitro Perfusion Model. *PLoS One* **8**, e57227 (2013).
124. Malek, A. & Izumo, S. Physiological fluid shear stress causes downregulation of endothelin-1 mRNA in bovine aortic endothelium. *Am. J. Physiol. - Cell Physiol.* **263**, (1992).
125. Takeshita, S., Inoue, N., Ueyama, T., Kawashima, S. & Yokoyama, M. Shear stress enhances glutathione peroxidase expression in

- endothelial cells. *Biochem. Biophys. Res. Commun.* **273**, 66–71 (2000).
126. Chiu, J. J. *et al.* Shear Stress Increases ICAM-1 and Decreases VCAM-1 and E-selectin Expressions Induced by Tumor Necrosis Factor- α in Endothelial Cells. *Arterioscler. Thromb. Vasc. Biol.* **24**, 73–79 (2004).
 127. Friedel, M., André, S., Goldschmidt, H., Gabius, H. J. & Schwartz-Albiez, R. Galectin-8 enhances adhesion of multiple myeloma cells to vascular endothelium and is an adverse prognostic factor. *Glycobiology* **26**, 1048–1058 (2016).
 128. Pasta, S. *et al.* Shear Stress and Aortic Strain Associations With Biomarkers of Ascending Thoracic Aortic Aneurysm. *Ann. Thorac. Surg.* **110**, 1595–1604 (2020).
 129. Wang, P. *et al.* Fluid shear stress-induced osteoarthritis: Roles of cyclooxygenase-2 and its metabolic products in inducing the expression of proinflammatory cytokines and matrix metalloproteinases. *FASEB Journal* vol. 27 4664–4677 (2013).
 130. Krams, R. *et al.* Shear stress is associated with markers of plaque vulnerability and MMP-9 activity. *EuroIntervention* **2**, 250–256 (2006).
 131. Chen, L. *et al.* Effect of laminar shear stress on the expression of matrix metalloproteinases-9 in rat bone marrow-derived mesenchymal stem cells. *Chinese* **27**, 1261–1265 (2010).
 132. Zhang, Y. *et al.* Shear stress regulates endothelial cell function through SRB1-eNOS signaling pathway. *Cardiovasc. Ther.* **34**, 308–313 (2016).
 133. Lund, T. *et al.* Shear stress regulates inflammatory and thrombogenic gene transcripts in cultured human endothelial progenitor cells. *Thromb. Haemost.* **104**, 582–591 (2010).
 134. Woodman, C. R., Price, E. M. & Laughlin, M. H. Shear stress induces eNOS mRNA expression and improves endothelium-dependent dilation in senescent soleus muscle feed arteries. *J. Appl. Physiol.* **98**, 940–946 (2005).
 135. Hazell, G. G. J. *et al.* PI16 is a shear stress and inflammation-regulated inhibitor of MMP2. *Sci. Rep.* **6**, (2016).
 136. Pearce, M. J., McIntyre, T. M., Prescott, S. M., Zimmerman, G. A. &

- Whatley, R. E. Shear stress activates cytosolic phospholipase A2 (cPLA2) and MAP kinase in human endothelial cells. *Biochem. Biophys. Res. Commun.* **218**, 500–504 (1996).
137. Flores, D., Liu, Y., Liu, W., Satlin, L. M. & Rohatgi, R. Flow-induced prostaglandin E2 release regulates Na and K transport in the collecting duct. *Am. J. Physiol. - Ren. Physiol.* **303**, F632 (2012).
138. Wang, Z. *et al.* Oscillatory shear stress induces oxidative stress via TLR4 activation in endothelial cells. *Mediators Inflamm.* **2019**, (2019).
139. Ozaki, C. K., Jiang, Z. & Berceci, S. A. TNF- α and Shear Stress-Induced Large Artery Adaptations. *J. Surg. Res.* **141**, 299–305 (2007).
140. Di Francesco, L. *et al.* Induction of prostacyclin by steady laminar shear stress suppresses tumor necrosis factor- α biosynthesis via heme oxygenase-1 in human endothelial cells. *Circ. Res.* **104**, 506–513 (2009).
141. Sheikh, S., Rainger, G. E., Gale, Z., Rahman, M. & Nash, G. B. Exposure to fluid shear stress modulates the ability of endothelial cells to recruit neutrophils in response to tumor necrosis factor- α : A basis for local variations in vascular sensitivity to inflammation. *Blood* **102**, 2828–2834 (2003).
142. dela Paz, N. G., Walshe, T. E., Leach, L. L., Saint-Geniez, M. & D'Amore, P. A. Role of shear-stress-induced VEGF expression in endothelial cell survival. *J. Cell Sci.* **125**, 831–843 (2012).
143. Conklin, B. S., Zhong, D. S., Zhao, W., Lin, P. H. & Chen, C. Shear stress regulates occludin and VEGF expression in porcine arterial endothelial cells. in *Journal of Surgical Research* vol. 102 13–21 (J Surg Res, 2002).
144. Migliori, S. *et al.* A framework for computational fluid dynamic analyses of patient-specific stented coronary arteries from optical coherence tomography images. *Med. Eng. Phys.* **47**, 105–116 (2017).
145. Migliori, S. *et al.* Application of an OCT-based 3D reconstruction framework to the hemodynamic assessment of an ulcerated coronary artery plaque. *Med. Eng. Phys.* (2020) doi:10.1016/j.medengphy.2019.12.006.
146. Bologna, M. *et al.* Automatic segmentation of optical coherence

tomography pullbacks of coronary arteries treated with bioresorbable vascular scaffolds: Application to hemodynamics modeling. *PLoS One* **14**, 1–17 (2019).

147. Chiastra, C. *et al.* Reconstruction of stented coronary arteries from optical coherence tomography images: Feasibility, validation, and repeatability of a segmentation method. *PLoS One* **12**, e0177495 (2017).
148. Lodi Rizzini, M. *et al.* Does the inflow velocity profile influence physiologically relevant flow patterns in computational hemodynamic models of left anterior descending coronary artery? *Med. Eng. Phys.* **82**, 58–69 (2020).
149. Gibson, C. M. *et al.* TIMI frame count: A quantitative method of assessing coronary artery flow. *Circulation* **93**, 879–888 (1996).
150. Chiastra, C. *et al.* Coronary fractional flow reserve measurements of a stenosed side branch: A computational study investigating the influence of the bifurcation angle. *Biomed. Eng. Online* **15**, 1–16 (2016).
151. Collet, C. *et al.* Quantitative angiography methods for bifurcation lesions: A consensus statement update from the European Bifurcation Club. *EuroIntervention* vol. 13 115–123 (2017).
152. Suzuki, N. *et al.* Clinical expert consensus document on quantitative coronary angiography from the Japanese Association of Cardiovascular Intervention and Therapeutics. *Cardiovascular Intervention and Therapeutics* vol. 35 105–116 (2020).
153. Stone, P. H. *et al.* Effect of endothelial shear stress on the progression of coronary artery disease, vascular remodeling, and in-stent restenosis in humans: In vivo 6-month follow-up study. *Circulation* **108**, 438–444 (2003).
154. Eshtehardi, P. *et al.* Association of Coronary Wall Shear Stress With Atherosclerotic Plaque Burden, Composition, and Distribution in Patients With Coronary Artery Disease. *J. Am. Heart Assoc.* **1**, 1–9 (2012).
155. Yamamoto, E. *et al.* Low Endothelial Shear Stress Predicts Evolution to High-Risk Coronary Plaque Phenotype in the Future: A Serial Optical Coherence Tomography and Computational Fluid Dynamics Study. *Circ. Cardiovasc. Interv.* **10**, (2017).

156. Biasucci, L. M. *et al.* Where Does Inflammation Fit? *Current Cardiology Reports* vol. 19 1–10 (2017).
157. Gijssen, F. J. H. *et al.* High shear stress induces a strain increase in human coronary plaques over a 6-month period. *EuroIntervention* **7**, 121–127 (2011).
158. Yamamoto, E. *et al.* Endothelial Shear Stress and Plaque Erosion: A Computational Fluid Dynamics and Optical Coherence Tomography Study. *JACC: Cardiovascular Imaging* vol. 12 374–375 (2019).
159. Fukumoto, Y. *et al.* Localized Elevation of Shear Stress Is Related to Coronary Plaque Rupture. A 3-Dimensional Intravascular Ultrasound Study With In-Vivo Color Mapping of Shear Stress Distribution. *J. Am. Coll. Cardiol.* **51**, 645–650 (2008).
160. McElroy, M. *et al.* Identification of the haemodynamic environment permissive for plaque erosion. *Sci. Rep.* **11**, 1–10 (2021).
161. Holzapfel, G. A., Mulvihill, J. J., Cunnane, E. M. & Walsh, M. T. Computational approaches for analyzing the mechanics of atherosclerotic plaques: A review. *J. Biomech.* **47**, 859–869 (2014).
162. Ohayon, J. *et al.* Influence of residual stress/strain on the biomechanical stability of vulnerable coronary plaques: Potential impact for evaluating the risk of plaque rupture. *Am. J. Physiol. - Hear. Circ. Physiol.* **293**, 1987–1996 (2007).
163. Akyildiz, A. C. *et al.* Effects of intima stiffness and plaque morphology on peak cap stress. *Biomed. Eng. Online* **10**, (2011).
164. Vengrenyuk, Y. *et al.* A hypothesis for vulnerable plaque rupture due to stress-induced debonding around cellular microcalcifications in thin fibrous caps. *Proc. Natl. Acad. Sci. U. S. A.* **103**, 14678–14683 (2006).
165. Burzotta, F. *et al.* Fractional Flow Reserve or Optical Coherence Tomography to Guide Management of Angiographically Intermediate Coronary Stenosis: A Single-Center Trial. *JACC Cardiovasc. Interv.* **13**, 49–58 (2020).
166. Aragam, K. G. & Natarajan, P. Polygenic Scores to Assess Atherosclerotic Cardiovascular Disease Risk: Clinical Perspectives and Basic Implications. *Circ. Res.* **126**, 1159–1177 (2020).

167. Libby, P. The changing landscape of atherosclerosis. *Nature* vol. 592 524–533 (2021).
168. Angelini, G. *et al.* Matrix metalloproteinase-9 might affect adaptive immunity in non-ST segment elevation acute coronary syndromes by increasing CD31 cleavage on CD4+ T-cells. *Eur. Heart J.* **39**, 1089–1097 (2018).
169. Zeiher, A. M., Goebel, H., Schächinger, V. & Ihling, C. Tissue endothelin-1 immunoreactivity in the active coronary atherosclerotic plaque: A clue to the mechanism of increased vasoreactivity of the culprit lesion in unstable angina. *Circulation* **91**, 941–947 (1995).
170. Rectenwald, J. E., Moldawer, L. L., Huber, T. S., Seeger, J. M. & Ozaki, C. K. Direct evidence for cytokine involvement in neointimal hyperplasia. *Circulation* **102**, 1697–1702 (2000).
171. Thondapu, V. *et al.* High spatial endothelial shear stress gradient independently predicts site of acute coronary plaque rupture and erosion. *Cardiovasc. Res.* **117**, 1974–1985 (2021).
172. Della Bona, R., Liuzzo, G., Pedicino, D. & Crea, F. Anti-inflammatory Treatment of Acute Coronary Syndromes. *Curr. Pharm. Des.* **17**, 4172–4189 (2012).
173. Boudoulas, K. D., Triposciadis, F., Geleris, P. & Boudoulas, H. Coronary Atherosclerosis: Pathophysiologic Basis for Diagnosis and Management. *Prog. Cardiovasc. Dis.* **58**, 676–692 (2016).
174. Antoniadis, A. P. *et al.* Impact of local flow haemodynamics on atherosclerosis in coronary artery bifurcations. *EuroIntervention* **11**, V18–V22 (2015).
175. Malek, A. M., Alper, S. L. & Izumo, S. Hemodynamic Shear Stress and Its Role in Atherosclerosis. *JAMA* **282**, 2035–2042 (1999).
176. Hoogendoorn, A. *et al.* Multidirectional wall shear stress promotes advanced coronary plaque development: comparing five shear stress metrics. *Cardiovasc. Res.* (2019) doi:10.1093/cvr/cvz212.
177. De Nisco, G. *et al.* The impact of helical flow on coronary atherosclerotic plaque development. *Atherosclerosis* (2020) doi:10.1016/J.ATHEROSCLEROSIS.2020.01.027.
178. Taylor, C. A. & Steinman, D. A. Image-based modeling of blood flow and vessel wall dynamics: Applications, methods and future

- directions: Sixth international bio-fluid mechanics symposium and workshop, March 28-30, 2008 Pasadena, California. *Ann. Biomed. Eng.* **38**, 1188–1203 (2010).
179. Morris, P. D. *et al.* Computational fluid dynamics modelling in cardiovascular medicine. *Heart* **102**, 18–28 (2016).
 180. Zhong, L. *et al.* Application of patient-specific computational fluid dynamics in coronary and intra-cardiac flow simulations: Challenges and opportunities. *Front. Physiol.* **9**, (2018).
 181. Sankaran, S., Kim, H. J., Choi, G. & Taylor, C. A. Uncertainty quantification in coronary blood flow simulations: Impact of geometry, boundary conditions and blood viscosity. *J. Biomech.* **49**, 2540–2547 (2016).
 182. Bozzi, S. *et al.* Uncertainty propagation of phase contrast-MRI derived inlet boundary conditions in computational hemodynamics models of thoracic aorta. *Comput. Methods Biomech. Biomed. Engin.* **20**, 1104–1112 (2017).
 183. Steinman, D. A. & Migliavacca, F. Editorial: Special Issue on Verification, Validation, and Uncertainty Quantification of Cardiovascular Models: Towards Effective VVUQ for Translating Cardiovascular Modelling to Clinical Utility. *Cardiovasc. Eng. Technol.* **9**, 539–543 (2018).
 184. Boccadifuoco, A., Mariotti, A., Capellini, K., Celi, S. & Salvetti, M. V. Validation of Numerical Simulations of Thoracic Aorta Hemodynamics: Comparison with In Vivo Measurements and Stochastic Sensitivity Analysis. *Cardiovasc. Eng. Technol.* **9**, 688–706 (2018).
 185. Boccadifuoco, A., Mariotti, A., Celi, S., Martini, N. & Salvetti, M. V. Impact of uncertainties in outflow boundary conditions on the predictions of hemodynamic simulations of ascending thoracic aortic aneurysms. *Comput. Fluids* **165**, 96–115 (2018).
 186. Hose, D. R. *et al.* Cardiovascular models for personalised medicine: Where now and where next? *Med. Eng. Phys.* **72**, 38–48 (2019).
 187. Antonuccio, M. N., Mariotti, A., Celi, S. & Salvetti, M. V. Effects of the Distribution in Space of the Velocity-Inlet Condition in Hemodynamic Simulations of the Thoracic Aorta BT - Bioinformatics and Biomedical Engineering. in (eds. Rojas, I., Valenzuela, O., Rojas, F., Herrera, L.

J. & Ortuño, F.) 63–74 (Springer International Publishing, 2020).

188. Markl, M. *et al.* Advanced flow MRI: emerging techniques and applications. *Clinical Radiology* (2016) doi:10.1016/j.crad.2016.01.011.
189. Giannopoulos, A. A. *et al.* Quantifying the effect of side branches in endothelial shear stress estimates. *Atherosclerosis* **251**, 213–218 (2016).
190. Vorobtsova, N. *et al.* Effects of Vessel Tortuosity on Coronary Hemodynamics: An Idealized and Patient-Specific Computational Study. *Ann. Biomed. Eng.* **44**, 2228–2239 (2016).
191. Chiastra, C. *et al.* Computational fluid dynamic simulations of image-based stented coronary bifurcation models. *J. R. Soc. Interface* **10**, (2013).
192. Beier, S. *et al.* Impact of bifurcation angle and other anatomical characteristics on blood flow - A computational study of non-stented and stented coronary arteries. *J. Biomech.* **49**, 1570–1582 (2016).
193. Doutel, E., Pinto, S. I. S., Campos, J. B. L. M. & Miranda, J. M. Link between deviations from Murray's Law and occurrence of low wall shear stress regions in the left coronary artery. *J. Theor. Biol.* **402**, 89–99 (2016).
194. Pinto, S. I. S. & Campos, J. B. L. M. Numerical study of wall shear stress-based descriptors in the human left coronary artery. *Comput. Methods Biomech. Biomed. Engin.* **19**, 1443–1455 (2016).
195. Morbiducci, U., Ponzini, R., Gallo, D., Bignardi, C. & Rizzo, G. Inflow boundary conditions for image-based computational hemodynamics: Impact of idealized versus measured velocity profiles in the human aorta. *J. Biomech.* **46**, 102–109 (2013).
196. Beier, S. *et al.* Dynamically scaled phantom phase contrast MRI compared to true-scale computational modeling of coronary artery flow. *J. Magn. Reson. Imaging* **44**, 983–992 (2016).
197. Bahrami, S. & Norouzi, M. A numerical study on hemodynamics in the left coronary bifurcation with normal and hypertension conditions. *Biomech. Model. Mechanobiol.* **17**, 1785–1796 (2018).
198. Doutel, E., Carneiro, J., Campos, J. B. L. M. & Miranda, J. M. Experimental and numerical methodology to analyze flows in a

- coronary bifurcation. *Eur. J. Mech. B/Fluids* **67**, 341–356 (2018).
199. Wellnhofer, E. *et al.* Flow simulation studies in coronary arteries-Impact of side-branches. *Atherosclerosis* **213**, 475–481 (2010).
200. Li, Y. *et al.* Impact of Side Branch Modeling on Computation of Endothelial Shear Stress in Coronary Artery Disease: Coronary Tree Reconstruction by Fusion of 3D Angiography and OCT. *J. Am. Coll. Cardiol.* **66**, 125–135 (2015).
201. Vardhan, M. *et al.* The importance of side branches in modeling 3D hemodynamics from angiograms for patients with coronary artery disease. *Sci. Rep.* **9**, 1–10 (2019).
202. Zovatto, L. & Pedrizzetti, G. Optimal helical entry flow in a helical vessel. *Fluid Dyn. Res.* **50**, (2018).
203. Dean, W. R. XVI. Note on the motion of fluid in a curved pipe. *London, Edinburgh, Dublin Philos. Mag. J. Sci.* **4**, 208–223 (1927).
204. WG Austen , JE Edwards , RL Frye , GG Gensini , VL Gott , LS Griffith , DC McGoon , ML Murphy, B. R. AHA COMMITTEE REPORT: A Reporting System on Patients Evaluated for Coronary Artery Disease Report of the Ad Hoc Committee for Grading of Coronary Artery. *Circulation* **51**, 5–40 (1975).
205. Bergman, T. L., Incropera, F. P., DeWitt, D. P. & Lavine, A. S. *Fundamentals of Heat and Mass Transfer.* (Wiley, 2011).
206. Shtilman, L., Levich, E., Orszag, S. A., Pelz, R. B. & Tsinober, A. On the role of helicity in complex fluid flows. *Phys. Lett. A* **113**, 32–37 (1985).
207. Everaars, H. *et al.* Doppler Flow Velocity and Thermodilution to Assess Coronary Flow Reserve: A Head-to-Head Comparison With [15O]H₂O PET. *JACC Cardiovasc. Interv.* **11**, 2044–2054 (2018).
208. Xaplanteris, P. *et al.* Catheter-based measurements of absolute coronary blood flow and microvascular resistance feasibility, safety, and reproducibility in humans. *Circ. Cardiovasc. Interv.* **11**, 1–8 (2018).
209. Wake, A. K., Oshinski, J. N., Tannenbaum, A. R. & Giddens, D. P. Choice of in vivo versus idealized velocity boundary conditions influences physiologically relevant flow patterns in a subject-specific

- simulation of flow in the human carotid bifurcation. *J. Biomech. Eng.* **131**, 7–13 (2009).
210. Campbell, I. C. *et al.* Effect of inlet velocity profiles on patient-specific computational fluid dynamics simulations of the carotid bifurcation. *J. Biomech. Eng.* **134**, 1–8 (2012).
 211. Pirola, S. *et al.* Computational study of aortic hemodynamics for patients with an abnormal aortic valve: The importance of secondary flow at the ascending aorta inlet. *APL Bioeng.* **2**, 026101 (2018).
 212. Youssefi, P. *et al.* Impact of patient-specific inflow velocity profile on hemodynamics of the thoracic aorta. *J. Biomech. Eng.* **140**, 1–14 (2018).
 213. Myers, J. G., Moore, J. A., Ojha, M., Johnston, K. W. & Ethier, C. R. Factors influencing blood flow patterns in the human right coronary artery. *Ann. Biomed. Eng.* **29**, 109–120 (2001).
 214. Collet, C. *et al.* Coronary computed tomography angiography for heart team decision-making in multivessel coronary artery disease. *Eur. Heart J.* **39**, 3689–3698 (2018).
 215. Pedley, T. J. *The Fluid Mechanics of Large Blood Vessels. Cambridge Monographs on Mechanics* (Cambridge University Press, 1980). doi:DOI: 10.1017/CBO9780511896996.
 216. Malvè, M., García, A., Ohayon, J. & Martínez, M. A. Unsteady blood flow and mass transfer of a human left coronary artery bifurcation: FSI vs. CFD. *Int. Commun. Heat Mass Transf.* **39**, 745–751 (2012).
 217. Eslami, P. *et al.* Effect of Wall Elasticity on Hemodynamics and Wall Shear Stress in Patient-Specific Simulations in the Coronary Arteries. *J. Biomech. Eng.* **142**, 1–10 (2020).
 218. Theodorakakos, A. *et al.* Simulation of cardiac motion on non-Newtonian, pulsating flow development in the human left anterior descending coronary artery. *Phys. Med. Biol.* **53**, 4875–4892 (2008).
 219. Javadzadegan, A. *et al.* Haemodynamic assessment of human coronary arteries is affected by degree of freedom of artery movement. *Comput. Methods Biomech. Biomed. Engin.* **20**, 260–272 (2017).
 220. Stone, P. H. *et al.* Prediction of progression of coronary artery disease and clinical outcomes using vascular profiling of endothelial shear

- stress and arterial plaque characteristics: The PREDICTION study. *Circulation* **126**, 172–181 (2012).
221. Candreva, A. *et al.* Risk of myocardial infarction based on endothelial shear stress analysis using coronary angiography. *Atherosclerosis* (2021) doi:10.1016/j.atherosclerosis.2021.11.010.
222. Pandey, R., Kumar, M., Majdoubi, J., Rahimi-Gorji, M. & Srivastav, V. K. A review study on blood in human coronary artery: Numerical approach. *Comput. Methods Programs Biomed.* **187**, 1–12 (2020).
223. Carvalho, V., Pinho, D., Lima, R. A., Teixeira, J. C. & Teixeira, S. Blood flow modeling in coronary arteries: A review. *Fluids* **6**, (2021).
224. Fleeter, C. M., Geraci, G., Schiavazzi, D. E., Kahn, A. M. & Marsden, A. L. Multilevel and multifidelity uncertainty quantification for cardiovascular hemodynamics. *Comput. Methods Appl. Mech. Eng.* **365**, (2020).
225. Ninos, G., Bartzis, V., Merlemis, N. & Sarris, I. E. Uncertainty quantification implementations in human hemodynamic flows. *Comput. Methods Programs Biomed.* **203**, 106021 (2021).
226. Schrauwen, J. T. C. *et al.* The impact of scaled boundary conditions on wall shear stress computations in atherosclerotic human coronary bifurcations. *Am. J. Physiol. - Hear. Circ. Physiol.* **310**, H1304–H1312 (2016).
227. Doucette, J. W. *et al.* Validation of a Doppler guide wire for intravascular measurement of coronary artery flow velocity. *Circulation* **85**, 1899–1911 (1992).
228. Gibson, C. M. *et al.* TIMI Frame Count . *Circulation* **93**, 879–888 (1996).
229. Tu, S. *et al.* Fractional flow reserve calculation from 3-dimensional quantitative coronary angiography and TIMI frame count: A fast computer model to quantify the functional significance of moderately obstructed coronary arteries. *JACC Cardiovasc. Interv.* **7**, 768–777 (2014).
230. Murray, C. D. The Physiological Principle of Minimum Work: I. The Vascular System and the Cost of Blood Volume. *Proc. Natl. Acad. Sci. U. S. A.* **12**, 207–214 (1926).

231. Aarnoudse, W. *et al.* Direct Volumetric Blood Flow Measurement in Coronary Arteries by Thermodilution. *J. Am. Coll. Cardiol.* **50**, 2294–2304 (2007).
232. Gallinoro, E. *et al.* Thermodilution-derived volumetric resting coronary blood flow measurement in humans. *EuroIntervention* **17**, e672–e679 (2021).
233. Candreva, A. *et al.* Basics of Coronary Thermodilution. *JACC Cardiovasc. Interv.* **14**, 595–605 (2021).
234. Kelshiker, M. A. *et al.* Coronary flow reserve and cardiovascular outcomes: a systematic review and meta-analysis. *Eur. Heart J.* 1–15 (2021) doi:10.1093/eurheartj/ehab775.
235. Konst, R. E. *et al.* Absolute Coronary Blood Flow Measured by Continuous Thermodilution in Patients With Ischemia and Nonobstructive Disease. *J. Am. Coll. Cardiol.* **77**, 728–741 (2021).
236. Busch, J., Giese, D., Wissmann, L. & Kozerke, S. Reconstruction of divergence-free velocity fields from cine 3D phase-contrast flow measurements. *Magn. Reson. Med.* **69**, 200–210 (2013).
237. Tresoldi, D. *et al.* Mapping aortic hemodynamics using 3D cine phase contrast magnetic resonance parallel imaging: Evaluation of an anisotropic diffusion filter. *Magn. Reson. Med.* **71**, 1621–1631 (2014).
238. Jaccard, P. The distribution of the flora in the alpine zone. *New Phytol.* **11**, 37–50 (1912).
239. Thurston, G. B. Frequency and shear rate dependence of viscoelasticity of human blood. *Biorheology* **10**, 375–381 (1973).
240. Altman, D. G. & Bland, T. M. Measurement in Medicine : The Analysis of Method Comparison Studies Author (s): D . G . Altman and J . M . Bland Published by : Wiley for the Royal Statistical Society Stable URL : <http://www.jstor.org/stable/2987937> REFERENCES Linked references are ava. *Statistician* **32**, 307–317 (1983).
241. Barbato, E. *et al.* Validation of coronary flow reserve measurements by thermodilution in clinical practice. (2003) doi:10.1016/j.ehj.2003.11.009.
242. Everaars, H. *et al.* Doppler Flow Velocity and Thermodilution to Assess Coronary Flow Reserve: A Head-to-Head Comparison With [15O]H₂O PET. *JACC Cardiovasc. Interv.* **11**, 2044–2054 (2018).

243. Schuurbiens, J. C. H. *et al.* In vivo validation of CAAS QCA-3D coronary reconstruction using fusion of angiography and intravascular ultrasound (ANGUS). *Catheter. Cardiovasc. Interv.* **73**, 620–626 (2009).
244. Ponzini, R., Lemma, M., Morbiducci, U., Montevecchi, F. M. & Redaelli, A. Doppler derived quantitative flow estimate in coronary artery bypass graft: A computational multiscale model for the evaluation of the current clinical procedure. *Med. Eng. Phys.* **30**, 809–816 (2008).
245. Schrauwen, J. T. C. *et al.* The impact of scaled boundary conditions on wall shear stress computations in atherosclerotic human coronary bifurcations. *Am. J. Physiol. - Hear. Circ. Physiol.* **310**, H1304–H1312 (2016).
246. De Bruyne, B., Pijls, N. H. J., Smith, L., Wievegg, M. & Heyndrickx, G. R. Coronary Thrombolysis to Assess Flow Reserve. *Circulation* **104**, 2003–2006 (2001).
247. Pijls, N. H. J. *et al.* Coronary thrombolysis to assess flow reserve: Validation in humans. *Circulation* **105**, 2482–2486 (2002).
248. Manginas, A. *et al.* Estimation of coronary flow reserve using the Thrombolysis In Myocardial Infarction (TIMI) frame count method. *Am. J. Cardiol.* **83**, 1562–1564 (1999).
249. Chugh, S. K. *et al.* Coronary flow velocity reserve does not correlate with TIMI frame count in patients undergoing non-emergency percutaneous coronary intervention. *J. Am. Coll. Cardiol.* **44**, 778–782 (2004).
250. Molony, D. S. *et al.* An assessment of intra-patient variability on observed relationships between wall shear stress and plaque progression in coronary arteries. *Biomed. Eng. Online* **14**, S2 (2015).
251. Hartman, E. M. J. *et al.* The definition of low wall shear stress and its effect on plaque progression estimation in human coronary arteries. *Sci. Rep.* **11**, 1–11 (2021).
252. Zhu, D., Bonanno, G., Hays, A. G., Weiss, R. G. & Schär, M. Phase contrast coronary blood velocity mapping with both high temporal and spatial resolution using triggered Golden Angle rotated Spiral k-t Sparse Parallel imaging (GASSP) with shifted binning. *Magn. Reson. Med.* **86**, 1929–1943 (2021).

253. Toth, G. G. *et al.* Standardization of Fractional Flow Reserve Measurements. *Journal of the American College of Cardiology* vol. 68 742–753 (2016).
254. Carlos, C. *et al.* Measurement of Hyperemic Pullback Pressure Gradients to Characterize Patterns of Coronary Atherosclerosis. *J. Am. Coll. Cardiol.* **74**, 1772–1784 (2019).
255. Piroth, Z. *et al.* Prognostic Value of Fractional Flow Reserve Measured Immediately After Drug-Eluting Stent Implantation. *Circ. Cardiovasc. Interv.* **10**, (2017).
256. Sianos, G. *et al.* The SYNTAX Score: an angiographic tool grading the complexity of coronary artery disease. *EuroIntervention J. Eur. Collab. with Work. Gr. Interv. Cardiol. Eur. Soc. Cardiol.* **1**, 219–227 (2005).
257. Ali, Z. A. *et al.* Optical coherence tomography compared with intravascular ultrasound and with angiography to guide coronary stent implantation (ILUMIEN III: OPTIMIZE PCI): a randomised controlled trial. *Lancet* **388**, 2618–2628 (2016).
258. Killick, R., Fearnhead, P. & Eckley, I. A. Optimal detection of changepoints with a linear computational cost. *J. Am. Stat. Assoc.* **107**, 1590–1598 (2012).
259. Lavielle, M. Using penalized contrasts for the change-point problem. *Signal Processing* **85**, 1501–1510 (2005).
260. Tonino, P. A. L. *et al.* Fractional Flow Reserve versus Angiography for Guiding Percutaneous Coronary Intervention. *N. Engl. J. Med.* **360**, 213–224 (2009).
261. Fournier, S. *et al.* Association of Improvement in Fractional Flow Reserve with Outcomes, Including Symptomatic Relief, after Percutaneous Coronary Intervention. *JAMA Cardiol.* **4**, 370–374 (2019).
262. Collet, C. *et al.* Measurement of Hyperemic Pullback Pressure Gradients to Characterize Patterns of Coronary Atherosclerosis. *J. Am. Coll. Cardiol.* **74**, 1772–1784 (2019).
263. Nijjer, S. S. *et al.* Pre-angioplasty instantaneous wave-free ratio pullback provides virtual intervention and predicts hemodynamic outcome for serial lesions and diffuse coronary artery disease. *JACC*

- Cardiovasc. Interv.* **7**, 1386–1396 (2014).
264. Maron, D. J. *et al.* Initial Invasive or Conservative Strategy for Stable Coronary Disease. *N. Engl. J. Med.* **382**, 1395–1407 (2020).
265. Hwang, D. *et al.* Role of Post-Stent Physiological Assessment in a Risk Prediction Model After Coronary Stent Implantation. *JACC Cardiovasc. Interv.* **13**, 1639–1650 (2020).
266. Mohamied, Y. *et al.* Change of Direction in the Biomechanics of Atherosclerosis. *Ann. Biomed. Eng.* **43**, 16–25 (2015).
267. Gallo, D. *et al.* Segment-specific associations between local haemodynamic and imaging markers of early atherosclerosis at the carotid artery: An in vivo human study. *J. R. Soc. Interface* **15**, (2018).
268. Habibi, M., D’Souza, R. M., Dawson, S. T. M. & Arzani, A. Integrating multi-fidelity blood flow data with reduced-order data assimilation. *Comput. Biol. Med.* **135**, 104566 (2021).
269. Kochkov, D. *et al.* Machine learning–accelerated computational fluid dynamics. *Proc. Natl. Acad. Sci. U. S. A.* **118**, (2021).
270. Ferdian, E., Dubowitz, D. J., Mauger, C. A., Wang, A. & Young, A. A. WSSNet: Aortic Wall Shear Stress Estimation Using Deep Learning on 4D Flow MRI. *Front. Cardiovasc. Med.* **8**, 1969 (2022).

List of publications

Journal publications

Lodi Rizzini M., Candreva A., Chiastra C., Gallinoro E., Calò K., D'Ascenzo F., De Bruyne B., Mizukami T., Collet C., Gallo D., Morbiducci U., Modelling coronary flows: impact of differently measured inflow boundary conditions on vessel-specific computational hemodynamic profiles, *Computer Methods and Programs in Biomedicine*, 2022, Volume 221:106882

Chiastra C., Mazzi V., **Lodi Rizzini M.**, Calò K., Corti A., Acquasanta A., De Nisco G., Belliggiano D., Cerrato E., Gallo D., Morbiducci U. Coronary Artery Stenting Affects Wall Shear Stress Topological Skeleton. *Journal of Biomechanical Engineering*, 2022, Volume 144(6):061002.

Candreva A., Pagnoni M., **Lodi Rizzini M.**, Mizukami T., Gallinoro E., Mazzi V., Gallo D., Meier D., Shinke T., Aben JP., Nagumo S., Sonck J., Munhoz D., Fournier S., Barbato E., Heggermont W., Cook S., Chiastra C., Morbiducci U., De Bruyne B., Muller O., Collet C., Risk of myocardial infarction based on endothelial shear stress analysis using coronary angiography, *Atherosclerosis*, 2022, Volume 342:28–35.

Lodi Rizzini M., Nagumo S., Gallo D., Sonck J., Mizukami T., D'Ascenzo F., Buytaert D., Morbiducci U., De Bruyne B., Chiastra C., Collet C., Mismatch between morphological and functional assessment of the length of coronary artery disease, *International Journal of Cardiology*, 2021, Volume 334: 1-9.

Mazzi V., Morbiducci U., Calò K., De Nisco G., **Lodi Rizzini M.**, Torta E., Caridi G.C.A., Chiastra C., Gallo D., Wall shear stress topological skeleton analysis in cardiovascular flows: Methods and applications, *MATHEMATICS*, 2021, Volume 9(7):720.

Lodi Rizzini M., Gallo D., De Nisco G., D'Ascenzo F., Chiastra C., Bocchino P. P., Piroli F., De Ferrari G. M., Morbiducci U., Does the inflow velocity profile influence physiologically relevant flow patterns in computational hemodynamic models of left anterior descending coronary artery?, *Medical Engineering & Physics*, 2020, Volume 82: 58-69.

Annone, U.; D'Ascenzo, F.; **Lodi Rizzini, M.**; Morbiducci, U., Searching into the invisible: Hunting for present and future ischaemia with fractional flow reserve pullback and wall shear stress, *European Heart Journal*, 2020, Volume 41(17):1686.

De Nisco G., Gallo, D.; Siciliano, K., Tasso, P., **Lodi Rizzini, M.**, Mazzi, V., Calò, K., Antonucci, M., Morbiducci, Umberto, Hemodialysis arterio-venous graft design reducing the hemodynamic risk of vascular access dysfunction, *Journal of Biomechanics*, 2020, Volume 100:1-11.

Tasso P., **Lodi Rizzini M.**, Raptis A., Matsagkas M., De Nisco G., Gallo D., Xenos M., Morbiducci U., In-stent graft helical flow intensity reduces the risk of migration after endovascular aortic repair, *Journal of Biomechanics*, 2019, Volume 94:170-179.

Tasso P., Raptis A., Matsagkas M., **Lodi Rizzini M.**, Gallo D., Xenox M., Morbiducci U., Abdominal Aortic Aneurysm Endovascular Repair: Profiling Postimplantation Morphometry and Hemodynamics with Image-Based Computational Fluid Dynamics, ASME. *Journal of Biomechanical Engineering*; 2018, Volume 140(11):111003-111003-12.

Submitted manuscripts

Russo G., Pedicino D., Chiastra C., Vinci R., **Lodi Rizzini M.**, Genuardi L., Sarraf M., d’Aiello A., Bologna M., Aurigemma C., Bonanni A., Bellantoni A., D’Ascenzo F., Ciampi P., Zambrano A., Mainardi L., Ponzo M., Trani C., Massetti M., Gallo D., Migliavacca F., Maisano F., Lerman A., Morbiducci U., Burzotta F., Crea F., Liuzzo G., Coronary Artery Plaque Rupture and Erosion: Role of Wall Shear Stress Profiling and Biological Patterns in Acute Coronary Syndromes, *submitted to Cardiovascular Research*.

Calò K., Gallo D., Guala A., **Lodi Rizzini M.**, Dux-Santoy L., Rodriguez-Palomares J., Scarsoglio S., Ridolfi L., Morbiducci U., Network-Based Characterization of Blood Large-Scale Coherent Motion in the Healthy Human Aorta with 4D Flow MRI, *submitted to IEEE Transactions on Biomedical Engineering*

Conference proceedings

Lodi Rizzini M., Candreva A., Gallo D., Aben JP., Chiastra C., De Bruyne B., Collet C., Morbiducci U., Risk of Myocardial Infarction Based on Endothelial Shear Stress Analysis, The 17th international symposium on Biomechanics in Vascular Biology and Cardiovascular Disease, 2022.

Lodi Rizzini M., Candreva A., Chiastra C., Mizukami T., Gallo D., Aben JP., Muller O., De Bruyne B., Collet C., Morbiducci U., Wall Shear Stress Topological Skeleton Variability Predicts Myocardial Infarction, 12th European symposium on vascular biomaterials, ESVB 2021, 2021.

De Nisco G., Mazzi V., Calo' K., **Lodi Rizzini M.**, Chiastra C., Wentzel J.J., Steinman D.A., Gallo D., Morbiducci U., EXPLORING THE LINK BETWEEN WALL SHEAR STRESS TOPOLOGICAL SKELETON AND NEAR-WALL MASS TRANSPORT IN CARDIOVASCULAR FLOWS USING A EULERIAN-BASED METHOD, Summer Biomechanics, Bioengineering and Biotransport Conference 2021, 2021.

De Nisco G., Mazzi V., Calo' K., **Lodi Rizzini M.**, Chiastra C., Wentzel J.J., Steinman D.A., Gallo D., Morbiducci U., EULERIAN-BASED WALL SHEAR STRESS TOPOLOGICAL SKELETON AS A TEMPLATE OF NEAR-WALL MASS TRANSPORT IN ARTERIES, ESB 2021, 2021.

Lodi Rizzini M., Russo G., Pedicino D., Vinci R., Gallo D., Genuardi L., Migliavacca F., Burzotta F., Morbiducci U., Crea F., Liuzzo G., Chiastra, C., HEMODYNAMIC AND MOLECULAR PROFILES OF STABLE AND UNSTABLE HUMAN CORONARY PLAQUES, ESB 2021, 2021.

Lodi Rizzini M., Tasso P., Raptis A., Matsagkas M., Gallo D., Xenos M., Morbiducci U., Patient-specific modelling for the assessment of the hemodynamics risk of failure in endovascular aneurysm repair, L'era delle 3R: modelli in silico, in vitro e in vivo per promuovere la ricerca traslazionale, 2021.

Lodi Rizzini M., Candreva A., Chiastra C., Mizukami T., Gallo D., Aben JP., Muller O., De Bruyne B., Collet C., Morbiducci U., WALL SHEAR STRESS TOPOLOGICAL SKELETON VARIABILITY PREDICTS MYOCARDIAL INFARCTION, Summer Biomechanics, Bioengineering and Biotransport Conference 2021, 2021.

Lodi Rizzini M., Tasso P., Gallo D., D'Avenio G., Amodeo A., Morbiducci, U., Grigioni M., Fontan Computational Hemodynamics: Impact of Inlet Velocity Profile Features with Implications on Clinically Relevant Parameters, Seventh National Congress of Bioengineering, 2021.

Lodi Rizzini M., Gallo D., Chiastra C., D'Ascenzo F., Morbiducci U., Does the shape of inflow velocity profiles affect hemodynamics in computational coronary artery models?, ESB-ITA 2019, 2019.

De Nisco G., Siciliano, K., Tasso P., **Lodi Rizzini M.**, Mazzi V., Calò K., Antonucci M., Gallo D., Morbiducci U., Exploring novel arterio-venous graft designs to reduce vascular access failure risk, ESB-ITA 2019, 2019.

Tasso P., **Lodi Rizzini M.**, Raptis A. Matsagkas M., Gallo D., Xenos M., Morbiducci U., Helical flow as possible mechanism of migration risk

reduction in EVAR-treated patients, 25th Congress of the European Society of Biomechanics, 2019.

Tasso P., Raptis A., Matsagkas M., **Lodi Rizzini M.**, Gallo D., Xenos M., Morbiducci U., Comparing hemodynamic and geometric profiles of commercial devices for endovascular AAA repair, World Congress of Biomechanics, 2018.

Raptis A., Tasso P., Xenos M., **Lodi Rizzini M.**, Gallo D., Morbiducci U., Matsagkas M., Profiling post-EVAR morphometry and hemodynamics through image-based computational analysis: comparison among endovascular devices, LIVE 2018 - Leading Innovative Vascular Education, 2018.

Tasso P., Raptis A., Matsagkas M., **Lodi Rizzini M.**, Gallo D., Xenos M., Morbiducci U.; Morphological and hemodynamic characterization of post endovascular AAA repair: comparison between two different commercial devices, 29th International Congress of the Society for Medical Innovation and Technology, 2017.

Tasso P., Raptis A., Xenos M., **Lodi Rizzini M.**, Gallo D., Matsagkas M.; Morbiducci U.; Anatomic-based analysis to screen post endovascular aneurysm repair patients; 23rd Congress of the European Society of Biomechanics; 2017.